



University  
of Glasgow

Dhirhe, Devnath (2013) *Monolithic tuneable quantum cascade lasers*. PhD thesis.

<http://theses.gla.ac.uk/4604/>

Copyright and moral rights for this thesis are retained by the author

A copy can be downloaded for personal non-commercial research or study, without prior permission or charge

This thesis cannot be reproduced or quoted extensively from without first obtaining permission in writing from the Author

The content must not be changed in any way or sold commercially in any format or medium without the formal permission of the Author

When referring to this work, full bibliographic details including the author, title, awarding institution and date of the thesis must be given

UNIVERSITY OF GLASGOW

# Monolithic Tuneable Quantum Cascade Lasers

by

Devnath Dhirhe

A thesis submitted in partial fulfillment for the  
degree of Doctor of Philosophy

in the

Division of Electronics and Nanoscale Engineering  
School of Engineering

September 2013

# Declaration of Authorship

I, **Devnath Dhirhe**, declare that this thesis titled, ‘**Monolithic Tuneable Quantum Cascade Lasers**’ and the work presented in it are my own. I confirm that:

- This work was done wholly or mainly while in candidature for a research degree at this University.
- Where any part of this thesis has previously been submitted for a degree or any other qualification at this University or any other institution, this has been clearly stated.
- Where I have consulted the published work of others, this is always clearly attributed.
- Where I have quoted from the work of others, the source is always given. With the exception of such quotations, this thesis is entirely my own work.
- I have acknowledged all main sources of help.
- Where the thesis is based on work done by myself jointly with others, I have made clear exactly what was done by others and what I have contributed myself.

Signed: **Devnath Dhirhe**

Date: **September 2013**

**UNIVERSITY OF GLASGOW****Abstract****Divison of Electronics and Nanoscale Engineering****School of Engineering****Doctor of Philosophy****by****Devnath Dhirhe**

This thesis is concerned with the design, fabrication and characterisation of monolithic tuneable quantum cascade lasers (QCLs), which are suitable for tuneable diode laser based absorption spectroscopy and polarisation dependent spectroscopy in the mid-infrared wavelength range. All investigations and device development work were carried out using the QCL structure based on strain-compensated  $\text{Ga}_{0.331}\text{In}_{0.669}\text{As}/\text{Al}_{0.659}\text{In}_{0.341}\text{As}$  grown on an InP substrate that emits light around 4500 nm wavelength. To make the QCLs electrically tuned, two laser designs were investigated : the double ring quantum cascade laser based on the Vernier-tuning effect, and the integrated tuneable birefringent waveguide utilising current controlled birefringence in quantum-wells.

The key advantage of the Vernier tuning effect based the double ring laser design is that it can facilitate both a single mode and wide-tuning range operation. The Vernier tuning enhancement factor associated with the coupled waveguide is responsible for a wide-tuning range observed in double ring configuration. However, the tuning range is limited by the available gain bandwidth (i.e. FWHM of spontaneous spectra) in the material and the maximum obtainable index change of the tuner ring. Theoretically, the tuning range of 155 nm was estimated for the double ring quantum cascade laser (DRQCL) design employed in this thesis. However, experimentally, a single mode ( $\sim 19$  dB single sideband suppression ratio) and tuning range of 59 nm which covers almost half the bandwidth were observed.

For the first time in the history of the QCL, a research into the design, fabrication and characterisation of integrated polarisation mode convertors (PMCs) has been carried out. The PMC design is based upon etching trenches, using the RIE lag effect, of sub-wavelength dimensions into one side of a waveguide in order to

achieve an asymmetric cross-sectional profile, resulting in a waveplating effect. This thesis presents such PMCs integrated with QCLs that emit 69% TE light with the polarisation angle of  $65^\circ$  from one facet and a pure TM light emitted from the other facet using a 256  $\mu\text{m}$  long PMC design (design D2).

An integrated tunable birefringent waveguide (ITBW) consisting of two PMCs with a differential phase shift (DPS) section between them. To probe the birefringence operation, a sub-threshold electroluminescence was employed to investigate the single pass operation of the ITBW. A theory based on the electro-optic properties of birefringence in QCL waveguides was used combined with a Jones-matrix-based description to gain an understanding of the electroluminescence results. With the QCL operating above threshold, polarisation and wavelength tuning of the signal output was demonstrated. By comparing the sub-threshold electroluminescence and active polarisation angle measurement result with the Jones-matrix model, the material birefringence (no DPS current),  $4n$ , was estimated to be around 0.005 for the QCL employed in this work. However, single mode emission was not observed and 24 nm discontinuous tuning was recorded. Despite this, using a QCL incorporating an ITBW device, active polarisation control over  $45^\circ$  was demonstrated, and currently, to the best of the authors knowledge there has been no other QCL device that is capable of electronically controlling the output polarisation.

# *Acknowledgements*

First of all, my sincere gratitude goes to my supervisor, Prof. Charles N. Ironside for his endless support and supervision. I would also like to thanks, Prof. Douglas J. Paul, Prof. David C. Hutchings, Dr. Mark Sorel, Dr. Barry M. Holmes, Dr. Thomas J. Slight, Dr. Corrie D. Farmer and Dr. Chidi C. Nshii, for their advice and encouragements received during tenure of my PhD studies.

For useful discussion, I would like to thanks Prof. John Arnold, Prof. Richard De La Rue, Dr. Michael Strain, Dr. Lianping Hou, Dr. Antonio Samaelli, Dr. Piotr Stolarz, Dr. Mohsin Haji, Dr. Muhammad A. Naeem, Shahid Mahmood, Vincenzo Pusino and Sanker Peralagu. Special thanks to Andrew Geer, Scott Watson and Dr. Wout Jansen for proof reading of my thesis.

Form the JWNC Team, I would like to thank Dr. Stephen Thoms, Dr. Hiaping, Dougi, Mark, Ronnie, Helen, Linda and Donald. I would like to thank Bill Ward for providing desired tools on time during laser characterisation.

Many thanks to Dr. Wyn Meredith from Compound Semiconductor Technologies for wafer supply and allowing us to use their ICP etching tool. Also thanks to Dr Nigel Langford from University of Strathclyde for CO gas supply for our gas phase spectroscopy experiments.

I acknowledge the financial support from Ministry of Social Justice and Empowerment, Government of India, New Delhi, India.

I am particularly thankful to my family for their constant support and encouragement during my study.

Finally, my wife (Kavita) and son (Suvigya), I love you and apologies for all the difficulties you have faced in my absence.

---

## Publications

### Peer Review Journal Papers

1. D. Dhirhe, T. J. Slight, C. C. Nshii, and C. N. Ironside, “A tunable single-mode double-ring quantum-cascade laser,” *Semicond. Sci. Technol.*, vol. 27, no. 9, pages 094007, July 2012.
2. D. Dhirhe, T. J. Slight, B. M. Holmes, D. C. Hutchings, and C. N. Ironside, “Quantum cascade lasers with an integrated polarization mode converter,” *OPTICS EXPRESS*, vol. 20, no. 23, pp. 25711-25717, November 2012.
3. D. Dhirhe, T. J. Slight, B. M. Holmes, and C. N. Ironside, “Active polarisation control of a quantum cascade laser using integrated tuneable birefringent waveguide,” *OPTICS EXPRESS*, (Accepted for publication).

### Peer Review Conference Papers

1. D. Dhirhe, T. J. Slight, B. M. Holmes, D. C Hutchings, and C. N. Ironside, “Polarization control of a quantum cascade laser,” *Conference on Lasers and Electro-Optics 2012*, OSA Technical Digest (Optical Society of America, 2012), paper JW2A.99.
2. D. Dhirhe, T. J. Slight, B. M. Holmes, D. C Hutchings, and C. N. Ironside, “Wavelength tuning and polarisation control with an integrated tuneable birefringent filter for quantum cascade lasers,” *The European Conference on Lasers and Electro-Optics and the International Quantum Electronics Conference (CLEO/Europe-IQEC)*, paper CB-1.5, Munich, Germany, 12-16 May 2013.

### Non-Peer Review Conference Papers

1. D. Dhirhe, T. J. Slight, B. M. Holmes, D. C Hutchings, and C. N. Ironside, “Polarization control of a quantum cascade laser,” *The second SU2P Solid-State Lasers and Nonlinear Optics Theme Workshop*, School of Engineering, University of Glasgow, Glasgow, UK, 25<sup>th</sup> June 2012

2. D. Dhirhe, T. J. Slight, B. M. Holmes, D. C Hutchings, and C. N. Ironside, “An Integrated tunable birefringent filter for quantum cascade lasers,” *International Quantum Cascade Lasers School and Workshop 2012*, Vienna, AUSTRIA, 2<sup>nd</sup> - 6<sup>th</sup> December 2012
3. D. Dhirhe, T. J. Slight, C. C. Nshii, M. Sorel and C. N. Ironside, “Spectroscopy with a double-ring quantum-cascade laser,” *International Quantum Cascade Lasers School and Workshop 2012*, Vienna, AUSTRIA, 2<sup>nd</sup> - 6<sup>th</sup> December 2012
4. T. J. Slight, D. Dhirhe, W. Meredith, and C. N. Ironside , “Wavelength and polarisation control of quantum cascade lasers,” *US-UK Workshop in Mid-IR to THz Technology and Applications*, Royal Society of Edinburgh, Edinburgh, UK, 18<sup>th</sup> - 19<sup>th</sup> February 2013
5. D. Dhirhe, T. J. Slight, B. M. Holmes, D. C Hutchings, and C. N. Ironside, “Active and passive polarisation control of quantum cascade lasers,” *HETECH 2013 - 22nd European Workshop on Heterostructure technology*, University of Glasgow, Glasgow, UK, 9-11th Sept. 2013.

# Contents

Declaration of Authorship	i
Abstract	ii
Acknowledgements	iv
Publications	v
List of Figures	xi
List of Tables	xvii
<b>1 Introduction</b>	<b>1</b>
1.1 Introduction	1
1.2 Quantum Cascade Laser	6
1.3 Material system and wafer structure employed	8
1.4 Aim	9
1.5 Objective	9
1.6 Thesis Outline	10
<b>2 Fabrication and Characterisation</b>	<b>11</b>
2.1 Introduction	11
2.2 Fabrication	12
2.2.1 Fabrication Process Overview	12
2.2.2 Dielectric Deposition	12
2.2.3 Electron Beam Lithography	14
2.2.3.1 Electron Beam Lithography Resists	15
2.2.4 Dry Etching	16
2.2.4.1 Insulator (SiO <sub>2</sub> and Si <sub>3</sub> N <sub>4</sub> ) Etching	17
2.2.4.2 InGaAs/InAlAs/InP Etching	18
2.2.4.3 RIE Lag Effect	19
2.2.5 Metal Contact Deposition	21
2.2.6 Step-by-Step Fabrication Processes	21

2.2.6.1	Sample Preparation . . . . .	21
2.2.6.2	First e-beam Lithography . . . . .	22
2.2.6.3	Second E-beam Lithography . . . . .	23
2.2.6.4	Third E-beam Lithography . . . . .	26
2.2.6.5	Substrate Thinning, Bottom Contact Metallisation and Annealing . . . . .	27
2.2.6.6	Cleaving, Mounting and Wire-bonding . . . . .	28
2.3	Characterisation . . . . .	28
2.3.1	Description of Experimental Setup . . . . .	30
2.3.2	Spectra Measurements . . . . .	32
2.3.3	Light-Current-Voltage (L-I-V) Characteristics . . . . .	33
2.3.4	Electro-Optics Polarisation Measurement Technique . . . . .	33
2.4	Conclusion . . . . .	35
<b>3</b>	<b>Double-Ring Quantum Cascade Laser</b>	<b>36</b>
3.1	Introduction . . . . .	36
3.1.1	Aim . . . . .	37
3.1.2	Objective . . . . .	37
3.2	Theory of the Double-Ring Quantum Cascade Laser . . . . .	38
3.2.1	Operation of the Double-Ring Quantum Cascade Laser . . . . .	38
3.2.2	Double Ring Quantum Cascade Laser (DRQCL) Numerical Model . . . . .	41
3.2.3	DRQCL Design Considerations . . . . .	44
3.2.3.1	Bending Loss . . . . .	44
3.2.3.2	Coupler Analysis . . . . .	46
3.3	DRQCL Modelling and Fitting Parameter . . . . .	49
3.4	Characterisation Results and Discussions . . . . .	50
3.4.1	Light output-Injection current-Voltage (L-I-V) . . . . .	50
3.4.2	Electroluminescence and Wavelength Tuning . . . . .	52
3.5	Spectroscopy . . . . .	56
3.5.1	CO Spectroscopy with Globar Source . . . . .	56
3.5.2	CO Spectroscopy Tuneable DRQCL . . . . .	56
3.6	Conclusion . . . . .	57
<b>4</b>	<b>Integrated Polarisation Mode Converter</b>	<b>60</b>
4.1	Introduction . . . . .	60
4.1.1	Aim . . . . .	62
4.1.2	Objective . . . . .	62
4.2	Polarisation Mode Conversion Theory . . . . .	62
4.2.1	Polarisation Purity . . . . .	63
4.2.2	Definition of Quarter Waveplate and Half Waveplate . . . . .	65
4.3	Integrated Polarisation Mode Converter Design . . . . .	66
4.3.1	Waveguide width Optimisation . . . . .	67
4.3.2	Polarisation Mode Converter Design . . . . .	69
4.3.3	Design Description and Analysis . . . . .	71

4.3.3.1	Design 1 (D1)	71
4.3.3.2	Design 2 (D2)	73
4.3.4	Integration with Distributed Bragg Reflector Grating	77
4.4	Characterisation and Results	79
4.4.1	DBR Laser	79
4.4.2	Integrated Polarisation Mode Converter	80
4.4.2.1	Integrated PMC (design D1)	80
4.4.2.2	Integrated PMC (design D2)	84
4.5	Conclusion	86
<b>5</b>	<b>Integrated Tuneable Birefringent Waveguide</b>	<b>88</b>
5.1	Introduction	88
5.1.1	Aim	90
5.1.2	Objective	91
5.2	Integrated Tuneable Birefringent waveguide Design	91
5.3	Electro-Optic Birefringence of the Quantum Cascade Laser and the Jones Matrix Description	92
5.3.1	Single Pass Jones Matrix Model for ITBW Device	93
5.3.1.1	Single Pass Jones Matrix Model for Alternative ITBW Design	95
5.3.2	Theory of Laser Operation with Birefringent Components	96
5.3.2.1	Description for Alternative ITBW Design	99
5.4	ITBW Device Description	100
5.5	Characterisation and Result	101
5.5.1	Sub-threshold Single Pass Measurements	102
5.5.1.1	Alternative Analysis of Sub-threshold Electroluminescence (EL) Results	108
5.5.2	Measurement of Operation of Laser Incorporate Birefringent Components	108
5.5.3	Active Polarisation Control	111
5.5.3.1	Alternative Analysis of Active Polarisation Control Results	113
5.5.4	Comparison of Analysis	114
5.6	Conclusion	115
<b>6</b>	<b>Conclusions and Recommendations for Future Works</b>	<b>117</b>
6.1	Recommendations for Future Works	120
<b>A</b>	<b>Tri-layer ZEP520A EBL resist deposition, development and removal process</b>	<b>122</b>
<b>B</b>	<b>Metal lift-off process</b>	<b>125</b>
<b>C</b>	<b>Published Papers</b>	<b>127</b>

<b>D Communicated Paper</b>	<b>141</b>
-----------------------------	------------

<b>Bibliography</b>	<b>156</b>
---------------------	------------

# List of Figures

1.1	Some of the molecules and their absorption wavelengths in the Mid Wave Infrared (MWIR) region [1] . . . . .	2
1.2	Schematic of conduction band energy profile used to illustrate the operating principle of a portion of the quantum cascade laser. The wavy line shows the moduli squared of the calculated wavefunction. Calculation was carried out for $\text{In}_{0.669}\text{Ga}_{0.331}\text{As}-\text{Al}_{0.659}\text{In}_{0.341}\text{As}/\text{InP}$ material system based Quantum Cascade Laser (QCL) design (employed in this thesis) under an average electric field of 70 kV/cm. Conduction band offset $\Delta E_c \sim 0.785\text{eV}$ and radiative intersubband transition energy between $E_3$ and $E_2$ , $\sim 0.273\text{eV}$ ( $\sim 4.5 \mu\text{m}$ ), was calculated. Calculation was carried out with the help of nanostructured modelling tool nextnano <sup>3</sup> . Further design description can be found on Ref. [2] . . . . .	7
1.3	Schematic diagram of a ridge waveguide quantum cascade laser. . .	9
2.1	The basic fabrication process steps used to fabricate QCLs reported in this thesis. Step-by-Step Fabrication Processes were detailed in section 2.2.6 . . . . .	13
2.2	Functional diagram of negative and positive resists before and after development. In negative resist unexposed area removed by the developer, with positive resist, exposed area removed by the developer. 15	15
2.3	Scanning Electron Microscope (SEM) image of variation of etch depth with respect to feature gap width, (a) $w = 0.3 \mu\text{m}$ (b), $w = 0.5 \mu\text{m}$ (c), $w = 0.6 \mu\text{m}$ , and (d) $w = 0.8 \mu\text{m}$ . RIE lag study were carried out using recipe and tool describe in Section 2.2.4.2 for 6 mins etch time on QCL wafer described in Section 1.3. . . . .	19
2.4	Shows the variation of etch depth as function of feature gap width for 6 mins etch time using using recipe and tool describe in Section 2.2.4.2. . . . .	20
2.5	SEM image is the cleaved front facet of fully processed device and showing the metal continuity over $4.9 \mu\text{m}$ deep etch waveguide. . .	22
2.6	Shows the top view SEM image after Inductively Coupled Reactive Ion Etching (ICP-RIE) etching (a) Double ring waveguide (b) Magnified view of ring coupler (c) Integrated Polarization Mode Convertors (PMCs) device (d) Magnified view of taper input section of PMCs (e) and (f) Cross marker and Global markers. . . . .	24

2.7	Top view photograph of 5ZEP520a resist after spinning (a) a Single layer: showing non-uniform surface morphology on deeply etch surface (b) Tri-layer: uniform and smooth surface morphology on deeply etch surface, coating/baking recipe are detailed in Appendix A	25
2.8	Shows the top view of SEM image showing contact window for metal deposition. Contact window open by etching 1 $\mu\text{m}$ insulator (500 nm $\text{Si}_3\text{N}_4$ and 500 nm $\text{SiO}_2$ ), etch chemistry are detailed in Table 2.3 and Table 2.4.	25
2.9	Shows the SEM image liftoff patterns of (a) Integrated PMCs device (b) Magnified view Distributed Bragg Reflector (DBR) and PMC area (c) Metal liftoff between two rings (d) Liftoff from device ID area.	27
2.10	Shows the SEM image of the fully processed devices (a) Integrated PMC and (b) Photograph of integrated tunable birefringence waveguide for Quantum Cascade Lasers (QCLs).	29
2.11	Schematic illustration of the experimental setup used to characterised QCLs at the University of Glasgow. The optical system comprises of the Burker Vertex 70 FTIR spectrometer and gold coated external parabolic mirrors. The laser heatsink temperature (Oxford instruments close cycle cooler (CCC1204)) was controlled by Oxford instrument temperature controller (Model ITC502) using a rhodium iron thermocouple. The electrical system comprises with High Voltage pulse generator (DEI-HV1000), Gated Integrator/BOXCAR Averager unit, lock-in amplifier and Oscilloscope	31
2.12	Shows the Transverse Magnetic (TM)/Transverse Electrical (TE) transmittance ratio as a function wavelength for the Vertex 70 Fourier Transform Infra-Red (FTIR) spectrometer. Measurement was carried out using a BaF2 polariser, Potassium Bromide (KBr) beam-splitter and DLATGS detector at resolution 4 $\text{cm}^{-1}$ (10 nm). Measurement was carried out by Dr Paul Turner, Applications Scientist, Bruker Optics Ltd., USA.	34
3.1	Shows a schematic illustration of generic double-ring laser adopted from ref. [3].	38
3.2	Shows the spontaneous emission spectra from the FP laser at 298 K we process from same wafer, which we utilise in this thesis. The measurement was carried out using lock-in step scan detection technique with 8 nm FTIR resolution. Mark as A and B are the gain peaks at 4540 nm and 4610 nm respectively	40
3.3	Shows the top of the chip SEM image of a double ring quantum cascade laser. In this structure, we employed two rings with slightly different radii and one output waveguide through which output measurements were carried out. The coupling fraction of the coupler between ring 2 and the output waveguide is calculated to be $K_1 \sim 0.036$ and the coupling fraction between the rings is calculated to $K_2 \sim 0.026$ , these parameters were calculated using the beam propagation method and used as input parameters to SM theory.	44

3.4	Shows the analytically computed bending loss as a function of curve radius for index contrast, $\frac{\Delta n}{n} = \frac{n_1 - n_2}{n_2} = 0.9765$ (for core index, $n_1 = 3.36$ and cover index $n_2 = 1.7$ ), and 0.9118 (for effective index, $n_1 = 3.25$ and cover index $n_2 = 1.7$ ). . . . .	45
3.5	Show the SEM image of various coupling scheme (a) Evanescent field coupler based on Reactive Ion Etching (RIE) lag effect (b) Multimode Interference (MMI) coupler (c) Y-coupler and (d) general purpose MMI coupler. . . . .	46
3.6	Shows the detailed illustration of general purpose MMI coupler between output waveguide and ring 1, where coupler length is around $60 \mu\text{m}$ and $21 \mu\text{m}$ wide. In the simulation, as indicated in this figure, input powers were launched from ring 1 from the bottom and coupled/launched power were monitored from the top. . . . .	47
3.7	Shows the Beam Propagation Method (BPM) simulation result for different coupler properties (i.e coupling fraction, launch power and Insertion loss) with respect to mode propagation distance. From the simulation we conclude the following: Simulation results are summarized as: (1) for rings coupler ( $55 \mu\text{m}$ long coupler), coupling fraction is $\sim 0.026$ , more than 52% launch power propagates within the launch ring waveguide (2) for output power waveguide and ring 1 coupler ( $60 \mu\text{m}$ long coupler), coupling fraction is $\sim 0.036$ , more than 54% launch power propagates within the launched ring waveguide. . . . .	48
3.8	Shows the Light output-Injection current-Voltage (L-I-V) curves of the DRQCL. The current density is the peak current density into Ring 1. . . . .	51
3.9	Shows the L-I-V curves of the SRQCL measured at $25^\circ\text{C}$ , where a ring and output coupler waveguide dimensions is identical as DRQCL . . . . .	52
3.10	(a) Shows the normalized spectra for DRQCLs device measured at DC current from 0, 30, 60 and 90 mA with the spectral resolution of 0.5 nm and (b) The tuning curve estimated by the SM theory for various dc current applications into ring 2. If we assume a linear dependence of the refractive index with injection current at $-8.25 \times 10^{-4} \text{ kA}^{-1}\text{cm}^2$ then we can fit the SM theory to the results . . . . .	53
3.11	The wavelength tuning as a function of dc current measured at different heat sink temperatures. . . . .	54
3.12	The spontaneous emission spectra measured using $3000 \mu\text{m}$ long and $8 \mu\text{m}$ wide Fabry-Perot laser (from the same wafer as the DRQCL) and the normalized single-mode output of the DRQCLs at various dc current injected into Ring 2. . . . .	55
3.13	Shows the IR absorption spectrum of the CO using Globar source from 4540 nm to 4950 nm. . . . .	57
3.14	(a) CO absorption spectra using Globar source. (b) and (c) Laser and CO absorption spectra at 0 mA dc current, (e) and ( f ) laser and CO absorption spectra at 90 mA dc current, (d) and (g) experimental absorption coefficient at 0 and 90 mA, respectively. . . . .	58

4.1	Illustration of the complete functionality of a PMC (a) Illustrates in 3D a side view of the PMC waveguides with asymmetric cross-sectional profiles employed in this work the red region indicates the approximation position of the active region of the device (description can be found in section 4.3) (b) Illustrates the propagation of TE and TM polarization modes (Hybrid TE - TM modes) along (z-direction) the PMC waveguides also indicated are the circular and elliptical states of polarization (SOP) and direction of polarization as a function of z (c) Illustrates the evolution of the circular and elliptical SOP and direction of polarization as a function of z (d) Resulting phase difference between TE - TM modes along the guide. . . . .	64
4.2	Schematic illustration of the chip layout of a QCL that includes a gain section, lateral DBR and an integrated PMC, the trenches of the PMC were etched using the reactive ion etching lag effect. There is no electrical contact to the PMC section. . . . .	66
4.3	Calculated effective index of the guided modes in a ridge waveguide at different ridge width for a laser operating wavelength $\lambda = 4445$ nm. Calculation was carried out using a full-vectorial, 3D eigensolver, as implemented in the software packages Lumerical Mode Solutions Lumerical Mode Solutions (LSM) [4] . . . . .	67
4.4	(a) & (b) Show the simulated mode profiles of the TM and TE components respectively of the lowest order guided mode (without asymmetric cross-section). Calculation was carried out using a full-vectorial, 3D eigensolver, as implemented in the software packages Lumerical Mode Solutions LSM [4] . . . . .	68
4.5	SEM images of a PMC waveguide after ICP-RIE etching (design D1) (a) Top view of taper input section of PMC (b) Cleaved cross-section view of PMC. . . . .	70
4.6	Detail design description of PMC design D1 using by etching two trench (a) Top view (b) cross-section view . . . . .	70
4.7	Calculation of mode profiles: (a) and (b) the TM and TE components respectively of the lowest order guided mode within the asymmetric section of design D1. Calculation was carried out at $z=10 \mu\text{m}$ just after tapered region of PMC. . . . .	71
4.8	(a) Calculated TM to TE conversion versus propagation distance using BPM of design D1 (b) Calculated TE polarisation purity (%) versus propagation distance using BPM of design D1 . . . . .	72
4.9	Shows the variations of TE polarisation purity at +/- 100 nm change in trench height of design D1. Where trench width is fixed at $0.5 \mu\text{m}$ and calculation was carried out using a BPM. . . . .	74
4.10	Detailed design descriptions of PMC design D2 (a) Top view (b) cross-section view . . . . .	74

4.11	(a) and (b) show the TM and TE components respectively of the lowest order guided mode within the asymmetric section of design D1. Calculation was carried out at $z=10 \mu\text{m}$ just after tapered region of PMC. . . . .	75
4.12	(a) Calculated TM to TE conversion versus propagation distance using BPM of design D1 (b) Calculated TE polarisation purity (%) versus propagation distance using BPM of design D2 . . . . .	76
4.13	Shows the variations of TE polarisation purity at $\pm 100 \text{ nm}$ change in trench height of design D1. Where trench width is fixed at $0.5 \mu\text{m}$ and calculation was carried out using a BPM. . . . .	77
4.14	The top view of fully integrated PMC device is shown. . . . .	78
4.15	Shown is the calculated stop-band of DBR gratings for gratings period of $700 \text{ nm}$ . The calculation was carried out using the GratingMOD tool by RSoft [5]. . . . .	79
4.16	Shows the output peak optical power vs drive current densities characteristics for a DBRs QCL without PMCs measured at $298 \text{ K}$ . . . . .	80
4.17	Emission spectra of pulse and chirped DBR QCL without PMC acquired with FTIR resolution $0.5 \text{ nm}$ at peak pulse current $1.3 \cdot I_{th}$ . . . . .	81
4.18	Polar plots of output power (red line) from DBR facet of the QCL as function of wire-grid polarizer angle. . . . .	81
4.19	(a),(c) and (e) Shows the light injection current (L-I) characteristics and (b), (d) and (f) are the spectral emission of a $56 \mu\text{m}$ , $71 \mu\text{m}$ and $119 \mu\text{m}$ long PMC devices, based upon design D1. . . . .	83
4.20	Polar plots of normalized output power from PMC facet as function of wire-grid polarizer angle for $56 \mu\text{m}$ and $119 \mu\text{m}$ long PMC (design D1). The maxima of the beam intensity were recorded around $5^\circ$ and $20^\circ$ , respectively. . . . .	84
4.21	(a) L-I characteristics of $265 \mu\text{m}$ PMC device showing the TM, TE and total power (b) showing TE and TM spectra by drive laser section above $1.3 \cdot I_{th}$ . . . . .	85
4.22	Polar plots of normalized output power from $256 \mu\text{m}$ long PMC & gain facet of the QCL as function of wire-grid polarizer angle. . . . .	86
5.1	Illustration of the Birefringent Filter, consisting of a sequence of birefringent crystals (BC) and polarisers (P). . . . .	89
5.2	Schematic design for an integrated tuneable birefringent waveguide for QCLs, it shows the gain section (GS) and trenches in the upper part of the waveguide that form the PMCs [6, 7] which are designed as $1/4$ waveplates, between the PMCs is the Differential Phase Shift (DPS) section where current can be applied to alter the phase relationship between the TE and TM modes. The approximate position of the active region is indicated in red . . . . .	92
5.3	Shows the equivalent optical circuit of Integrated Tuneable Birefringent Waveguide (ITBW) for full round trip consideration. Figure also indicates the different components of optical circuit. The X marks the starting point for the round trip analysis. . . . .	97

5.4	A photograph shows the top view of the processed ITBW device. Underneath the Gain section (GS) and DPS section waveguide contact windows were opened for current injection and the rest of the structure is protected by 500 nm $Si_3N_4$ and 500 nm $SiO_2$ insulating layers. . . . .	101
5.5	Shows a schematic of the experimental setup for characterising the QCL that includes an ITBW; the GS is injected with current $i_g$ and the ITBW has a current $i_{DPS}$ injected, that electro-optically alters the birefringence of the DPS section. The polarisation is selected using a linear polariser and the output spectrum of device is measured using a FTIR spectrometer. All experiments were conducted at 250 K QCL heat sink temperature. . . . .	102
5.6	The TM spectrum of the sub-threshold EL spectra of a QCL incorporating a ITBW measured at various DC current densities injected into the DPS section. . . . .	103
5.7	Shows the sub-threshold TM EL spectra emitted from the facet next to the gain section of the QCL ITBW device. For detailed experimental setup, refer Figure 5.5. . . . .	104
5.8	Experimental result (red curve) and Jones matrix model fitting curve (black curve and mark as theory) of the EL spectra of the ITBW device without current injection into the DPS section is shown. . . . .	105
5.9	Measured gain spectra by injecting DC current density $0.33 \text{ kA/cm}^2$ and $0.69 \text{ kA/cm}^2$ into DPS section. . . . .	106
5.10	Wavelength and current dependence of the refractive index which is calculated from the data using a Kramers-Kronig-transformation of the gain spectra. More details about the gain measurement can be found in reference [8]. . . . .	106
5.11	The experimental EL spectra and Jones matrix model curve fit of the ITBW device (a) $i_{DPS} = 0.33 \text{ kA/cm}^2$ and (b) $i_{DPS} = 0.69 \text{ kA/cm}^2$ . . . . .	107
5.12	The experimental EL spectra and Jones matrix model curve fit of the ITBW device (a) $i_{DPS} = 0 \text{ kA/cm}^2$ (b) $i_{DPS} = 0.33 \text{ kA/cm}^2$ and (c) $i_{DPS} = 0.69 \text{ kA/cm}^2$ . . . . .	109
5.13	The wavelength tuning at different DC current densities injected into DPS section. . . . .	110
5.14	Free running FP mode plot for gain section and DPS section. Figure clearly indicates that FP modes are in-phase every 11 nm. . . . .	111
5.15	Shows the change in polarization angle as a various current density injection values into DPS section. the GS pulsed current was fixed at $6.8 \text{ kA/cm}^2$ ( $1.3 \cdot I_{th}$ ) and the current to the DPS section was varied between $0 \text{ kA/cm}^2$ and $0.97 \text{ kA/cm}^2$ in steps of $0.13 \text{ kA/cm}^2$ . . . . .	112
5.16	Shows the change in polarization angle as a various current density injection values into DPS section. the GS pulsed current was fixed at $6.8 \text{ kA/cm}^2$ ( $1.3 \cdot I_{th}$ ) and the current to the DPS section was varied between $0 \text{ kA/cm}^2$ and $0.97 \text{ kA/cm}^2$ in steps of $0.13 \text{ kA/cm}^2$ . . . . .	114

# List of Tables

1.1	Waveguide layer, materials, thicknesses and doping level of the QCL material we used for this project are shown. . . . .	8
2.1	PECVD SiO <sub>2</sub> deposition process parameter used to deposit SiO <sub>2</sub> using Plasmalab 80plus tool. Process parameters used for SiO <sub>2</sub> in Plasmalab80 plus tool were optimised by the dry etch laboratory technical staff . . . . .	14
2.2	PECVD Si <sub>3</sub> N <sub>4</sub> deposition process parameters. Process parameters used for Si <sub>3</sub> N <sub>4</sub> in Plasmalab80 plus tool were optimised by the dry etch laboratory technical staff . . . . .	14
2.3	Process parameter used to etch the 500 nm SiO <sub>2</sub> . Process parameters used for 500 nm SiO <sub>2</sub> in Plasmalab 80plus RIE tool were optimised by the dry etch laboratory technical staff . . . . .	17
2.4	Process parameter used to etch the 500 nm Si <sub>3</sub> N <sub>4</sub> . Process parameters used for 500 nm Si <sub>3</sub> N <sub>4</sub> in Plasmalab 80plus RIE tool were optimised by the dry etch laboratory technical staff. . . . .	17
2.5	Process parameter used for resist micro-mask and complete e-beam resist removal. . . . .	18
2.6	Fitting parameters for Equation 2.1 to calculate etch depth for given feature gap width. . . . .	21
3.1	Shows the parameters input into the SM theory to fit the theory to the observed wavelengths of the single mode outputs at different DC currents injected into ring 2 of the DRQCL. . . . .	50
4.1	Waveguide layer, materials, thicknesses and refractive indices of the QCL material we used for this project are shown. Refractive indices of the QCL material at $\lambda \sim 4445$ nm were calculated using ref. [9]. . . . .	67
4.2	Comparison of calculated and measured TE polarisation fraction as a function of PMC length. . . . .	82

# List of abbreviations/symbols

<b>THz</b> Terahertz	<b>JWNC</b> James Watt Nanofabrication Centre
<b>QCLs</b> Quantum Cascade Lasers	<b>CST</b> Compound Semiconductor Technology Ion Etching
<b>ITBW</b> Integrated Tunable Birefringent Waveguide	<b>ICP-RIE</b> Inductively Coupled Reactive Ion Etching
<b>PMC</b> polarisation mode converter	<b>GS</b> Gain Section
<b>GS</b> Gain Section	<b>QW</b> Quantum Well
<b>DPS</b> Differential Phase Shift	<b><math>SiO_2</math></b> Silica
<b>EBL</b> Electron Beam Lithography	<b><math>Si_3N_4</math></b> Silicon Nitride
<b>TE</b> Transverse Electrical	<b>PECVD</b> Plasma Enhanced Chemical Vapour Deposition
<b>TM</b> Transverse Magnetic	<b>IPA</b> Isopropyl alcohol
<b>FTIR</b> Fourier Transform Infra-Red	

---

<b>RF</b> Radio Frequency	<b>L-I-V</b> Light output-Injection current-Voltage
<b>RIE</b> Reactive Ion Etching	<b>InSb</b> Indium Antimonide
<b>InP</b> Indium Phosphide	<b>KBr</b> Potassium Bromide
<b>ISBT</b> Intersubband Transition	<b>GPIB</b> General Purpose Interface Bus
<b>Si</b> Silicon	<b>DC</b> Direct Current
<b>EBE</b> Electron Beam Evaporator	<b>DRQCL</b> Double-Ring Quantum Cascade Laser
<b>SEM</b> Scanning Electron Microscope	<b>ITBW</b> Integrated Tuneable Birefringent Waveguide
<b>QCL</b> Quantum Cascade Laser	<b>KRS-5</b> Thallium Bromoiodide
<b>DI</b> Deionised	<b>PMC</b> Polarization Mode Convertor
<b>VRU</b> Variable Resolution Unit	<b>DBR</b> Distributed Bragg Reflector
<b>HF</b> Hydrofluoric Acid	<b>CW</b> Continuous Wave
<b>LOR</b> Lifftoff Resists	<b>eV</b> Electron Volt
<b>AlN</b> Aluminium Nitrate	

---

<b>DFB</b> Distributed Feedback	<b>DRQCL</b> Double Ring Quantum Cascade Laser
<b>SMSR</b> Side Mode Suppression Ratio	<b>MWIR</b> Mid Wave Infrared
<b>HR</b> High Reflection	<b>FWHM</b> Full Width at Half Maximum
<b>PHR</b> Partial High Reflection	<b>FSR</b> Free Spectral Range
<b>SOI</b> Silicon on Insulator	<b>DRL</b> Double Ring Laser
<b>SOP</b> States of Polarization	<b>TDLAS</b> Tuneable Diode Laser Absorption Spectroscopy
<b>QW</b> Quarter Waveplate	<b>FIB</b> focused ion beam
<b>HW</b> Half Waveplate	<b>ICP</b> Inductively Coupled Plasma
<b>LSM</b> Lumerical Mode Solutions	<b>MMI</b> Multimode Interference
<b>BPM</b> Beam Propagation Method	<b>LMS</b> Lumerical Mode Solutions
	<b>EL</b> Electroluminescence

# Chapter 1

## Introduction

### 1.1 Introduction

This thesis presents an investigation of monolithic tuneable quantum cascade lasers (QCLs). QCLs are light sources based on intersubband transitions (i.e. transition between energy levels within the conduction band) in quantum wells [10]. Currently, they are made from largely the same set of III-V semiconductor alloys (InP and AlGaAs based alloys) as most conventional interband semiconductor lasers. Based on this, QCLs can benefit from the relatively mature materials technology associated with the fabrication of particularly InP based optical communications lasers. QCLs emission cover a broad range of wavelengths from mid-wave infrared (MWIR) to terahertz (THz) [11]. The MWIR atmospheric window ( $\lambda \sim 3 - 6\mu\text{m}$ ) is important because many greenhouse gases and hydrocarbons show strong molecular absorption fingerprints compare to long-wave infrared (LWIR) atmospheric window-see HITRAN [12]. Some of these molecules and their characteristic absorption wavelengths in the MWIR region are shown in Figure 1.1. These molecules can be detected using laser based absorption spectroscopy techniques, provided the emission wavelength of the laser is in resonance to the absorption energy of the targeted molecules.

## Molecular Absorption Fingerprints of some Gases

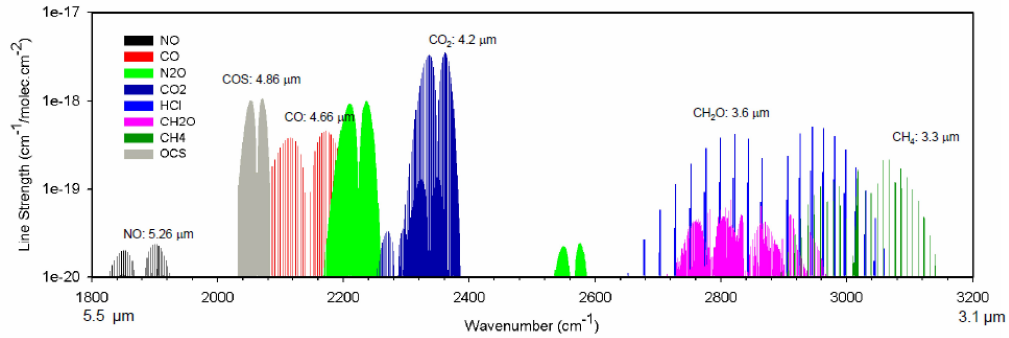


FIGURE 1.1: Some of the molecules and their absorption wavelengths in the MWIR region [1]

Tunable Diode Laser Absorption Spectroscopy (TDLAS) is a sensitive technique for the measurement and detection of low concentration of gases using tuneable diode laser based absorption spectrometry [13]. The key advantage of TDLAS over other techniques is the ability to detect very low concentration less than 100 ppt levels [14]. The basic components of a TDLAS system include, a tuneable diode laser light source, transmitting optics, optically accessible absorbing medium, receiving optics, and detectors. The laser is tuned over the characteristic absorption lines of the gas molecules. Using the Beer-Lambert law, the gas absorbance can be deduced based on intensity variation between gas presence and absence in the medium [15].

Interband cascade lasers (ICL) and quantum cascade lasers (QCLs), in the MWIR atmospheric window for TDLAS application, are important light sources due to single mode CW operation above room temperature. The theoretical concept of ICL has been proposed by Yang et al in 1995 [16], but an ICL was first realised in 1997 by Lin et al. [17] by demonstrating 3.8  $\mu\text{m}$  wavelength at 120 K. The structures comprise of a single GaInSb hole quantum well sandwiched by two InAs electron quantum wells, structure yielding a 'W' like geometry [18] similar to Type-II diode lasers [19]. Through indirect interband transitions, electrons and holes recombine between the InAs quantum well and valence band of two GaSb hole injector quantum wells to emit photons, where they relax into an InAs/AlSb superlattice and are then injected into the next cascade stage. Single mode CW

operation of an ICL-DFB, working above room temperature at  $\sim 3.7 \mu\text{m}$  wavelength with 50 mW peak power, has been recently reported [20]. The ultimate advantage of ICL is that they can operate at threshold current densities 30 times lower than the QCLs [20]. However, due to low power compare to QCL, trace gas detection sensitivity is limited to ppm level [21]. In the QCLs, wide single mode tunability, high power and CW operation above room temperature make them reliable candidates for sensitive trace gas sensing in the MWIR atmospheric window.

To obtain single mode operation in these devices, a variety of monolithic chip designs have been investigated and reported. Some of these include Distributed Feedback (DFB) [22], DFB with overgrown [23], lateral gratings [24], discrete mode lasers [25], square ring resonator [26], candy-cane shaped cavity [27].

The QCLs discussed above can be tuned by means of the thermal effect by varying the heatsink temperature. Using this technique, wavelength tuning coefficient ( $d\lambda/dT$ ) of  $\sim 0.2$  to  $\sim 0.49 \text{ nm}/^\circ\text{C}$ , has been demonstrated [24, 25, 28]. The typical wavelength tuning range is of the order of 10-12 nm, which is less than 10% compared with the available material gain bandwidth (i.e. Full Width at Half Maximum (FWHM) of spontaneous emission spectra). To maximise the tuning range, three different approaches were reported in the literature. The approaches are: coupled resonator lasers [29], DFB QCL arrays [30–32] and external cavity QCL [33–36]. Each approach has its advantages and disadvantages as discussed below:

**Coupled resonator:** The coupled resonator QCL, this working principal is based on the Vernier-tuning effect which was proposed by Fuchs et al. in 2010 [29]. Single mode quasi-continuous tuning of about 242 nm was realised between two areas of 8394 nm and 8785 nm wavelength by injecting current into the tuning section of the device.

**DFB arrays:** In 2007, the DFB QCL array approach was proposed by Lee et al. The device is based on an array of DFB QCLs with closely spaced

emission wavelengths spanning the gain bandwidth of the QCL material 32 buried DFB gratings were fabricated monolithically on the same chip. Each DFB were driven individually by a microelectronic controller and in order to obtain continuous spectral coverage between the individual lasers in the array, the lasers are tuned over a small range. This can be done by applying a subthreshold DC current to an individual laser. By utilising a DFB QCL array, single mode continuous tuning of about 70 nm was realised between wavelengths of 8700 nm and 9400 nm. Further progress has been reported by the Lee et al., the beams emerging from the individual lasers in the array are combined into a single beam using a beam combiner [37]. The major drawback of this is the requirement of complex individual laser controller and processing circuit.

**External cavity QCL:** The realisation of an external cavity (EC) QCL was first reported in 2001 by Luo et al. [33], In EC QCL, mirrors are arranged in a configuration external to the QCL to create the optical cavity and the output was taken from the zeroth order reflection. In their paper, a tuning range of 65 nm for a 4.5  $\mu\text{m}$  QCL design was reported. One of the key advantages is the tuning range, which is determined by the material gain bandwidth. By maximising the gain bandwidth (i.e. FWHM of spontaneous spectra) tuning range can also be maximised. This can be achieved by utilising the concept of heterogeneous QCLs which was first demonstrated by Gmachl et al. at Bell Laboratories who realized a two-wavelength laser emitting simultaneously [38]. The external cavity with heterogeneous QCL could be tuned over 3.8  $\mu\text{m}$  from 11.4  $\mu\text{m}$  to 7.6  $\mu\text{m}$ . Compared to tuneable QCLs, discussed above, the tuning mechanisms of EC QCL are much more complicated and sensitive toward mechanical instabilities and vibrations [39], thus making them unreliable for applications out of the laboratory.

In this thesis, two approaches were investigated for the development of electrically tuned QCLs. First, a double ring quantum cascade laser DRQCL based on Vernier-tuning effect, and second, an integrated tuneable birefringent waveguide (ITBW)

by utilising the intersubband transition induced birefringence of the quantum well.

On the **DRQCL** project, we investigate electrically tuneable **DRQCLs** based on the Vernier tuning effect [3]. This technique has been demonstrated for telecommunication wavelength semiconductor lasers (1.55  $\mu\text{m}$ ), experimentally by Choi et al [40], [41], and Liu et al [42] and theoretically by Oda et al [3] and Kim et al [43]. The key feature of the Vernier tuning effect based laser design is the single mode wide tuning operation [3]. In the double ring configuration **DRQCLs** have the potential of achieving,  $F \cdot FSR_2$  tuning range, where  $F$  is the Vernier tuning enhancement factor associated with coupled waveguide [3] and  $FSR_2$  is the Free Spectral Range (FSR) of the tuner ring (i.e. Ring 2). The tuning enhancement factor is responsible for a wide tuning range observed in double ring configuration. However, the maximum tuning range of the coupled ring laser is limited by the available gain bandwidth in the material and maximum obtainable index change of tuner ring [44]. **DRQCLs** offer many advantages over other tuneable **QCLs**, such as lower fabrication tolerance, simpler fabrication, and the ability to tune over wide wavelength range (<50nm) with small current injected (<7 mA) [41]. A more detailed investigation is reported in Chapter 3.

In the **ITBW** project, we investigated the design, modelling, fabrication and characterisation of integrated tuneable birefringent waveguides for quantum cascade lasers. In the typical waveguide arrangement, used in a **QCL**, there is only optical gain for **TM** polarised modes. In addition it means that, at the operating wavelengths, **QCL** waveguides exhibit birefringence and indeed it has been previously reported [45] that intersubband transitions can lead to birefringence. In the **QCL** waveguides the strength of the intersubband transition can be altered by injecting current into the waveguide and therefore the **QCL** waveguides have birefringence effect that can be adjusted with the amount of injected current. Therefore, by injecting current into the **QCL** waveguide we can alter the phase relationship between the **TM** and **TE** modes. Altering the phase relationship between the polarisations is the basis of the wavelength tuning of birefringent filters but wavelength tuning requires that both **TM** and **TE** modes are present and that is usually achieved

by incorporating waveplates into the birefringent waveguides. We used Jones matrices to describe the operation of the integrated tunable birefringent waveguide. This is further described in Chapter 5.

Essentially, we required **PMC** that that convert to 50% **TM** and 50% **TE** to design the **ITBW**. The **PMC** is used to control and/or alter the state of polarisation of the incoming light. The working principals of waveguide **PMCs** are based upon the principal of mode beating, first proposed by Shani et al [46]. The **PMC** devices, based upon this mode beating effect, use waveguides with asymmetric cross-sectional profiles. This is described in more detail in Chapter 4.

## 1.2 Quantum Cascade Laser

The operation of conventional diode lasers (including quantum well lasers) depends on the transitions between energy bands (conduction band and valance band) - in which electrons and holes are injected into the active layer and radiatively recombine across the material bandgap. The band gap energy of the active layer material essentially determines the emission wavelength. On the other hand, in **QCLs**, the optical transitions occur between conduction band energy states (subbands) arising from size quantisation within the quantum wells, and thus, the emission wavelength depends on the energy separation between subbands. These transitions are popularly denoted as intersubband transitions. In the intersubband transitions processes electrons remain within the conduction band and consequently **QCLs** are unipolar device. In **QCLs** the emission wavelength can be altered by varying the layer thickness.

Historically, **QCLs** uses a multistage cascade scheme, where electrons are recycled from period to period, contributing each time to the gain and the photon emission. In principle, a single electron can generate photons equal to the number of cascade, thus, this can lead to a quantum efficiency greater then 1.

### Schematic of Conduction Band and Moduli Squared of the Calculated Wavefunction of the QCL Structure Based on a Double Phonon Resonant Design [2]

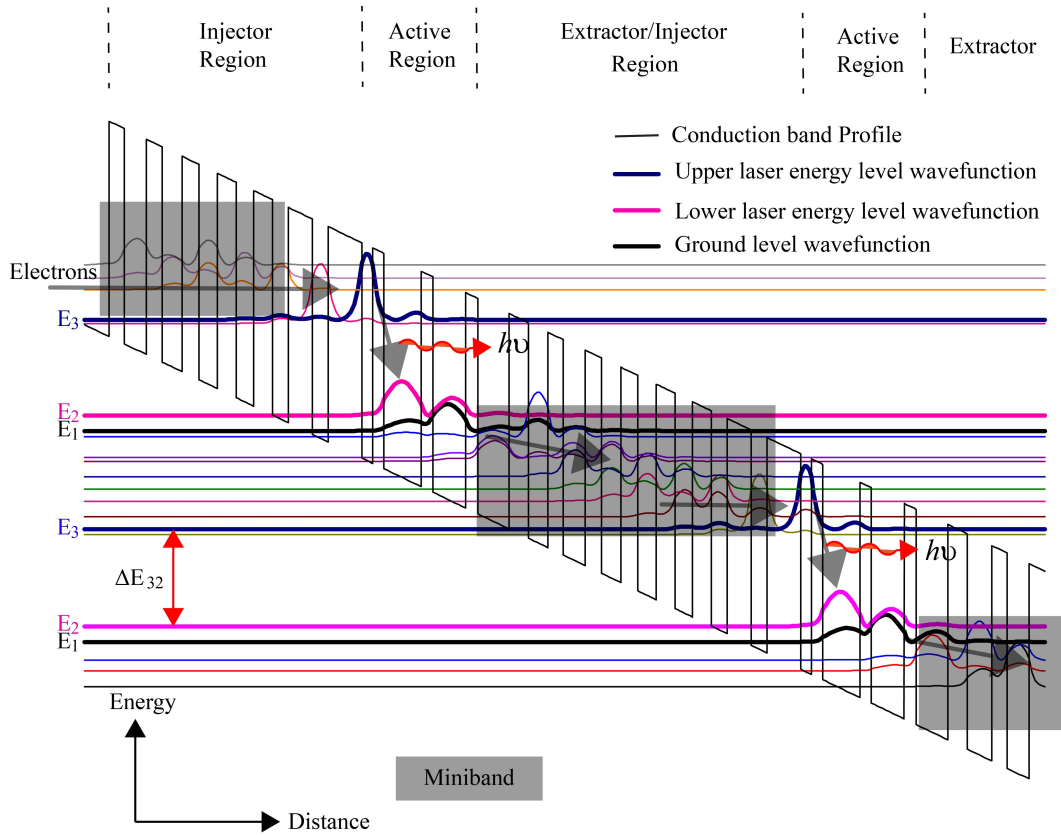


FIGURE 1.2: Schematic of conduction band energy profile used to illustrate the operating principle of a portion of the quantum cascade laser. The wavy line shows the moduli squared of the calculated wavefunction. Calculation was carried out for  $\text{In}_{0.669}\text{Ga}_{0.331}\text{As}-\text{Al}_{0.659}\text{In}_{0.341}\text{As}/\text{InP}$  material system based QCL design (employed in this thesis) under an average electric field of 70 kV/cm. Conduction band offset  $\Delta E_c \sim 0.785\text{eV}$  and radiative intersubband transition energy between  $E_3$  and  $E_2$ ,  $\sim 0.273\text{eV}$  ( $\sim 4.5 \mu\text{m}$ ), was calculated. Calculation was carried out with the help of nanostructured modelling tool nextnano<sup>3</sup>.

Further design description can be found on Ref. [2]

QCLs are multi quantum well heterostructures. Their intersubband transition, between energy levels within the conduction band, is illustrated in Figure 1.2. A typical QCL structure is divided into three regions: (1) Active region, where the radiative transition takes place, (2) Extractor region, after radiative transition electron is extracted from active region by the left side of upper corner of the miniband, (3) Injector region, usually doped region, which relax electrons from one active region to the next cascade active region. On the application of sufficient

TABLE 1.1: Waveguide layer, materials, thicknesses and doping level of the QCL material we used for this project are shown.

Layer	layer name	Semiconductor	Si doping level	Thickness( $\mu\text{m}$ )
6	Contact	InGaAs	$>1 \times 10^{19}$	0.1
5	Upper cladding layer	InP	$1 \times 10^{17}$ to $5 \times 10^{18}$	2.5
4	Upper waveguide layer	InGaAs/AlInAs	$6 \times 10^{16}$	0.324
3	Active core	InGaAs/AlInAs	undoped	1.447
2	Lower waveguide	InGaAs/AlInAs	$6 \times 10^{16}$	0.344
1	Buffer layer	InP	$2 \times 10^{17}$	0.2
0	Substrate	InP	$2 \times 10^{17}$	-

electric field, electrons are injected into the cascade structure from the left side, as indicated in Figure 1.2, and undergo a radiative transition from energy level  $E_3$  to energy level  $E_2$ . The energy difference between the two levels determines the emission wavelength and can be engineered for desired wavelengths by altering the widths of the quantum wells and barriers.

For more theoretical aspect on quantum cascade laser including active layer design fundamentals, the reader is refers to review papers [47–49] and books [50, 51].

### 1.3 Material system and wafer structure employed

The material system and QCL structure employed in this research work have been previously reported in Ref. [2]. The material utilised here is a strain-compensated  $\text{Ga}_{0.331}\text{In}_{0.669}\text{As}/\text{Al}_{0.659}\text{In}_{0.341}\text{As}$  as on InP substrate and the conduction band offset ( $\Delta E$ ) for the material system reported is 0.789 eV. Twenty eight active/extractor/injector regions were used as emissive layers grown by IQE Ltd. The QCL structure design is based on a double phonon resonant design. The layer sequence of one period starting from the injection barrier is (in nanometers): 2.88/*1.8*/2.58/*1.9*/**2.29**/**2.0**/**2.19**/**2.19**/2.09/*2.19*/1.86/*2.85*/1.86/*3.96*/1.26/*1.33*/4.40/*1.33*/3.87/*1.43*/3.72/*2.28*, where  $\text{Al}_{0.659}\text{In}_{0.341}\text{As}$  layers are italic and bold layers are Si doped to  $n = 2.8 \times 10^{16} \text{ cm}^{-3}$ . The calculated conduction band profile operates at a typical operating electric field,  $\sim 70 \text{ kV/cm}$ . This, together with the moduli squared of the relevant wave functions is shown in Figure 1.2. The conduction

band offset  $E_c \sim 0.785\text{eV}$  and radiative intersubband transition energy between  $E_3$  and  $E_2$ ,  $0.273\text{eV}$  ( $\sim 4.5\text{m}$ ), was calculated. Calculation is carried out with the help of nanostructured modelling tool “nextnano<sup>3</sup>”, result showing close agreement with published result [52]. The wafer waveguide is re-design by our former group member **Dr. Thomas J. Slight**, currently based on CST, Hamilton, and is detailed in Table 1.1. Schematic diagram of a ridge waveguide quantum cascade laser is shown in Figure 1.3.

### Illustration of a Ridge Waveguide

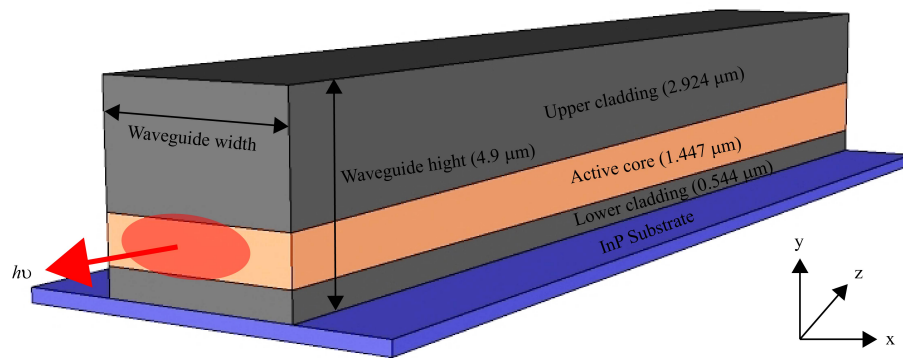


FIGURE 1.3: Schematic diagram of a ridge waveguide quantum cascade laser.

## 1.4 Aim

The main aim of the research work described in this thesis is to design, fabricate and characterise monolithic tuneable quantum cascade lasers.

## 1.5 Objective

The aim was achieved through the following objectives:

- To design, fabricate and characterise a double ring quantum cascade laser.
- To design, fabricate and characterise the polarisation mode converter for quantum cascade lasers.

- To design, fabricate and characterise the integrated tuneable birefringent waveguide for quantum cascade lasers.

## 1.6 Thesis Outline

This thesis consists of six chapters and their layout is as follows:

**Chapter 2** describes the E-beam based wafer processing techniques used to produce the devices reported in this thesis. Greatest achievement of the chapter is development of the device fabrication process based on E-beam lithography.

**Chapter 3** covers the work carried out to realise the double ring quantum cascade laser. These includes, design, modelling, fabrication, characterisation and result analysis. In this chapter we demonstrated, first single mode tuneable double-ring quantum cascade laser tuneable upto 59 nm for 0.72 kA/cm<sup>2</sup> DC current density injection into Ring 2 that covers 42% of the FWHM of the gain curve.

**Chapter 4** describes the polarisation mode converters and chapter also describes the PMC waveguide integrated equivalent of waveplates. Here for the first time, we demonstrated a polarisation mode converter integrated with a QCL that emit 69% TE light with the polarisation angle of 65° from one facet (PMC facet), and pure TM light from other facet.

**Chapter 5** details the realisation of integrated tuneable birefringent waveguide. We demonstrated that the polarisation state of the light can be controlled by varying the current injection.

**Chapter 6** summarise the main achievements, conclusions and recommendations for future works.

# Chapter 2

## Fabrication and Characterisation

### 2.1 Introduction

This chapter describes the fabrication and characterisation techniques for the QCLs considered in this thesis. The QCLs reported possess sub-micron features and required precise layer-by-layer alignment. To realise these devices, a fabrication process based on Electron Beam Lithography (EBL) was used. The QCL devices reported previously from our group were fabricated using either photolithography [9] or photolithography/E-beam lithography process [24, 25, 53]. In this work, for the first time, a complete e-beam lithography based process was used to fabricate the QCLs. The section begins with a description of fabrication tools followed by processes such as e-beam lithography, dry etching, dielectric deposition and metal contact deposition. Subsequent sections focus on the description of the experimental setup and techniques used to characterise the realised devices. Previously no characterisation of QCLs that emit both TE and TM polarised light had been carried out at our characterisation facility. We will discuss how we can characterise QCLs that emit both TE and TM polarised light using Fourier Transform Infra-Red (FTIR) spectroscopy.

## 2.2 Fabrication

### 2.2.1 Fabrication Process Overview

The basic fabrication steps used to fabricate the QCLs reported in this thesis are shown in Figure 2.1. All processing steps were carried out in the James Watt Nanofabrication Centre (JWNC) cleanroom facility based in the School of Engineering, University of Glasgow. During the tenure of my device processing, the (Inductively Coupled Plasma (ICP)) etching facility was under commission and so deep etching was carried out at Compound Semiconductor Technologies (CST) using their ICP machine and CSTs proprietary QCL waveguide etching processes.

### 2.2.2 Dielectric Deposition

In the fabrication of QCLs, dielectric ( $\text{SiO}_2$  and  $\text{Si}_3\text{N}_4$ ) films were used for three different applications.

**As Hardmask:** Unlike a conventional interband laser, QCLs require deep (typically  $\sim 5 \mu\text{m}$ ) dry etching in order to define the waveguide. To protect the unexposed areas during deep waveguide etching a resilient hard mask is required. Silica ( $\text{SiO}_2$ ) was used for this application. The required thickness of silica ( $\text{SiO}_2$ ) depends on the selectivity of the ICP-RIE process in this work a 500 nm thick ( $\text{SiO}_2$ ) hard mask was used.

**As Electrical Insulator:** Composite dielectric layers (500 nm  $\text{Si}_3\text{N}_4$  and 500 nm  $\text{SiO}_2$ ) were used as electrical insulators so that injected electrons were restricted within the ohmic contact region and also to passivate the side walls. Another desirable quality of composite dielectric layers are their ability to withstand the high electric field produced as a result of the higher bias voltages applied to QCLs over conventional interband lasers.

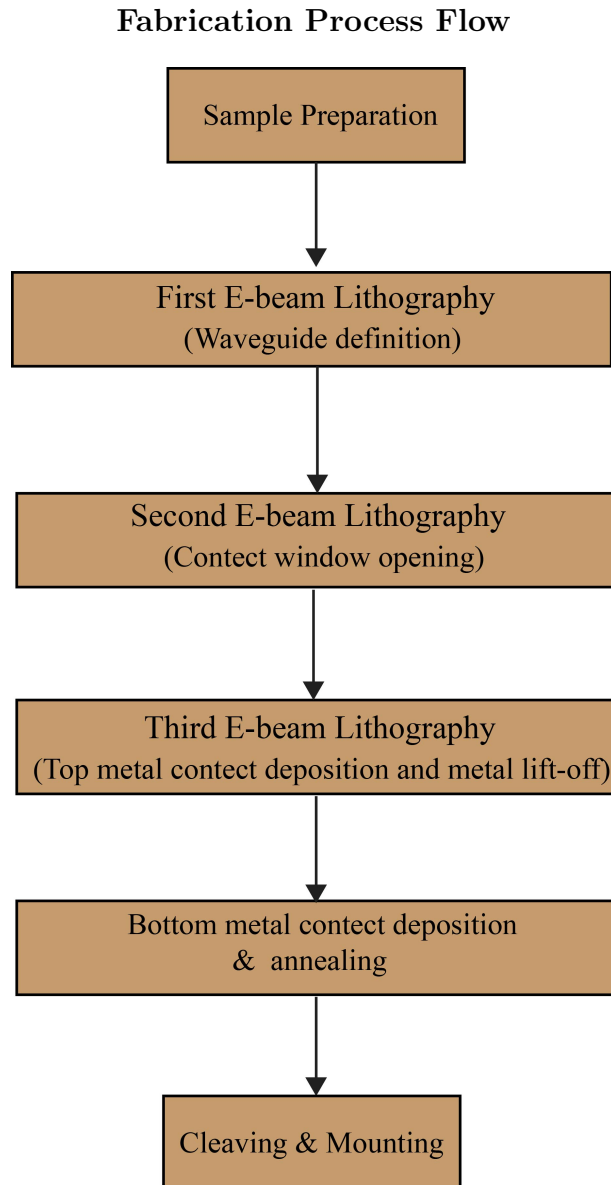


FIGURE 2.1: The basic fabrication process steps used to fabricate QCLs reported in this thesis. Step-by-Step Fabrication Processes were detailed in section 2.2.6

***As Optical Buffer:*** Composite dielectric layers (500 nm  $\text{Si}_3\text{N}_4$  and 500 nm  $\text{SiO}_2$ ), have a low refractive index so can be use as an optical buffer to reduce the modal overlap between waveguide and metal contact.

500 nm  $\text{Si}_3\text{N}_4$  and 500 nm  $\text{SiO}_2$  thin films were deposited by Plasma Enhanced Chemical Vapour Deposition ([PECVD](#)) process using an Oxford instrument Plasmalab 80plus tool. The [PECVD](#) depositions provide uniform thickness on both horizontal flat surface and vertical walls. The quality of deposition will depend

TABLE 2.1: PECVD SiO<sub>2</sub> deposition process parameter used to deposit SiO<sub>2</sub> using Plasmalab 80plus tool. Process parameters used for SiO<sub>2</sub> in Plasmalab80 plus tool were optimised by the dry etch laboratory technical staff

Parameter	Value
Gas	SiH <sub>4</sub> /N <sub>2</sub> O/N <sub>2</sub>
Flow(sccm)	9/710/171
RF power (W)	10
Pressure (mT)	1010
Temperature (°C)	300

TABLE 2.2: PECVD Si<sub>3</sub>N<sub>4</sub> deposition process parameters. Process parameters used for Si<sub>3</sub>N<sub>4</sub> in Plasmalab80 plus tool were optimised by the dry etch laboratory technical staff

Parameter	Value
Gas	SiH <sub>4</sub> /NH <sub>3</sub> /N <sub>2</sub>
Flow(sccm)	20/44/171
RF power (W)	25
Pressure (mT)	1000
Temperature (°C)	300

on how clean the substrate surface is. To ensure high quality (lower pinhole density) deposition, the substrate must be cleaned as described in **Section 2.2.6.1**. Table 2.1 and 2.2 summarised the process parameter used for 500 nm SiO<sub>2</sub> and 500 nm Si<sub>3</sub>N<sub>4</sub> deposition, respectively.

### 2.2.3 Electron Beam Lithography

High resolution lithography was at the heart of device processing, and allowed us to transfer the fine device features onto the substrate. In this work, only electron beam lithography (Vistec Vector Beam 6 (VB6) e-beam tool [54]) was used and not photolithography. The reasons behind this were:

1. Features sizes down to 300 nm were required. It is not possible to expose such features using photolithography
2. Use of a electron beam spot size down to around 4 nm allows one to define sharp corners and smooth curves. The write resolution can be as low as 0.5 nm [54] while pattern placement accuracy can be down to 10 nm [54].

- Another benefit of EBL tools is the automatic layer-by-layer alignment with accuracy of  $\pm 10$  nm [54], which is desirable in our device processing; any horizontal and rotational misalignment will spoil the devices. In our process, a window opening of  $1.5 \mu\text{m}$  for metallisation on the  $3.6 \mu\text{m}$  waveguide was required with precise alignment. Disadvantages of EBL over photolithography include a lengthy patterning time (the pattern is written serially) and higher equipment cost.

### 2.2.3.1 Electron Beam Lithography Resists

Resists can be classified into two types; i.e negative resist and positive resist. In negative resist unexposed areas dissolve into developer, while with a positive resist, exposed areas dissolve in developer. Figure 2.2 shows the functional diagram of negative and positive resists before and after development.

#### Illustration of e-beam Resists Functionality

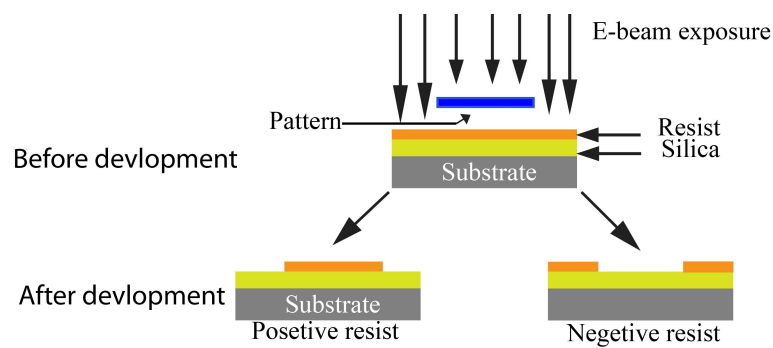


FIGURE 2.2: Functional diagram of negative and positive resists before and after development. In negative resist unexposed area removed by the developer, with positive resist, exposed area removed by the developer.

ZEP520a (manufactured by ZEON Corporation, Japan) is a positive tone, high resolution and high etch resistance EBL resist which was used to define patterns on the sample. Resists are applied uniformly on the sample by spinning at speeds between 2000 (for 500 nm thickness) to 6000 (for 300 nm thickness) rpm and baked at  $180^{\circ}\text{C}$  for 3 minutes on a hotplate [55]. The e-beam exposure energy will depend on the thickness of the resist layer, but normally ranges from 170 to 220  $\mu\text{C}/\text{cm}^2$ . The exposed sample is then developed with developer solution o-Xylene

(ortho-xylene),  $C_8H_{10}$ , at  $23^{\circ}C$  for 60 seconds and then rinsed with Isopropyl alcohol (IPA). After dry etching, residual ZEP520a was removed using either Microposit Remover 1165 ( $50^{\circ}C$  for 2 hour) or with  $O_2$  plasma ashing (50 watt RF power for 12 minutes) using a Plasmalab 80plus RIE tool.

The etch selectivity of the ZEP520a versus  $SiO_2$ , in Plasmalab 80plus RIE tool, using  $CHF_3 + Ar$  chemistry, is around 1:5 [53].

In this work, a single layer of ZEP520a EBL resist was used for defining alignment markers and waveguides (along with pattern for PMCs and gratings). Tri-layer ZEP520a was used for contact window openings (detailed in Appendix A). Similarly, for the metal lift-off process, a single layer of ZEP520a along with a tri-layer of lift-off resist (LOR 5A) were used in the development of the recipe (detailed in Appendix B).

## 2.2.4 Dry Etching

Dry etching of both the insulator and semiconductor, after EBL, is the most critical step in actually transferring the pattern to the sample. In dry etching techniques, a high energy ion beam or plasma-driven chemical reactions are used to remove the selected area of an insulator and/or semiconductor. During this process gasses flow into a discharge chamber and a plasma generated by a radio frequency (RF) source, which decomposes the target gas into high energy reactive and non-reactive ions. The highly directional (perpendicular to the plane of the substrate), high energy bombardment with reactive ions weakens the surface chemical bonds of the target material, resulting in anisotropic etching with vertical smooth side walls. This process is known as reactive ion etching (RIE). In this work, reactive ion etching RIE was used to etch the insulators ( $SiO_2$  and  $Si_3N_4$ ) and ICP-RIE was used to etch the semiconductor. Various dry etch chemistries were developed for insulator and semiconductor anisotropic etching (no undercut) [53].

TABLE 2.3: Process parameter used to etch the 500 nm SiO<sub>2</sub>. Process parameters used for 500 nm SiO<sub>2</sub> in Plasmalab 80plus RIE tool were optimised by the dry etch laboratory technical staff

Parameter	Value
Gas	CHF <sub>3</sub> /Ar
Flow(sccm)	25/18
RF power (W)	200
Pressure (mT)	30
Temperature (°C)	20
Process Time (Minutes)	18

TABLE 2.4: Process parameter used to etch the 500 nm Si<sub>3</sub>N<sub>4</sub>. Process parameters used for 500 nm Si<sub>3</sub>N<sub>4</sub> in Plasmalab 80plus RIE tool were optimised by the dry etch laboratory technical staff.

Parameter	Value
Gas	CHF <sub>3</sub> /O <sub>2</sub>
Flow(sccm)	50/5
RF power (W)	150
Pressure (mT)	55
Temperature (°C)	20
Process Time (Minutes)	17

#### 2.2.4.1 Insulator (SiO<sub>2</sub> and Si<sub>3</sub>N<sub>4</sub>) Etching

An Oxford instruments Plasmalab 80plus RIE machine was used to etch the insulator (SiO<sub>2</sub> and Si<sub>3</sub>N<sub>4</sub>) hard mask for waveguide definition and contact window opening. To etch the SiO<sub>2</sub>, Freon (CHF<sub>3</sub>) and Argon (Ar) gas composition were used. To etch the Si<sub>3</sub>N<sub>4</sub>, CHF<sub>3</sub> and O<sub>2</sub> gas composition were used. With the chemistry described above, etch rate around 29 nm/mins was found for insulators and provided slow (~ 2-3 nm/min) etching of the underneath semiconductor material after completion of insulators etching. The process parameters used for insulator (SiO<sub>2</sub> and Si<sub>3</sub>N<sub>4</sub>) is given in Table 2.3 and 2.4.

Prior to starting the etch, it is useful to ash the sample with O<sub>2</sub> plasma (using same machine) in order to remove any residual resist left in the pattern area so as to avoid micro-masking. The process parameter is given in Table 2.5. This recipe was also used to wipe out the residual e-beam resist left after dry etching.

TABLE 2.5: Process parameter used for resist micro-mask and complete e-beam resist removal.

Parameter	Value
Gas	O <sub>2</sub>
Flow(sccm)	20
RF power (W)	50
Pressure (mT)	55
Process Time (Minutes)	0.30 (To remove micro-masking) and 12 (To wipe out the residual e-beam resist)

#### 2.2.4.2 InGaAs/InAlAs/InP Etching

A surface technology systems (STS) Multiplex (based at CST Global Ltd, Hamilton) **ICP-RIE** machine was used to etch the semiconductor (InGaAs/InAlAs/InP) for waveguide definition and its associated small features such as grating etc. The fundamental difference between **RIE** and **ICP-RIE** processes is the **ICP-RIE** machine uses two Radio Frequency (**RF**) sources; one is coupled inductively with a low pressure gas mixture resulting in high density plasma, and another **RF** source is connected to the platen and is used to accelerate the reactive ions towards the target substrate being etched. Using two independent **RF** power sources allows the control of the ion density and energy, resulting in a high etch rate and low damage **ICP** process. To ensure smooth **ICP** etching in **QCLs**, a two stage **ICP-RIE** etching process was developed by **Dr. Thomas Slight** (currently based at CST). In first stage, top indium phosphide (InP) cladding layers are etched using a Chlorine Nitrogen (Cl<sub>2</sub>/N) chemistry and in second stage, Boron trichloride/Argon (BCl<sub>3</sub>/Ar) chemistry for the active region (InGaAs/InAlAs). Using the above **ICP-RIE** process to define the waveguide, CSTs proprietary **QCL** waveguide etching processes, samples were etched to around 4.9 μm deep. The **ICP-RIE** process parameters used in this work are not detailed here as they are commercially sensitive.

### 2.2.4.3 RIE Lag Effect

In RIE etching, the variation of etch depths with respect to the feature gap width, also known as RIE lag effect, becomes a critical issue for small and high aspect ratio feature etching. In small features, this variation of etch depth is mainly due to depletion of reactive ions from the etching area and thus less number of reactive ions impacting upon it, as well as restrictions in the angular trajectories of incident reactive ions. The SEM image in Figure 2.3 illustrates the RIE lag effect; clearly, etch rate is higher in wider openings.

#### Illustration of RIE Lag Effect

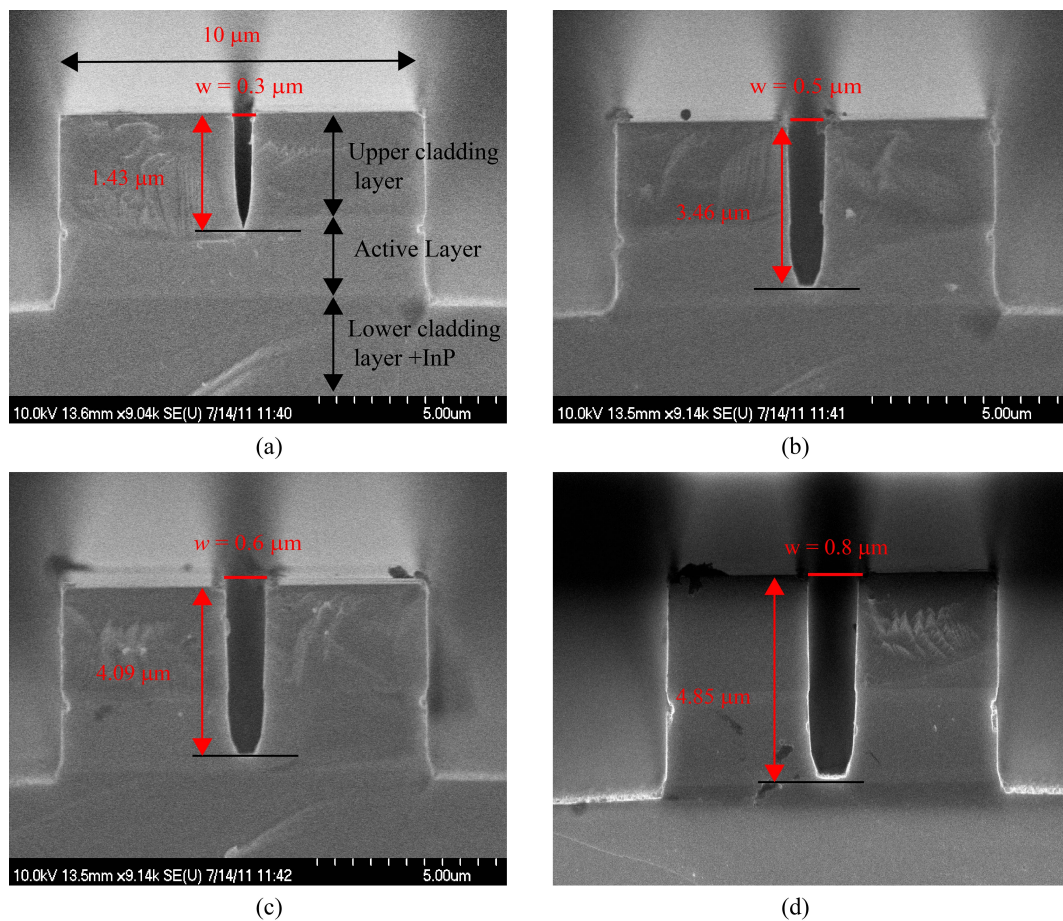


FIGURE 2.3: SEM image of variation of etch depth with respect to feature gap width, (a)  $w = 0.3 \mu\text{m}$  (b),  $w = 0.5 \mu\text{m}$  (c),  $w = 0.6 \mu\text{m}$ , and (d)  $w = 0.8 \mu\text{m}$ . RIE lag study was carried out using recipe and tool describe in Section 2.2.4.2 for 6 mins etch time on QCL wafer described in Section 1.3.

As we described later in **Chapter 4**, to design and fabricate the polarisation mode converters **PMCs** we adopted a **PMC** design based on the **RIE** lag effect. Before carrying out the design work, **RIE** lag effect studies were made, unfortunately, due to lack of **QCL** material, only a single **RIE** lag test was carried out. Figure 2.4 shows a plot of etch depth as function of gap width at the etch time of 6 minutes. From Figure 2.4, it is clear that **RIE** lag effects is critical below  $0.9 \mu\text{m}$  and above this point etch depth flattens. This **RIE** lag effect can be positively utilised to design various components such as evanescent field couplers, gratings and components for **PMCs**.

**RIE Lag Effect:Plot of Etch Depth vs. Feature Gap Width**

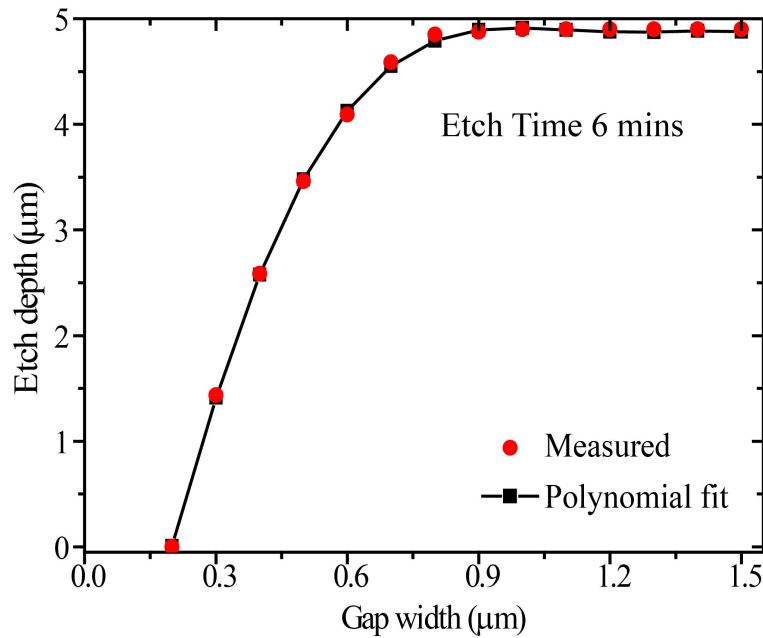


FIGURE 2.4: Shows the variation of etch depth as function of feature gap width for 6 mins etch time using using recipe and tool describe in Section 2.2.4.2.

To utilise the **RIE** lag effect, a polynomial fit to the experimental results, yields the equation

$$y = a_1w^5 + a_2w^4 + a_3w^3 + a_4w^2 + a_5w + a_6 \quad (2.1)$$

where  $y$  is the etch depth and  $w$  is the gap width. The fitting parameter is given in Table 2.6. For  $w = 0.4 \mu\text{m}$  and  $0.5 \mu\text{m}$  gap width utilised in **PMCs** design

TABLE 2.6: Fitting parameters for Equation 2.1 to calculate etch depth for given feature gap width.

$a_1$	$a_2$	$a_3$	$a_4$	$a_5$	$a_6$
-5.253	21.76	-27.3	2.17	16.83	-3.258

(in Chapter 4), the value of etch depth was estimated to be  $2.6 \mu\text{m}$  and  $3.47 \mu\text{m}$  respectively.

## 2.2.5 Metal Contact Deposition

In QCLs light is generated by a single carrier type, electrons, making Intersubband Transition (ISBT) within the conduction band. Being a unipolar device, the QCLs require only n-type semiconductor contact layers. For QCLs, the most commonly used n-type contacts are Ti/Pt/Au and Ti/Pd/Au. In contrast to other n-type contacts, for example Au/Ge/Ni/Au, Ti/Pt/Au and Ti/Pd/Au, these will provide good adhesion on a dielectric insulator [9]. In this research work, Ti/Pd/Au n-type metals were used to form ohmic contacts and were deposited using a Plassys MEB 450 Electron Beam Evaporator (EBE). The metal deposition using an electron beam evaporator is anisotropic, so thicker metal is deposited on the horizontal surface than on the vertical side walls. Thus, to ensure the metal continuity on the side walls, 500 nm gold was sputtered on the sample. SEM image in Figure 2.5 show the metal continuity over the waveguide.

## 2.2.6 Step-by-Step Fabrication Processes

This section details the step by step fabrication processes used to fabricate the device reported in thesis.

### 2.2.6.1 Sample Preparation

The sample processing starts with scribing and cleaving of the sample material. A quarter portion of the 2 inch QCL wafer was allocated for this project; it

### Metal Continuity Over the Deeply Etch Waveguide

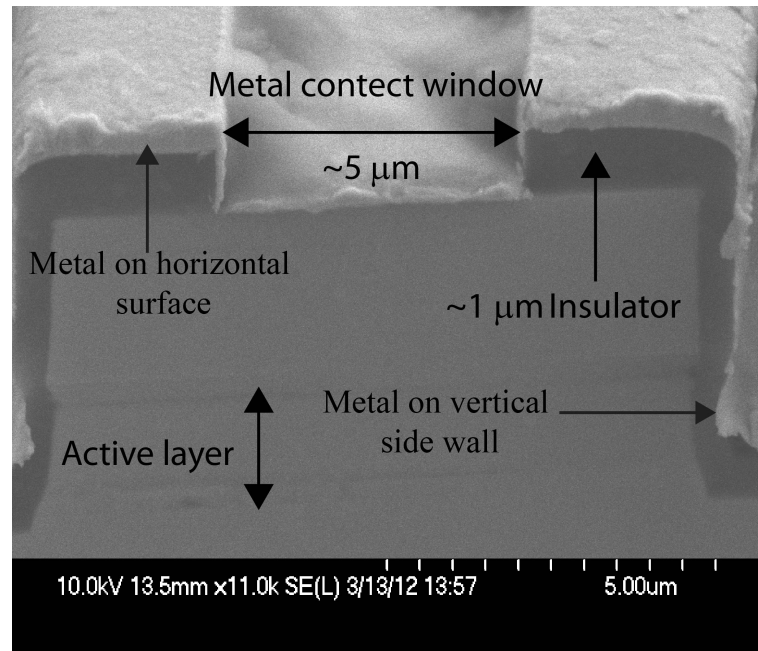


FIGURE 2.5: SEM image is the cleaved front facet of fully processed device and showing the metal continuity over 4.9  $\mu\text{m}$  deep etch waveguide.

was further cleaved into 3 pieces of roughly 10 mm x 12 mm in size. Cleaved samples were solvent cleaned in an ultrasonic bath. The cleaning steps are: 3 minutes in acetone, 3 minutes in methanol, 3 minutes in IPA. To remove any polymer layers formed during the solvent cleaning process, samples were rinsed with Deionised (DI) water and then blow dry with dry nitrogen. Finally, before further processing, in order to remove the moisture, the sample was baked for half an hour at 90°C.

#### 2.2.6.2 First e-beam Lithography

This lithography step was used to define the waveguide and its associated small features such as grating etc.

The waveguide definition process started with deposition of a 500 nm thick  $\text{SiO}_2$  hard mask on the sample, followed by spin coating (6000 rpm for 60 seconds) of 300 nm of ZEP520a electron beam resist and baked on a hotplate at 180°C

for 3 minutes. Resist patterning was carried out using a [EBL](#) tool described in [Section 2.2.3](#). Patterning was carried out using the following the [EBL](#) parameters: exposure dose  $170 \mu\text{C}/\text{cm}^2$ , resolution 1.25 nm, beam spot size 19 nm and variable resolution unit (VRU) of 19. Patterned ZEP520a resist was developed in o-xylene at  $23^\circ\text{C}$  for 60 secs and it was then rinse in [IPA](#) for 60 seconds. The sample was then loaded into Plasmalab 80plus [RIE](#) machine, where the machine performs three different tasks;  $\text{O}_2$  plasma ashing to remove any micro-mask left after development in pattern area, hard mask  $\text{SiO}_2$  etching and decommissioning the residual e-beam resist left after [RIE](#) etching. The process parameters for all three tasks are given in [Table 2.3](#) and [2.5](#). After hardmask etching, the sample was sent to CST, Hamilton for deep waveguide etching using their [ICP-RIE](#) machine. Finally, after [ICP-RIE](#) etching,  $\text{SiO}_2$  was removed by immersing in hydrofluoric acid (HF) : water ( $\text{H}_2\text{O}$ ) (1:5) mixture for 3 minutes and rinsed in [DI](#) water for 3 minutes. [Figure 2.6](#) shows the top view [SEM](#) image of deeply etch waveguide, gratings, trench for [PMCs](#) and markers.

### 2.2.6.3 Second E-beam Lithography

In the second e-beam lithography step, a contact window is opened through the composite dielectric layers (500 nm  $\text{Si}_3\text{N}_4$  and 500 nm  $\text{SiO}_2$ ).

The process started with deposition of a 500 nm thick  $\text{Si}_3\text{N}_4$  and 500 nm  $\text{SiO}_2$ , followed by spin coating of a tri-layer ZEP520a electron beam resist. A tri-layer e-beam resists was used because a single layer coating was not uniform on or around the waveguides (shown in [Figure 2.7\(a\)](#)). A tri-layer ZEP520a will give a thickness of  $\sim 1.5 \mu\text{m}$  on flat surface with good surface uniformity (shown in [Figure 2.7\(b\)](#)) and coating/baking recipes are detailed in [Appendix A](#). Resists patterning and development were similar to that described in the first e-beam lithography section except that a  $220 \mu\text{C}/\text{cm}^2$  dose was used instead of  $170 \mu\text{C}/\text{cm}^2$ . The sample was then loaded into a Plasmalab 80plus [RIE](#) machine where ashing,  $\text{SiO}_2$  etching,  $\text{Si}_3\text{N}_4$  etching and removal of the residual e-beam resist was carried out. The process parameters for all four tasks are given in [Table 2.3](#), [2.4](#) and [2.5](#), respectively.

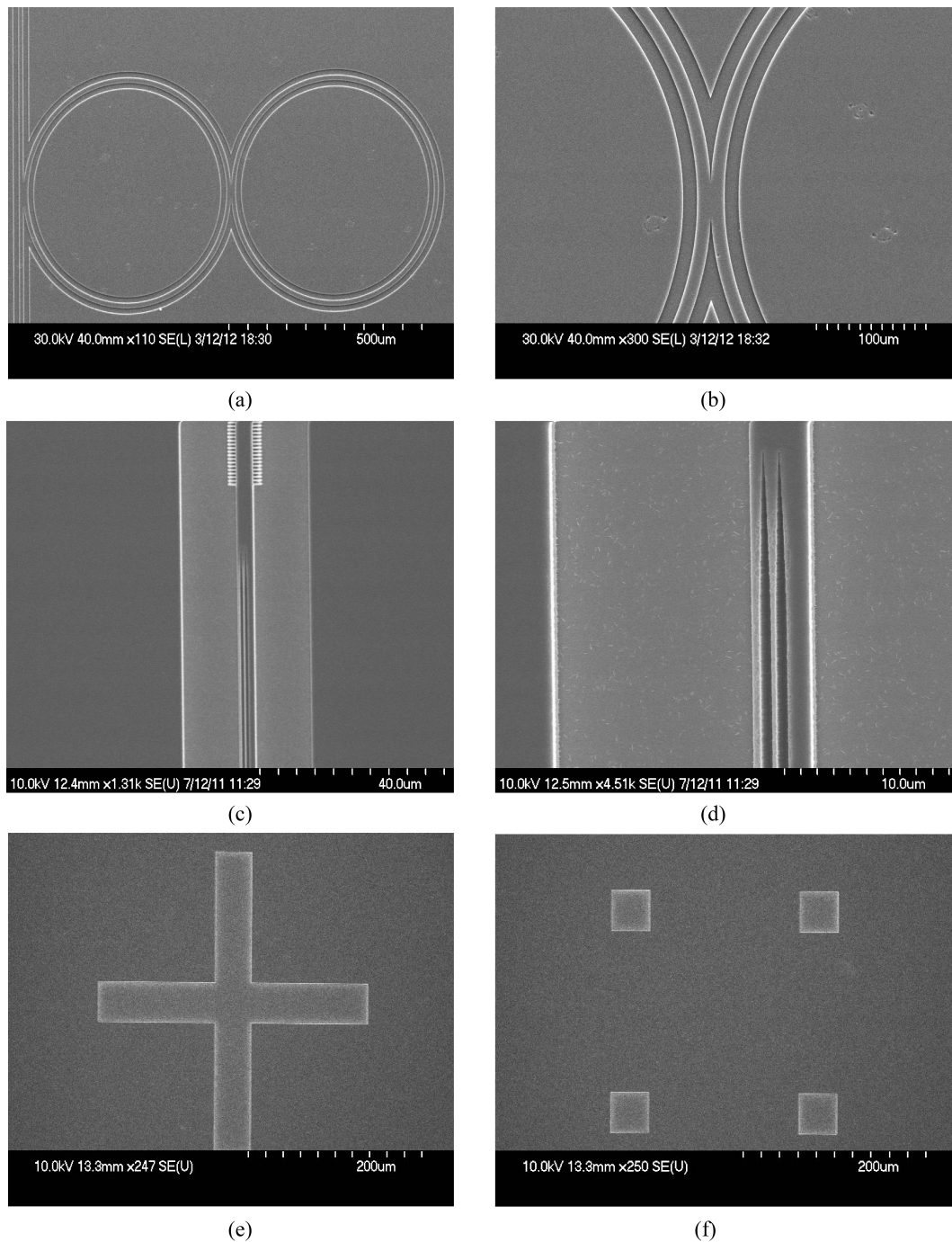
**Wafer Surface after First E-beam Lithography Step**

FIGURE 2.6: Shows the top view SEM image after ICP-RIE etching (a) Double ring waveguide (b) Magnified view of ring coupler (c) Integrated PMCs device (d) Magnified view of taper input section of PMCs (e) and (f) Cross marker and Global markers.

Shown in Figure 2.8 is the top view of SEM image of the contact window for metal deposition.

### E-beam Resists Surface Morphology after Spinning Resist

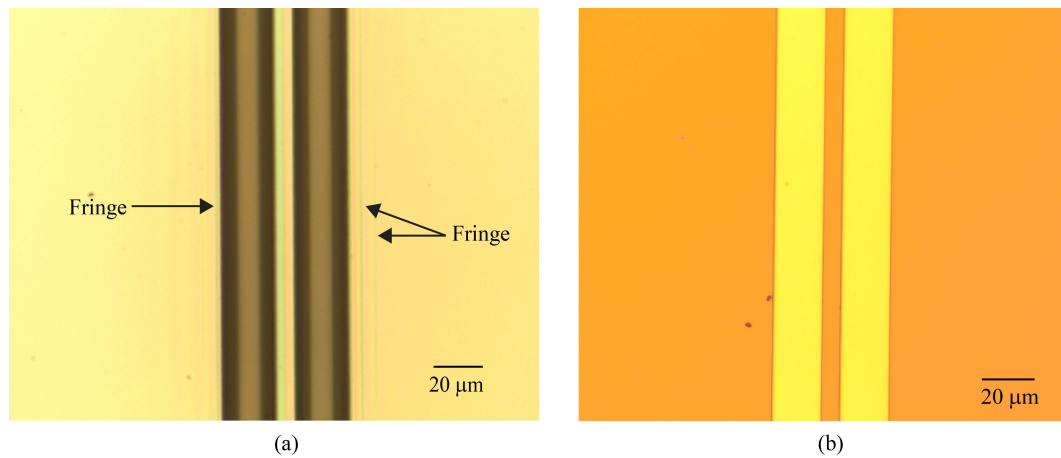


FIGURE 2.7: Top view photograph of 5ZEP520a resist after spinning (a) a Single layer: showing non-uniform surface morphology on deeply etch surface (b) Tri-layer: uniform and smooth surface morphology on deeply etch surface, coating/baking recipe are detailed in Appendix A

### Contact Window for Metal Deposition: Second E-beam Lithography Step

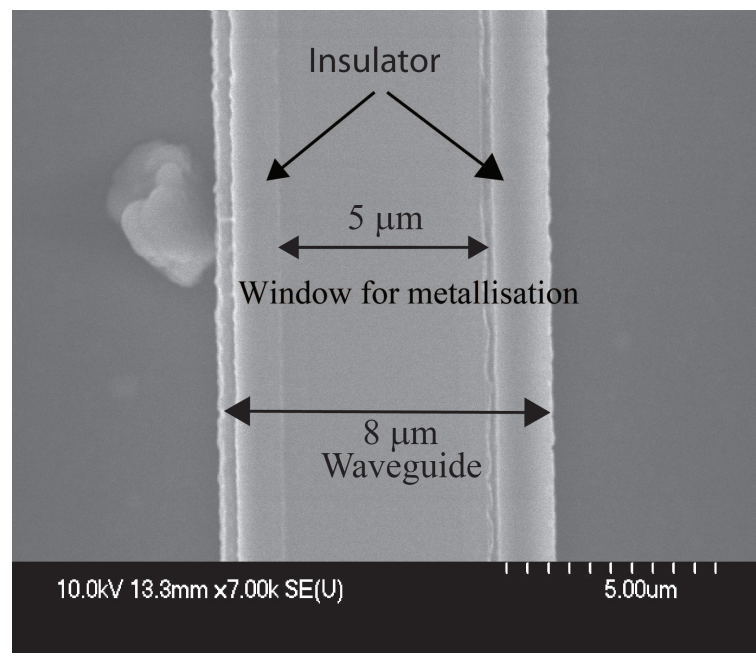


FIGURE 2.8: Shows the top view of SEM image showing contact window for metal deposition. Contact window open by etching  $1\ \mu\text{m}$  insulator ( $500\ \text{nm}\ \text{Si}_3\text{N}_4$  and  $500\ \text{nm}\ \text{SiO}_2$ ), etch chemistry are detailed in Table 2.3 and Table 2.4.

#### 2.2.6.4 Third E-beam Lithography

The major works carried out in this step are: top metal contact metallisation and metal liftoff technique. For QCLs, a metal liftoff technique for non-planarised waveguide was developed by our former group member **Dr. Chidi Nshii**, using a photolithography process. In this work, a metal liftoff technique based on e-beam lithography process is described.

The process starts with spinning of three layers of liftoff resists (Microchem LOR5A) followed by one layer of ZEP520a, spin and baking recipes are detailed in Appendix B. Three layers of LOR and one layer of ZEP520a will give approximately 2  $\mu\text{m}$  thickness on a flat surface. The liftoff pattern was exposed into the sample using EBL (the parameters are the same as those described in the first EBL step with exposure dose of 220  $\mu\text{C}/\text{cm}^2$ ). The exposed ZEP520a was first developed in o-xylene at 23<sup>o</sup>C for 60 seconds and then LOR5a was developed in CD 26 developer until a useful undercut was visible on the pattern area, we observed useful undercutting after 90 second of developments. The sample was then loaded into a Plasmalab 80plus RIE for O<sub>2</sub> plasma ashing for 60 seconds.

Prior to metal evaporation on the sample, to remove any native oxides grown on the surface, oxide stripping was carried out by dipping the sample in HCl:H<sub>2</sub>O (1:4) mixture for 30 seconds. After a blow dry with dry nitrogen, the sample is then immediately loaded into a metal evaporator chamber to prevent any further native oxide formation. Using the EBE method, Ti(30 nm)/Pd(30 nm)/Au(300 nm) were deposited followed a sputtering of 500 nm of Au on top of the waveguide. For lift-off the sample was then dipped on SVC-14 solvent for 20 minutes at 50<sup>o</sup>C. For small areas, due to thick metal, some gentle brushing is required to remove the metal, for example, liftoff between two rings where the liftoff area is around 10  $\mu\text{m}$ . Figure 2.9 shows the SEM image of various liftoff patterns.

### Metal liftoff: Third E-beam Lithography Step

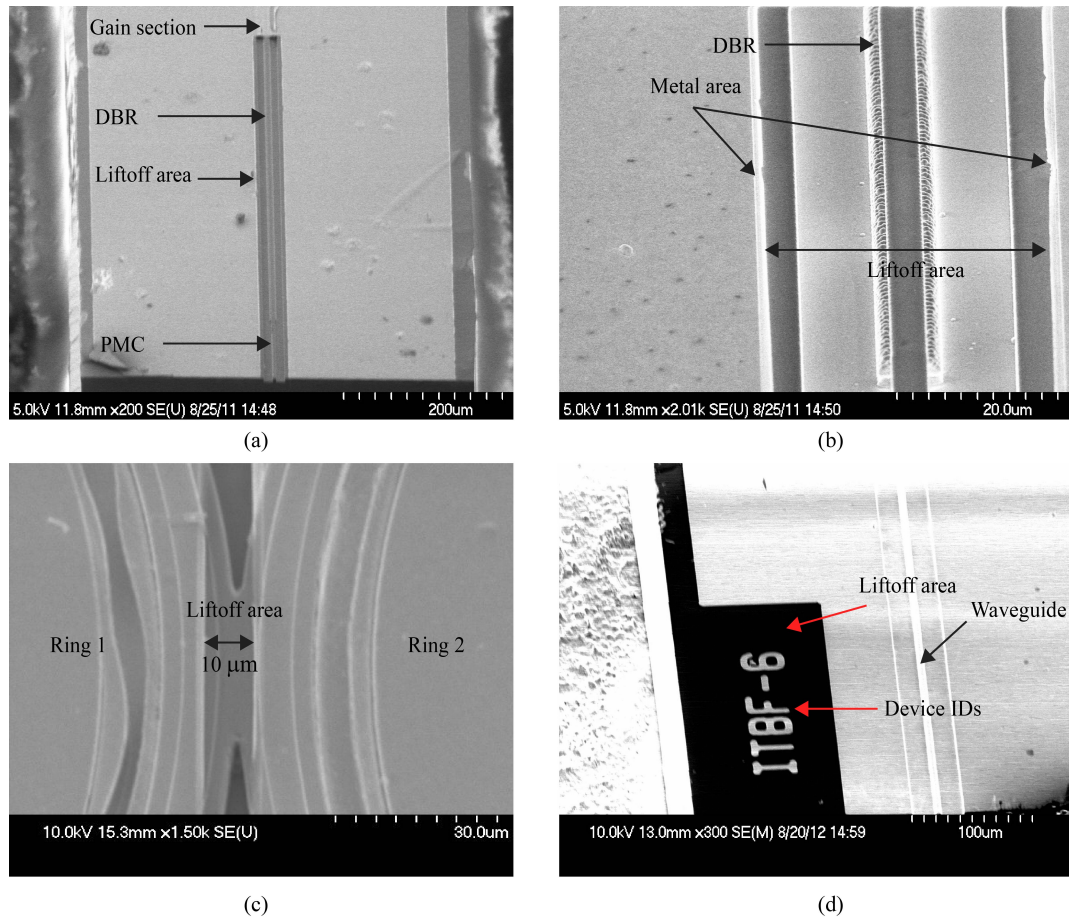


FIGURE 2.9: Shows the SEM image liftoff patterns of (a) Integrated PMCs device (b) Magnified view DBR and PMC area (c) Metal liftoff between two rings (d) Liftoff from device ID area.

#### 2.2.6.5 Substrate Thinning, Bottom Contact Metallisation and Annealing

The QCL epilayer was grown on an approximately 360  $\mu\text{m}$  thick InP substrate. To extract heat efficiently from the waveguides, the substrate required to be thinned by approximately 200  $\mu\text{m}$ . To prepare the sample for thinning, the sample was mounted on a coverslip using S1818 resist and baked for 60 seconds at 180 $^{\circ}\text{C}$  on a hotplate and then mounted on a metal chuck using wax. The substrate was then thinned from 360  $\mu\text{m}$  to 160  $\mu\text{m}$  using 9  $\mu\text{m}$  aluminium oxide ( $\text{Al}_3\text{O}_2$ ) powder and water solution. Then, the thinned rough surface was polished by etching with III-V semiconductor etching solution (HBr:Nitric: $\text{H}_2\text{O}$ , 1:1:10 mixture) for

30 seconds. After a rinse with reverse osmosis (RO) water and a blow dry with dry nitrogen, the sample is then immediately loaded into a metal evaporator and Ti(30 nm)/Pd(30 nm)/Au(250 nm) was deposited to form the bottom contact. To remove the coverslip, the sample was immersed into hot acetone for 2 hours. Finally, samples were annealed at 360°C for 60 seconds to reduce the contact resistance.

#### **2.2.6.6 Cleaving, Mounting and Wire-bonding**

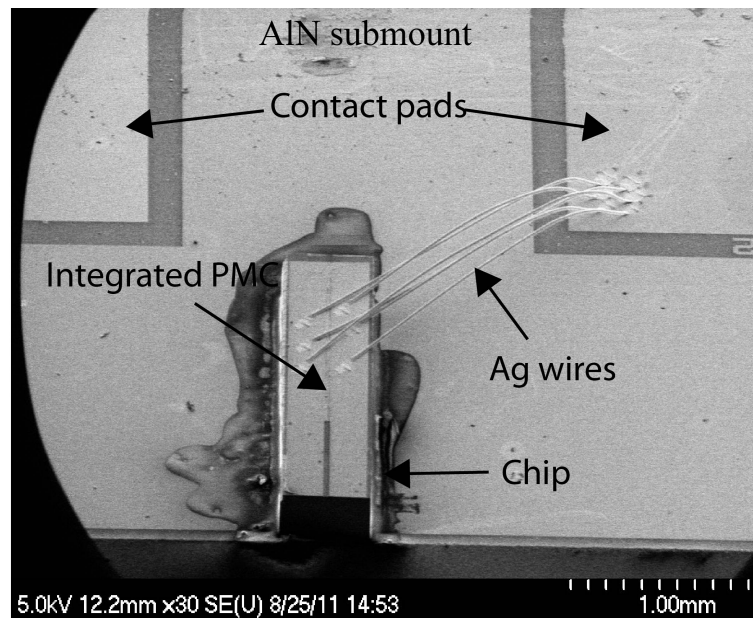
In order to characterise the fabricated devices, the individual QCL devices need to be cleaved and wire-bonded onto suitable tiles.

The processed wafer was first scribed using a semi-automatic scribe and then manually cleaved into devices using a fine tip tweezer. Cleaved devices were mounted on an Aluminium Nitrate (AlN) submount using indium solder. All devices reported in this thesis were epi-up mounted onto submount. These submounts are specially designed and fabricated by CST, Hamilton, to match our cryostat probes. Due to the high thermal conductivity ( $285 \text{ Wm}^{-1}\text{K}^{-1}$  for single crystal) of these AlN submounts, they provide a good thermal link between chip and heatsink. Finally, using a semi-automatic universal wedge bonder, the device top contacts were wire bonded to the contact pads on the AlN tiles. Figure 2.10 shows the SEM image and photograph of the fully processed devices.

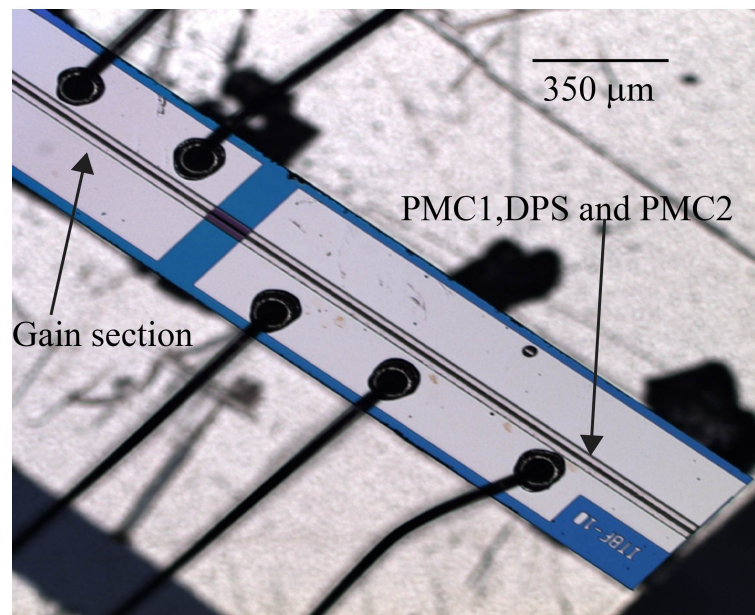
## **2.3 Characterisation**

To fulfil the aim and objective of the thesis, characterisations of fabricated devices are essential. In this section we detail the experimental technique and experimental setup used to characterise the device reported in this thesis. The majority of the characterisation work was focused on observations of the wavelength tuning operation, carried out using FTIR spectroscopy, using sensitive lock-in step scan and rapid scan detection techniques. The general performance of the devices were

## Fully Processed Quantum Cascade Lasers



(a)



(b)

FIGURE 2.10: Shows the SEM image of the fully processed devices (a) Integrated PMC and (b) Photograph of integrated tunable birefringence waveguide for QCLs.

characterised by the L-I-V characteristics. The techniques used to obtain L-I-V characteristics will be discussed. We will also discuss how we can characterise the QCLs that emit both TE and TM light using FTIR spectroscopy.

### 2.3.1 Description of Experimental Setup

The schematic illustration of the experimental setup which was used to characterise the QCL reported in this thesis is shown in Figure 2.11. The characterisation system comprises of four sub-systems:

- Cooling System
- Optical System
- Laser power supply
- Data display and acquisition system

Our characterisation facility is equipped with an Oxford instruments closed cycle cooler (CCC1204), to control the operating temperature of the laser diode heatsink. The heatsink temperature was controlled by an Oxford instrument temperature controller (Model ITC502) using a rhodium iron thermocouple.

The optical system comprises of the Burker Vertex 70 FTIR spectrometer and gold coated external parabolic mirror (to collect and collimate incoming light from the cryostat window). The FTIR unit is made up of a Michelson interferometer with KBr beamsplitter, plane fixed and moving mirror and parabolic mirrors. The light passes through a Michelson interferometer and is focused onto a liquid nitrogen cooled Indium Antimonide (InSb) detector, where the FTIR can be operated in either rapid-scan or step-scan mode. With the rapid-scan technique, one full spectral scan was carried out by sweeping the movable mirror by a predetermined distance in one single motion, with the laser operating above its threshold. To improve the spectral quality and minimize the signal to noise ratio, a number of scans can be made and the data averaged. When the laser is operating below the threshold (also known as single pass measurement), a lock-in step detection technique is used. With step detection technique, a movable mirror is moved in equal steps, and the mirror stops while collecting and averaging the signal using a Boxcar averager. On completion of the scan, interferogram data is sent to a PC,

### Typical Quantum Cascade Laser Characterisation Setup

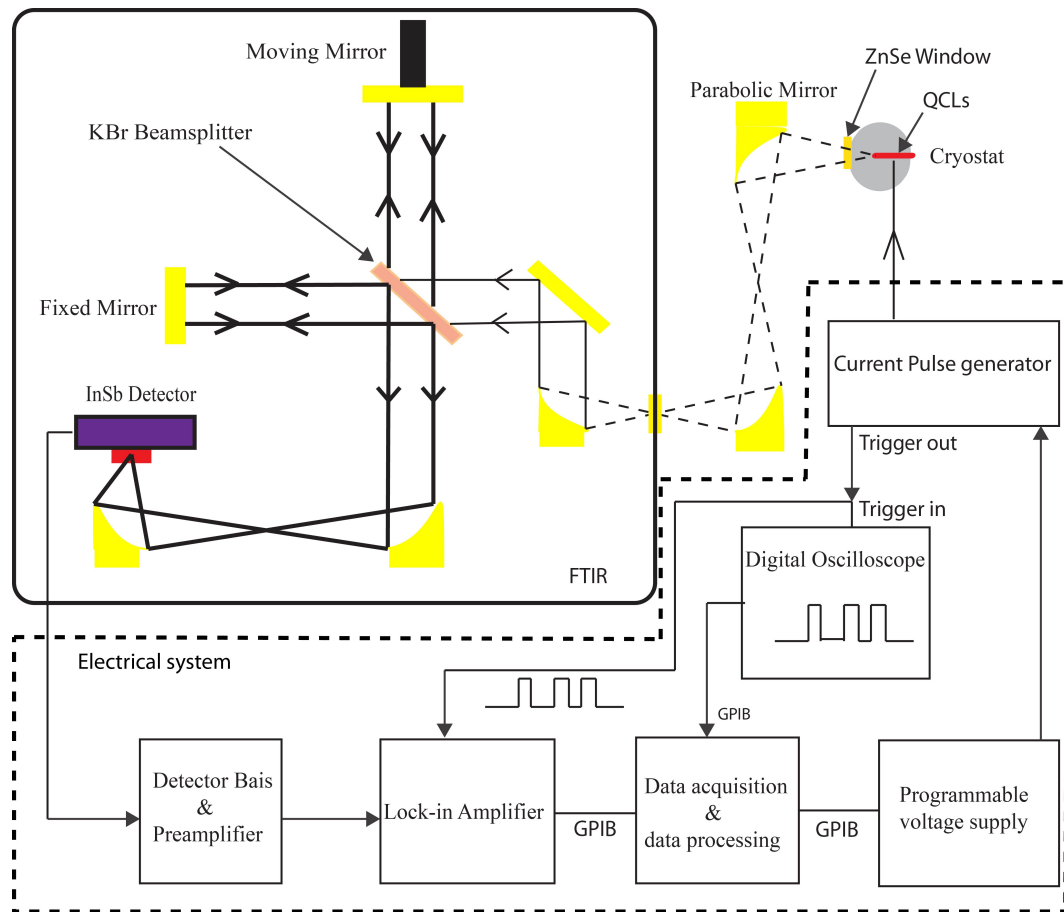


FIGURE 2.11: Schematic illustration of the experimental setup used to characterised QCLs at the University of Glasgow. The optical system comprises of the Burker Vertex 70 FTIR spectrometer and gold coated external parabolic mirrors. The laser heatsink temperature (Oxford instruments close cycle cooler (CCC1204)) was controlled by Oxford instrument temperature controller (Model ITC502) using a rhodium iron thermocouple. The electrical system comprises with High Voltage pulse generator (DEI-HV1000), Gated Integrator/BOXCAR Averager unit, lock-in amplifier and Oscilloscope

where the PC retrieves the spectral contents of the light source using a Fourier transform algorithm.

Two types of laser power supply were used to characterise the device reported in this thesis. The first type power supply is ALRAD High Voltage pulse generator (DEI-HV1000) positive pulser, capable of providing high current upto 17 A with pulse width 50 ns to 10  $\mu$ s at repetition rates of 500 Hz to 4.5 MHz.

This high current power supply can be computer controlled via a LABVIEW programme, General Purpose Interface Bus ([GPIB](#)) and Stanford research system (model No SR250) Gated Integrator/BOXCAR Averager. A Protek (Model No. B1010) pulse generator was used to trigger the high voltage pulse generator. The second type of power supply system is an AGILENT 50 Watt DC Power Supply (Model No. 6614C), 0-100V/0-0.5A.

To control and monitor the characterisation process, a data display and acquisition unit were used, consisting of a LABVIEW installed PC and an Oscilloscope.

### 2.3.2 Spectra Measurements

In this thesis, all [EL](#) and laser emission presented were measured using a Burker Vertex 70 Fourier Transform Infra-Red ([FTIR](#)) spectrometer.

For characterization, the devices are soldered epilayer-up onto a ceramic submount with wire bonds connecting the top of the device to the contact pads on the submount. The submount is then properly placed on a cryostat rod assembly system between a copper heatsink and spring loaded pins. To drive and bias the device, a  $50\ \Omega$  coaxial cable was wired between the spring loaded pins and the cryostat rods external electrical access connectors. To roughly match the load impedance with the output impedance of the high voltage pulsar, a  $50\ \Omega$  Meggit CGS high power thick film, low inductance resistor was connected in series. Next the device and wired cryostat rod assembly are mounted in the top of the cold finger of the cryostat. The cold finger temperature was controlled and monitored by Oxford instruments temperature controller (Model ITC502) at the desired value. The light emitted from the device is collected by parabolic mirrors and then focused into a beamsplitter. The beamsplitter generates an interference signal (also known as interferogram) and then focuses the light onto a liquid nitrogen cooled indium antimonide [InSb](#) detector. Finally, a Fourier transformation algorithm retrieves the spectral content from time dependent interferogram.

For the tuning application, the QCL devices reported in **Chapter 3** and **Chapter 5** require an additional power supply. The DC power supply detailed in **Section 2.3.1** is connected to Ring 2 of the DRQCL and DPS section of the ITBW devices using a  $50\ \Omega$  coaxial cable without the  $50\ \Omega$  series resistor on the cryostat rod.

The laser section (or gain section) of the QCL devices reported in thesis were driven in pulsed mode with a 100 ns duration current pulses at a 60 kHz repetition rate. The majority of measurements were carried out at room temperature (298 K).

### 2.3.3 Light-Current-Voltage (L-I-V) Characteristics

The experimental setup described in section 2.3.2 was also used for L-I-V measurements along with lock-in amplifier (EG&G, Model No. 5209, single phase lock-in amplifier) and Gated Integrator/BOXCAR Averager unit. The lock-in amplifier (used for signal recovery) output DC single, injected laser current and voltage were fed into a Gated Integrator/BOXCAR Averager. The BOXCAR Averaging unit was then connected to a PC via GPIB. To record electro-optics data and control the drive electronics, LABVIEW software based code was written and loaded on to a PC.

### 2.3.4 Electro-Optics Polarisation Measurement Technique

The PMC and ITBW devices reported in **Chapter 4** and **Chapter 5** are polarisation sensitive, essentially the device emits both TE and TM polarised light. To measure and report results accurately, requires an understanding of the polarisation dependent transmission behaviour of the optical setup used for measurements. Due to the lack of necessary facilities, we asked Bruker Corporation (Vertex 70 FTIR spectrometer manufacturer) to check the polarisation dependent transmission behaviour of Vertex 70 FTIR spectrometer. Figure 2.12 shows the TM/TE transmittance ratio as a function of wavelength for the Vertex 70 FTIR spectrometer. The measurement was carried out using a BaF<sub>2</sub> polariser, KBr

beamsplitter and deuterated triglycine sulfate (DLATGS) detector at resolution of 10 nm. From Figure 2.12, the **TM/TE** transmittance ratio is 89% at our working wavelength. Thus, to equalise with **TE** polarised light transmission, all measured electro-optic **TM** polarised data require compensation by a factor of 11%.

### Polarisation Dependence of Vertex 70 FTIR Spectrometer

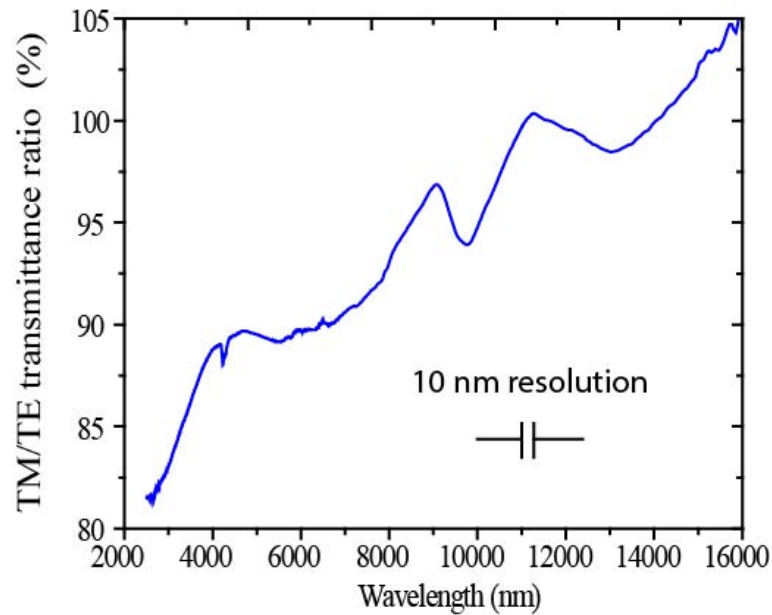


FIGURE 2.12: Shows the **TM/TE** transmittance ratio as a function wavelength for the Vertex 70 **FTIR** spectrometer. Measurement was carried out using a BaF2 polariser, **KBr** beamsplitter and DLATGS detector at resolution  $4\text{ cm}^{-1}$  (10 nm). Measurement was carried out by Dr Paul Turner, Applications Scientist, Bruker Optics Ltd., USA.

A grid polariser, comprising of  $0.12\ \mu\text{m}$  strips of aluminium, on a thallium bromide (KRS-5) window was mounted in front of the detector (in a rotatable mount) in order to determine the state of polarisation of the device output. Where the **TM** and **TE** polarised light emitted from the **PMC** and **ITBW** facet was measured as described below:

1. without the grid polariser (Total power)
2. with the grid polariser axis parallel to **QCL** waveguide (**TM** polarisation)
3. with the grid polariser axis perpendicular to the **QCL** waveguide (**TE** polarisation)

## 2.4 Conclusion

In this chapter we have presented the device fabrication and characterisation techniques employed in this thesis. The main fabrication achievements are: development of the device fabrication recipe based on e-beam lithography, developing multilayer ZEP520a e-Beam resist process for contact window opening and a metal lift-off recipe for non a planarised deeply etched waveguide. Finally, we discussed how one can characterise the QCLs that emit both TE and TM polarised light using FTIR spectroscopy.

# Chapter 3

## Double-Ring Quantum Cascade Laser

### 3.1 Introduction

In this chapter, we investigate tuneable double ring quantum cascade laser ([DRQCL](#)) based on the Vernier tuning effect [[40](#)]. This technique has been demonstrated for telecommunication wavelength semiconductor laser ( $1.55 \mu\text{m}$ ), experimentally by Choi et al. [[40](#)], Segawa et al. [[41](#)], and Liu et al. [[42](#)] and theoretically by Oda et al. [[3](#)] and Kim et al. [[43](#)]. The key feature of Vernier tuning effect based laser designing is single mode wide tuning operation [[3](#), [43](#)]. In [QCLs](#), several designs of coupled ring [QCLs](#) were investigated and 13 nm multimode wavelength tuning was reported by Chidi et al. [[53](#), [56](#)]. However, single mode tuneable operation and application still required demonstration as a [QCL](#).

Another premise of these [DRQCL](#) is their compact in size (typical chip dimensions are  $\sim 1000 \mu\text{m}$  wide x  $500 \mu\text{m}$  long) compared to distributed feedback [DFB QCLs](#) (typically chip dimension are  $\sim 300 \mu\text{m}$  wide x  $3000 \mu\text{m}$  long).

### 3.1.1 Aim

The aim is to design, fabricate and characterise an electrically tuneable [DRQCL](#) for spectroscopy and gas detection in the [MWIR](#) atmospheric window. The basic components of a [TDLAS](#) system include a single mode tuneable diode laser light source, transmitting optics, optically accessible absorbing medium, receiving optics, and detectors. The laser is tuned over the characteristic absorption lines of the gas molecules. Using the Beer-Lambert law, gas absorbance can be deduced based on intensity variation between the presence and absence of gas molecules [15]. Multimode behaviour of a laser in trace gas detection is not desirable as it reduces the spectral contrast and prevents the use of the Beer-Lambert law as a means for gas detection. To tune the QCLs, three different approaches were discussed in Chapter 1. The focus of this chapter is on achieving alternative tuneable lasers using the Vernier tuning effect on coupled ring waveguides.

### 3.1.2 Objective

The objectives of this research are;

1. To demonstrate single mode emission with Side Mode Suppression Ratio ([SMSR](#)) over 15 dB from [DRQCLs](#). [SMSR](#)  $\sim$ 15 dB is the benchmark for single mode emission and desire for traces gas detection [57].
2. To demonstrate single mode tuneable operation of a [DRQCL](#).
3. To demonstrate spectroscopy of Carbon monoxide gas with a [DRQCL](#).

## 3.2 Theory of the Double-Ring Quantum Cascade Laser

### 3.2.1 Operation of the Double-Ring Quantum Cascade Laser

Figure 3.1 shows a schematic illustration of generic double-ring laser. The figure and theory in this section is based on [3] and adapted for DRQCLs. The linear systems scattering matrix (SM) theory is used to calculate the passive resonance wavelengths of a double ring waveguide structure. We can compare this with the observed laser wavelengths at different Direct Current (DC) levels injected into ring two of the generic double-ring laser model illustrated in Figure 3.1 and thus use the theory to estimate the dependence of the refractive index on the current injected into one ring of the laser.

#### Schematic Illustration of Generic Double-Ring Laser

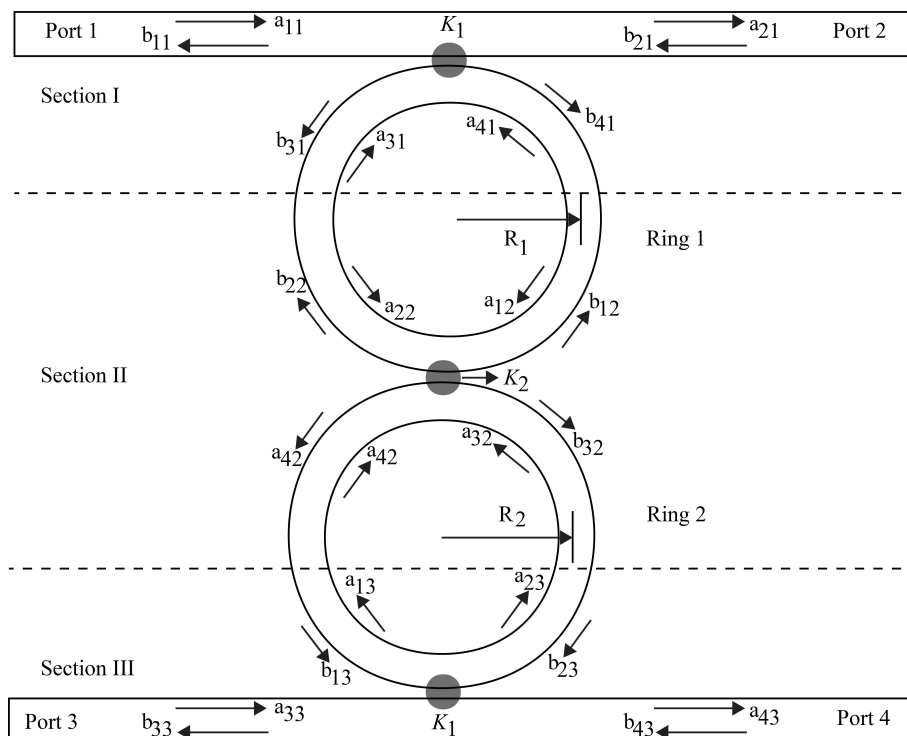


FIGURE 3.1: Shows a schematic illustration of generic double-ring laser adopted from ref. [3].

A generic Double Ring Laser (DRL) is composed of two rings of slightly different radii and two straight waveguides coupled by three directional couplers. When the rings are uncoupled, the Free Spectral Range (FSR) of individual ring is determined by the effective length and group refractive index of the rings. The FSR of the ring is given by

$$FSR_{i=1,2} = \frac{\lambda^2}{n_g L_i} \quad (3.1)$$

where  $\lambda$  is the resonance wavelength,  $n_g$  is the group refractive index,  $L_i (= 2\pi R_i)$  is the effective length and  $R_i$  is the ring radius. When the coupled combs of modes of the rings are in resonance via Vernier effects by setting  $N/r_1 = M/r_2$ , the FSR of the coupled ring can be expressed as

$$FSR = N.FSR_1 = M.FSR_2 \quad (3.2)$$

where  $FSR_1$  and  $FSR_2$  are the FSRs in ring 1 and 2, respectively. The  $N$  and  $M$  are the resonant numbers of comblike peaks of individual rings, where  $N$  and  $M (= N - 1)$  are natural and coprime numbers [43]. The tuning enhancement factor of the coupled ring is equal to natural number ( $N$ th peak of ring 1), where the tuning enhancement factor ( $F$ ) can be defined as

$$F = \frac{FSR_2}{FSR_2 - FSR_1} \quad (3.3)$$

At  $\lambda = 4545$  nm and  $n_g = 3.41$ , tuning enhancement factor 33 was estimated for DRQCL design. At the resonance, the 33<sup>rd</sup> peak of ring 1 will coincide with the 32<sup>nd</sup> peak of ring 2 and all other peaks will be suppressed. The wavelength tuning range ( $\Delta\lambda_{tune}$ ) is defined as  $\frac{\lambda^2}{2\pi n_g (R_1 - R_2)} = FSR_2 * F$  [43]. The wavelength tuning range can be increase by increasing the radius of ring 2, 155 nm tuning range was estimated for DRQCL design. The maximum tuning range of the coupled ring laser is limited by the available gain bandwidth in the material and maximum obtainable index change of the tuner ring(Ring 2) [44]. To obtain the material gain

bandwidth, a spontaneous emission measurement was carried out from the Fabry Perot (FP) laser we processed from the same wafer. Spontaneous emission was measured using experimental setup and lock-in step scan detection technique as described in Chapter 2 (in section 2.3) at pulse current of 100 ns duration with a 60 kHz repetition rate at 298 K. Figure 3.2 shows the measured spontaneous emission for an 8  $\mu\text{m}$  wide and 3000  $\mu\text{m}$  long FP laser using 8 nm FTIR resolutions. The measured material gain bandwidth at FWHM is  $\sim 139$  nm. Clearly, the measured material gain bandwidth is smaller than the tuning range ( $\sim 155$  nm) estimated from the DRQCL design. Furthermore, we observed multiple gain peaks (mark as A and B in Figure 3.2) within gain bandwidth which can complicate the DRQCL design to obtain mode hop free and continuous wavelength tuning [53].

#### Sub-threshold EL Emission measured from the Fabry-Perot (FP) Laser

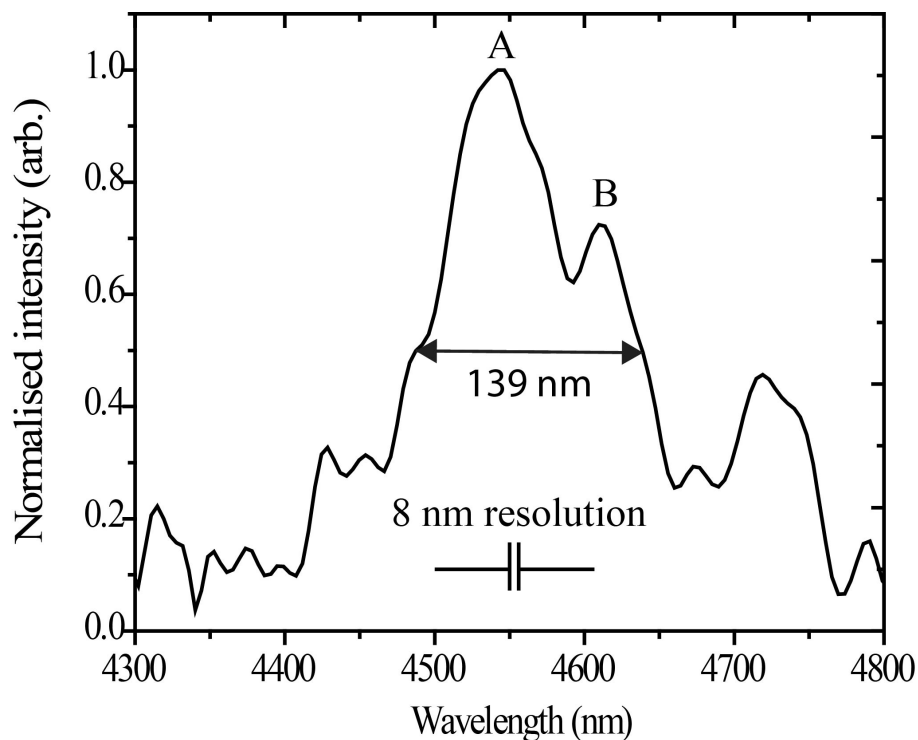


FIGURE 3.2: Shows the spontaneous emission spectra from the FP laser at 298 K we process from same wafer, which we utilise in this thesis. The measurement was carried out using lock-in step scan detection technique with 8 nm FTIR resolution. Mark as A and B are the gain peaks at 4540 nm and 4610 nm respectively

### 3.2.2 DRQCL Numerical Model

Figure 3.1 shows a schematic illustration of a generic double-ring laser. The figure, theory and mathematical model in this section is based on [3] and adapted for modelling DRQCL and discussions were summarised below.

To model DRQCL, the generic double-ring resonator was divided into three sections shown by two broken lines and each section corresponds to a directional coupler used in the resonator (shown in Figure 3.1). In Figure 3.1, a's and b's are the scattering matrix parameters at the coupling region and  $K$ 's are the amplitude coupling ratio for directional couplers. To simplify the model, the following assumptions were made: (1) no coupling loss in the directional couplers (2) no facets reflection from the input/output waveguides. Therefore, we can derive the following equation:

$$a_{21} = a_{41} = a_{22} = a_{42} = a_{23} = a_{43} = b_{11} = b_{31} = b_{12} = b_{32} = b_{13} = b_{33} = 0 \quad (3.4)$$

The generalised coupling matrix for  $n$  number of directional coupler regions can be represented by [58]

$$\begin{bmatrix} b_1 \\ b_2 \\ \cdot \\ b_n \end{bmatrix} = \begin{bmatrix} K_{11} & K_{12} & \cdot & K_{1n} \\ \cdot & \cdot & \cdot & \cdot \\ \cdot & \cdot & \cdot & \cdot \\ K_{n1} & K_{n2} & \cdot & K_{nn} \end{bmatrix} * \begin{bmatrix} a_1 \\ a_2 \\ \cdot \\ a_n \end{bmatrix} \quad (3.5)$$

Based on assumption we have made and using Equation 3.5, coupling matrix for section 1 can be written as

$$\begin{bmatrix} b_{11} \\ b_{21} \\ b_{31} \\ b_{41} \end{bmatrix} = [\mathbf{S}]_{K=K_1} * \begin{bmatrix} a_{11} \\ a_{21} \\ a_{31} \\ a_{41} \end{bmatrix} = [\mathbf{S}]_{K=K_1} * \begin{bmatrix} a_{11} \\ 0 \\ a_{31} \\ 0 \end{bmatrix} \quad (3.6)$$

Where  $\mathbf{S}$  is given by

$$[\mathbf{S}] = \begin{bmatrix} 0 & \sqrt{1-K^2} & 0 & -jK \\ \sqrt{1-K^2} & 0 & -jK & 0 \\ 0 & -jK & 0 & \sqrt{1-K^2} \\ -jK & 0 & \sqrt{1-K^2} & 0 \end{bmatrix} \quad (3.7)$$

Similarly, coupling matrix for section II and III are given in Equation 3.8 and 3.9

$$\begin{bmatrix} b_{12} \\ b_{22} \\ b_{32} \\ b_{42} \end{bmatrix} = [\mathbf{S}]_{K=K_2} * \begin{bmatrix} a_{12} \\ a_{22} \\ a_{32} \\ a_{42} \end{bmatrix} = [\mathbf{S}]_{K=K_2} * \begin{bmatrix} a_{41}e^{-j\phi_1} \\ 0 \\ a_{23}e^{-j\phi_2} \\ 0 \end{bmatrix} \quad (3.8)$$

and

$$\begin{bmatrix} b_{13} \\ b_{23} \\ b_{33} \\ b_{43} \end{bmatrix} = [\mathbf{S}]_{K=K_1} * \begin{bmatrix} a_{13} \\ a_{23} \\ a_{33} \\ a_{43} \end{bmatrix} = [\mathbf{S}]_{K=K_1} * \begin{bmatrix} a_{42}e^{-j\phi_2} \\ 0 \\ 0 \\ 0 \end{bmatrix} \quad (3.9)$$

where  $\phi_1, \phi_2$  are the phase delay on the half of the ring and depends on propagation loss ( $\alpha$ ) and propagation constant ( $\beta$ ) of the waveguide, as given by

$$\phi_{i=1,2} = (\beta_i - j\alpha) \cdot \pi R_i \quad (3.10)$$

The propagation constant ( $\beta$ ) for ring 1 is given by

$$\beta_1 = \frac{2\pi n_{eff1}}{\lambda} \quad (3.11)$$

and for ring 2

$$\beta_2 = \frac{2\pi n_{eff2}(i)}{\lambda} \quad (3.12)$$

where  $n_{eff1}$  is the effective refractive index for ring 1,  $n_{eff2}(i)$  is the DC current dependent refractive index for ring 2 and  $\lambda$  is resonance wavelength.

Using Equation 3.6 - 3.12, the transmission equation from the input port (port.1 of section 1) to the output port (port.4 of section III) can be derived as

$$\left| \frac{b_{43}}{a_{11}} \right|^2 = \left| \frac{jK_2^2 e^{-j(\phi_1 + \phi_2)}}{1 - \sqrt{(1-K_1^2)(1-K_2^2)}(e^{-j2\phi_1} + e^{-j2\phi_2}) + (1-K_1^2)e^{-j2(\phi_1 + \phi_2)}} \right|^2 \quad (3.13)$$

Similarly, the transmission equation from the input port (port 1 of section 1) to the through port (port 2 of section I) can be derived as

$$\left| \frac{b_{21}}{a_{11}} \right|^2 = \left| \frac{1}{\sqrt{1-K_1^2}} \left( 1 - \frac{K_1^2(1 - \sqrt{(1-K_1^2)(1-K_2^2)})K_2 e^{-j(\phi_1 + \phi_2)}}{1 - \sqrt{(1-K_1^2)(1-K_2^2)}(e^{-j2\phi_1} + e^{-j2\phi_2}) + (1-K_1^2)e^{-j2(\phi_1 + \phi_2)}} \right) \right|^2 \quad (3.14)$$

The double ring structure given in Figure 3.1 is normally utilized in optical communication lasers and transmissions from each port were measured by coupling the fiber to the port [41, 42]. In our QCL characterisation facility, the measurement was carried out by mounting the device into cryostat, thus measurement from each port became complex. Figure 3.3 shows the SEM image of the simplified structure we analysed and fabricated for QCL. In this structure we remove the through port (port 3 and port 4) output coupling waveguide along with its coupler. In absence of through port waveguide, transmission from this port becomes zero (i.e Equation 3.14 becomes zero) and analysis is not carried out in this work. The DRQCL structure employed in this work is analyzed using the above transmission Equation 3.13 with simulation parameters given in Table 3.1. Figure 3.10(b) shows the simulation results of the DRQCL. The coupling fraction of the coupler between ring 2 and the output waveguide ( $K_1 \sim 0.036$ ) and the coupling fraction between the rings ( $K_2 \sim 0.026$ ), required for the SM theory, were calculated using the beam propagation method as implemented in the software package RSoft [5].

### Realised Double-Ring Quantum Cascade Laser

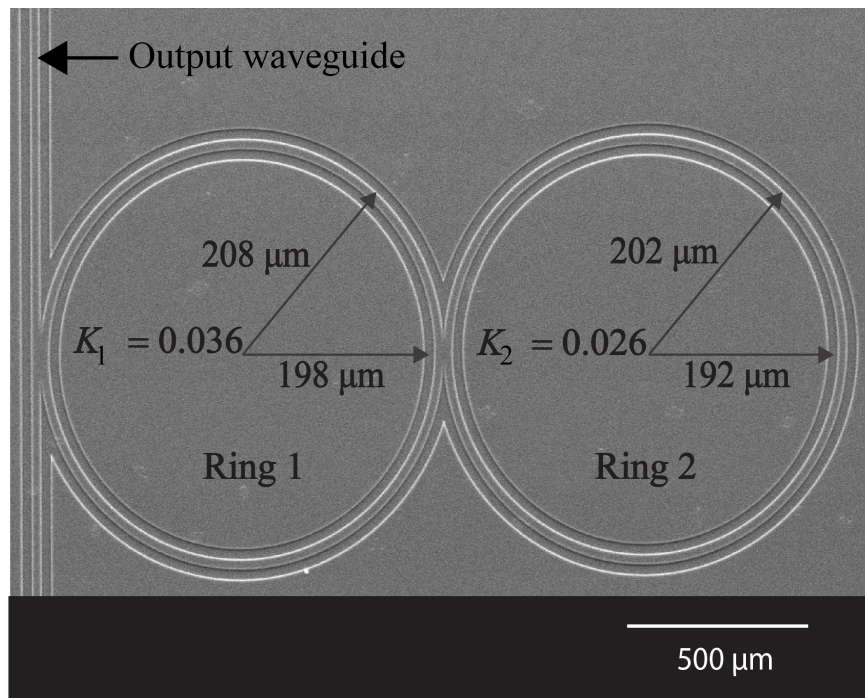


FIGURE 3.3: Shows the top of the chip SEM image of a double ring quantum cascade laser. In this structure, we employed two rings with slightly different radii and one output waveguide through which output measurements were carried out. The coupling fraction of the coupler between ring 2 and the output waveguide is calculated to be  $K_1 \sim 0.036$  and the coupling fraction between the rings is calculated to be  $K_2 \sim 0.026$ , these parameters were calculated using the beam propagation method and used as input parameters to SM theory.

## 3.2.3 DRQCL Design Considerations

### 3.2.3.1 Bending Loss

A very important consideration for ring laser waveguide design is the bending losses. Bending loss is the loss of guided mode propagating in a curved waveguide. Bending loss mainly occurs because guided modes are propagated near the outer edge of the curve and leak out from the edge [59]. A previous theoretical study shows that the magnitude of loss exponentially depends on the curve radius and index difference between core and cover index [59]. Thus, bending loss can be minimised by utilising a larger curve radius and by increasing the index contrast [53]. Unlike the shallow etched waveguide (i.e. QW laser), the deeply etched waveguide

(i.e. QCL) will provide better index contrast due to the semiconductor active core exposed into the air, thus lower bending loss in QCL.

### Bending Loss as a Function of Curve Radius

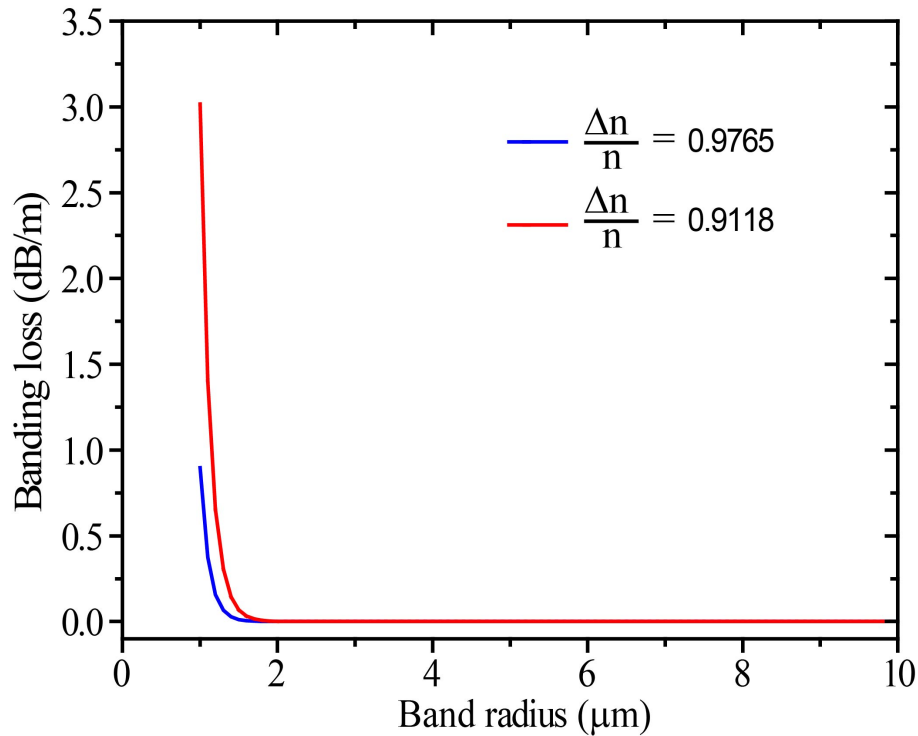


FIGURE 3.4: Shows the analytically computed bending loss as a function of curve radius for index contrast,  $\frac{\Delta n}{n} = \frac{n_1 - n_2}{n_2} = 0.9765$  (for core index,  $n_1 = 3.36$  and cover index  $n_2 = 1.7$ ), and  $0.9118$  (for effective index,  $n_1 = 3.25$  and cover index  $n_2 = 1.7$ ).

To find out the appropriate curve waveguide radius, where bending loss become minimum or close to zero, bending losses were calculated using analytical method for the fundamental TM mode as described in ref. [59]. Calculation was carried out for a  $10 \mu\text{m}$  wide and  $4.92 \mu\text{m}$  deep QCL waveguide with a composite dielectric insulator ( $500\text{nm Si}_3\text{N}_4$  and  $500 \text{ nm SiO}_2$ ) index  $n = 1.7$  [60] used as cover material. Figure 3.4 shows the analytically computed bending loss as a function of curve radius for index contrast,  $\frac{\Delta n}{n} = \frac{n_1 - n_2}{n_2} = 0.9765$  (for core index,  $n_1 = 3.36$  and cover index  $n_2 = 1.7$ ), and  $0.9118$  (for effective index,  $n_1 = 3.25$  and cover index  $n_2 = 1.7$ ). Analytical calculation results clearly indicate bending loss exponentially decreases as curve radius increases and at a curve radius of  $\sim 2.2 \mu\text{m}$  (critical radius), bending loss becomes zero. Similar results were obtained by **Dr. Chidi**

## SEM image of Couplers

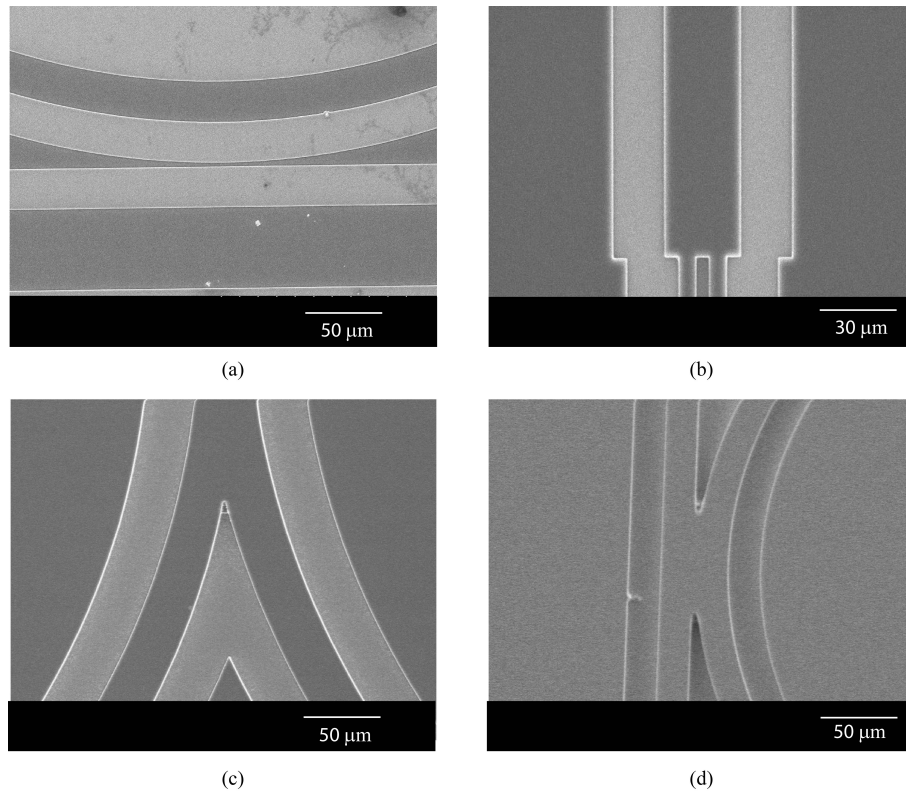


FIGURE 3.5: Show the SEM image of various coupling scheme (a) Evanescent field coupler based on RIE lag effect (b) MMI coupler (c) Y-coupler and (d) general purpose MMI coupler.

C. Nishii in his calculations and a critical curve radius of  $\sim 2 \mu\text{m}$  [53] is reported in his thesis.

### 3.2.3.2 Coupler Analysis

In DRQCL, essentially a require to couple the optical path to a ring or output coupler waveguide, so coupling coefficient amplitudes ( $K_1$  and  $K_2$ ) are critical to achieve single mode operation. Through the design and modelling process, we estimate the coupling fraction of the coupler between ring 2 and the output waveguide ( $K_1 \sim 0.036$ ) and the coupling fraction between the rings ( $K_2 \sim 0.026$ ), required for the SM theory to achieve single mode operation. Based on the analysis made, we design and fabricated the DRQCL by employing various coupling schemes, i.e

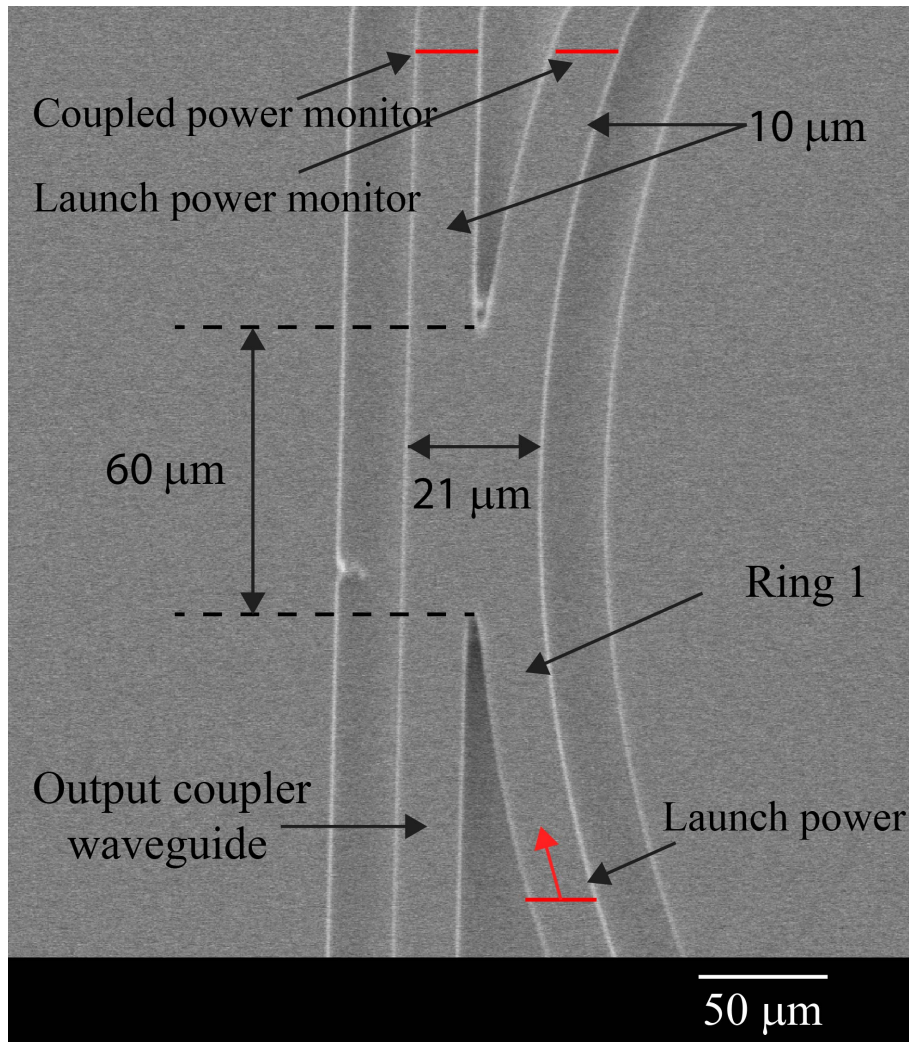
Detailed Illustration of General Purpose **MMI** Coupler

FIGURE 3.6: Shows the detailed illustration of general purpose **MMI** coupler between output waveguide and ring 1, where coupler length is around  $60\ \mu\text{m}$  and  $21\ \mu\text{m}$  wide. In the simulation, as indicated in this figure, input powers were launched from ring 1 from the bottom and coupled/launched power were monitored from the top.

evanescent field coupler [61], multimode interference coupler (**MMI**) [62] and Y-junction coupler [63]. Unfortunately, the first processed sample was broken during the processing and the majority of the **DRQCL** designs were lost except the device reported in this Chapter and Chapter 4. Figure 3.5 shows the **SEM** images of various coupling schemes employed during the design process.

The coupling scheme adopted in the device reported in this chapter is **MMI** coupling. Operation of **MMI** coupler is based on the principal of self-imaging proposed

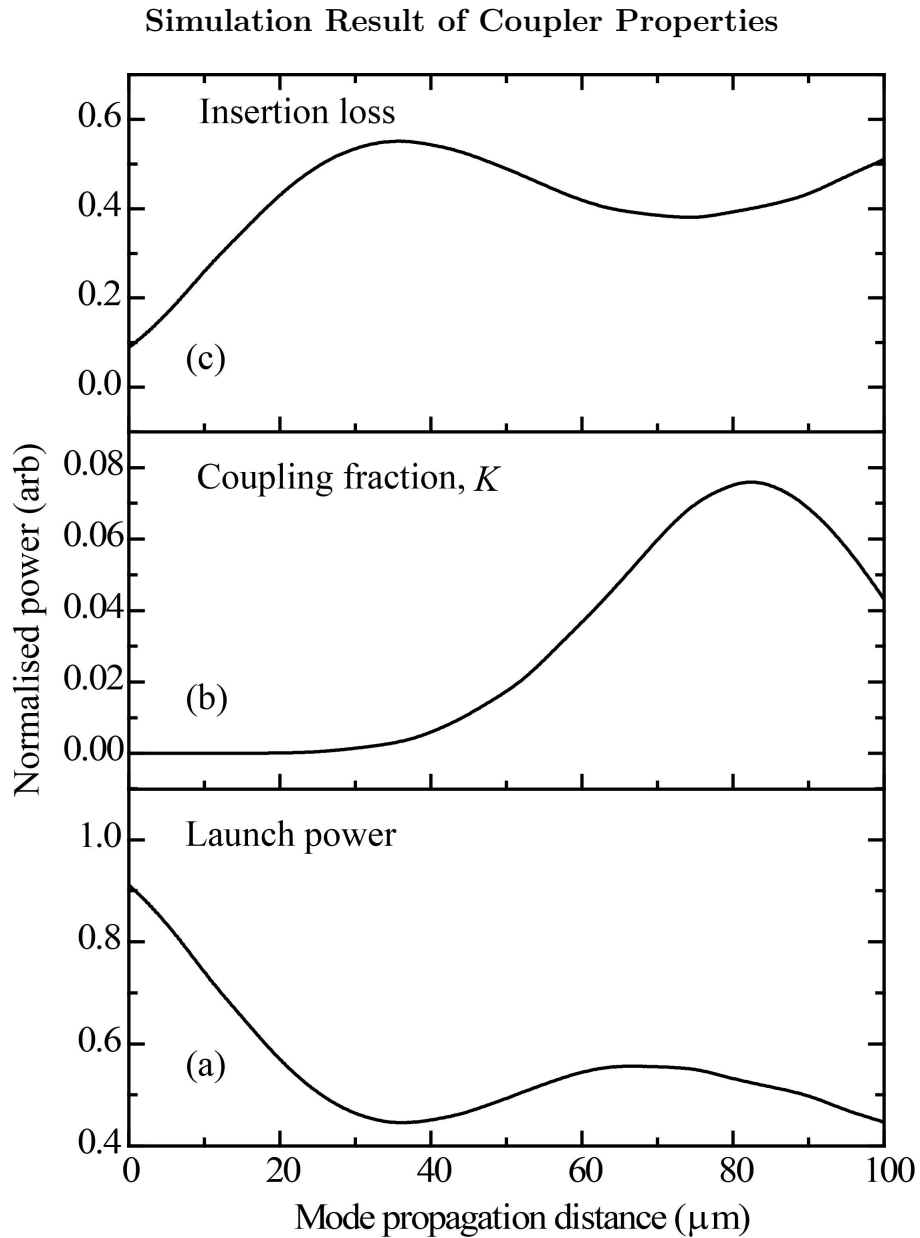


FIGURE 3.7: Shows the BPM simulation result for different coupler properties (i.e coupling fraction, launch power and Insertion loss) with respect to mode propagation distance. From the simulation we conclude the following: Simulation results are summarized as: (1) for rings coupler (55  $\mu\text{m}$  long coupler), coupling fraction is  $\sim 0.026$ , more than 52% launch power propagates within the launch ring waveguide (2) for output power waveguide and ring 1 coupler (60  $\mu\text{m}$  long coupler), coupling fraction is  $\sim 0.036$ , more than 54% launch power propagates within the launched ring waveguide.

by Bryngdahl et al [64]. In which, the applied input field profile is reproduced in

single or multiple images at periodic intervals along with the propagation direction of the guide [65]. The DRQCL reported in this chapter utilised a general purpose MMI coupler (Figure 3.6 shows the detail description of general purpose MMI coupler between output waveguide and ring 1) and 3-D BPM simulation [5] was carried out to find out the desired coupling fraction. To simulate, modes were launched from ring 1 (indicated in Figure 3.6) to the coupler and both the coupled and launch power were measured after coupling (indicated in Figure 3.6). Figure 3.7 shows the BPM simulation result different coupler properties (i.e coupling fraction, launch power and insertion loss) with respect to mode propagation distance. From the simulation we can conclude the following:

1. for rings coupler (55  $\mu\text{m}$  long coupler, not shown in figure), the coupling fraction is  $\sim 0.026$ , more than 52% launch power propagates within the launched ring waveguide
2. for the output power waveguide and the ring 1 coupler (60  $\mu\text{m}$  long coupler), the coupling fraction is  $\sim 0.036$ ; more than 54% launch power propagates within the launched ring waveguide.

the application of a general purpose MMI coupler has a disadvantage of high insertion loss and  $\sim 45\%$  insertion loss was estimated for couplers utilised in the DRQCL.

### 3.3 DRQCL Modelling and Fitting Parameter

Table 3.1 Shows the parameters input into the SM theory to fit the theory to the observed wavelengths of the single mode outputs at different DC currents injected into ring 2 of the DRQCL.

TABLE 3.1: Shows the parameters input into the SM theory to fit the theory to the observed wavelengths of the single mode outputs at different DC currents injected into ring 2 of the DRQCL.

Parameter	Value
Group index ( $n_g$ )	3.41
$n_{eff1}$ (effective index ring 1)	3.25
$n_{eff2}$ (effective index ring 2) @ 0 mA	3.2496
$n_{eff2}$ (effective index ring 2) @ 30 mA	3.2494
$n_{eff2}$ (effective index ring 2) @ 60 mA	3.2492
$n_{eff2}$ (effective index ring 2) @ 90 mA	3.2490
$R_1$ ( $\mu\text{m}$ )	203
$R_2$ ( $\mu\text{m}$ )	197
$K_1$	0.036
$K_2$	0.026
$\alpha$ , propagation loss (dB/m)	$1 \times 10^{-6}$ [53]

## 3.4 Characterisation Results and Discussions

In this section we report the electro-optics and tuning characteristics of DRQCL and the characterisation techniques used are discussed in Chapter 2. To characterise the DRQCL, Ring 1 is operated by pulse current of 100 ns duration with a 60 kHz repetition rate and Ring 2 is biased with a DC current source. Otherwise stated, all measurements were carried out at 25°C.

### 3.4.1 Light output-Injection current-Voltage (L-I-V)

Figure 3.8 shows the L-I-V curve from DRQCL measured at 25°C with zero DC current into ring 2. The threshold current ( $I_{th}$ ) of the DRQCL was around 1.1 A. The threshold peak current divided by the area of ring 1 gives a threshold current density of 8.62 kA/cm<sup>2</sup> for the DRQCL. At a drive current of  $1.3 \cdot I_{th}$ , optical peak powers of 6 and 7 mW were measured at 0 and 90 mA dc injected into ring 2.

For comparison, we fabricate a single ring quantum cascade laser (SRQCL) without ring 2 from the same wafer, where a ring and output coupler waveguide dimensions were identical to DRQCL. Figure 3.9 shows that the L-I-V curve from SRQCL

## L-I-V Curves of the DRQCL

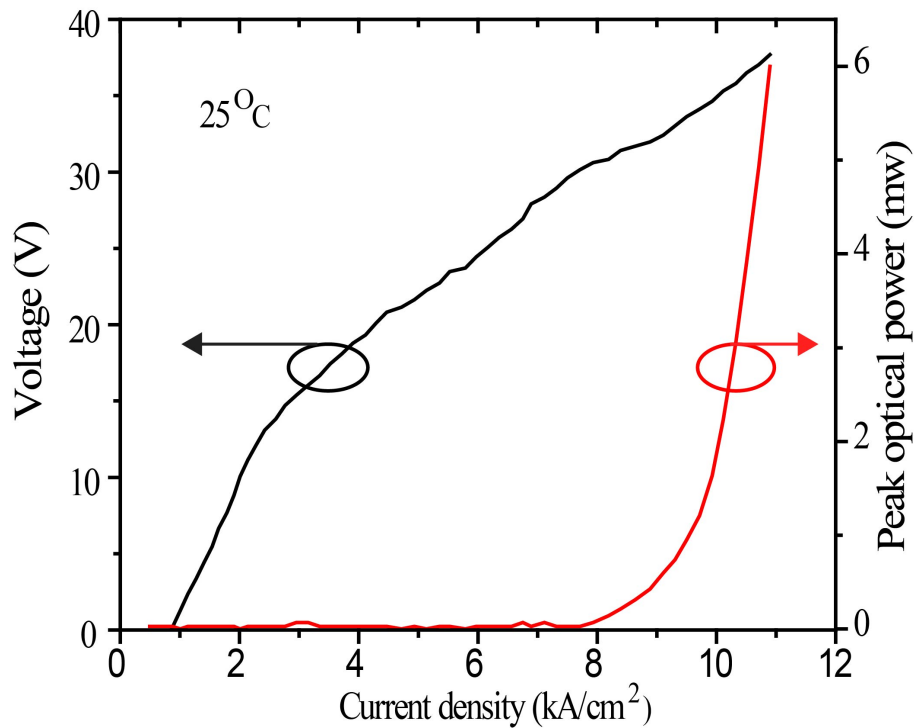


FIGURE 3.8: Shows the L-I-V curves of the DRQCL. The current density is the peak current density into Ring 1.

yielded a threshold current density of  $6.2 \text{ kA/cm}^2$  and optical peak powers of 12 mW at  $1.3 \cdot I_{th}$ .

The I-V dependence of the DRQCL and SRQCL are also shown in Figure 3.8 and 3.9. The measured turn-on voltage are  $\sim 11 \text{ V}$  and  $\sim 9 \text{ V}$  respectively which show close agreement with the reported value  $\sim 10 \text{ V}$  [52].

From the L-I comparison study; it is clear that DRQCL has a higher threshold current density (1.3 times higher than SRQCL) and lower optical peak powers (1/2 times of SRQCL). To estimate the losses associated with the DRQCL, we compared light vs injection current density curves of SRQCL. From these results it can be estimated that the loss introduced by the rings coupler and ring 2 (i.e passive without application of DC current) is approximately 1.2 dB estimated from the change in the threshold current density.

### L-I-V Curves of the SRQCL

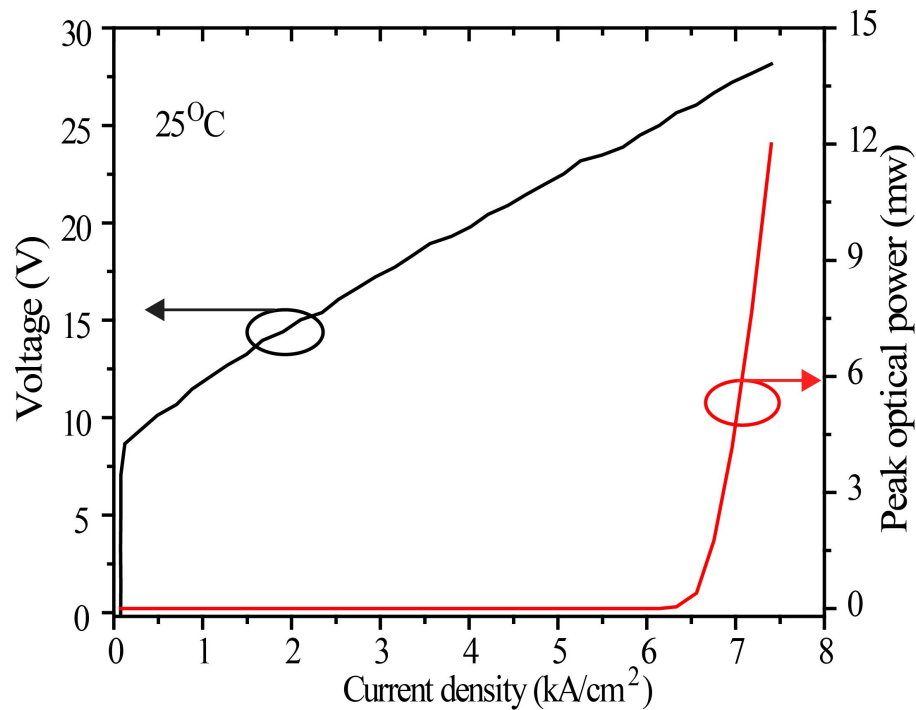


FIGURE 3.9: Shows the L-I-V curves of the SRQCL measured at  $25^{\circ}\text{C}$ , where a ring and output coupler waveguide dimensions is identical as DRQCL

### 3.4.2 Electroluminescence and Wavelength Tuning

In broad outline the tuneable single mode operation of the DRQCL is obtained as follows: Ring 1 is operated above threshold by injecting current pulses of around 100ns duration with 60 kHz repetition rate and amplitudes of  $1.3 \cdot I_{th}$  A (where  $I_{th} = 1.1$  A is the laser threshold current). Ring 1 is coupled to Ring 2 and Ring 2 has a much smaller DC (up to 100 mA) current applied to it which is below the laser threshold and used to control the effective refractive index of the Ring 2 waveguide and thus its resonance condition. The resonance wavelength of the DRQCL can be tuned by the small DC current applied to Ring 2.

Figure 3.10(a) shows the observed emission spectra and wavelength tuning as a function of DC current at 30 mA steps applied into ring 2 with drive pulse current of  $1.3 \cdot I_{th}$  into ring 1. Single mode emission was observed with a side mode suppression ratio of more than 19 dB for all dc currents injected into ring 2.

## Emission Spectra and SM Theory Fit at Different Current

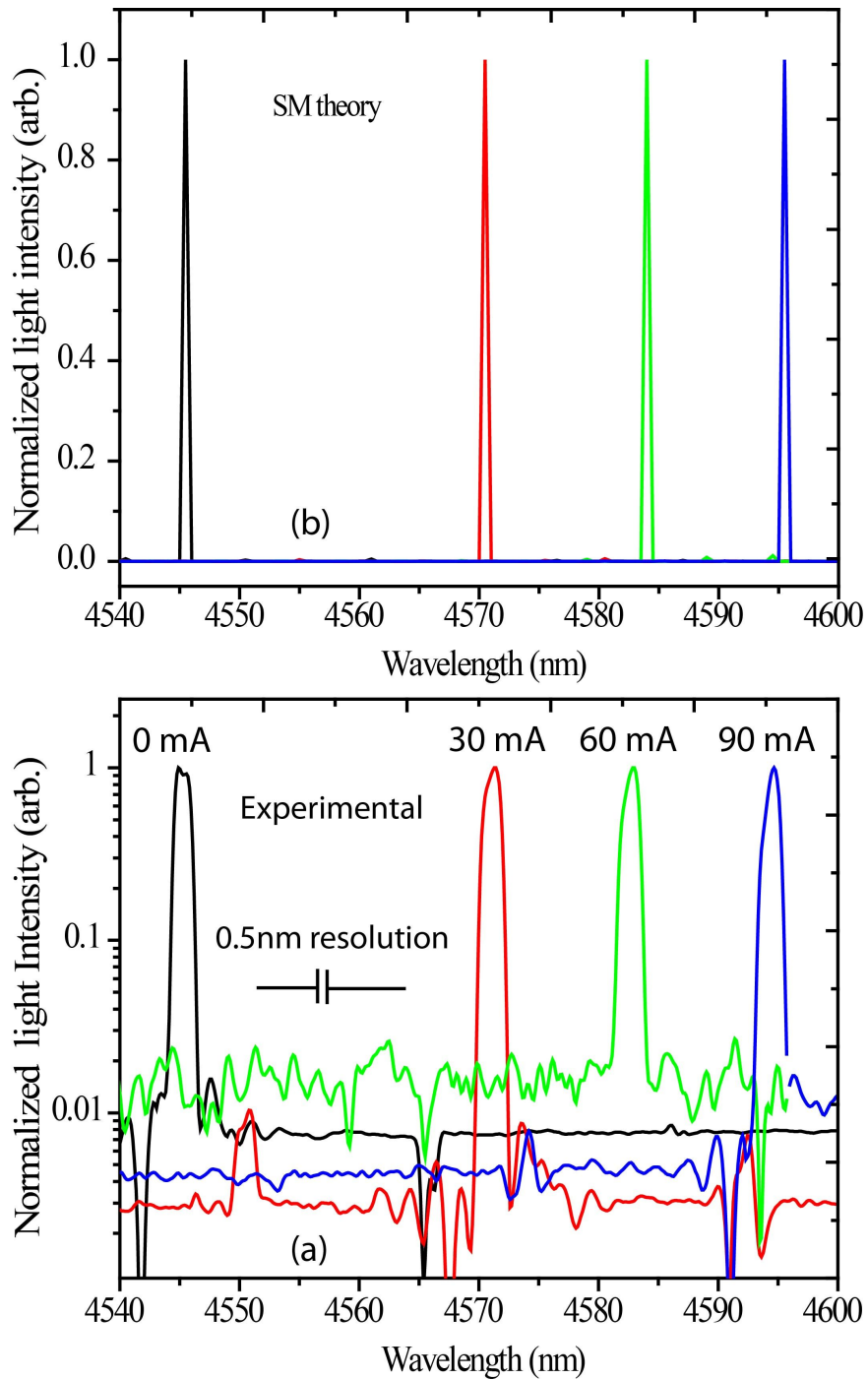


FIGURE 3.10: (a) Shows the normalized spectra for DRQCLs device measured at DC current from 0, 30, 60 and 90 mA with the spectral resolution of 0.5 nm and (b) The tuning curve estimated by the SM theory for various dc current applications into ring 2. If we assume a linear dependence of the refractive index with injection current at  $-8.25 \times 10^{-4} \text{ kA}^{-1} \text{ cm}^2$  then we can fit the SM theory to the results

In Figure 3.10(b) we compare the results of current tuning with the SM theory as summarised in Equation 3.13. Table 3.1 shows the parameters input into the theory to fit the theory to the observed wavelengths of the single-mode outputs at different dc currents injected into ring 2 of the DRQCL. Estimated from SM theory, the effective index at zero injection current is  $n_{eff2,i=0}$ .

If we assume the following form of linear dependence of the  $n_{eff2}(i)$  on the dc current,

$$n_{eff2}(i) = n_{eff2,i=0} + i \frac{dn_{eff2}}{di} \quad (3.15)$$

then by comparing with results shown in Table 3.1 this gives  $\frac{dn_{eff2}}{di} = -8.25 \times 10^{-4} \text{ kA}^{-1} \text{ cm}^2$ . which is in approximate agreement with results reported in [66] and thus the SM theory gives a reasonable prediction of the resonance condition as illustrated in Figure 3.10.

**Emission Wavelength and SM Theory Fit at Different Current/Temperature**

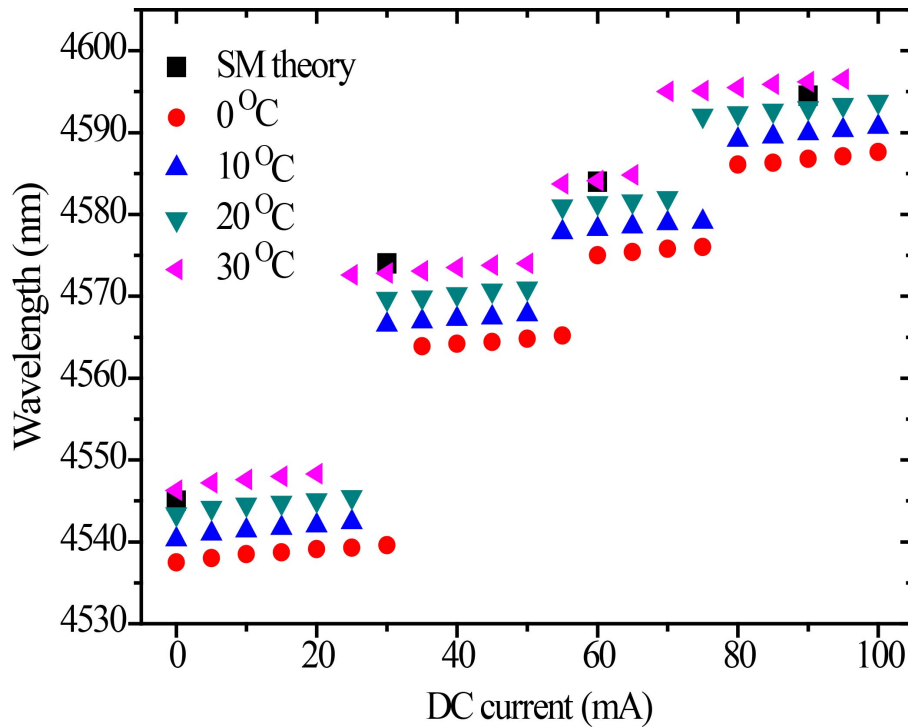


FIGURE 3.11: The wavelength tuning as a function of dc current measured at different heat sink temperatures.

Figure 3.11 shows the wavelength tuning of the DRQCL measured as a function of the dc current injection into ring 2 at 5 mA steps and different heat sink temperatures. It also illustrates the limitations of the SM theory which can only predict the resonance wavelengths of the DRQCL as a passive resonance structure. However, what we observe is discontinuous tuning over a range of 59 nm in a mode pulling and hopping manner which covers almost half of the gain width shown in Figure 3.11. There are mode pulling regions of slow tuning at  $0.04 \text{ nm mA}^{-1}$  followed by mode hops of order 10 nm. To fully understand this type of discontinuous tuning requires further experimental work and the application of nonlinear dynamical theory [67] which is beyond the scope of the thesis.

### Comparison of Tuning Spectra with Spontaneous Emission Spectra

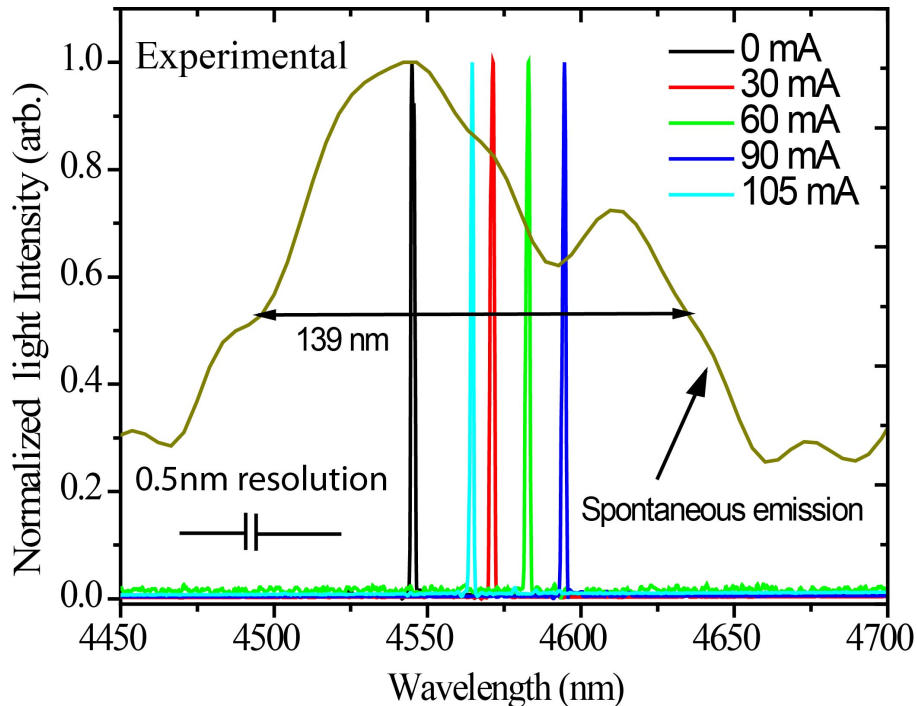


FIGURE 3.12: The spontaneous emission spectra measured using  $3000 \mu\text{m}$  long and  $8 \mu\text{m}$  wide Fabry-Perot laser (from the same wafer as the DRQCL) and the normalized single-mode output of the DRQCLs at various dc current injected into Ring 2.

Although the mode pulling and hopping complicates the use of the DRQCL as a spectroscopic source, it is still possible to utilize it if we combine the tuning obtained by the dc current in ring 2 with heat sink temperature tuning and the

chirp tuning arising from the current pulse into ring 1. We demonstrate this by carrying out spectroscopy of selected absorption lines in CO gas.

## 3.5 Spectroscopy

For a general description of molecular vibration-rotation spectroscopy see ref. [68].

Carbon monoxide (CO) gas has a strong fundamental vibrationalrotational absorption lines in the MWIR region centered at around 4666 nm [68]. Using the DRQCL as the IR source for a FTIR spectrometer we were able demonstrate spectroscopy of CO gas.

### 3.5.1 CO Spectroscopy with Globar Source

Initially, for reference, an absorption spectrum was measured by FTIR spectroscopy using a broadband silicon carbide (SiC) Globar IR source (the blackbody source [69] supplied with the FTIR). The FTIR sample cell was filled with CO at a pressure 105 Torr and had a path length of 11 cm. Figure 3.13 shows the IR absorption spectrum of the CO from 4540 nm to 4950 nm.

### 3.5.2 CO Spectroscopy Tuneable DRQCL

The DRQCL then replaced the Globar as the IR source in the FTIR spectrometer and spectra were measured using two different DRQCL drive conditions. Figure 3.13(b) & (e) show the FTIR spectra of the DRQCL without the CO cell present and at DC bias currents of 0 & 90 mA respectively at 25°C. The DRQCL emission lines at these bias currents approximately align with the R(16) & R(9) lines of the CO absorption spectrum [68]. Due to pulse induced chirp [70], the width of the DRQCL emission lines (~1.5 nm) are broadened beyond the FTIR resolution (0.5 nm). This effect is used to tune the laser through absorption line.

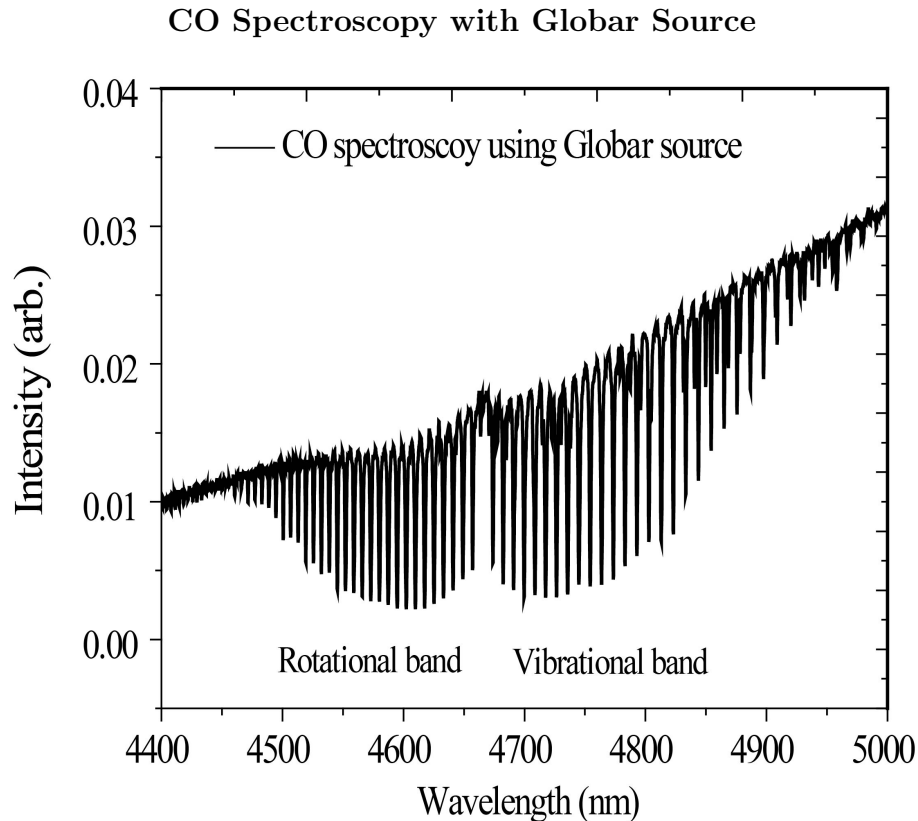


FIGURE 3.13: Shows the IR absorption spectrum of the CO using Globar source from 4540 nm to 4950 nm.

The emission spectra of the DRQCL with the CO cell present are shown in Figure 3.13(c) & (f) and exhibit a dip in transmission where the laser emission exactly coincides with the CO absorption lines. Figure 3.13(d) & (g) show the experimentally derived absorption coefficients ( $\alpha$ ) of  $0.116 \text{ cm}^{-1}$  and  $0.0674 \text{ cm}^{-1}$  for the R(9) and R(16) lines [68].

## 3.6 Conclusion

We have described the design, fabrication and characterization of a DRQCL and demonstrated its application to CO spectroscopy.

We have demonstrated first time single mode electrically tuneable operation of a DRQCL at room temperature. Single mode emission is observed with a side mode suppression ratio of over 19 dB. However, what we observed is discontinuous

## CO Spectroscopy with DRQCL

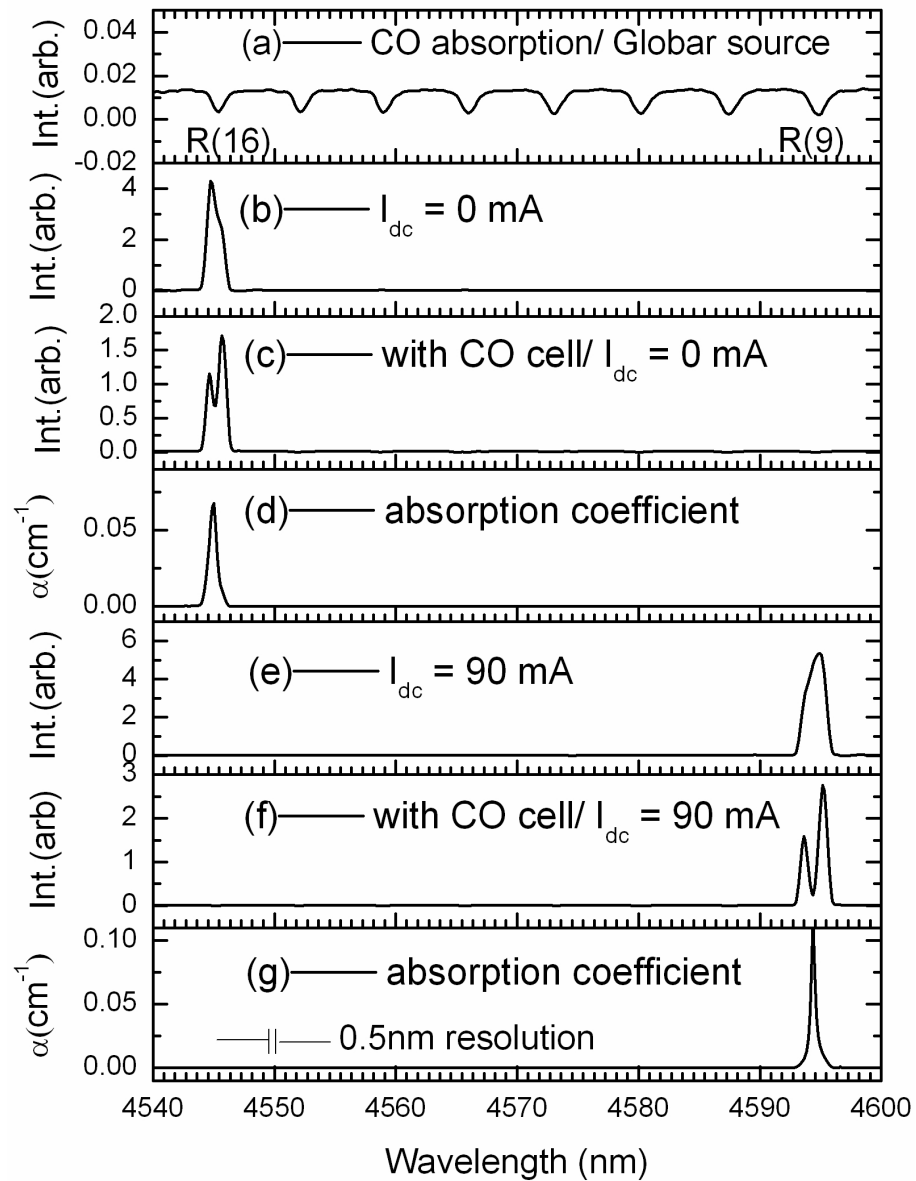


FIGURE 3.14: (a) CO absorption spectra using Globar source. (b) and (c) Laser and CO absorption spectra at 0 mA dc current, (e) and (f) laser and CO absorption spectra at 90 mA dc current, (d) and (g) experimental absorption coefficient at 0 and 90 mA, respectively.

tuning over a range of 59 nm in a mode pulling and hopping manner which covers wavelength from  $\sim 4537$  nm to  $\sim 4596$  nm, almost half of the gain width (i.e. full width at half maximum (FWHM) of spontaneous emission spectra. To some extent the discontinuous tuning can be mitigated by changing the temperature of the heat sink.

Using the SM theory of a passive device we could estimate the resonance condition of the DRQCL and thereby predict a current dependent refractive index of  $-8.25 \times 10^{-4} \text{ kA}^{-1} \text{ cm}^2$ . We observed mode pulling and hopping in the active devices as a function of DC injected into ring 2. Further work on active devices is required to gain detail understanding of the nonlinear dynamics that leads to mode pulling [67].

However, even with a fixed heat sink temperature we are able to tune the laser to align the output wavelength with a CO gas absorption line using pulse induced chirp of the output wavelength. We could then measure the absorption coefficient of the CO absorption. By combining both DC current and temperature, 59 nm quasi-continuous tuning from  $\sim 4537 \text{ nm}$  to  $\sim 4596 \text{ nm}$  was observed and this plus the chirp tuning can be used for spectroscopy of the absorption lines R(16) to R(9) of the CO gas [68].

# Chapter 4

## Integrated Polarisation Mode Converter

### 4.1 Introduction

Polarisation mode converters (**PMCs**), also referred to as waveplates, are used to control and/or alter the state of polarisation of incoming light. The working principals of waveguide **PMCs** are based upon the principal of mode beating, first proposed by Shani et al. [71]. The **PMC** devices based upon this mode beating use waveguides with asymmetric cross-sectional profiles. They can be fabricated as a single section [72–81] or multi section [46, 81–85], and both have been experimentally and theoretically realised in GaAs/AlGaAs, InP/InGaAsP, Silicon on Insulator (**SOI**) and InGaAsP/InP quantum well (**QW**) material structures. In 2009, a Fabry-Perot **TE** laser including a monolithically integrated single section **PMC** based upon an AlGaAs/GaAs material structure (for an operating wavelength of 867.1 nm) was realised by Bregenzner et al. [86]. This device emitted predominately over 80% **TM** light from the **PMC** facet. More recently, a dynamic polarisation modulator/converter has been demonstrated by Holmes et al., where the realised device consists of a Fabry-Perot laser with an integrated polarisation mode converter, followed by a differential phase shifter [87]. Work on producing linearly

polarised light from QCLs by employing integrated plasmonic polarisers on the output facets of the laser has also been reported [88].

Many applications would benefit from an elliptically polarized output, as required in some forms of spectroscopy [89] and ellipsometry [90]. The basic component of a typical polarisation dependent ellipsometry system includes, a light source, linear polariser, optical system under measurement, linear polarisation analyser, and a photodetector, respectively. A collimated monochromatic beam from suitable light source is passes through a variable angle polariser to produce light of known polarisation and wavelength. This polarised light reflects from the sample under study and due to the different reflection coefficients of the ‘p’ and ‘s’ states of polarisation, the effect is to modify the polarisation of the reflected beam. The modified state of polarisation at the output of the system is then measured by passing through a linear polarisation analyser followed by photodetector. The measured response depends upon the optical properties of material under investigation. Knowledge of the angle of incidence, along with wavelength, azimuth and analyser angle can be used to determine physical properties of individual materials, such as refractive index and film thickness. Presently, bulk optics elements are routinely used for polarisation dependent ellipsometry systems. The focus of this chapter is on developing integrated polarisation mode converter alternative to the bulk element used in the input section of the ellipsometry system. The polarisation mode converter is used to control and/or alter the state of polarisation of the input light.

In this chapter, we describe how it is possible to control the SOP of the light emitted from QCLs, using coupled modes. The work presented here is based upon similar work on conventional interband semiconductor lasers [86] where integrated PMC are reported. We describe how the design of PMCs are adapted for QCLs and how the PMCs are fabricated and characterised for QCLs with an emission wavelength of  $\sim 4450$  nm. The work reported in this chapter has already been published in ref. [91].

### 4.1.1 Aim

The aim is to design, fabricate and characterise the polarisation mode converter for quantum cascade laser operating at a wavelength around 4450 nm.

### 4.1.2 Objective

The objectives of this research are;

- To design and fabricate a polarisation mode converter for a quantum cascade laser.
- To integrate this polarisation mode converter with a Distributed Bragg Reflector [QCL](#). The [DBR](#) provides the required single frequency laser operation to the [PMC](#). This is one of the essential requirements for the [PMC](#) in order to avoid multimode beating effects inside the [PMC](#).
- To demonstrate polarisation mode conversion for the quantum cascade laser.

## 4.2 Polarisation Mode Conversion Theory

As in the case of conventional interband semiconductor lasers [86], the [PMCs](#) design employed throughout this work are also based upon waveguides with asymmetric cross-sectional profiles as indicated in Figure 4.1(a). This asymmetric cross-section results in a rotation of the optical axis of the birefringent guide, such that as a [TM](#) mode enters this asymmetric section, it excites both the single lobed fundamental modes of the guide (Hybrid [TE](#) - [TM](#) modes), with the relative propagation constant (and refractive indices) being dependent upon the degree of asymmetry and birefringence of the guide. For an offset of the optical axis of  $45^\circ$  ( $\pi/4$ ) these modes are, essentially, fully hybridised which leads to beating with

the characteristics half beat length given by

$$L_{Beat/2} = \frac{\pi}{\beta_{TE} - \beta_{TM}} \quad (4.1)$$

or

$$L_{Beat/2} = \frac{\lambda}{2(n_{eff,TE} - n_{eff,TM})} \quad (4.2)$$

where  $\beta_{TE} - \beta_{TM} = \Delta\beta$  is the difference in propagation constants between two fundamental (single-lobed) modes that propagate in the asymmetric guide [79, 81, 86]. At the half beat length  $L_{Beat/2}$ , for a phase difference  $\Gamma = \pi$  and optical axis angle  $\theta = \frac{\pi}{4}$ , a complete **TM**  $\rightarrow$  **TE** or **TE**  $\rightarrow$  **TM** polarisation conversion takes place. The working principal of **PMCs** is illustrated in Figure 4.1. The **PMC** employed in this work (further description can be found in section 4.3) is shown in Figure 4.1. Figure 4.1(b) shows the propagation of single lobed fundamental modes (Hybrid **TE** - **TM** modes) along the asymmetric guide. The evolution of the SOP of a linearly planarised **TM** input beam through various States of Polarization (**SOP**) profiles along the guide and corresponding phase difference between **TE** - **TM** modes along the guide are shown in Figure 4.1(c)-(d). Clearly, by varying the length, and/or, the asymmetry of the waveguide, it is possible to adjust the fraction of **TM** and **TE** polarisation emerging from the asymmetric section, and fabricate waveguide versions of bulk optic polarisation components, such as, quarter waveplates and half waveplates.

### 4.2.1 Polarisation Purity

The polarisation purity, also referred to as polarisation conversion efficiency,  $P_c$ , at the output of the **PMC**, is the percentage of light emerging from the asymmetric section with polarity different to that of the input light. For example, assuming **TM** polarised light as the input for **PMC**, for a phase difference of  $\Gamma = \pi$  and optics axis angle of  $\theta = \pi/4$ , a complete  $90^\circ$  rotation of the polarisation (**TM** to **TE** conversion) will take place after propagating the half beat length  $L_{Beat/2}$

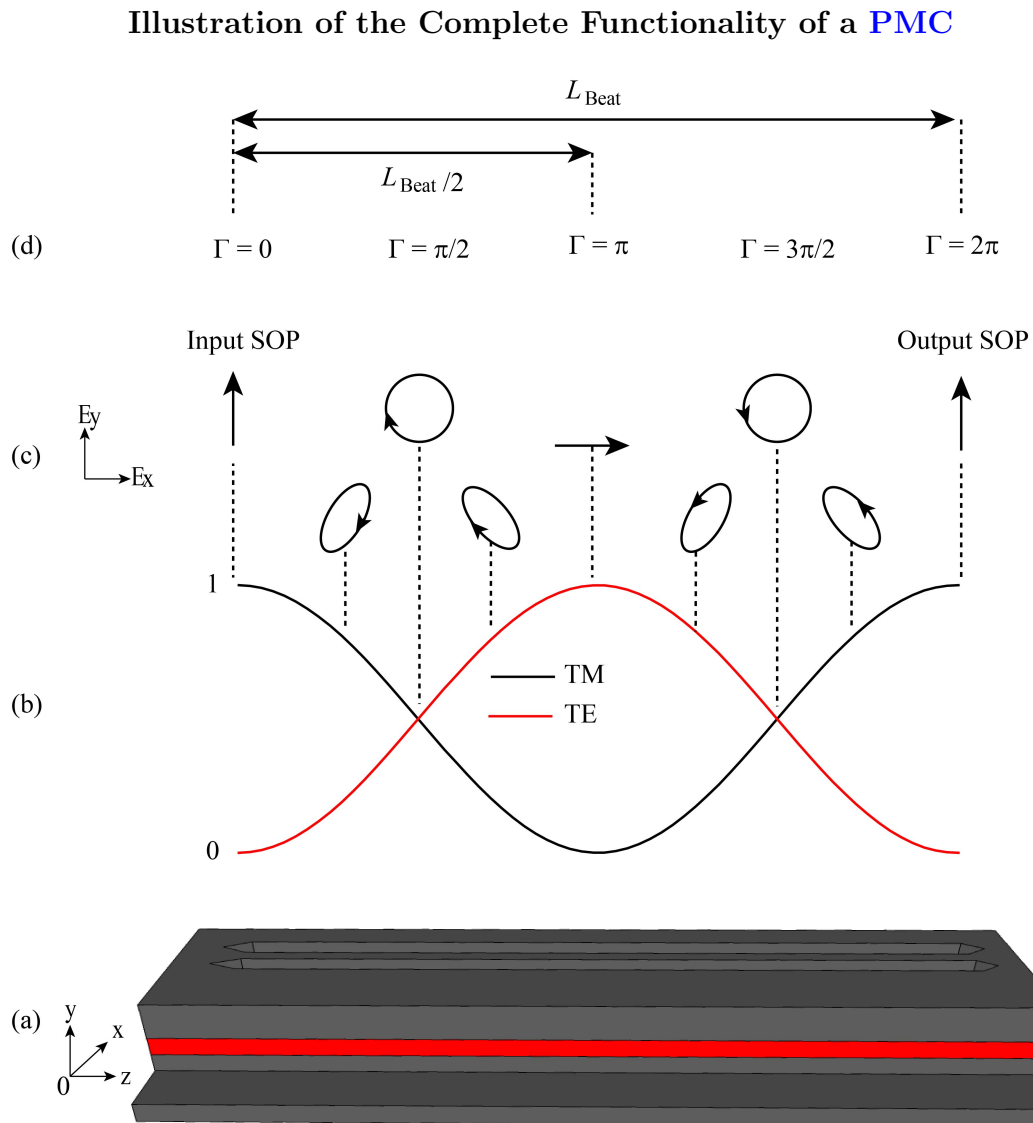


FIGURE 4.1: Illustration of the complete functionality of a PMC (a) Illustrates in 3D a side view of the PMC waveguides with asymmetric cross-sectional profiles employed in this work the red region indicates the approximation position of the active region of the device (description can be found in section 4.3) (b) Illustrates the propagation of TE and TM polarization modes (Hybrid TE - TM modes) along (z-direction) the PMC waveguides also indicated are the circular and elliptical states of polarization (SOP) and direction of polarization as a function of z (c) Illustrates the evolution of the circular and elliptical SOP and direction of polarization as a function of z (d) Resulting phase difference between TE - TM modes along the guide.

and the **TE** polarisation purity  $P_c$  equals 100%. The polarisation purity  $P_C$  can be found using

$$P_c = \frac{P_{TE}}{P_{TM} + P_{TE}} \times 100\% \quad (4.3)$$

where  $P_{TM}$  and  $P_{TE}$  are the **TM** and **TE** polarised light output power. Experimentally, the polarisation conversion can approach 100%, but requires increasingly stringent tolerance requirements for a single waveguide element. Holmes et al. and Hutchings et al. have identified an alternative approach of exploiting a universal 50% converter (Quarter waveplate) [79, 81] in a half-beat-length which can approach 100% by using two elements [92].

## 4.2.2 Definition of Quarter Waveplate and Half Waveplate

The Quarter Waveplate (**QW**) is a **PMC** waveguide with asymmetric cross-sectional profile length equal to a quarter beat length  $L_{Beat/4}$ . A **PMC** with this length has a phase difference between Hybrid **TE** - **TM** modes equal to  $\pi/2$  and polarisation purity becomes 50%, which manifests as a linearly polarised input being converted into circularly polarised output. The optical path length difference between **TM** and **TE** light is equal to a quarter of the wavelength and can be defined as

$$(n_{eff,TE} - n_{eff,TM})L_{Beat/4} = \frac{\lambda}{4} \quad (4.4)$$

The **QW** is a particular matter of interest because many applications would benefit from an elliptically polarised output, as required in some forms of spectroscopy [89], ellipsometry [90] and integrated optics (such as integrated birefringent waveguide described in **Chapter 5**).

The **PMC** waveguides with asymmetric cross-sectional profiles and of length equal to a half beat length  $L_{Beat/2}$  are referred to as a half waveplate. At the **PMC** with this length the phase difference between Hybrid **TE** - **TM** modes is equals to  $\pi$  and polarisation purity becomes 100%, which means a complete  $90^\circ$  polarisation rotation ( **TM** - **TE** or **TE** - **TM**) will take place and the light will still emerge

### Schematic Illustration of the PMC Chip Layout

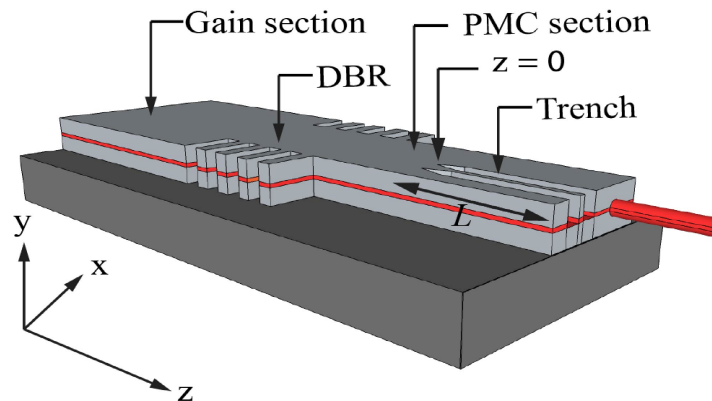


FIGURE 4.2: Schematic illustration of the chip layout of a QCL that includes a gain section, lateral DBR and an integrated PMC, the trenches of the PMC were etched using the reactive ion etching lag effect. There is no electrical contact to the PMC section.

linearly polarised however the polarisation will be perpendicular to that of the input polarisation. The optical path length difference between TM and TE light is half of the wavelength and can be defined as

$$(n_{eff,TE} - n_{eff,TM})L_{Beat/2} = \frac{\lambda}{2} \quad (4.5)$$

## 4.3 Integrated Polarisation Mode Converter Design

The device configuration employed and realised in this chapter is shown in Figure 4.2. The integrated device consists of a gain section, a lateral DBR and a polarisation mode converter. In this section we detail the design description of the polarisation mode converter and its integration with the DBR QCL. Table 4.1 shows the values of the refractive indices and the thicknesses of the layers used to design the PMC and lateral DBR. The required refractive indices of the QCL layers at  $\lambda \sim 4445$  nm were calculated using ref. [9].

TABLE 4.1: Waveguide layer, materials, thicknesses and refractive indices of the QCL material we used for this project are shown. Refractive indices of the QCL material at  $\lambda \sim 4445$  nm were calculated using ref. [9].

Layer	layer name	Semiconductor	Index	Thickness( $\mu\text{m}$ )
6	Contact	InGaAs	3.0	0.1
5	Upper cladding layer	InP	3.008	2.5
4	Upper waveguide layer	InGaAs/AlInAs	3.39	0.324
3	Active core	InGaAs/AlInAs	3.36	1.447
2	Lower waveguide	InGaAs/AlInAs	3.39	0.344
1	Buffer layer	InP	3.06	0.2
0	Substrate	InP	3.06	-

### Illustration of the Waveguide Width Dependence Effective Refractive Indices of Exited Modes

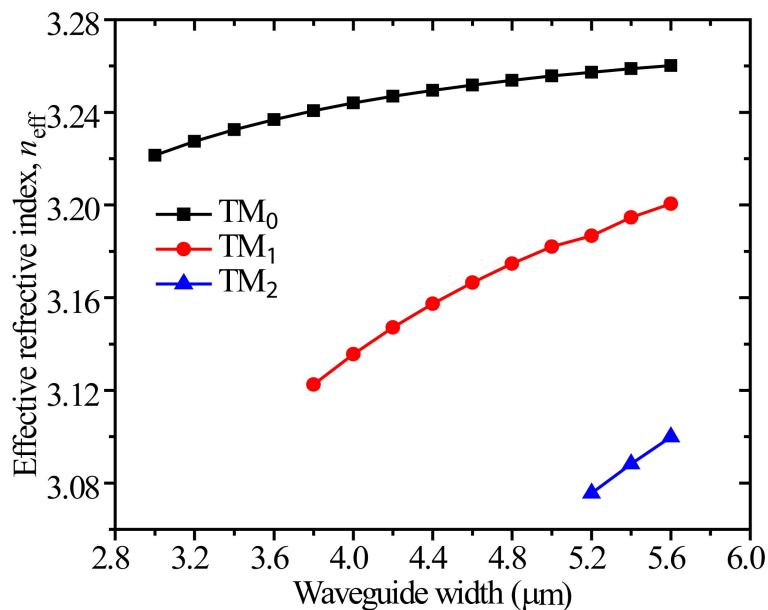


FIGURE 4.3: Calculated effective index of the guided modes in a ridge waveguide at different ridge width for a laser operating wavelength  $\lambda = 4445$  nm. Calculation was carried out using a full-vectorial, 3D eigensolver, as implemented in the software packages Lumerical Mode Solutions LSM [4]

#### 4.3.1 Waveguide width Optimisation

The first step towards designing the PMC is the optimisation of the waveguide width in which asymmetric cross-sectional profiles are to be fabricated. Generally speaking a PMC requires a guide that supports only single lobed fundamental spatial modes (TE and TM modes) [81, 93], of the guide.

### Lowest Order Guided Mode (TM and TE) without Asymmetric Cross-section

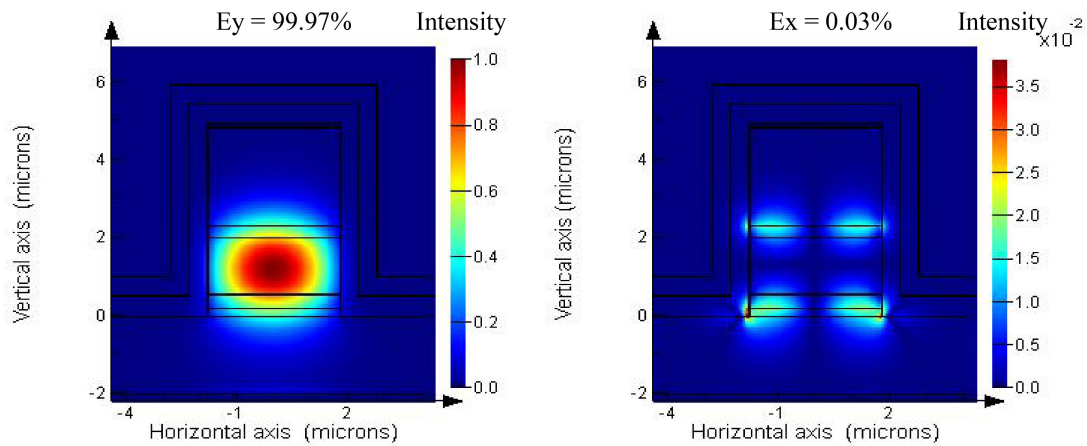


FIGURE 4.4: (a) & (b) Show the simulated mode profiles of the **TM** and **TE** components respectively of the lowest order guided mode (without asymmetric cross-section). Calculation was carried out using a full-vectorial, 3D eigensolver, as implemented in the software packages Lumerical Mode Solutions **LSM** [4]

The waveguide width optimisation work was carried out using a full-vectorial, 3D eigensolver, as implemented in the software packages Lumerical Mode Solutions **LSM** [4]. Figure 4.3 illustrates the waveguide width dependant effective refractive indices of the exited modes in a  $4.9 \mu\text{m}$  high waveguide. Clearly, for waveguide ridge widths below  $3.8 \mu\text{m}$  ( $n_{eff} \sim 3.12$ ) exited higher order modes are cut-off, where as the fundamental mode cut-off was found to be below  $3.0 \mu\text{m}$  ( $n_{eff} \sim 3.22$ ). Thus, single mode **TM** propagation is ensured within the range between  $3.0 \mu\text{m}$  to  $3.8 \mu\text{m}$  wide waveguides. Within this range, a fundamental **TM** (**TM<sub>0</sub>**) mode is launched from the **DBR QCL**. To minimise the optical coupling loss and insertion loss, a  $3.6 \mu\text{m}$  wide waveguide, close to the first order cut-off condition ( $3.8 \mu\text{m}$ ,  $n_{eff} \sim 3.22$ ), was chosen to be designed and fabricated for the **PMC**.

**QCLs** are based on intersubband transitions in quantum wells. The selection rules for intersubband transitions dictate that only light polarised with its electric vector perpendicular to the plane of the quantum well can couple to the intersubband transitions. In the typical waveguide arrangement used in a **QCL**, the optical axis is perpendicular to the plane of the quantum wells, this means that there is only optical gain for **TM** polarised modes. Figure 4.4(a)- 4.4(b) shows the mode profile

of the TM (99.97%) and TE (0.03%) components of the lowest order guided mode calculated for symmetric QCL waveguide. Calculation was carried out using a full-vectorial, 3D eigensolver, as implemented in the software package Lumerical Mode Solutions (LMS).

### 4.3.2 Polarisation Mode Converter Design

To gain knowledge, a review of the different designs of already realised PMCs on different material systems, namely, GaAs/AlGaAs, InP/InGaAsP and SOI and InGaAsP based QW material structures, was conducted. Most of these PMCs are shallow etched, asymmetric cross-sectional profile types which required a two step etch process, generally for telecommunication wavelength. The majority of these designs suffer from high optical losses due to mode size mismatching between symmetric and asymmetric waveguide sections. In this regards, Holmes et al reported relatively simple low loss PMC designs using a single-mask and single dry etch process [79]. In their design, asymmetric cross sectional profiles were realised by etching **ribs** and **trenches** on one side of the symmetric waveguide using a phenomena called RIE lag [79]. The RIE lag phenomena can also be used to create such asymmetric waveguides for deeply etched QCL waveguides. The work presented in this chapter is based upon a similar design reported by Bregenzer et al. for conventional interband semiconductor lasers [86].

The waveguide, with tapered input section and cleaved cross section profile of a PMC, was fabricated by etching the **ribs** and **trenches** on one side of the symmetric waveguide, using RIE lag effects, as shown in Figure 4.5. Figure 4.5(a) clearly shows that the trenches are tapered to **grade** the degree of asymmetry between the symmetric and PMC sections, which results in a smooth rotation of the optical axis of the guide [79]. This **smooth** transition ensures minimum optical loss and a corresponding low reflection between the symmetric and asymmetric waveguide sections.

## SEM Images of a PMC Waveguide after ICP-RIE Etching (design D1)

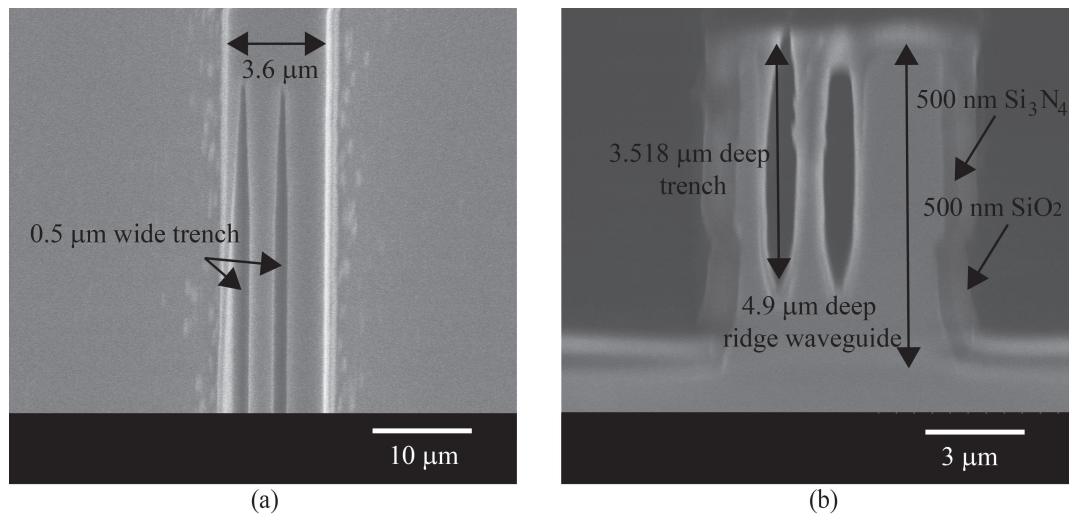


FIGURE 4.5: SEM images of a PMC waveguide after ICP-RIE etching (design D1) (a) Top view of taper input section of PMC (b) Cleaved cross-section view of PMC.

## Detail PMC Design Description (Design D1)

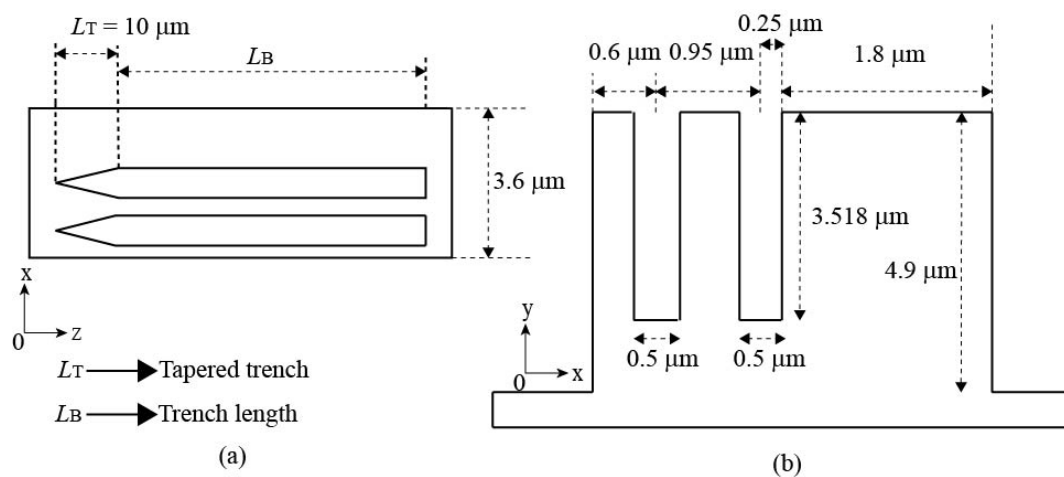


FIGURE 4.6: Detail design description of PMC design D1 using by etching two trench (a) Top view (b) cross-section view

### Calculation of Mode Profiles of the PMC (Design D1)

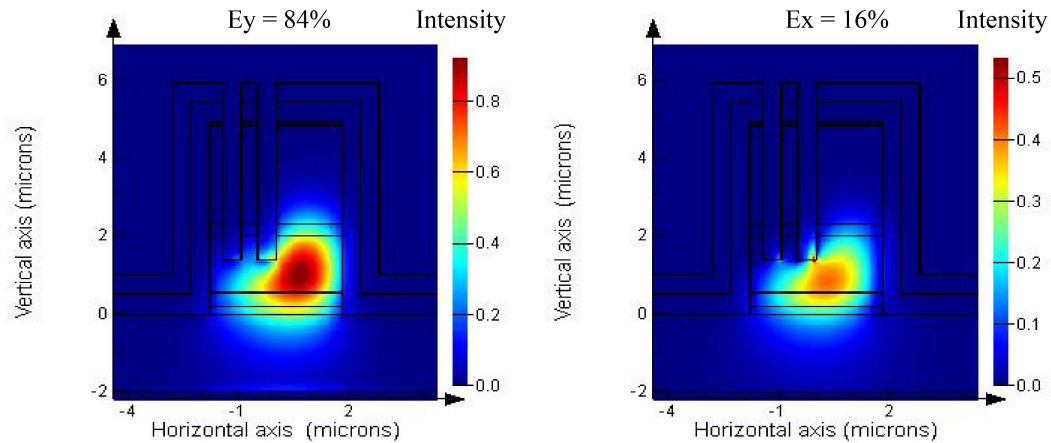
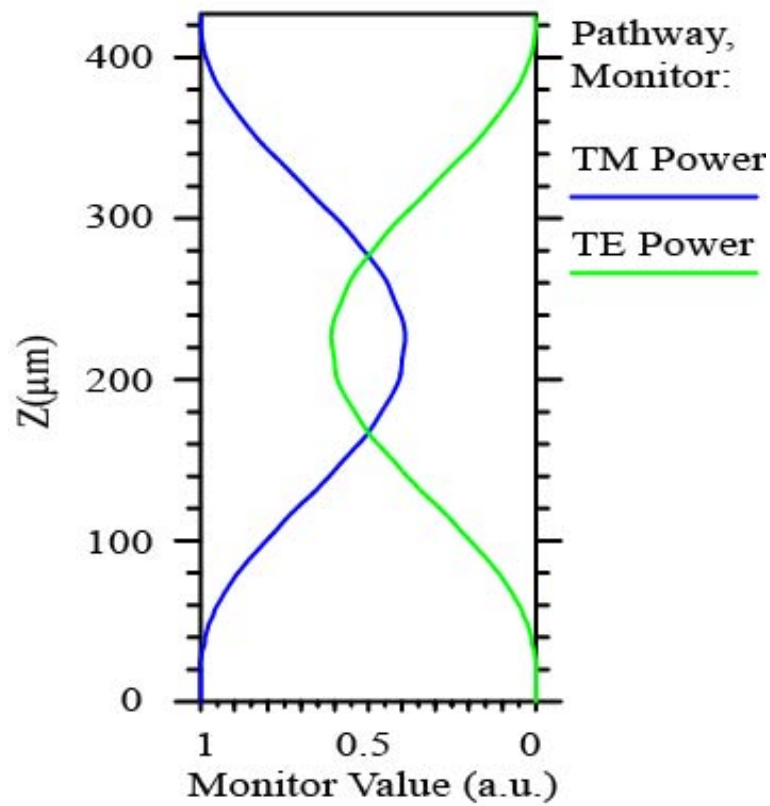


FIGURE 4.7: Calculation of mode profiles: (a) and (b) the **TM** and **TE** components respectively of the lowest order guided mode within the asymmetric section of design D1. Calculation was carried out at  $z=10 \mu\text{m}$  just after tapered region of **PMC**.

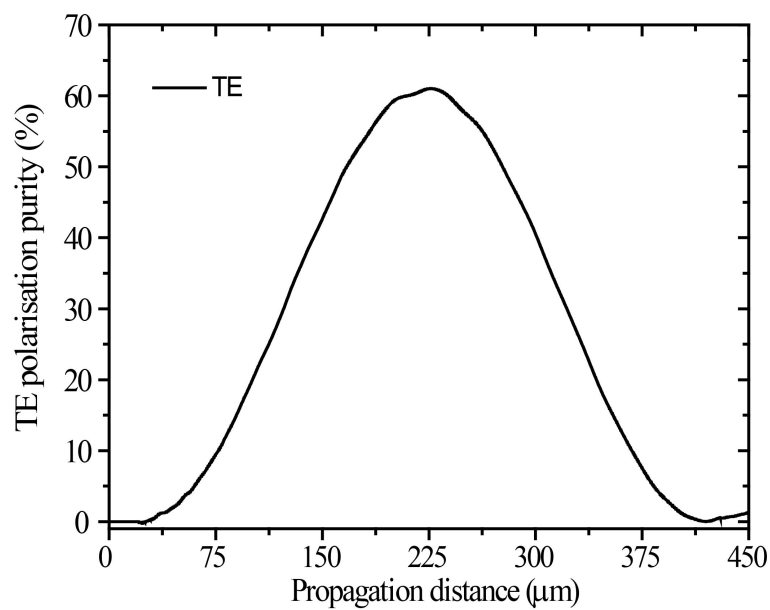
## 4.3.3 Design Description and Analysis

### 4.3.3.1 Design 1 (D1)

A detailed design description of **PMC** design D1, obtained by etching two trenches, top and cross-section view are illustrated in the Figure 4.6. The dimensions and position of the trenches are also indicated in the figure. These trenches are used to control the degree of asymmetry of the waveguide. This asymmetric cross-section results in a rotation of the optical axis of the birefringent guide, such that as a **TM** mode enters this asymmetric section, it excites both the single lobed fundamental modes of the guide (Hybrid **TE** - **TM** modes), with the relative propagation constant being dependent upon the degree of asymmetry of the guide. To model the operation of the **PMC**, we first calculate the mode profiles for the the asymmetric waveguide (Figure 4.7). The hybrid mode separate into **TM** and **TE** components at the start of the **PMC** just after the taper trench region. Figure 4.7(a) - 4.7(b) shows the calculated mode profile of the **TM** and **TE** components of the lowest order guided mode for design D1. The **TM** and **TE** fraction calculated by using an eigensolver for the **PMC** design described above are 84% and 18%, respectively.

**TM to TE Conversion Vs Propagation Distance & TE Polarisation Purity**

(a)



(b)

FIGURE 4.8: (a) Calculated TM to TE conversion versus propagation distance using BPM of design D1 (b) Calculated TE polarisation purity (%) versus propagation distance using BPM of design D1

Shown in Figure 4.8(a) is the calculated TM to TE conversion as a function of PMC propagation distance. The calculation was carried out using BPM, as implemented in the software package RSoft [5]. The calculated TE polarisation purity (%) is shown in Figure 4.8(b). From this figure, a maximum TE polarisation purity of up to 60% can be achieved for a  $\sim 200 \mu\text{m}$  long PMC. A TE polarisation purity around 50% is observed for  $151 \mu\text{m}$  (including  $10 \mu\text{m}$  long tapered trench) and  $256 \mu\text{m}$  (including  $10 \mu\text{m}$  long tapered trench) long PMCs. The grid size used for the BPM simulation are  $\Delta x=20 \text{ nm}$ ,  $\Delta y=20 \text{ nm}$ , and  $\Delta z=20 \text{ nm}$ . However, software default grid sizes are  $\Delta x = 50 \text{ nm}$ ,  $\Delta y = 50 \text{ nm}$  and  $\Delta z = 200 \text{ nm}$  and less than 5% difference was found in the polarisation purity calculation compared to the 20 nm grid size simulation. Nevertheless, the minimum grid size is limited by the computer memory. The minimum grid size that is permitted by the software is 10 nm but this requires more than 12 hours of processor time using a Core2 Quad 2.3 GHz 3.21 RAM processor to complete the simulation. Therefore, a 20 nm grid size was used for faster ( $\sim 1.5$  hours) simulation. The calculated conversion efficiency of the PMCs with 20 nm simulation grid size showing good agreement with experimental results, as can be seen in Table 4.2.

The variations of TE polarisation purity at  $\pm 100 \text{ nm}$  change in trench depth of design D1 are shown in Figure 4.9. Clearly, we observed a very large change in polarisation purity above  $150 \mu\text{m}$  and changes are negligibly small below  $150 \mu\text{m}$ . Thus, from a fabrication point of view precise control over the trench depth is required, as small variations in the trench depth will lead to large changes in polarisation purity for PMC's longer than  $150 \mu\text{m}$ .

#### 4.3.3.2 Design 2 (D2)

After characterisation of design D1, and re-examining the RIE lag effect, we revised the PMC design to improve the TE polarisation purity. Design D2 also has two trenches, one of  $0.5 \mu\text{m}$  and another one of  $0.4 \mu\text{m}$  wide, of depth  $3.518 \mu\text{m}$  and  $2.82 \mu\text{m}$  respectively, on a  $3.6 \mu\text{m}$  wide, and  $4.9 \mu\text{m}$  height, waveguide. Detailed design descriptions of PMC design D2, top and cross-section views, are illustrated in

## Variations of TE Polarisation Purity with Trench Height

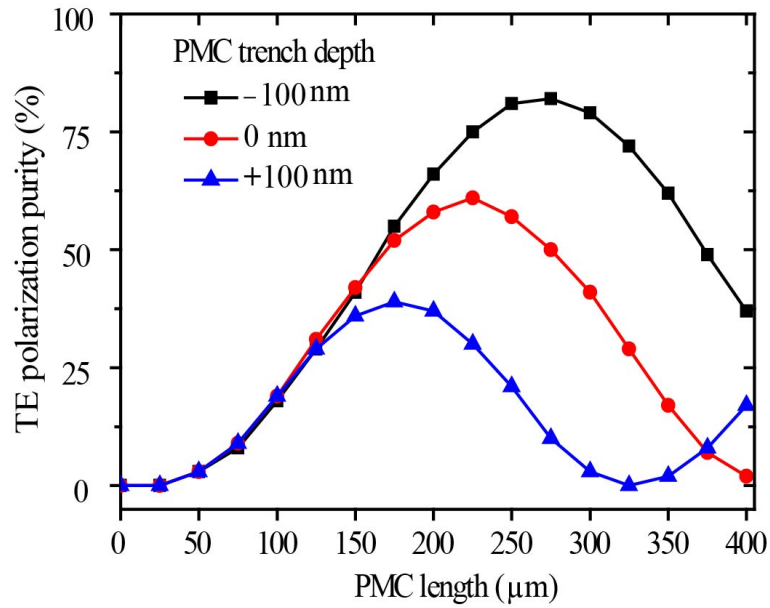


FIGURE 4.9: Shows the variations of TE polarisation purity at +/- 100 nm change in trench height of design D1. Where trench width is fixed at  $0.5 \mu\text{m}$  and calculation was carried out using a BPM.

## Detail PMC Design Description (Design D2)

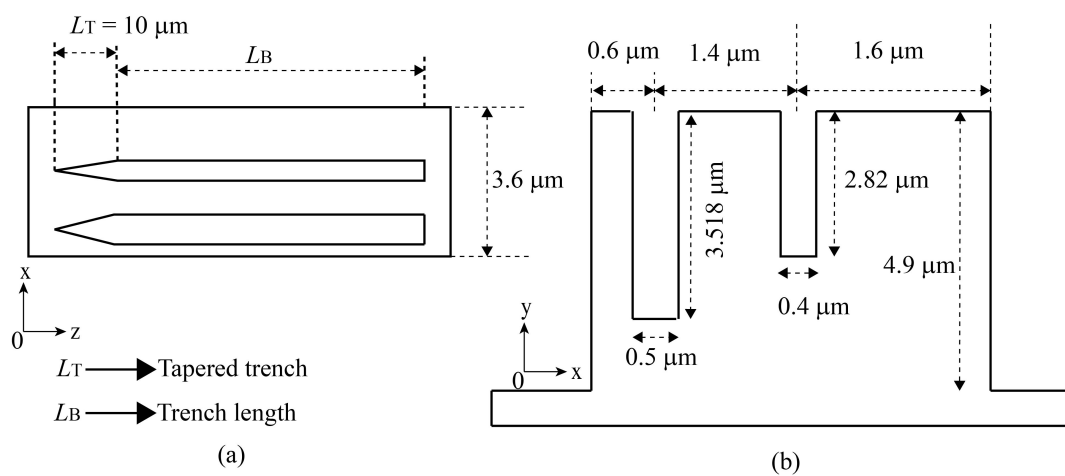


FIGURE 4.10: Detailed design descriptions of PMC design D2 (a) Top view (b) cross-section view

### Calculation of Mode Profiles of the PMC (Design D2)

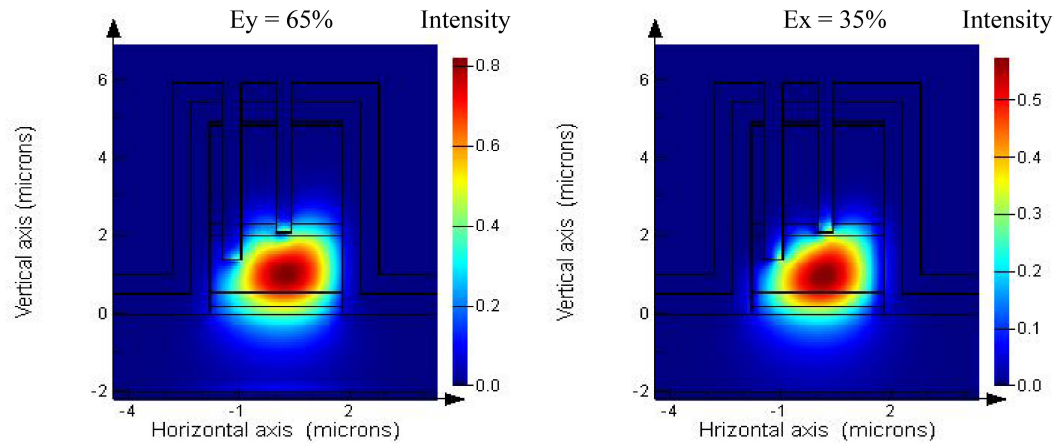
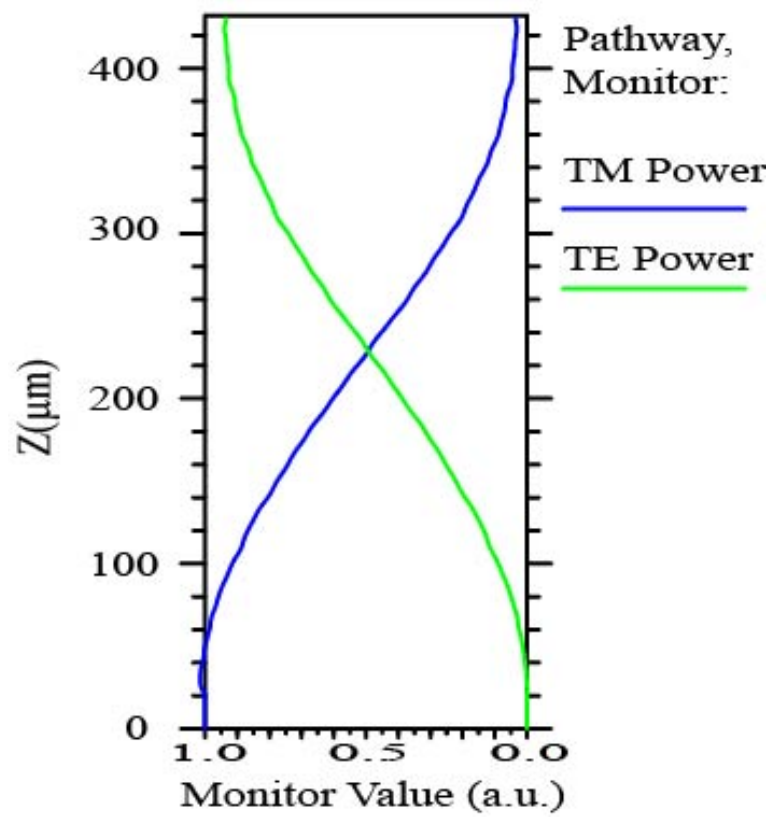


FIGURE 4.11: (a) and (b) show the **TM** and **TE** components respectively of the lowest order guided mode within the asymmetric section of design D1. Calculation was carried out at  $z=10 \mu\text{m}$  just after tapered region of **PMC**.

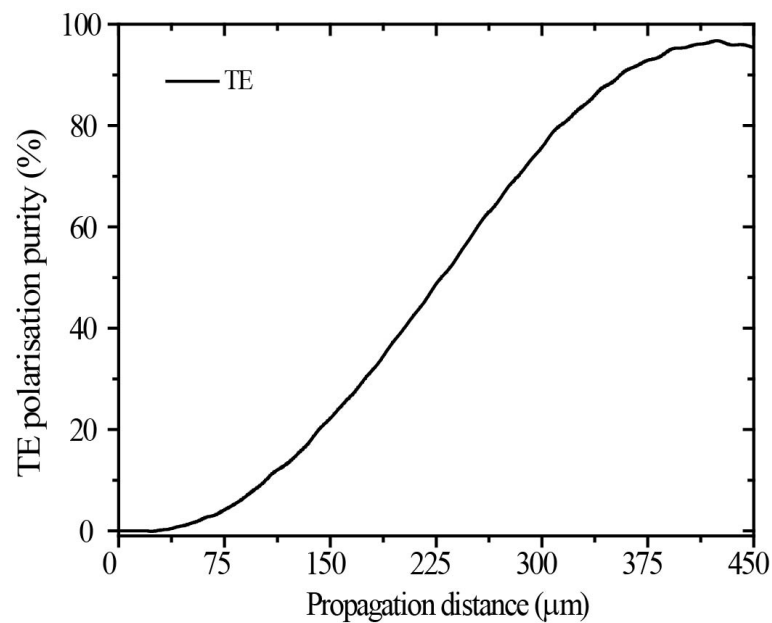
Figure 4.10, where the dimensions and positions of the trenches on the waveguide are indicated in the figure.

In a manner similar to design D1, we first calculate the mode profiles for the the asymmetric waveguide (Figure 4.11). The hybrid mode separated into **TM** and **TE** components at the start of the **PMC** just after the taper trench region. Figure 4.11(a) - 4.11(b) shows the calculated mode profile of the **TM** and **TE** components of the lowest order guided mode for design D1. The **TM** and **TE** fraction calculated by using an eigensolver for the **PMC** design described above are 65% and 35%, respectively.

Shown in Figure 4.12(a) is the calculated **TM** to **TE** conversion as a function of **PMC** propagation distance. The calculation was carried out using BPM, as implemented in the software package RSoft [5]. The calculated **TE** polarisation purity (%) is shown in Figure 4.12(b). From this figure, the maximum **TE** polarisation purity of up to 96% can be achieved with a  $425 \mu\text{m}$  long **PMC**. The **TE** polarisation purity around 50%, equivalent to a quarter waveplate or a quarter beat length ( $L_{Beat/4}$ ), is observed with a  $231 \mu\text{m}$  long **PMC**. The BPM simulation settings are the same as described in Section 4.3.3.1

**TM to TE Conversion Vs Propagation Distance & TE Polarisation Purity**

(a)



(b)

FIGURE 4.12: (a) Calculated TM to TE conversion versus propagation distance using BPM of design D1 (b) Calculated TE polarisation purity (%) versus propagation distance using BPM of design D2

### Variations of TE Polarisation Purity with Trench Height

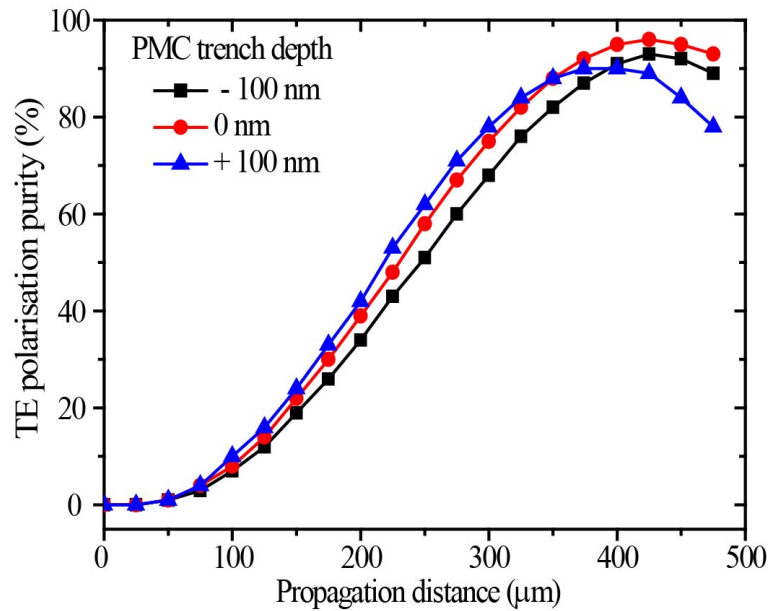


FIGURE 4.13: Shows the variations of TE polarisation purity at +/- 100 nm change in trench height of design D1. Where trench width is fixed at  $0.5 \mu\text{m}$  and calculation was carried out using a BPM.

The variations of TE polarisation purity at +/- 100 nm change in trench depth of design D2 are shown in Figure 4.13(a). Clearly, design D2 shows less sensitivity with respect to design D1. -3% changes in polarisation purity were observe for +/- 100 nm changes in trench depth. Thus, from a fabrication point of view design D2 is a more robust design compared to design D1.

#### 4.3.4 Integration with Distributed Bragg Reflector Grating

In this work, a DBR was integrated with a PMC; the DBR provides the required single frequency laser operation to the PMC. This is one of the essential requirements for the PMC in order to avoid multimode beating effects inside the PMC. The DBR mirror on QCLs can be formed on a waveguide by using several types of gratings, including surface [94], discrete-mode [95], buried [96] and lateral gratings [97]. The lateral grating, recently developed for QCLs by Thomas et al [97], can be formed by etching either side of the waveguide.

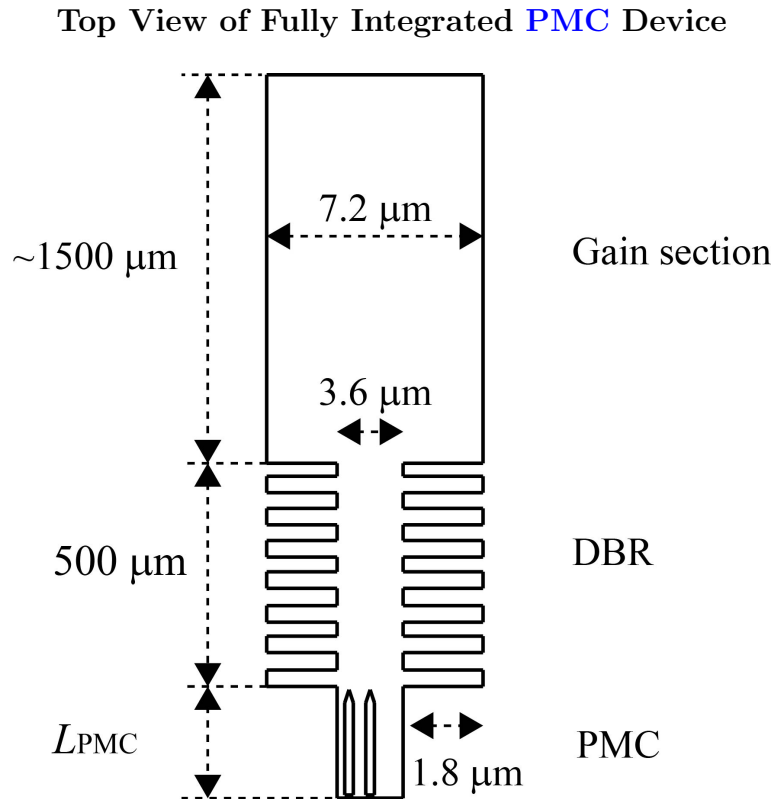


FIGURE 4.14: The top view of fully integrated PMC device is shown.

We exploit lateral grating technology for integration with PMCs. The top view of a fully integrated PMC device is shown in Figure 4.14. Clearly, a  $3.6 \mu\text{m}$  wide asymmetric PMC waveguide is integrated by etching  $1.8 \mu\text{m}$  either side of the  $7.2 \mu\text{m}$  gain section waveguide. To integrate the gain section and PMC we employed a first order DBR grating with grating period of  $700 \text{ nm}$  (50% duty cycle). For the dimension describe above, a reflectivity around 70% and coupling coefficient of  $63 \text{ cm}^{-1}$  were estimated for the  $500 \mu\text{m}$  long grating at  $\sim 4456 \text{ nm}$  wavelength. This calculation was carried out using the GratingMOD tool, as implemented in the software package RSoft [5]. The calculated stop-band of DBR grating for grating period of  $700 \text{ nm}$  is shown in Figure 4.15. Further description and discussion concerning lateral grating technology applied to QCLs can be found in ref. [97].

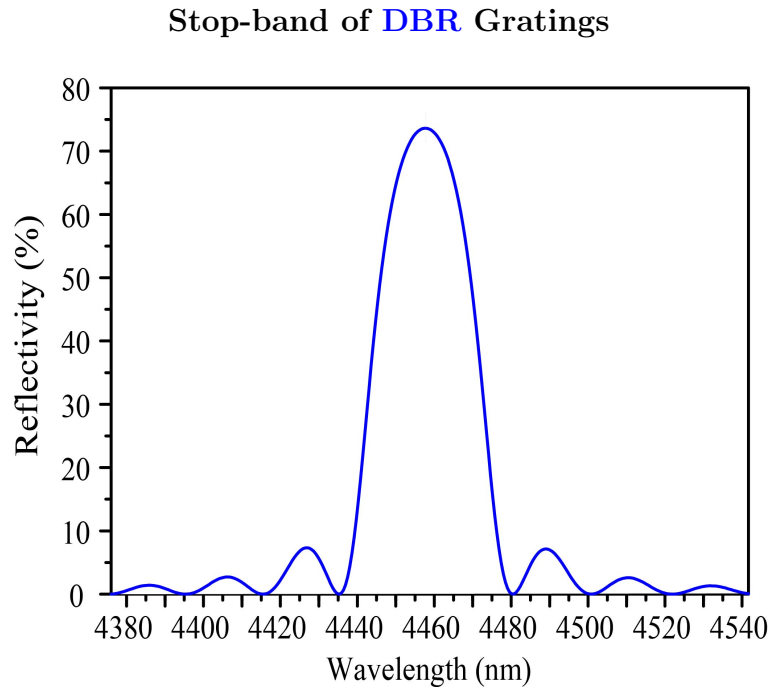


FIGURE 4.15: Shown is the calculated stop-band of DBR gratings for gratings period of 700 nm. The calculation was carried out using the GratingMOD tool by RSoft [5].

## 4.4 Characterisation and Results

The QCLs incorporating PMC devices reported in this section were characterised using the technique described in **Chapter 2**. The DBR and PMC design D1 characterisation was carried out at 298 K and design 2 at 250 K, with devices driven by 100 ns duration current pulses at a 60 kHz repetition rate. First, for reference, electro-optic and polarisation measurements were carried out for a DBR QCL laser without a PMC section. Essentially, we require single mode and purely TM polarised emission from the DBR QCL to integrate with the PMCs, since multimode emission will affect the polarisation purity of the PMCs.

### 4.4.1 DBR Laser

Figure 4.16 shows the light output intensity vs injection current (L-I) characteristics for a DBR QCL without a PMC. The threshold current density was found to be 2.98 kA/cm<sup>2</sup> and a peak optical power of around 0.8 mW was measured at a

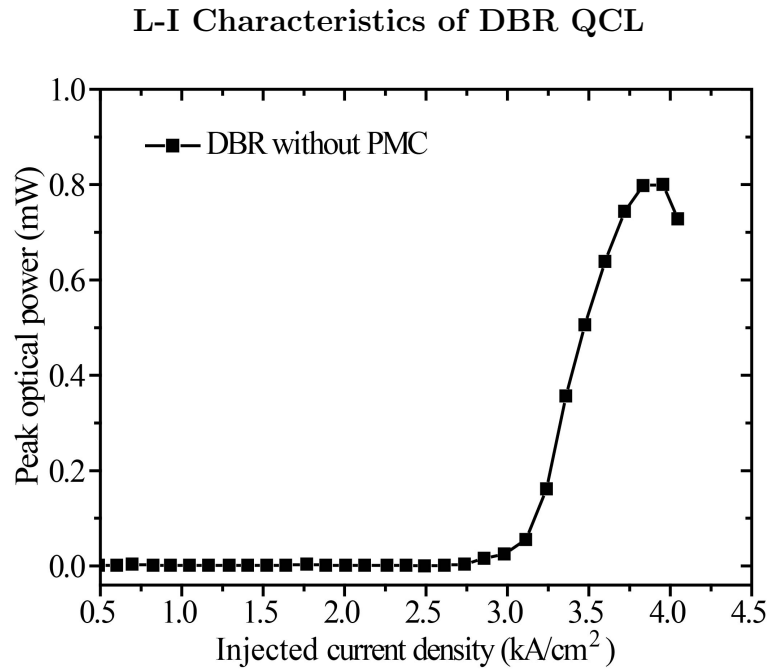


FIGURE 4.16: Shows the output peak optical power vs drive current densities characteristics for a DBRs QCL without PMCs measured at 298 K.

peak pulse current density of  $1.3 \cdot I_{th}$ . The emission spectra at a drive current density of  $1.3 \cdot I_{th}$  is shown in Figure 4.17. Clearly, single mode emission was recorded with a SMSR of around 21 dB, at an emission wavelength of 4444 nm.

The polarisation of the DBR output beam can be determined by recording the detector signal as a function of wire-grid polariser rotation angle ( $\theta = 0^\circ$  to  $360^\circ$ ), where  $\theta = 0^\circ$  is defined as the angle of the first maxima in transmission for TM light through the wire grid polariser. First and for reference, the polarisation was measured from a DBR QCL laser without PMCs (from front and back facets) and with pure TM emission recorded from the DBR facets as shown in Figure 4.18. A similar result was recorded from the gain facets.

## 4.4.2 Integrated Polarisation Mode Converter

### 4.4.2.1 Integrated PMC (design D1)

Results reported in this section are from the first processed sample where three integrated PMCs with different lengths were recovered from a damaged sample,

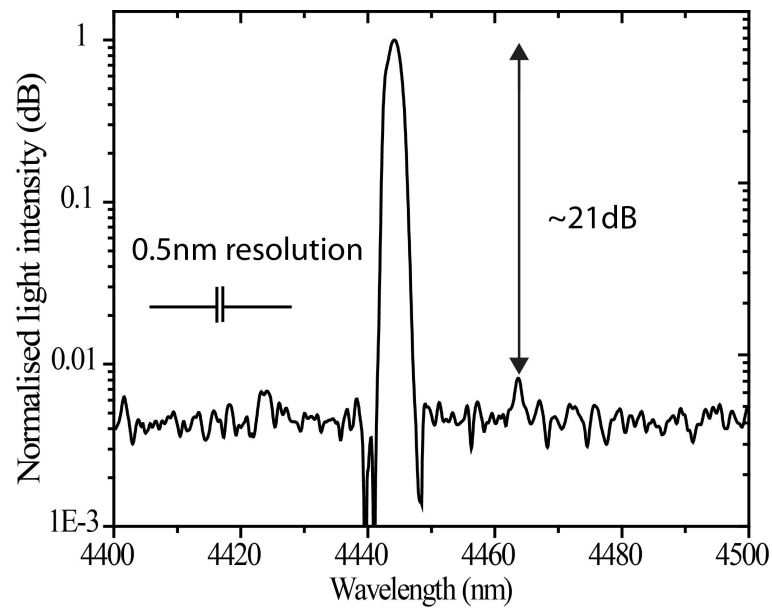
Emission Spectra of **DBR QCL** without **PMC**

FIGURE 4.17: Emission spectra of pulse and chirped **DBR QCL** without **PMC** acquired with **FTIR** resolution 0.5 nm at peak pulse current  $1.3 \cdot I_{th}$ .

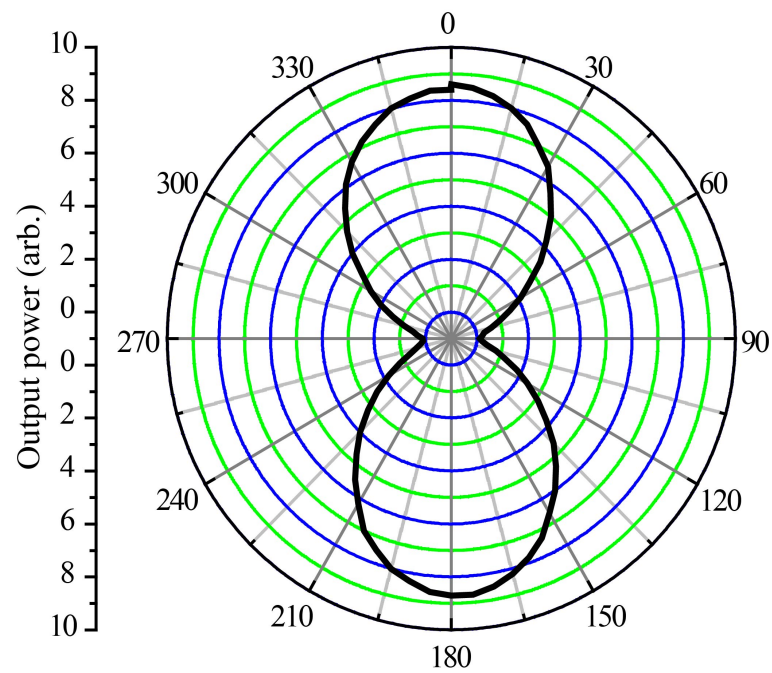
Polar Plot **DBR QCL** without **PMC**

FIGURE 4.18: Polar plots of output power (red line) from **DBR** facet of the **QCL** as function of wire-grid polarizer angle.

TABLE 4.2: Comparison of calculated and measured TE polarisation fraction as a function of PMC length.

Design	PMC length ( $\mu\text{m}$ )	TE(%) Measured	TE(%) Calculated
1	56	8	7
1	71	7	11
1	119	18	27
2	256	69	65

along with the DRQCL reported in **Chapter 3**. The QCLs incorporating PMC devices reported in this section were characterised using the technique described in **Chapter 2**. The power emitted from the PMC facet was measured: a) without the grid polarizer, b) with the grid polarizer axis parallel to QCL waveguide (TM polarisation), and c) with the grid polarizer axis perpendicular to the QCL waveguide (TE polarisation). All measured electro-optic TM polarised results shown in Figure 4.19 are compensated by a factor of 11% because with the Vertex 70 FTIR spectrometer the TM/TE transmittance ratio is 89% at our working wavelength.

The light output intensity vs injection current (L-I) characteristics of a 56  $\mu\text{m}$ , 71  $\mu\text{m}$  and 119  $\mu\text{m}$  long PMC device, based upon design D1 are shown in Figure 4.19(a), 4.19(c) and 4.19(e). The threshold current densities of 3.25  $\text{kA}/\text{cm}^2$ , 3.35  $\text{kA}/\text{cm}^2$  and 3.5  $\text{kA}/\text{cm}^2$  respectively, were extracted from L-I curves. The emission spectra measured with similar conditions to those described above are shown on Figure 4.19(b), 4.19(d) and 4.19(f), where measurements were carried out by driving the laser section above  $1.3 \cdot I_{th}$ . Polarisation purities ( $= P_{TE}/(P_{TE} + P_{TM}) \times 100\%$ ) of 8% for 56  $\mu\text{m}$ , 7% for 71  $\mu\text{m}$  and 18% for 115  $\mu\text{m}$ , long PMCs (design D1) were obtained from L-I characteristics and emission spectra. The relative TE polarisation component of different integrated PMCs with PMC lengths experimentally derived from both L-I characteristics and emission spectrum are summarised in Table 4.2. The calculated values in Table 4.2 come from a simulation using the full vectorial 3-D BPM as described above. The polarisation of the beam can be determined by recording the detector signal as a function of wire-grid polariser rotation angle ( $\theta = 0^\circ$  to  $360^\circ$ ), where  $\theta = 0^\circ$  is defined as the angle of the first maxima in transmission for TM light and  $\theta = 90^\circ$  is defined as the angle of the maxima in transmission for TE light, through the wire grid polariser. The

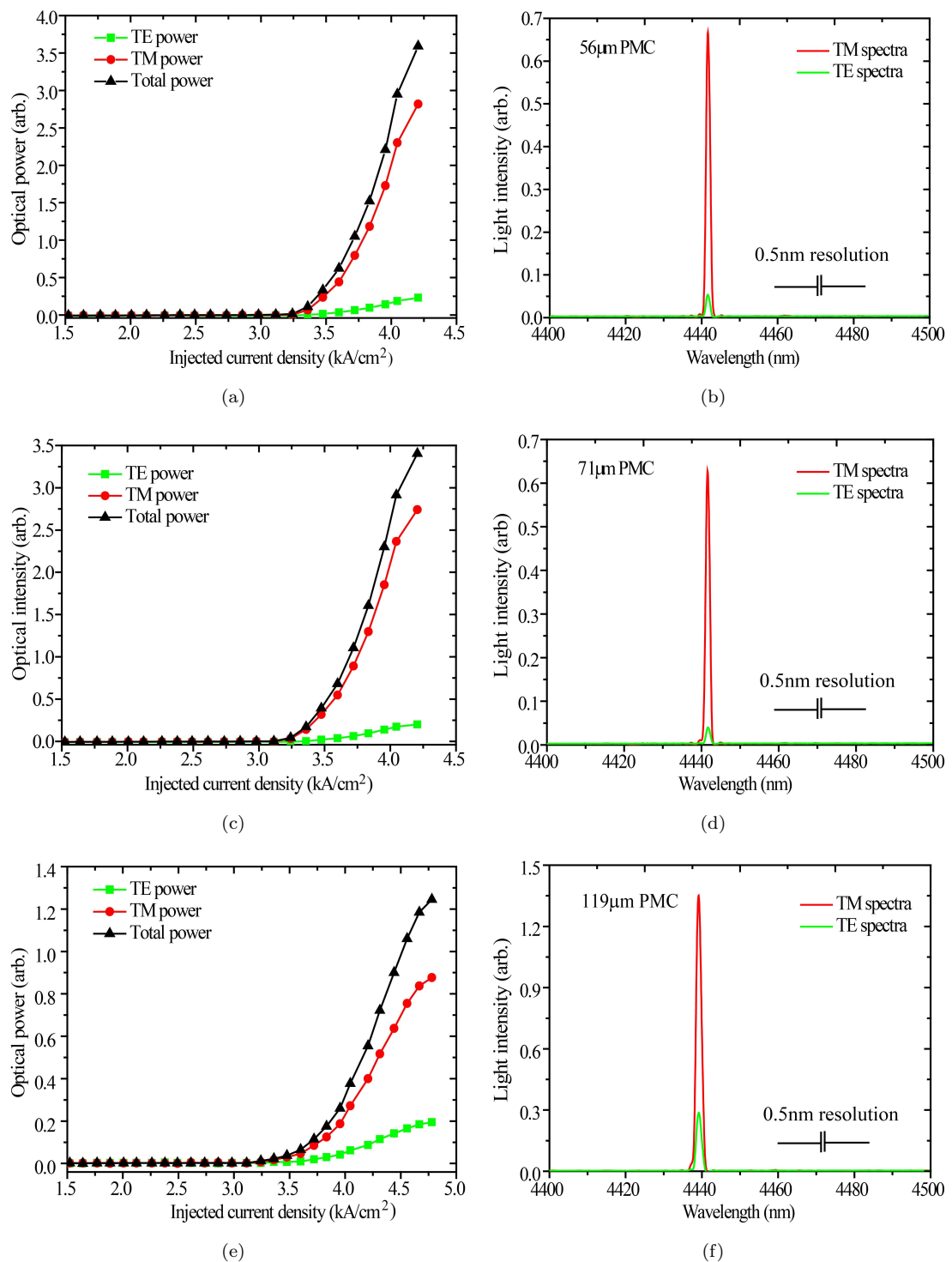
**L-I and Emission Spectra of a 56  $\mu\text{m}$ , 71  $\mu\text{m}$  and 119  $\mu\text{m}$  long PMC devices (Design D1)**

FIGURE 4.19: (a),(c) and (e) Shows the light injection current (L-I) characteristics and (b), (d) and (f) are the spectral emission of a 56  $\mu\text{m}$ , 71  $\mu\text{m}$  and 119  $\mu\text{m}$  long PMC devices, based upon design D1.

### Polar Plots of 56 $\mu\text{m}$ and 119 $\mu\text{m}$ long PMC devices (Design D1)

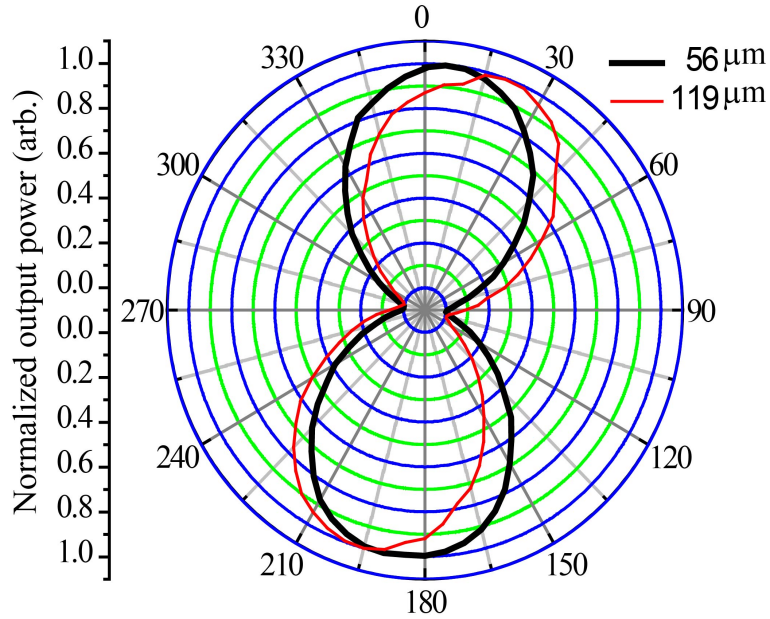


FIGURE 4.20: Polar plots of normalized output power from PMC facet as function of wire-grid polarizer angle for 56  $\mu\text{m}$  and 119  $\mu\text{m}$  long PMC (design D1). The maxima of the beam intensity were recorded around  $5^\circ$  and  $20^\circ$ , respectively.

Polar plots of normalized output power from PMC facet as function of wire-grid polarizer angle for 56  $\mu\text{m}$  and 119  $\mu\text{m}$  long PMCs (design D1) are shown in Figure 4.20. The maxima of the beam intensities were recorded at approximately  $5^\circ$  and  $20^\circ$ , respectively. The maxima of the beam intensity for a 71  $\mu\text{m}$  long PMC was recorded at approximately  $7^\circ$ , not shown in figures.

#### 4.4.2.2 Integrated PMC (design D2)

Based on experimental results from design D1, we revised our PMC design for final fabrication to improve the TE polarisation purity. The design description is detailed in section 4.3.3.2 and characterisation was carried out at 250 K.

The light output vs injection current (L-I) characteristics of a 265  $\mu\text{m}$  long PMC device based upon design D2 are shown in Figure 4.21(a). A threshold current density of 2.19  $\text{kA}/\text{cm}^2$  was obtained for this device. At a drive current of  $1.3 \cdot I_{th}$ , a peak optical power of nearly 2 mW (1.18 mW for TE and 0.53 mW for TM) was

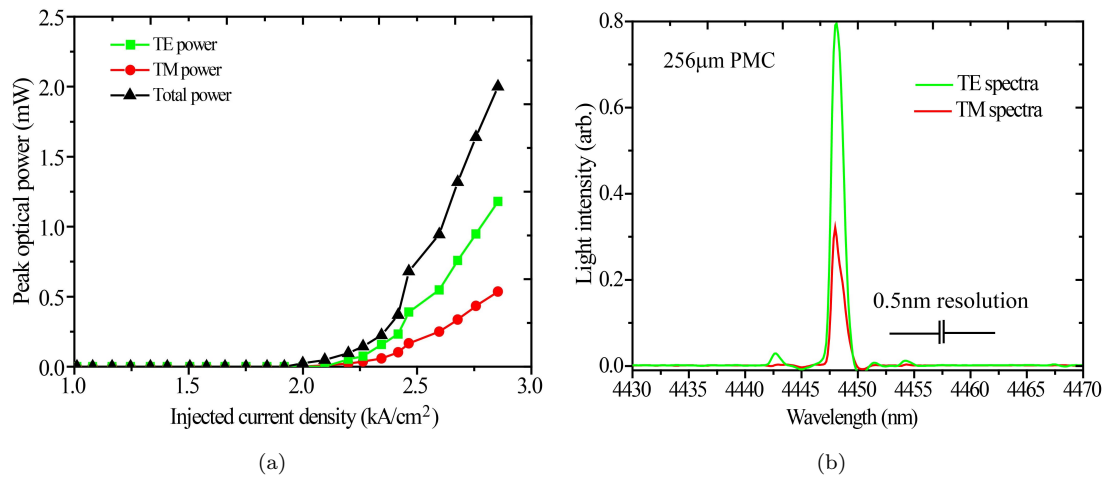
L-I and Emission Spectra of a 265  $\mu\text{m}$  long PMC devices (Design D2)

FIGURE 4.21: (a) L-I characteristics of 265  $\mu\text{m}$  PMC device showing the TM, TE and total power (b) showing TE and TM spectra by drive laser section above  $1.3 \cdot I_{th}$

measured from the PMC facet (design D2) and 18 mW from the gain section facet. The majority of the power in our QCLs was emitted from the gain section facets. The emission spectra, measured with similar conditions to those described above, are shown on Figure 4.21(b). Measurements were carried out by driving the laser section above  $1.3 \cdot I_{th}$ . Polarisation purities ( $= P_{TE}/(P_{TE} + P_{TM}) \times 100\%$ ) of 69% for a 256  $\mu\text{m}$  long PMC (design D2) were obtained from L-I characteristics and emission spectra.

The Polar plots of normalised output power from the PMC facet and gain facet, as a function of wire-grid polarizer angle, for the 256  $\mu\text{m}$  long PMC device, are shown in Figure 4.22. The maxima of the beam intensity were recorded at approximately  $65^\circ$  and pure TM emission was recorded from the gain facet. Table 4.2 shows the relative TE polarisation component of different integrated PMCs with PMC lengths experimentally derived from both L-I characteristics and emission spectrum. The calculated values in Table 4.2 were obtained from a simulation using the full vectorial 3-D BPM as described previously.

Whilst losing some devices during fabrication, PMC conversion efficiencies of up to 18% were obtained with design D1 and 69% for design D2, with PMC lengths of

### Polar Plots of 265 $\mu\text{m}$ long PMC devices (Design D1)

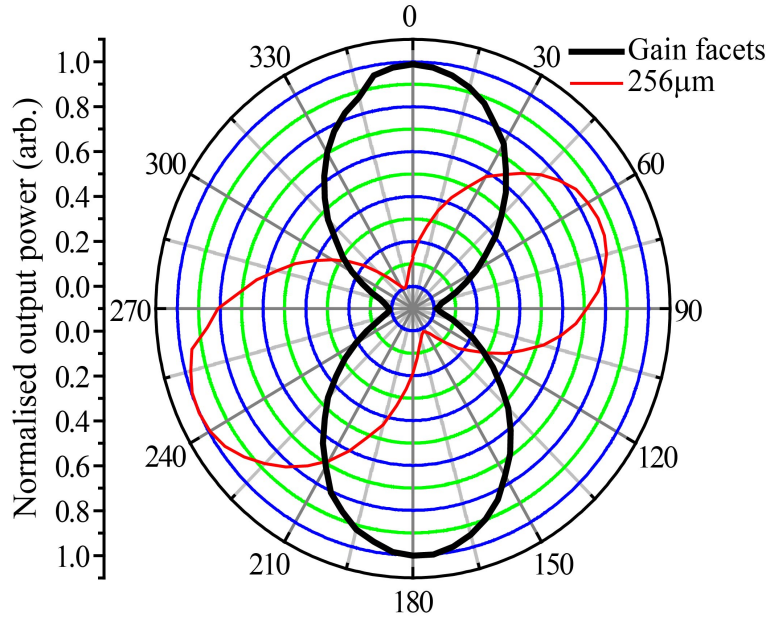


FIGURE 4.22: Polar plots of normalized output power from 256  $\mu\text{m}$  long PMC & gain facet of the QCL as function of wire-grid polarizer angle.

around 119  $\mu\text{m}$  and 256  $\mu\text{m}$ , respectively. Theoretically, the polarisation conversion can approach 100%, but requires increasingly stringent fabrication tolerance requirements. We have identified an alternative approach of exploiting a universal 50% converter [92] in a half-beat-length which can approach 100% by using two elements.

## 4.5 Conclusion

In this chapter, we have described the design, fabrication and characterisation of PMCs for QCLs operating in the MWIR, and demonstrated that by integrating a PMC with a QCL, the output polarisation can be controlled. We have demonstrated that it is possible to have a QCL that emits TM from one facet and predominately (69%) TE from the other facet. We have shown that there is a good agreement between our simulation and experiment.

With further optimization, control of the polarisation of a QCL will become important in several applications and in the operation of future designs of QCLs.

For example, as indicated in **Chapter 5**, if we combine **PMCs** with an integrated waveguide section that tunes the relative phase between **TM** and **TE** modes, a so called **DPS** section, then a tuneable integrated birefringent waveguide [98] can be integrated with a **QCL** to electronically tune the output wavelength and/or polarization as recently demonstrated in conventional interband lasers [99].

# Chapter 5

## Integrated Tuneable Birefringent Waveguide

### 5.1 Introduction

The birefringent filter [100] was first designed for astronomical purposes by Lyot in 1933, and Solc designed a similar birefringent filter which is known as Solc filter [101]. A typical birefringent filter consists of linear polarisers and waveplates of birefringent material, as shown in Figure 5.1. If electrically tuneable birefringent elements are inserted, such as liquid crystal or electro-optic element, then electrically tuneable birefringent filter is obtained. The birefringent filters are routinely used for wavelength [102, 103] and polarisation control [104]. In Chapter 4 we described an polarisation mode converter integrated with a quantum cascade laser. In this Chapter a novel wavelength technique for quantum cascade lasers is presented based on the polarisation mode converter elements demonstrated in the previous Chapter.

Quantum cascade lasers(QCLs) are based on intersubband transitions in quantum wells [22] but we can expect that QCL material will exhibit electro-optic properties based on intersubband transitions and interband transitions [105, 106]. The selection rules for intersubband transitions dictate that only light polarised with

### Illustration of the Birefringent Filter

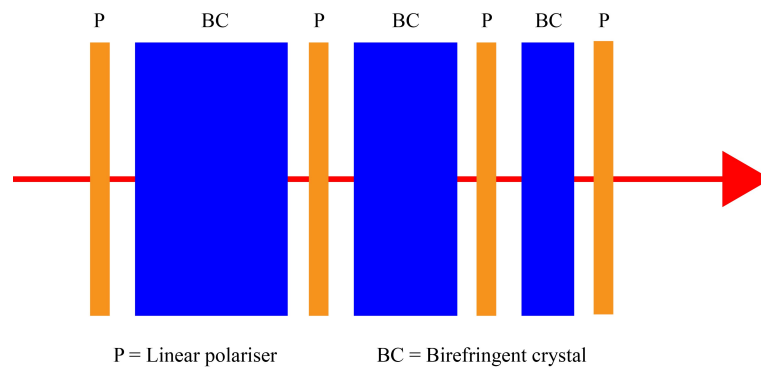


FIGURE 5.1: Illustration of the Birefringent Filter, consisting of a sequence of birefringent crystals (BC) and polarisers (P).

its electric vector perpendicular to the plane of the quantum well can couple to the intersubband transitions. In the typical waveguide arrangement used in a QCL this means that there is only optical gain for TM polarised modes. In addition, it means that at the operating wavelengths, QCL waveguides exhibit birefringence and indeed it has been previously reported [107] that intersubband transitions can lead to birefringence. In the QCL waveguides the strength of the intersubband transition can be altered by injecting current into the waveguide and therefore the QCL waveguides have birefringence that can be adjusted with injection current. Also associated with the quantum wells that make up the QCL material are interband transitions and these transitions are strong and highly dispersive at photon energies close to the band gap resonance [106]; at the photon energies well away from the band-edge where the QCL operates the effect of the interband transitions is weaker and much less dispersive. The interband transitions are also a function of applied electric field and injected current and so at the QCL operating wavelength we can expect an interband electro-optic effect which is not dispersive. Altering the phase relationship between the polarisations is the basis of the wavelength tuning and polarisation control of birefringent waveguides but wavelength and polarisation tuning requires that both TM and TE modes are present and that is usually achieved by incorporating waveplates into the laser.

The feasibility of electro-optically altering the phase relationship between polarisations has been recently demonstrated for quantum well semiconductor laser diodes by monolithically integrating the laser, polarisation mode control (PMC) section and differential phase shift (DPS) section [99].

The integrated equivalents of waveplates are polarisation mode convertors [6, 7]. We have discussed how PMCs are fabricated in Chapter 4. The PMCs are made by etching trenches on the waveguides to make the waveguide cross-section asymmetric. With PMCs it is possible to make the integrated equivalent of a bulk quarter waveplate and to produce a hybrid mode that is 50% TE and 50% TM. The other component required for a tuneable waveguide is a DPS section; this is a section of the QCLs waveguide with electrical contacts that allow the injection of current which alters the strength of the intersubband transitions.

In this Chapter we discuss the design of the ITBW and we report results on experiments that employ the sub-threshold electroluminescence (EL) to probe the operation of the ITBW. We develop a theory of the operation based on a Jones matrix [108] description of the ITBW and a description of the electro-optic properties of the birefringence of the QCL waveguide. This splits the electro-optic birefringence into a current dependent but wavelength independent effect that arises from interband transitions and current and wavelength dependent birefringence that arises from the intersubband transitions. Finally we demonstrate wavelength and polarisation tuning of the quantum cascade laser operating above threshold.

### 5.1.1 Aim

The main aim of this research work is to design, fabricate and characterise an integrated tuneable birefringent waveguide for quantum cascade lasers within operating wavelength at 4450 nm.

### 5.1.2 Objective

The aim was achieved through the following objectives:

1. Design, fabrication and characterisation of integrated tuneable birefringent waveguide for quantum cascade laser.
2. Sub-threshold electroluminescence characterisation to probe the operation of the [ITBW](#).
3. Demonstration of wavelength and polarisation tuneable [QCL](#) operating above threshold.

## 5.2 Integrated Tuneable Birefringent waveguide Design

Our design for an [ITBW](#) for [QCLs](#) is shown in Figure 5.2. It consists of 2 [PMCs](#) configured as quarter waveplates with a [DPS](#) section between them. The [PMCs](#) are passive optical waveguides that are made asymmetric by, for example, etching trenches on one side on the waveguide. Full theoretical and design details of [PMCs](#) on [QCLs](#) can be found in Chapter 4. The [DPS](#) section adjusts the relative phase of the [TM](#) and [TE](#) components of the circularly polarised light from the first [PMCs](#). This is achieved because of the selection rules of the intersubband transitions and in a [QCL](#) structure the strength of the intersubband transitions can be altered by the injection of current so the birefringence of [DPS](#) section can be adjusted by injection current. The relative phase of the [TE](#) and [TM](#) components at the input into the second birefringent waveguide determines the output polarisation of the second [PMC](#). In a [QCL](#), only [TM](#) light will be amplified and the wavelengths that are rotated back to [TM](#) polarisation are determined by the current in the [DPS](#) section thus we have a [QCL](#) that has its operating wavelength selected by an electro-optic tuneable birefringent waveguide.

### Illustration of Integrated Tuneable Birefringent Waveguide

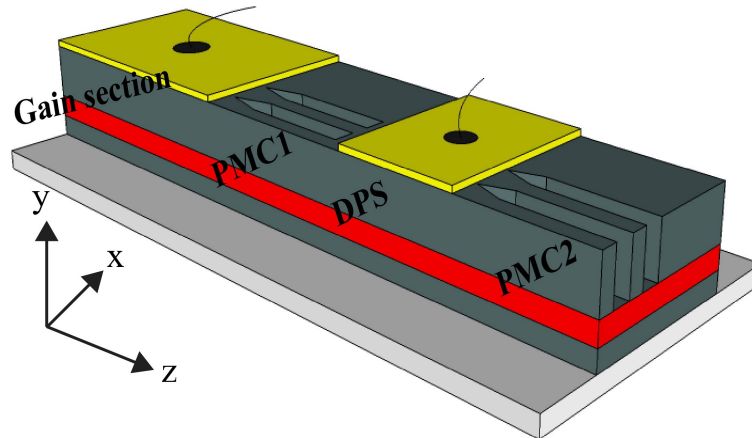


FIGURE 5.2: Schematic design for an integrated tuneable birefringent waveguide for QCLs, it shows the gain section (GS) and trenches in the upper part of the waveguide that form the PMCs [6, 7] which are designed as 1/4 waveplates, between the PMCs is the DPS section where current can be applied to alter the phase relationship between the TE and TM modes. The approximate position of the active region is indicated in red

## 5.3 Electro-Optic Birefringence of the Quantum Cascade Laser and the Jones Matrix Description

In the DPS section of the ITBW we utilize the electro-optic birefringent properties of the quantum cascade laser structure to tune the polarisation and wavelength. We regard the electro-optic birefringence of the DPS section as made up three parts, a natural birefringence (i.e birefringence with zero injection current into the DPS section),  $\Delta n$ , an interband birefringence,  $\Delta n_{IB}(i_{DPS})$ , and an intersubband birefringence,  $\Delta n_{IS}(\lambda, i_{DPS})$ . The electro-optic interband birefringence comes from interband transitions and arises from the effect of current on interband transitions and the electro-optic intersubband birefringence arises from the effect of the current on the intersubband transitions. For  $\Delta n_{IB}(i_{DPS})$ , we ignore the wavelength dependence because a QCL operates at wavelengths far from the band-gap resonance of our quantum well material and so is almost constant for wavelengths close to the laser wavelength. For  $\Delta n_{IS}(\lambda, i_{DPS})$ , we explicitly

include the wavelength dependence because it is much more dispersive for wavelengths close to the laser wavelength [107]. Note that the  $\Delta n_{IS}(\lambda, i_{DPS})$ , only results from change in **TM** polarisation. So we have:-

$$\Delta n(\lambda, i_{DPS}) = \Delta n + \Delta n_{IB}(i_{DPS}) + \Delta n_{IS}(\lambda, i_{DPS}) \quad (5.1)$$

Jones matrices are routinely used to describe the polarisation behaviour of bulk optics systems [108] and have been used to describe the operation of a laser incorporating a birefringent filter and the gain medium [109]. Here we use Jones matrices to describe the operation of the integrated tuneable birefringent waveguide. The coordinate system we use is as follows; y is the direction of growth of the epilayers (so **TM** light is y-polarised) and x is perpendicular to the direction of growth ( **TE** light is x-polarised).

In what follows we assume that the **PMCs** can be described by Jones matrix description and that operation is wavelength independent [6]. For the co-ordinate system illustrated in Figure 5.2 the generic Jones matrix is:-

$$\begin{bmatrix} \cos^2(\theta) + e^{-i\delta} \sin^2(\theta) & (1 - e^{-i\delta}) \cos(\theta) \sin(\theta) \\ (1 - e^{-i\delta}) \cos(\theta) \sin(\theta) & \sin^2(\theta) + e^{i\delta} \cos^2(\theta) \end{bmatrix} \quad (5.2)$$

where  $\theta$  is the angle the optic axis makes with the x direction and  $\delta$  is the phase retardation.

### 5.3.1 Single Pass Jones Matrix Model for ITBW Device

From our previous work on **PMCs** (Chapter 4) we have designed a **PMC** that converts a **TM** mode into a hybrid mode that is 50% **TM** and 50% **TE**. Our experiments do not allow us to measure the relative phase between the **TM** and **TE** modes and so we can adapt the generic Jones matrix to describe this behaviour in various ways; for example an optics axis rotation of  $\theta = \frac{\pi}{4}$  and phase retardation of  $\delta = \frac{\pi}{2}$ , or we could set  $\theta = \frac{\pi}{8}$  and  $\delta = \pi$ . As explained in [6] it appears that **PMCs** that convert to 50% **TM** and 50% **TE** in a half beat length are described by setting

$\theta = \frac{\pi}{8}$  and  $\delta = \pi$ :- Using these values into Equation 5.2 we obtain the Jones matrix for the **PMC**.

$$\mathbf{PMC} = \frac{1}{\sqrt{2}} \begin{bmatrix} 1 & 1 \\ 1 & -1 \end{bmatrix} \quad (5.3)$$

The Jones matrix for the **DPS** is given by setting  $\theta = 0$ , because the plane of the quantum wells is in the x- direction and  $\delta = \frac{2\pi\Delta n(\lambda, i_{DPS})L}{\lambda}$ , where  $L$  is the length of the **DPS**, is the free space wavelength. Thus the Jones matrix for **DPS** section is,

$$\mathbf{DPS} = \begin{bmatrix} 1 & 0 \\ 0 & e^{-i\frac{2\pi\Delta n(\lambda, i_{DPS})L}{\lambda}} \end{bmatrix} \quad (5.4)$$

Thus the overall single pass Jones matrix (or Transfer Matrix),  $\mathbf{T}_D$  for the **ITBW** is given by:-

$$\mathbf{T}_D = \mathbf{PMC} \times \mathbf{DPS} \times \mathbf{PMC} \quad (5.5)$$

We assume the input into the **ITBW** section is **TM** polarised because the **QCL** gain section selects for **TM** polarisation,  $\begin{bmatrix} 0 \\ 1 \end{bmatrix}$ , then the polarisation vector representing the **ITBW** response is given by:-

$$\mathbf{I}(\lambda, i_{DPS}) = \mathbf{T}_D \begin{bmatrix} 0 \\ 1 \end{bmatrix} = \frac{1}{2} \begin{bmatrix} 1 - e^{-i\frac{2\pi\Delta n(\lambda, i_{DPS})L}{\lambda}} \\ 1 + e^{-i\frac{2\pi\Delta n(\lambda, i_{DPS})L}{\lambda}} \end{bmatrix} \quad (5.6)$$

For **TM** and **TE** polarisation intensity fraction of the **ITBW** response is given by:-

$$\mathbf{I}_{TM}(\lambda, i_{DPS}) = \frac{1}{2} \left| 1 + e^{-i\frac{2\pi\Delta n(\lambda, i_{DPS})L}{\lambda}} \right|^2 \quad (5.7)$$

$$\mathbf{I}_{TE}(\lambda, i_{DPS}) = \frac{1}{2} \left| 1 - e^{-i\frac{2\pi\Delta n(\lambda, i_{DPS})L}{\lambda}} \right|^2 \quad (5.8)$$

In the dynamic polarisation control operation of **ITBW** we measure the angle of polarisation,  $\varphi$ , of the output from the **QCL** as a function of input current into the **DPS** and if we assume a single pass through the **ITBW** then that is given by

$$\varphi = \arctan \left( \frac{\mathbf{I}_{TM}(\lambda, i_{DPS})}{\mathbf{I}_{TE}(\lambda, i_{DPS})} \right) \quad (5.9)$$

### 5.3.1.1 Single Pass Jones Matrix Model for Alternative ITBW Design

If **ITBW** uses **PMCs** that convert to a 50% **TM** and 50% **TE** in a quarter beat length (described by setting  $\theta = \frac{\pi}{4}$  and  $\delta = \frac{\pi}{2}$ ). For example **PMC** design (design D2) described in Chapter 4, that convert to a 50% **TM** and 50% **TE** in a quarter beat length.

Similarly, as described above, we can derive equations for **TM** and **TE** polarisation intensity fraction of the **ITBW** response, and, angle of polarisation of the output from the **QCL** as a function of input current into the **DPS**. The **TM** and **TE** polarisation intensity fraction of the **ITBW** response is given by

$$\mathbf{I}'_{TM}(\lambda, i_{DPS}) = \frac{1}{2} \left| i - ie^{-i\frac{2\pi\Delta n(\lambda, i_{DPS})L}{\lambda}} \right|^2 \quad (5.10)$$

$$\mathbf{I}'_{TE}(\lambda, i_{DPS}) = \frac{1}{2} \left| 1 + e^{-i\frac{2\pi\Delta n(\lambda, i_{DPS})L}{\lambda}} \right|^2 \quad (5.11)$$

and angle of polarisation,  $\varphi'$ , can be given as

$$\varphi' = \arctan \left( \frac{\mathbf{I}'_{TM}(\lambda, i_{DPS})}{\mathbf{I}'_{TE}(\lambda, i_{DPS})} \right) \quad (5.12)$$

In the realised **ITBW** device, we employed the **PMCs** that convert to 50% **TM** and 50% **TE** in a half beat length and described by setting  $\theta = \frac{\pi}{8}$  and  $\delta = \pi$ ). However we analysed our experimental results with both conditions to see the difference.

The single pass EL results for the **ITBW** device structure employed in this work is analysed using **ITBW** response Equation 5.7 and Equation 5.10 in Matlab with

the conditions described above. Where the active polarisations control operations were analysed using Equation 5.9 and Equation 5.12 also in Matlab.

### 5.3.2 Theory of Laser Operation with Birefringent Components

As is discussed in [109], the operation of a laser with polarisation dependent gain and including birefringent components is a more complex situation than the single pass case we have analysed in the previous section.

In general the resonance requirement for a resonator with birefringent components imposes the following conditions, first the phase change in a round trip must be a multiple of  $2\pi$  and second the polarisation must repeat after a round trip. These two conditions were expressed in the following equation:-

$$\mathbf{M} \cdot \mathbf{X} = \beta \cdot \mathbf{X} \quad (5.13)$$

Where  $\mathbf{M}$  is the round trip Jones matrix,  $\mathbf{X}$  is the two-component vector representing polarisation and  $\beta$  is a positive real number.

We can get some insight into the operation of the laser by analysing the QCL that includes the ITBW optical circuit using Jones matrix method as described in ref. [109]. In this analysis we will derive the phase conditions for laser action and so we ignore the amplitude of the modes and assume an amplitude normalised to one for all the components. First, analysis were carried out by considering PMCs as half beat length and then for PMCs as quarter beat length.

The Jones matrix of an ideal mirror ( $\sim 100\%$  reflection) is given by

$$\mathbf{MR} = \begin{bmatrix} 1 & 0 \\ 0 & -1 \end{bmatrix} \quad (5.14)$$

### Illustration of Full Round Trip Optical Circuit for ITBW

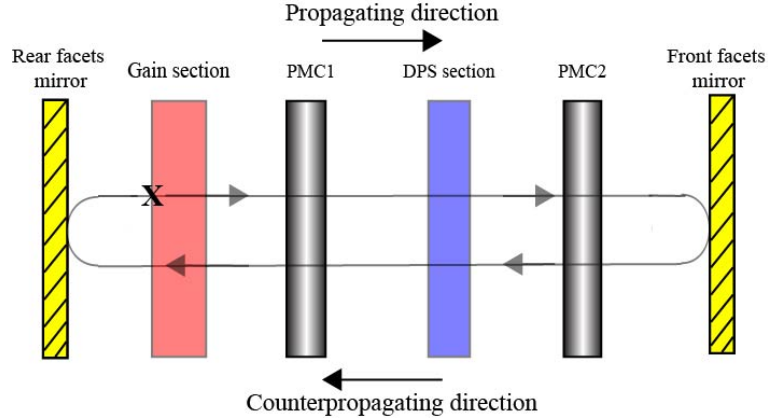


FIGURE 5.3: Shows the equivalent optical circuit of ITBW for full round trip consideration. Figure also indicates the different components of optical circuit. The X marks the starting point for the round trip analysis.

Using the convention described in [109], when the direction of light propagation through a reciprocal element is reversed, the Jones matrix of the element is transformed as follows:

$$\begin{bmatrix} m_1 & m_4 \\ m_3 & m_2 \end{bmatrix} \rightarrow \begin{bmatrix} m_1 & -m_3 \\ -m_4 & m_2 \end{bmatrix} \quad (5.15)$$

In the ITBW the only element modified by the above transformation is that of the PMC (for  $\theta = \frac{\pi}{8}$  and  $\delta = \pi$ ). Thus, the Jones matrix of the PMC for forward propagation is given by Equation 5.4, and for counterpropagating light is then given by

$$PMC_{cp} = \frac{1}{\sqrt{2}} \begin{bmatrix} 1 & -1 \\ -1 & -1 \end{bmatrix} \quad (5.16)$$

The gain section (GS) provides gain for TM modes only, so we approximate its effect on the polarisation by describing it as TM linear polariser. The Jones matrix for GS is then given by

$$GS = \begin{bmatrix} 0 & 0 \\ 0 & 1 \end{bmatrix} \quad (5.17)$$

For the DPS section the Jones Matrix is given by Equation 5.4 for both forward

and counterpropagating light. Starting at the position indicated on Figure 5.3, the overall round trip Jones matrix,  $\mathbf{M}$ , for the ITBW is given by the following multiplication of matrices:-

$$\mathbf{M} = \mathbf{MR.GS.PMC}_{CP}.\mathbf{DPS.PMC}_{CP}.\mathbf{MR.PMC.DPS.PMC.GS}$$

$$= \begin{bmatrix} 0 & 0 \\ 0 & 0.5 + 0.5e^{-i\frac{4\pi\Delta n(\lambda,i_{DPS})L}{\lambda}} \end{bmatrix} \quad (5.18)$$

In the above we have followed the usual convention for the Jones matrices and omitted the phase factor that describes the common phase change for TM and TE modes as the wave travels through the component. In order to completely take account of the phase change in the round trip matrix we follow [109] and explicitly include the phase factor that is common for TM and TE modes. If we assign the following variables:  $L_d$  is the average path for a single pass and the average refractive index for the round trip of the whole device;  $n_d$  is as follows -then Equation 5.18 becomes:-

$$\begin{bmatrix} 0 & 0 \\ 0 & 0.5 + 0.5e^{-i\frac{4\pi\Delta n(\lambda,i_{DPS})L}{\lambda}} \end{bmatrix} e^{\frac{4\pi n_d L_d}{\lambda}} \quad (5.19)$$

Returning to Equation 5.13 and setting  $\mathbf{X} = \begin{bmatrix} 0 \\ 1 \end{bmatrix}$  that is TM polarisation we have

$$\begin{aligned} \mathbf{M} &= \begin{bmatrix} 0 & 0 \\ 0 & 0.5 + 0.5e^{-i\frac{4\pi(\Delta n(\lambda,i_{DPS})L+n_d L_d)}{\lambda}} \end{bmatrix} \begin{bmatrix} 0 \\ 1 \end{bmatrix} \\ &= 0.5 + 0.5e^{-i\frac{4\pi(\Delta n(\lambda,i_{DPS})L+n_d L_d)}{\lambda}} \begin{bmatrix} 0 \\ 1 \end{bmatrix} \end{aligned} \quad (5.20)$$

If we compare Equation 5.20 with Equation 5.13 then it is apparent that the phase exponential in Equation 5.20 can only be a real number, that is 1, if the following phase condition is satisfied:-

$$\frac{1}{\lambda}(n(\lambda, i_{DPS})L + n_d L_d) = 0, 0.5, 1, 1.5... \quad (5.21)$$

The laser modes in the QCL ITBW device must satisfy this phase condition.

In general  $n_d$  and  $L_d$  ( $L_d \approx$  total length of device) will be a weighted mixture of TM and TE refractive indices and paths as the laser mode swaps between TM and TE propagation. In an approximate approach we can expect that  $n_d \approx \frac{n_{TM} + n_{TE}}{2}$  and  $n_{TM}$  effective index for the TM mode and  $n_{TE}$  effective index for the TE mode.

According to this simple analysis the mechanism for tuning the QCL ITBW will be the injection current induced change of the phase condition given by Equation 5.21 and although this gives some insight it does not include the effect of gain. For lasing to occur, in addition to the phase condition the optical gain experienced by the TM mode must equal the optical loss after a round trip. But it can be seen from Equation 5.20 that the phase condition for positive feedback in the QCL ITBW device can be tuned by injecting current in the DPS section and altering the  $\Delta n(\lambda, i_{DPS})$  factor. However, there will also be some injection current dependence of the  $n_d$  factor.

### 5.3.2.1 Description for Alternative ITBW Design

Similar analysis can be made for PMC that convert to a 50% TM and 50% TE in a quarter beat length by setting  $\theta = \frac{\pi}{4}$  and  $\delta = \frac{\pi}{2}$ . Similarly, as described above, we can derive the round trip Jones matrix,  $\mathbf{M}'$ , for the ITBW which is given by

$$\begin{bmatrix} 0 & 0 \\ 0 & e^{-i\frac{4\pi\Delta n(\lambda, i_{DPS})L}{\lambda}} \end{bmatrix} e^{\frac{4\pi n_d L_d}{\lambda}} \quad (5.22)$$

Returning to Equation 5.13 and setting  $\mathbf{X} = \begin{bmatrix} 0 \\ 1 \end{bmatrix}$  that is **TM** polarisation we have

$$\mathbf{M}' = \begin{bmatrix} 0 & 0 \\ 0 & e^{-i\frac{4\pi(\Delta n(\lambda, i_{DPS})L + n_d L_d)}{\lambda}} \end{bmatrix} \begin{bmatrix} 0 \\ 1 \end{bmatrix} = e^{-i\frac{4\pi(\Delta n(\lambda, i_{DPS})L + n_d L_d)}{\lambda}} \begin{bmatrix} 0 \\ 1 \end{bmatrix} \quad (5.23)$$

If we compare Equation 5.23 with Equation 5.13 then it is apparent that the phase exponential in Equation 5.23 can only be a real number, that is 1, if the following phase condition is satisfied:-

$$\frac{1}{\lambda}(n(\lambda, i_{DPS})L + n_d L_d) = 0, 0.5, 1, 1.5... \quad (5.24)$$

The laser modes in the QCL-ITBW device have to satisfy this phase condition.

Thus, for both **PMC** descriptions, an **QCL ITBW** device satisfies the condition described in Equation 5.13 i.e. the phase change in a round trip is multiple of  $2\pi$  and second the polarisation repeat after a round trip. Furthermore, we conclude that we can use both **PMCs** design for future **ITBW** device fabrication.

## 5.4 ITBW Device Description

The **ITBW** we report here was the device that had the gain section length of 2500  $\mu\text{m}$  then DPS section length 1125  $\mu\text{m}$  and the **PMC** sections were designed to split 50% TE and 50% TM in half beat length [6] with a length of 151  $\mu\text{m}$ , cross-section width of 3.6  $\mu\text{m}$  and 4.9  $\mu\text{m}$  waveguide height. The **PMC** design employed in this work is described in **Chapter 4** as Design D1. The **PMCs** were designed to split 50% TE and 50% TM in half beat length; so that in the first **PMC** (**PMC1** in Figure 5.4) light at the input from the GS, (polarised **TM**), originating from intersubband transitions was converted into circularly polarised light at the output of the **PMC**. This required a trench to be etched into the waveguide. The trenches etched were 0.5  $\mu\text{m}$  wide and 3.518  $\mu\text{m}$  deep and were fabricated using a reactive ion etching technique by exploiting the **RIE** lag effect (-see **Chapter 4**).

A photograph of the wire bonded **QCL ITBW** device with different sections is shown in Figure 5.4. Gain section, **PMC1**, **DPS** and **PMC2** is indicated on photograph. In the **ITBW** device, only the gain section and **DPS** section contact windows were etched onto the top of the waveguides, with the rest of the structure protected by 500 nm  $Si_3N_4$  and 500 nm  $SiO_2$  insulating layers. Gain section and **DPS** section metal contacts were electrically isolated using a metal lift-off technique.

#### Photograph of the Realised **ITBW** Device

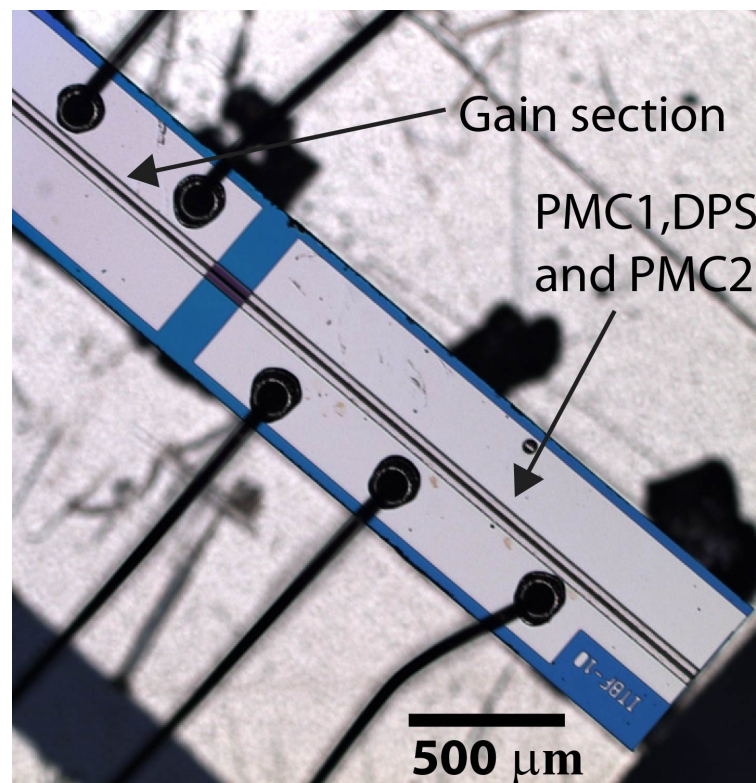


FIGURE 5.4: A photograph shows the top view of the processed **ITBW** device. Underneath the Gain section (GS) and **DPS** section waveguide contact windows were opened for current injection and the rest of the structure is protected by 500 nm  $Si_3N_4$  and 500 nm  $SiO_2$  insulating layers.

## 5.5 Characterisation and Result

The **QCL ITBW** devices reported in this chapter were characterised using a technique described in **Chapter 2.2**. For polarisation measurements, a grid polariser

was mounted in front of the detector, in a rotatable mounting. Characterisation was carried out at a laser heat sink temperature of 250 K. The GS current density was pulsed and had values around 4.2 kA/cm<sup>2</sup>. The DPS had direct current (DC) injection at around 1/10 of the GS current density to avoid excessive TM gain in the DPS section.

### 5.5.1 Sub-threshold Single Pass Measurements

To gain an insight into the operation of the ITBW we carried out single pass measurement using the sub-threshold EL from the GS. This allows us to estimate the values of  $\Delta n$ , natural birefringence without DPS current and  $\Delta n(\lambda, i_{DPS})$  of the DPS. The intersubband birefringence,  $\Delta n_{IS}(\lambda, i_{DPS})$ , was estimated by measuring the small amount of current dependent gain as a function of wavelength in the DPS and taking a Kramers-Kronig (KK) transformation [110] of the gain spectra.

**Block Diagram of experimental Setup Used to Characterise ITBW Device**

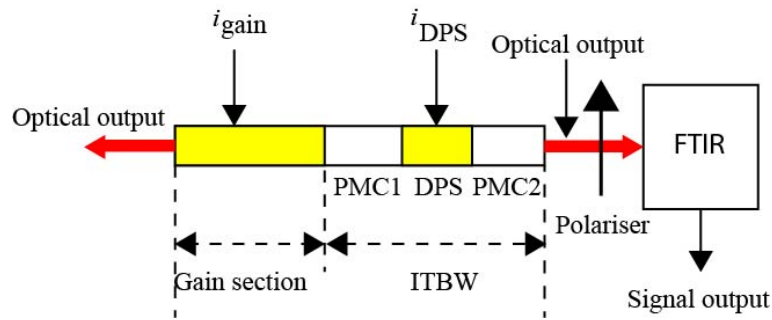


FIGURE 5.5: Shows a schematic of the experimental setup for characterising the QCL that includes an ITBW; the GS is injected with current  $i_g$  and the ITBW has a current  $i_{DPS}$  injected, that electro-optically alters the birefringence of the DPS section. The polarisation is selected using a linear polariser and the output spectrum of device is measured using a FTIR spectrometer. All experiments were conducted at 250 K QCL heat sink temperature.

The experimental setup used to characterise the integrated ITBW is illustrated in Figure 5.5. The GS was driven with 100 ns duration current pulses with a 60 kHz repetition rate and the DPS section driven with DC current. The device was

driven 20% below the lasing threshold current density at  $i_g = 4.2 \text{ kA/cm}^2$  to ensure single-pass operation and avoid multimode beating effects on PMCs [111, 112]. The TM fraction of the EL spectra was measured by placing a grid polariser between the ITBW device and FTIR (with the optical axis of the grid polariser parallel to the QCL waveguide). The experimental TM response curve of the sub-

#### Sub-threshold EL at Different DPS Current Densities

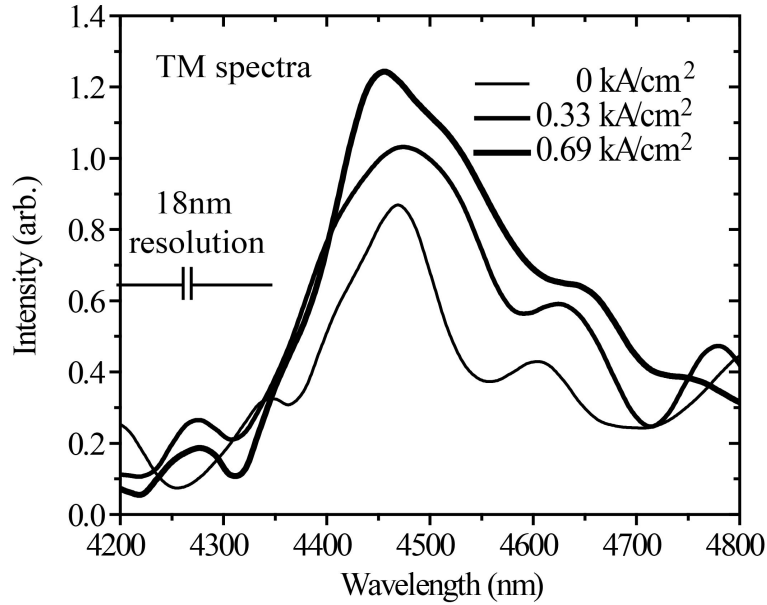


FIGURE 5.6: The TM spectrum of the sub-threshold EL spectra of a QCL incorporating a ITBW measured at various DC current densities injected into the DPS section.

threshold EL spectra emitted from the ITBW device with and without application of DC current into the DPS section is shown in Figure 5.6. When DC current ( $0.33 \text{ kA/cm}^2$  and  $0.69 \text{ kA/cm}^2$ ) is applied into the DPS section, increased transmission is observed through electrically modulating the gain [113]. Furthermore, when  $0.69 \text{ kA/cm}^2$  DC current is applied into the DPS section, 13 nm tuning (blue shift of the peak of EL) with rate of  $\sim 19 \text{ nm}/(\text{kA/cm}^2)$  was recorded.

To gain an insight into the operation of the QCL ITBW device we compare the theory of the electro-optic birefringence and the Jones matrix description of the ITBW against the experimental results. To make the comparison we calculate the TM

intensity fraction of the **ITBW** response function using Equation 5.7 and multiply the result with the **EL** spectra measured from the GS facets (shown in Figure 5.7). We assume that when no current is injected that the birefringence is entirely dominated by the material (natural) birefringence,  $\Delta n$ , thus in Equation 5.1  $\Delta n(\lambda, i_{DPS})$  replace with  $\Delta n$ , and we regard  $\Delta n$ , as an adjustable parameter. We take  $\Delta n$  as positive when the **TE** refractive index is greater than the **TM** refractive index. To fit the Jones matrix model to the experimental result, we adjust the value of  $\Delta n = 0.005$ , with these values we obtain an approximate fit with the experimental result as is shown in Figure 5.8.

### Sub-threshold **EL** Spectra Measured from Gain Section Facets

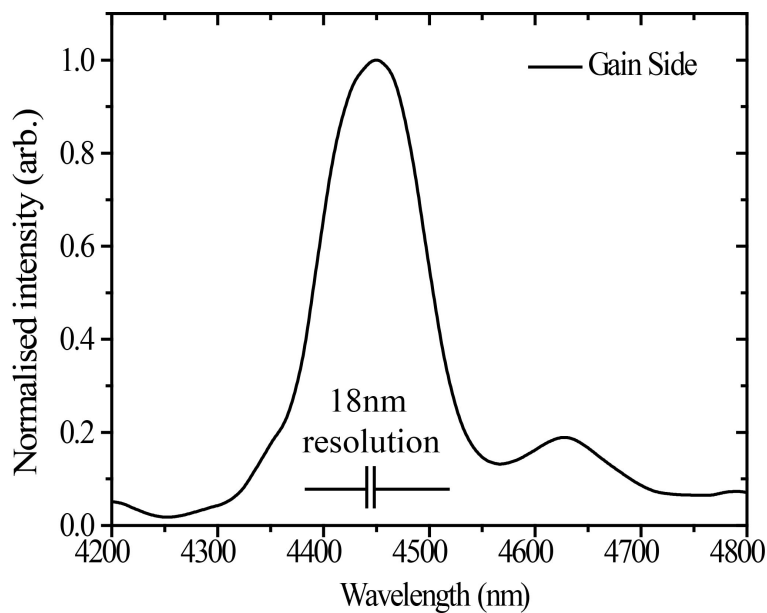


FIGURE 5.7: Shows the sub-threshold **TM EL** spectra emitted from the facet next to the gain section of the **QCL ITBW** device. For detailed experimental setup, refer Figure 5.5.

Similarly, in order to fit the Jones matrix model with the experimental results, when DC current is applied into the **DPS** section, we require to estimate the value of  $\Delta n_{IS}(\lambda, i_{DPS})$ . To estimate the  $\Delta n_{IS}(\lambda, i_{DPS})$ , we require to measure the gain using  $I = I_o e^{-\rho L}$ , where  $I_o$  is **TM EL** intensity without the **DPS** current,  $I$  is the **TM EL** intensity with the **DPS** current,  $L$  is the length of the **DPS** section and  $-\rho$  is the amount of gain. More details about the gain measurement can be found in reference [8]. At **DPS** current of  $0.33 \text{ kA/cm}^2$  and  $0.69 \text{ kA/cm}^2$ , the

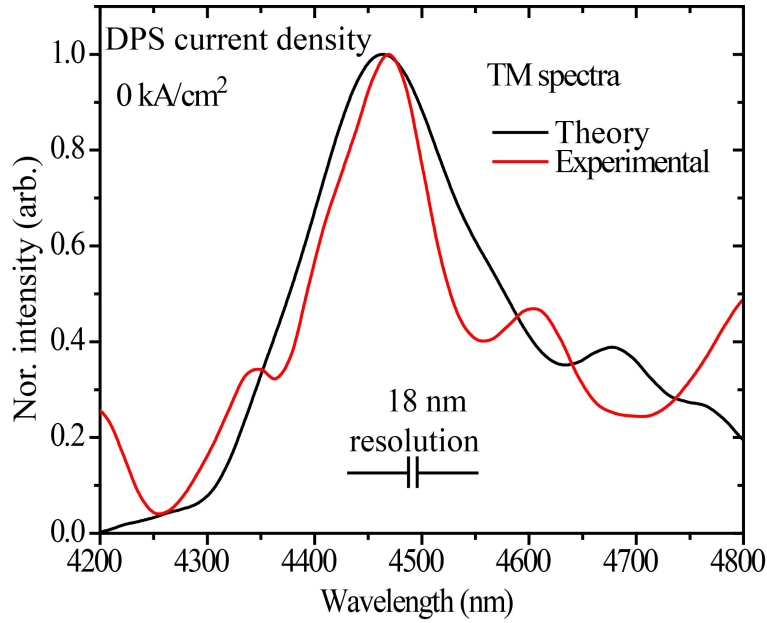
Sub-threshold **EL** and Jones Matrix Model Fit at 0 kA/cm<sup>2</sup>

FIGURE 5.8: Experimental result (red curve) and Jones matrix model fitting curve (black curve and mark as theory) of the **EL** spectra of the **ITBW** device without current injection into the **DPS** section is shown.

measured gain is shown in Figure 5.9, the modulation observed with a period of  $\sim 130$  nm in the gain spectra fits with a Fabry-Perot resonance associated with an additional  $\sim 40$   $\mu\text{m}$  long waveguide section between the end of PMC2 and the end facet (present due to imprecise cleaving). using the KK relation [110] the gain measurement is transformed into current and wavelength dependent intersubband birefringence,  $\Delta n_{IS}(\lambda, i_{DPS})$  is shown in Figure 5.10. In our model we also include the electro-optic interband birefringence contribution,  $\Delta n_{IB}(i_{DPS})$ , -0.0014 and -0.0022 were the values used, for 0.33 kA/cm<sup>2</sup> and 0.69 kA/cm<sup>2</sup> respectively that gave the best fit to the results.

So using the Jones matrix description, regarding  $\Delta n$  and  $\Delta n_{IB}(i_{DPS})$ , as an adjustable parameter and calculating  $\Delta n_{IS}(\lambda, i_{DPS})$  from the gain measurements we obtain an approximate fit of the theory to the experimental results - see Figure 5.11. Clearly, from Figure 5.11, for high current densities and at the longer wavelengths there is substantial deviation of the theory from the measured response and some more refinements to the theory may be required, for example

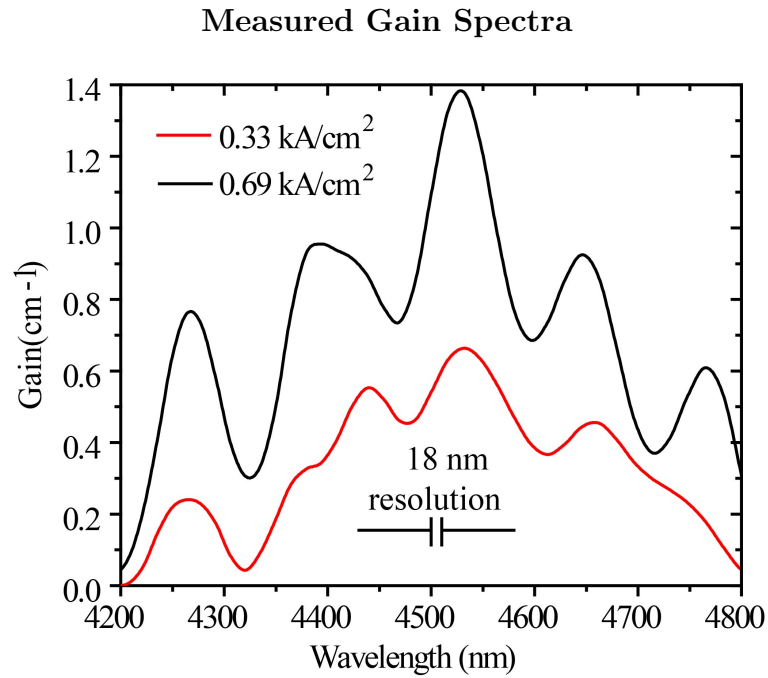


FIGURE 5.9: Measured gain spectra by injecting DC current density 0.33  $\text{kA}/\text{cm}^2$  and 0.69  $\text{kA}/\text{cm}^2$  into DPS section.

### Kramers-Kronig Transformation of Gain Spectra

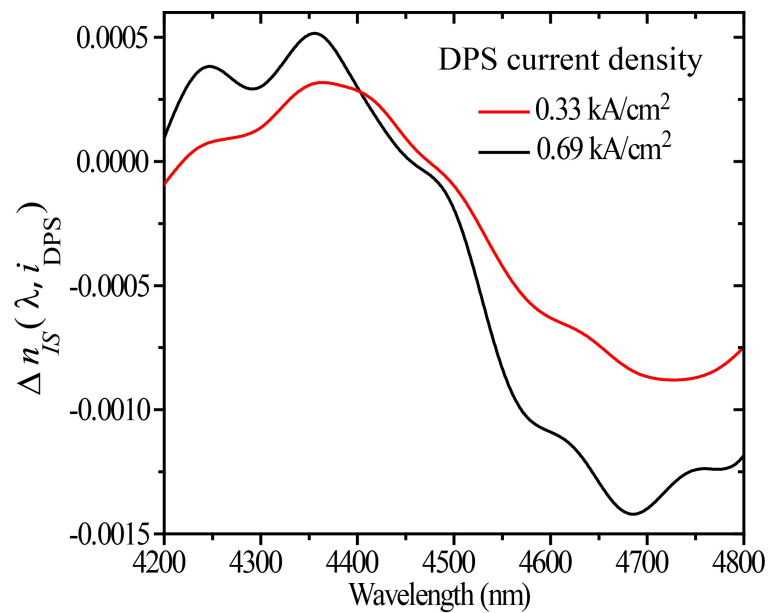
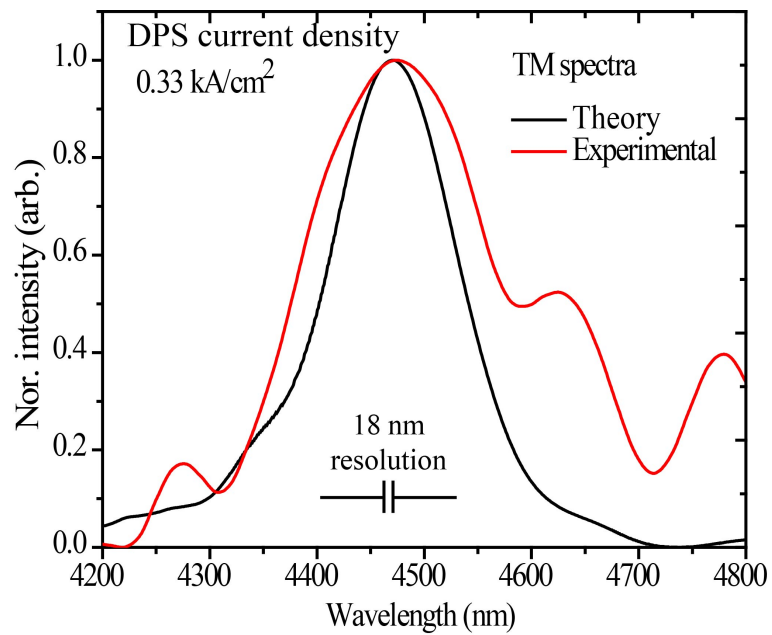
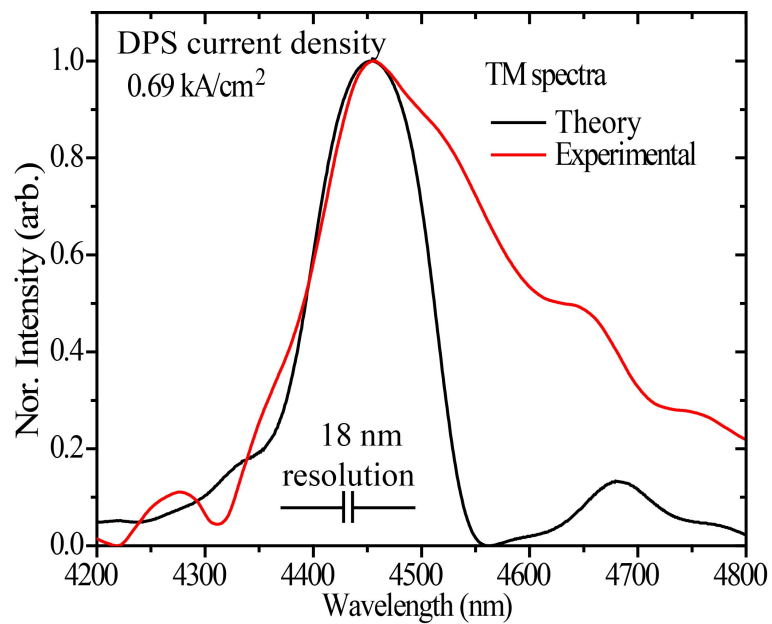


FIGURE 5.10: Wavelength and current dependence of the refractive index which is calculated from the data using a Kramers-Kronig-transformation of the gain spectra. More details about the gain measurement can be found in reference [8].

taking account of relative TE and TM losses [114], for a more complete understanding of the QCL-ITBW device.

Sub-threshold EL and Jones Matrix Model Fit at 0.33 and 0.69  $\text{kA/cm}^2$ 

(a)



(b)

FIGURE 5.11: The experimental EL spectra and Jones matrix model curve fit of the ITBW device (a)  $i_{DPS} = 0.33 \text{ kA/cm}^2$  and (b)  $i_{DPS} = 0.69 \text{ kA/cm}^2$ .

### 5.5.1.1 Alternative Analysis of Sub-threshold EL Results

We have done similar analysis as above for TM polarisation intensity fraction of the ITBW response using Equation 5.10. Where we consider PMCs that convert 50% TM and 50% TE in a quarter beat length and described by setting  $\theta = \pi/4$  and  $\delta = \pi/2$ . We obtain an approximate fit to the experimental result as shown in Figure 5.12 by setting natural birefringence,  $\Delta n = 0.0036$  and electro-optic interband birefringence contribution,  $\Delta n_{IB}(i_{DPS})$ , -0.0007 and -0.0012 at DPS current density of 0.33 kA/cm<sup>2</sup> and 0.69 kA/cm<sup>2</sup> respectively, together with measured wavelength and current dependence of the intersubband birefringence shown in Figure 5.12.

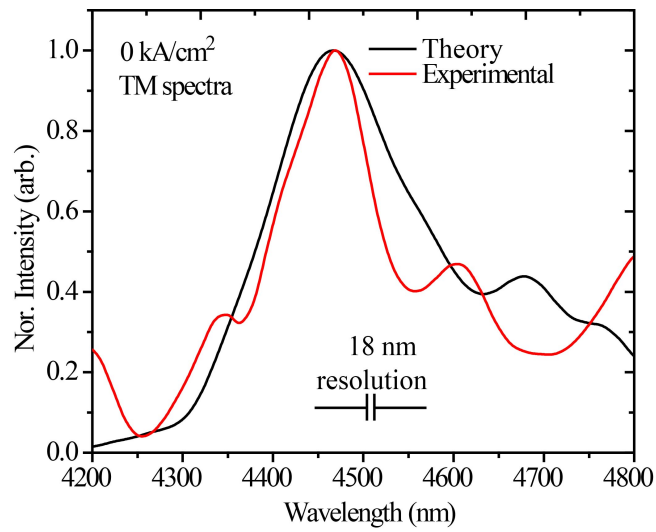
Two different values for natural birefringence,  $\Delta n$ , 0.005 and 0.0036 were estimated from analysis by considering PMCs at half beat length and quarter beat length respectively. Later, in the Section 5.5.3, we will compare this analysis with active polarisation control analysis to estimate the accurate value of birefringence for QCL employed in this work.

## 5.5.2 Measurement of Operation of Laser Incorporate Birefringent Components

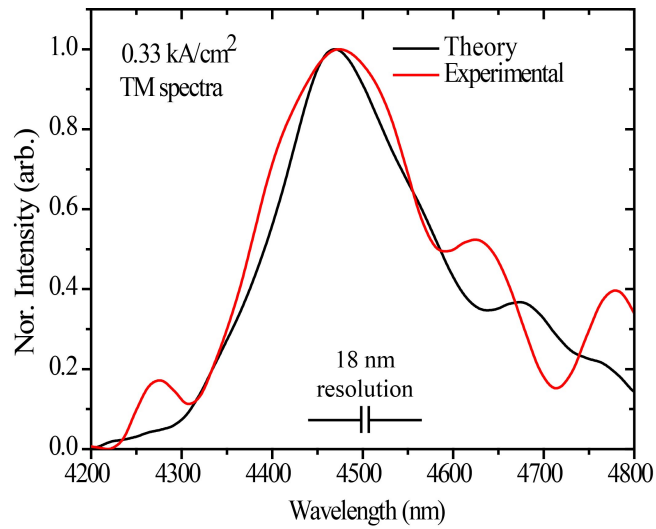
Figure 5.13 shows the observed emission spectra and tuning at different DC current densities from 0 to 1.11 kA/cm<sup>2</sup> applied to the DPS while a fixed pulsed peak current of  $1.3 \cdot I_{th}$  (6.8 kA/cm<sup>2</sup>) is applied to the GS. No single mode emission was observed and 24 nm discontinuous tuning with tuning rate of 25 nm/(kA/cm<sup>2</sup>) was recorded.

The spacing between the modes shown in Figure 5.13(b) and Figure 5.13(e) is 11 nm. According to the phase condition theory in section 5.3.2, Equation 5.21, and using the values  $\Delta n(\lambda, i_{DPS})L \approx 10^3$  nm and  $\Delta n_d L_d \approx 10^6$  nm the mode spacing is dominated by the second factor and we would have expected mode spacing more

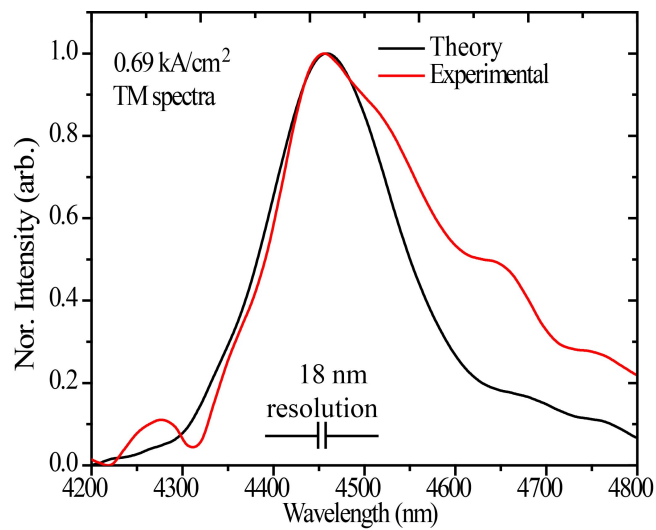
## Sub-threshold EL and Jones Matrix Model Fit



(a)



(b)



(c)

FIGURE 5.12: The experimental EL spectra and Jones matrix model curve fit of the ITBW device (a)  $i_{DPS} = 0$  kA/cm<sup>2</sup> (b)  $i_{DPS} = 0.33$  kA/cm<sup>2</sup> and (c)  $i_{DPS} = 0.69$  kA/cm<sup>2</sup>.

### Laser Emission with Birefringent Components at Various Current Densities

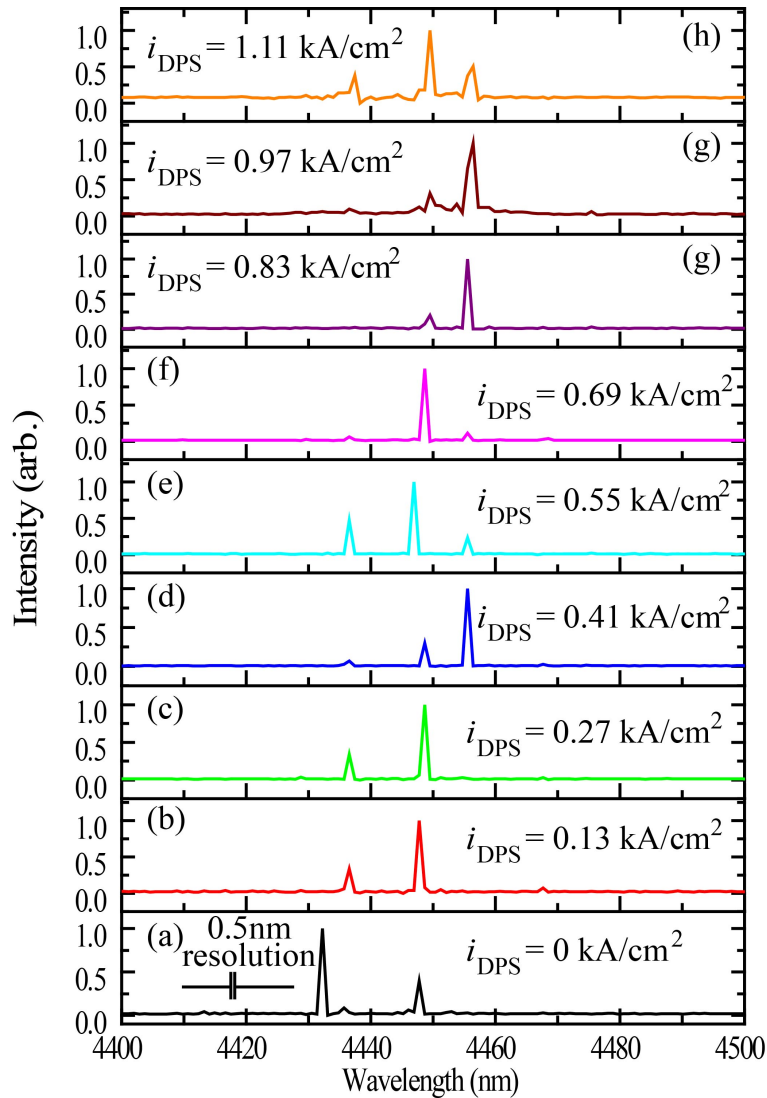


FIGURE 5.13: The wavelength tuning at different DC current densities injected into DPS section.

like 0.7 nm. The 11 nm spacing that we do observe is consistent with there being sub-cavities present in the device.

The PMC, employed in the ITBW, is an asymmetric waveguide and is formed by etching trenches into one side of the symmetric waveguide. The index contrast between symmetric and asymmetric waveguide can lead to reflections and we have from a finite-difference time-domain analysis estimated that the mirror reflectivity

could to be as large as 0.2. This reflectivity may lead to the formation of sub-cavities. The 11 nm spacing that we observe is consistent with the gain section and DPS section acting as coupled sub-cavities as indicated in Figure 5.14. This is similar to the Vernier mode selection described in **Chapter 3**. To eliminate this effect the interfaces between waveguide elements will need to be redesigned with optimized etch depths and tapering, ensuring smooth mode transitions without reflections.

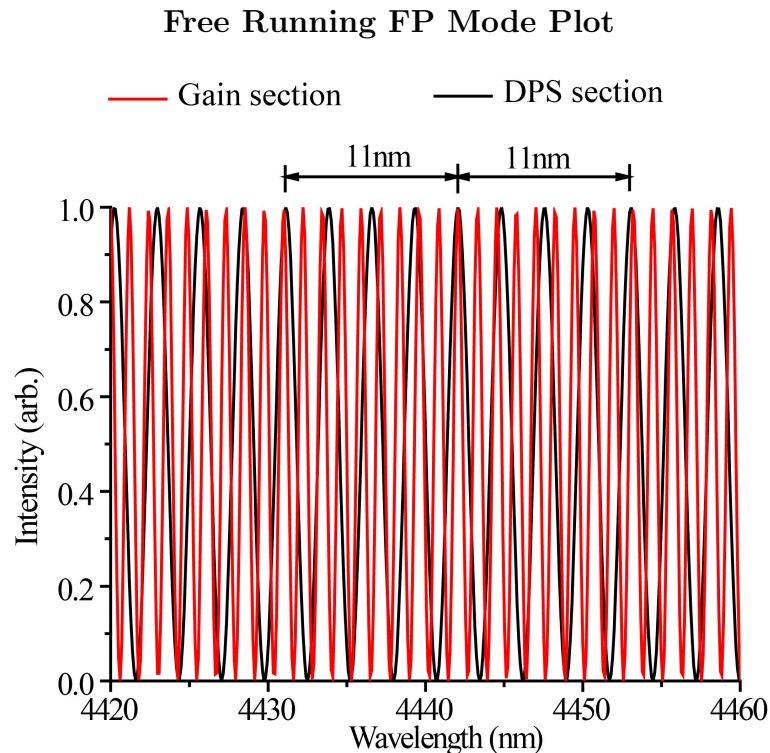


FIGURE 5.14: Free running FP mode plot for gain section and DPS section. Figure clearly indicates that FP modes are in-phase every 11 nm.

### 5.5.3 Active Polarisation Control

For polarisation control measurements, the GS pulsed current was fixed at 6.8 kA/cm<sup>2</sup> ( $1.3 \cdot I_{th}$ ) and the current to the DPS section was varied between 0 kA/cm<sup>2</sup> and 0.97 kA/cm<sup>2</sup> in steps of 0.13 kA/cm<sup>2</sup>. We measured the maximum transmission as a function of wire-grid polariser rotation angle ( $\varphi = 0^\circ$  to  $360^\circ$ ), where  $\varphi = 0^\circ$  is defined as the angle of the first maxima in transmission for the TM light

## Active Polarisation Control with Jones Matrix Model Fit

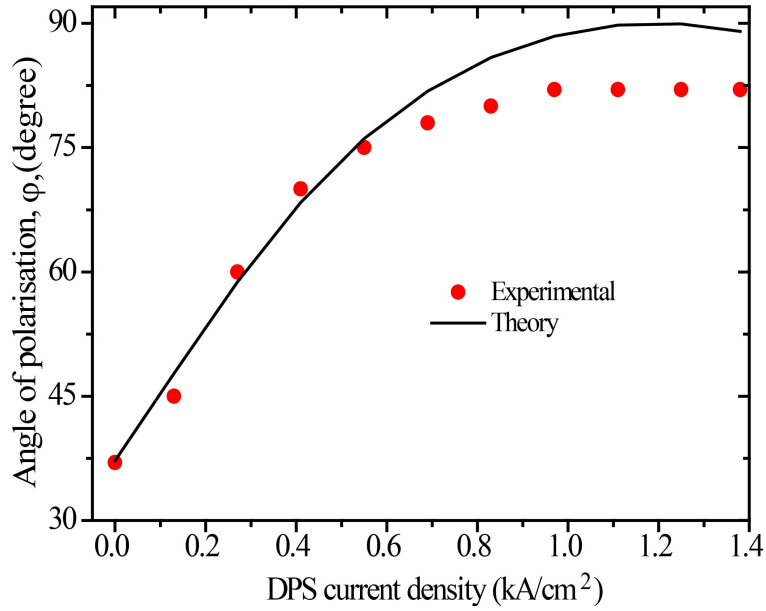


FIGURE 5.15: Shows the change in polarization angle as a various current density injection values into DPS section. the GS pulsed current was fixed at  $6.8 \text{ kA/cm}^2$  ( $1.3 \cdot I_{th}$ ) and the current to the DPS section was varied between  $0 \text{ kA/cm}^2$  and  $0.97 \text{ kA/cm}^2$  in steps of  $0.13 \text{ kA/cm}^2$ .

through the wire grid polariser. This experiment does not completely determine the output polarisation; for example, it cannot discriminate between elliptical and linear polarisation but it does indicate that the polarisation state can be tuned by the current injected into the DPS.

Figure 5.15 shows the change in polarisation angle for maximum transmission as a function of the current injection into the DPS section. At  $0 \text{ kA/cm}^2$  a polarisation angle of  $37^\circ$  (TM fraction > TE fraction) was recorded and the polarisation angle increases upto  $82^\circ$  (TM fraction < TE fraction) with an applied DC current of  $0.97 \text{ kA/cm}^2$  with no further change in polarisation angle recorded above  $0.97 \text{ kA/cm}^2$  current.

In order to fit the polarisation angle measurement result with the Jones matrix model, we are required to estimate the phase retardation with and without the DPS current. Phase retardation of DPS section can be written as:

$$\delta_{DPS} = \delta(i_{DPS} = 0) + \delta(\lambda, i_{DPS}) \quad (5.25)$$

where

$$\delta(i_{DPS} = 0) = \frac{2\pi\Delta nL}{\lambda} \quad (5.26)$$

and

$$\delta(\lambda, i_{DPS}) = \frac{2\pi\Delta n_{i_{DPS}}i_{DPS}L}{\lambda} \quad (5.27)$$

$\delta(i_{DPS} = 0)$  and  $\delta(\lambda, i_{DPS})$  are the phase retardation without and with DPS current,  $\Delta n$  is the birefringence before current is applied,  $n_{i_{DPS}}$  is the rate of change of birefringence with respect to current density,  $i_{DPS}$ , we assume a simple linear dependence. Equation 5.25 is substituted with the single pass Jones matrix Equation 5.7 and 5.8, the polarisation control operation is then analysed using Equation 5.9, where PMCs are defined by setting  $\theta = \pi/8$  and  $\delta = \pi$ . To fit the Jones matrix model to the experimental result, we adjust the value of  $\Delta n = 0.005$ , and,  $\Delta n_{i_{DPS}} = -1 \times 10^{-3}$  kA/cm<sup>2</sup> and with these values we obtain a good fit with the experimental result for lower current densities as is shown in Figure 5.15. The discrepancy between the theory and experiment at higher current densities may be due the fact that the theory is incomplete and it does not take account of gain and loss for the TE and TM mode in the DPS section. At the higher DPS injection currents there will be some gain for TM light and this prevents the output from being completely TE polarised.

### 5.5.3.1 Alternative Analysis of Active Polarisation Control Results

Let us now analyse polarisation angle measurement with second case: where PMCs are defined by setting  $\theta = \pi/4$  and  $\delta = \pi/2$ . Equation 5.25 is substituted with the single pass Jones matrix Equation 5.10 and 5.11, the polarisation control operation is then analysed using Equation 5.12. To fit the Jones matrix model to the experimental result, we adjust the value of  $\Delta n = 0.00306$ , and,  $\Delta n_{i_{DPS}} = -9.0 \times 10^{-4}$  kA/cm<sup>2</sup> and with these values we obtain a good fit with the experimental result for lower current densities as is shown in Figure 5.16. However in this case too,

we observe the discrepancy between the theory and experiment at higher current densities.

#### Active Polarisation Control with Jones Matrix Model Fit

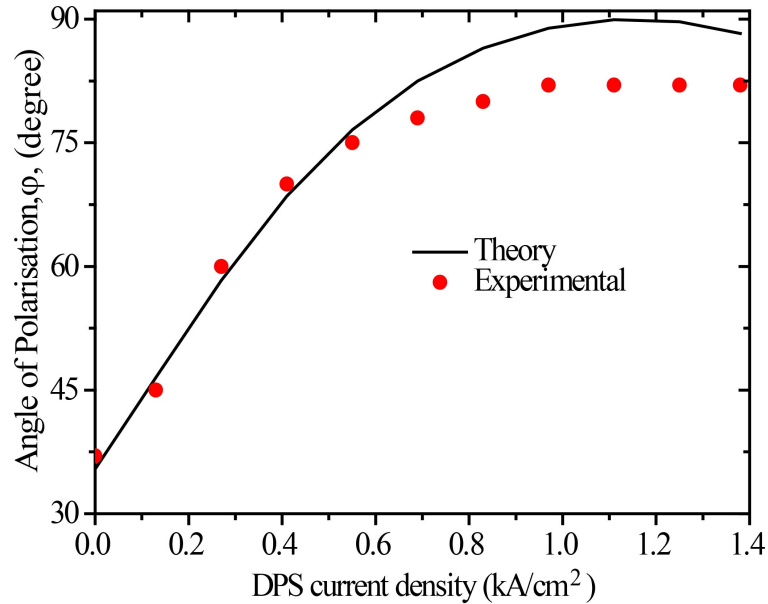


FIGURE 5.16: Shows the change in polarization angle as a various current density injection values into DPS section. the GS pulsed current was fixed at  $6.8 \text{ kA/cm}^2$  ( $1.3 \cdot I_{th}$ ) and the current to the DPS section was varied between  $0 \text{ kA/cm}^2$  and  $0.97 \text{ kA/cm}^2$  in steps of  $0.13 \text{ kA/cm}^2$ .

#### 5.5.4 Comparison of Analysis

We now compare the single pass measurement and Jones matrix analysis with polarisation angle measurement and Jones matrix analysis, to estimate the natural birefringence or material birefringence, at zero DPS current. By comparing we conclude the following:

- If PMCs are defined by setting  $\theta = \pi/8$  and  $\delta = \pi$ ; from single pass and polarisation angle measurement analysis, in both cases we estimate the natural birefringence are consistent with  $\Delta n = 0.005$ .

- If **PMCs** are defined by setting  $\theta = \pi/4$  and  $\delta = \pi/2$ ; from single pass and polarisation angle measurement analysis, we estimated the natural birefringence are inconsistent and two different values were estimated  $\Delta n$ , 0.0036 and 0.0030, respectively. We have found a discrepancy of around  $\sim 15\%$  in  $\Delta n$ .

Thus we conclude that **PMCs** (Design D1 in **Chapter 4**) utilised in the **ITBW** device are **PMCs** that convert to a 50% **TM** and 50% **TE** in a half beat length and can be describe by setting  $\theta = \pi/8$  and  $\delta = \pi$ . Furthermore, the natural birefringence for **QCL** employed in this work could be around 0.005. However, we did not find any literature to compare the value.

## 5.6 Conclusion

In thesis, for the first time in **MWIR** wavelength regime, we have described the design, modelling, fabrication and characterization of integrated tuneable birefringent for **QCLs** and demonstrated that an electro-optically tuneable birefringent property can be used in quantum cascade laser waveguides to achieve active control of the polarisation and the wavelength.

We have used a simple Jones matrix description of the polarisation components in the **QCL ITBW** device to construct a Jones matrix model that gives a good fit to the results obtained by measuring the output polarisation rotation as a function of **DPS** injection current. The model also helps explain the single pass experiments obtained by operating the device below the laser threshold. Further, from the Jones matrix description, we developed a simple phase only theory for the phase condition for modes in a laser with birefringent components, however applying our theory to the observed wavelength output spectra and **DPS** injection current tuning was complicated by sub-cavity effects.

By comparing the active polarisation angle measurement result with the Jones matrix model, we estimate the natural birefringence (no **DPS** current),  $\Delta n$  around

0.005 for the QCL employed in this work. This compares with the value that we obtain from the single pass measurements which is also 0.005. Also we can fit the dynamical polarisation angle control results if we assume a value of  $\Delta n_{i_{DPS}} = -1 \times 10^{-3} \text{ cm}^2/\text{kA}$  the value indicated by the fit to the single pass measurements is  $3.1 \times 10^{-3} \text{ cm}^2/\text{kA}$ . The results in Fig. 6 indicate that at the laser wavelengths, the intersubband contribution,  $\Delta n_{IS}$ , to birefringence is small at around  $1.0 \times 10^{-5}$  compared to the values given above. This value of  $\Delta n_{IS}$  is in approximate agreement for the values reported in [66, 115] for the linewidth enhancement factor for QCL albeit for different structures and wavelengths. Therefore we conclude that for laser operation, the electro-optic effect the current dependent birefringence, is dominated by the interband transition and is not highly dispersive. This limits the wavelength tuning. To obtain significant wavelength tuning requires a redesign of the QCL active region.

Further experimental and theory work is required to obtain a more complete understanding of the operation of the QCL- ITBW device. Experimentally a QCL active region designed specifically to enhance the electro-optic properties is required and a variety of device architectures should be investigated. The theory of birefringent effects in lasers needs to be extended to include both amplitude and phase effects.

The polarisation angle control range is  $45^\circ$  and we are not aware of any other QCL device that is capable of electronically controlling the output polarisation. Active control of the polarisation state of a QCL output could find applications in polarisation dependent spectroscopy [116] and in infrared ellipsometry [117].

# Chapter 6

## Conclusions and Recommendations for Future Works

The goal of this work was to design, fabricate and characterise monolithically tuneable quantum cascade lasers, operating around 4450 nm wavelength. This aim was achieved with the double-ring quantum cascade laser, polarisation mode converter and integrated tuneable birefringent waveguide. The significant achievements of this work are:

1. We have described how for the first time, the development of the device fabrication process based on e-beam lithography for non-planarised deeply etched waveguide were demonstrated. The benefits of EBL are: (i) the write resolution can be as low as 0.5 nm, (ii) pattern placement accuracy can be down to 10 nm and (iii) the automatic layer-by-layer alignment with accuracy of +/- 10 nm, which is desirable in our device processing.
2. The first ever single mode tuneable double-ring quantum cascade laser tuneable upto 59 nm for 0.72 kA/cm<sup>2</sup> DC current density injection into Ring 2 that covers 42% of the [FWHM](#) of the gain curve was demonstrated. This

is comparable to the 3800 nm [35], 242 nm [29] and 70 nm [30] tuning using EC-QCL, FP coupled cavity QCL and DFB QCL arrays, respectively. However, we observe mode hopping and pulling in the DRQCL and further work on active devices is required to gain a detailed understanding of the nonlinear dynamics that leads to mode pulling.

3. To the authors knowledge, first polarisation mode converter integrated with the QCLs that emit 69% TE light with the polarisation angle of  $65^\circ$  from one facet and pure TM light from other facet was demonstrated. The PMC designs are based on RIE lag effect and we can fabricate PMCs that emit  $\sim 69\%$  TE light based on PMC design D2. However, using QCL with integrated plasmonic polariser,  $45^\circ$  linearly polarised light was demonstrated in Ref. [118].
4. Demonstration of the first active polarisation control of QCLs using ITBW,  $45^\circ$  polarisation tuning was recorded from  $37^\circ$  to  $82^\circ$  by injecting  $0.97$  kA/cm<sup>2</sup> DC current into the DPS section. However, we are not aware of any other QCL capable of electronically controlling the output polarisation over this range.

A summary of main conclusions obtained from the previous chapters are as follows:

In this thesis, investigation and device development were carried out using the QCL structure based on strain-compensated Ga<sub>0.331</sub>In<sub>0.669</sub>As/Al<sub>0.659</sub>In<sub>0.341</sub>As/InP material system reported by Yu et al. [52]. To realise devices, a fabrication process based on electron beam lithography (EBL) was used. In this thesis, for the first time, a complete E-beam lithography based process was described to fabricate the QCLs. The main fabrication achievements are: development of the device fabrication process based on E-beam lithography, developing a multilayer ZEP520a E-Beam resist process for contact window opening and a metal lift-off recipe for non planarised deeply etched waveguide. The contact window opening and metal lift-off process are in Appendix A and Appendix B.

By exploiting the Vernier-tuning effect, we have demonstrated the single mode electrically tuneable operation of a DRQCL at room temperature. Single mode emission is observed with a side mode suppression ratio of over 19 dB. However, what we observed is discontinuous tuning over a range of 59 nm in a mode pulling and hopping manner which covers wavelength from  $\sim 4537$  nm to  $\sim 4596$  nm, almost half of the gain width (i.e. full width at half maximum (FWHM) of spontaneous emission spectra. To some extent the discontinuous tuning can be mitigated by changing the temperature of the heat sink. Furthermore, using the SM theory of a passive device we could estimate the resonance condition of the DRQCL and thereby predicting a current dependent refractive index of  $8.25 \times 10^{-4} \text{ kA}^{-1} \text{ cm}^2$ . Future work on active devices is required to gain a detailed understanding of the nonlinear dynamics that leads to mode pulling. However, even with fixed heat sink temperature we are able to tune the laser to align the output wavelength with a CO gas absorption line using pulse induced chirp of the output wavelength. We experimentally derived absorption coefficients ( $\alpha$ ) of  $0.116 \text{ cm}^{-1}$  and  $0.0674 \text{ cm}^{-1}$  for the R(9) and R(16) lines [68].

We have described how for the first time, polarisation mode convertors (PMCs) are realised in quantum cascade lasers. Polarisation mode convertors (PMCs) are waveguides with asymmetric cross-sectional profiles integrated monolithically with QCLs. The RIE lag phenomena was used to fabricate the asymmetric cross-sectional profiles by etching **ribs** and **trenches** on one side of the symmetric QCLs waveguide. From our first batch of fabrication, design D1, polarisation purities of 18% 115  $\mu\text{m}$  long PMCs were obtained from L-I characteristics and emission spectra with maxima of the beam intensities were recorded at  $20^\circ$ . From the last batch, design D2, polarisation purities of 69% for a 256  $\mu\text{m}$  long PMC were obtained from L-I characteristics and emission spectra with maxima of the beam intensities were recorded at  $65^\circ$ . With PMC lengths of around 419  $\mu\text{m}$  (design 2), PMC, polarisation purities of upto 94% could be obtained. The polarisation conversion can approach 100%, but requires increasingly stringent tolerance requirements for a single waveguide element. We have identified an alternative

approach of exploiting a universal 50% converter [81] in a half-beat-length which can approach 100% by using two elements.

In this thesis we have made a first attempt to design, fabricate and characterise integrated tuneable birefringence waveguide (ITBW) using the current controlled birefringence in quantum wells. The ITBW design reported in this thesis consists of 2 PMCs that convert to 50% TM and 50% TE in a half beat length with a DPS section between them. We have developed a numerical model based on the Jones matrix to explain the experimental results of ITBW. By comparing the active polarisation angle measurement result with the Jones matrix model, we estimate the natural birefringence (no DPS current),  $\Delta n$  around 0.005 for the QCL employed in this work. The current dependent intersubband contribution to birefringence is small at around  $3.6 \times 10^{-4} \text{ kA}^{-1}\text{cm}^2$  (@  $\lambda \sim 4445 \text{ nm}$ ), is dominated by the interband transition and was not highly dispersive. This limits the wavelength tuning. To obtain significant wavelength tuning requires a redesign of the QCL active region to increase the current dependent birefringence. No single mode emission is observed and 24 nm discontinuous wavelength tuning with tuning rate of  $25 \text{ nm}/(\text{kA}/\text{cm}^2)$  is recorded. For active polarisation control measurements,  $45^\circ$  polarisation tuning was recorded from  $37^\circ$  to  $82^\circ$  by injecting  $0.97 \text{ kA}/\text{cm}^2$  DC current into the DPS section. We are not aware of any other QCL capable of electronically controlling the output polarisation over this range.

The ITBW device was realised in the last phase of the project and no wafers were left for further design and optimisation. The Jones matrix employed in this work is a normalised model and is unable to predict the laser emission and discontinuous tuning behaviour. To understand the discontinuous behaviour and its theoretical verification requires more devices with different DPS section length and design.

## 6.1 Recommendations for Future Works

Some suggestions for future work as a follow up to this research are as follows:

1. In the [DRQCL](#), we observed 10 nm mode hopping which is twice of the [FSR](#) ( $\sim 5$  nm for 203  $\mu\text{m}$  ring radius) of the ring 1. The mode hopping may be minimised by utilising large ring radii (smaller [FSR](#)), for instance 1000  $\mu\text{m}$  ring radii will give  $\sim 0.9$  nm FSR.
2. We have identified an alternative approach of exploiting a universal 50% converter in a half-beat-length which can approach 100% by using two elements. This novel concept is recently realised by Naeem et al [92] for telecommunication wavelength. Further work is required to translate this design concept for quantum cascade lasers.
3. In this thesis, we reported the work on integrated tuneable birefringent waveguide and we have demonstrated the  $45^\circ$  active polarisation control using 1125  $\mu\text{m}$  long [DPS](#) section. The polarisation control over 90 degree may be achieved by double the [DPS](#) section length.
4. Recently, Holmes et al [99] reported relatively simple active polarisation controller design for telecommunication wavelengths compared to the ITBW design reported in this thesis. The design consists of, the laser section, polarisation mode control ([PMC](#)) section and differential phase shift ([DPS](#)) section. Further work is required to translate this design for quantum cascade lasers.
5. In [ITBW](#) device, no single mode emission is observed and the spacing between the modes is 11 nm. The 11 nm spacing that we observe is consistent with the presence of sub-cavities in the device. The index contrast between symmetric and asymmetric waveguides can lead to reflections [119] and this may lead to the formation of sub-cavities. To minimise this effect the interfaces between waveguide elements will need to be redesigned with optimised etch depths and tapering, ensuring smooth mode transitions without reflections [120].

# Appendix A

## Tri-layer ZEP520A EBL resist deposition, development and removal process

Process begin just after waveguide etching using [ICP-RIE](#) tool

### 1. SiO<sub>2</sub> hardmask removal process

- Sample dip into 5HF:H<sub>2</sub>O for 5 mins
- Rinse with [DI](#) water
- Blow dry with N<sub>2</sub>

### 2. Sample solvent cleaning without ultrasonic

- 3 mins in Acetone
- 3 mins in methanol
- 3 mins in [IPA](#)
- Rinse with [DI](#) water flow for 2 mins
- Blow dry with N<sub>2</sub>
- Bake on hotplate at 120<sup>o</sup>C for 1 mins

### 3. Insulator deposition

- 500 nm SiO<sub>2</sub>(see Table 2.1 for process)
- 500 nm Si<sub>3</sub>N<sub>4</sub> (see Table 2.2 for process)

### 4. Layer 1 and layer 2 ZEP deposition process

- Spin ZEP EBL resist first at 300 RPM for 5 secs than at 500 RPM for 5 secs and finally 2000 RPM for 60 secs
- Bake on oven at 120<sup>o</sup>C for 1 mins
- Allow sample to cool down the sample
- Spin second layer of ZEP EBL resist first at 300 RPM for 5 secs than at 500 RPM for 5 secs and finally 2000 RPM for 60 secs
- Bake on oven at 120<sup>o</sup>C for 1 mins
- Allow to cool down the sample

### 5. Layer 3 ZEP deposition process

- Spin ZEP EBL resist first at 300 RPM for 5 secs than at 500 RPM for 5 secs and finally 2000 RPM for 60 secs
- Bake on oven at 120<sup>o</sup>C for 1 mins
- Bake on hotplate at 180<sup>o</sup>C for 1 mins

### 6. Tri-Layer ZEP development process after EBL

- Soak into *o*-xylene at 23<sup>o</sup>C for 60 secs and agitate the sample
- Rinse with IPA flow for 25 secs (60 secs for high resolution feature)
- Blow dry with N<sub>2</sub>

### 7. Tri-Layer ZEP removal process

#### Chemical Process

- Soak sample in Microposit 1156 stripper for overnight
- Rinse with DI water flow for 2 mins

- Blow dry with N<sub>2</sub>
- O<sub>2</sub> plasma ash in Plasmafeb 80pulse RIE tool for 60 secs

**Dry process**

- Follow the Table 2.5 for Plasmafeb 80pulse RIE tool settingt
- O<sub>2</sub> plasma ash for 12 mins

# Appendix B

## Metal lift-off process

Listed below is the metal lift-off process developed for devices reported in this thesis. This process was developed for non planarised waveguide.

### 1. Sample solvent cleaning without ultrasonic

- 3 min in Acetone
- 3 min in methanol
- 3 min in IPA
- Rinse with DI water flow for 2 min
- Blow dry with N<sub>2</sub>
- Bake on hotplate at 120°C for 1 mins

### 2. Layer 1, Layer 2 and layer 3 LOR5a deposition process

- Spin LOR5A lift-off resist first at at 500 RPM for 5 secs and finally 2000 RPM for 60 secs
- Bake on oven at 120°C for 1 mins
- Allow to cool down the sample
- Spin second layer of LOR5A resist first 500 RPM for 5 secs and finally 2000 RPM for 60 secs

- Bake on oven at  $120^{\circ}C$  for 1 mins
- Allow to cool down the sample
- Spin third layer of LOR5A resist first 500 RPM for 5 secs and finally 2000 RPM for 60 secs
- Bake on oven at  $120^{\circ}C$  for 1 mins
- Allow to cool down the sample

### 3. Layer 4 ZEP EBL resist deposition process

- Spin ZEP EBL resist first at 300 RPM for 5 secs than at 500 RPM for 5 secs and finally 2000 RPM for 60 secs
- Bake on oven at  $120^{\circ}C$  for 1 mins
- Bake on hotplate at  $180^{\circ}C$  for 1 mins

### 4. Development process after EBL

- Soak into *o*-xylene at  $23^{\circ}C$  for 60 secs and agitate the sample
- Rinse with IPA flow for 60 secs
- Develop LOR5A on CD26 developer for 90 secs
- Rinse with DI water for 60 secs
- Blow dry with  $N_2$

### 5. Metal lift-off process

- Deposit Ti/Pd/Au(30 nm/30 nm/250 nm) metal on sample (see section 2.2.5)
- Deposit 500 nm Au sputtering method
- Soak sample in SVC-14 for 20 mins
- Blow dry with  $N_2$

# Appendix C

## Published Papers

# A tunable single-mode double-ring quantum-cascade laser

D Dhirhe<sup>1</sup>, T J Slight<sup>2</sup>, C C Nshii<sup>3</sup> and C N Ironside<sup>1</sup>

<sup>1</sup> School of Engineering, University of Glasgow, Glasgow G12 8LT, UK

<sup>2</sup> CST Global Ltd, Hamilton International Technology Park, Glasgow G72 0BN, UK

<sup>3</sup> Department of Physics, University of Strathclyde, Glasgow G4 0NG, UK

E-mail: [d.dhirhe.1@research.gla.ac.uk](mailto:d.dhirhe.1@research.gla.ac.uk)

Received 2 July 2012, in final form 10 July 2012

Published 22 August 2012

Online at [stacks.iop.org/SST/27/094007](http://stacks.iop.org/SST/27/094007)

## Abstract

The design, fabrication and characterization of a monolithic double-ring quantum-cascade laser (DRQCL) are described. At a wavelength of 4.6  $\mu\text{m}$ , we demonstrate tunable, single-mode operation of a DRQCL and use it as a source for spectroscopy of CO gas.

(Some figures may appear in colour only in the online journal)

## 1. Introduction

Quantum cascade lasers (QCLs) were invented in 1994 [1] and their operation is based on intersubband transitions in quantum wells. Currently, they are made from largely the same set of III–V semiconductor alloys (InP and AlGaAs based alloys) as most conventional interband semiconductor lasers. QCLs cover a broad range of wavelengths from mid-infrared to THz. QCLs can benefit from the relatively mature material technology associated with the fabrication of particularly InP-based optical communication lasers. For many applications, single-mode tunable operation is required and the mature fabrication technology associated with the InP process can be employed to make single-mode QCLs, and, furthermore, many of the concepts developed for communication lasers can be utilized for single-mode QCLs [2].

A variety of monolithic chip designs have been used to obtain single-mode QCL operation; these include distributed feedback with both overgrown [3] and lateral gratings [4], discrete mode lasers [5] and coupled resonator lasers [6]. The coupled resonator QCL was used as a source for gas phase spectroscopy. In this paper, we report on the design, fabrication and characterization of a new variety of monolithic coupled resonator QCL based on a double-ring structure, the double-ring quantum cascade laser (DRQCL) which gives tunable single-mode operation. We employ the DRQCL as a source for spectroscopy in the mid-infrared (Mid-IR) of gas phase CO.

## 2. Theory of the double-ring quantum cascade laser

Figure 1 shows a schematic illustration of the generic double-ring laser (DRL). The figure and theory in this section is based on [7] and adapted for DRQCLs. The linear systems scattering matrix (SM) theory is used to calculate the passive resonance wavelengths of a double-ring waveguide structure. We can compare this with the observed laser wavelengths at different direct current (dc) levels injected into ring 2 of the generic double-ring laser model illustrated in figure 1 and thus use the theory to estimate the dependence of the refractive index on the current injected into one ring of the laser.

The generic DRL is composed of two rings of slightly different radii and two straight waveguide coupled by three directional couplers. When the rings are uncoupled, the free spectral range (FSR) of an individual ring is determined by the effective length and group refractive index of the rings. The FSR of the ring is given by

$$\text{FSR}_i = \frac{\lambda^2}{n_g L_i} \quad (i = 1, 2), \quad (1)$$

where  $\lambda$  is the resonance wavelength,  $n_g$  is the group refractive index,  $L_i (= 2\pi R_i)$  is the effective length and  $R_i$  is the ring radius. When the coupled combs of modes of the rings are in resonance via Vernier effects by setting  $N/r_1 = M/r_2$ , the FSR of the coupled ring can be expressed as

$$\text{FSR} = N \cdot \text{FSR}_1 = M \cdot \text{FSR}_2, \quad (2)$$

where  $\text{FSR}_1$  and  $\text{FSR}_2$  are the FSRs in rings 1 and 2, respectively. The  $N$  and  $M$  are the resonant numbers of comblike peaks of individual ring, where  $N$  and  $M (= N - 1)$

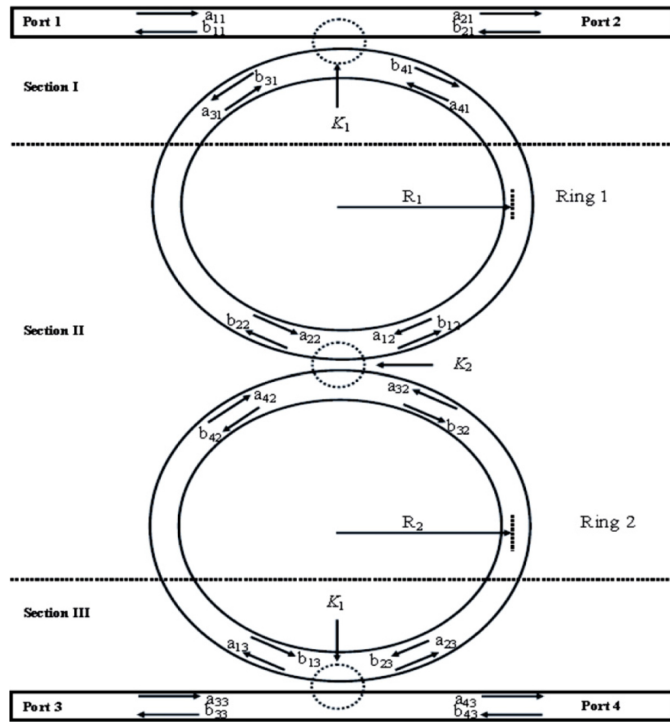


**Figure 1.** The schematic illustration of the top view of a generic double-ring laser; the waveguides that make up the laser are shown as two coupled rings and two straight sections. The scattering parameters that are used in the SM theory are shown in the figure.

are natural and coprime numbers [8]. The tuning enhancement factor of the coupled ring is equal to the natural number ( $N$  peak of ring 1), where the tuning enhancement factor ( $F$ ) can be defined as

$$F = \frac{\text{FSR}_2}{\text{FSR}_2 - \text{FSR}_1}. \quad (3)$$

At  $\lambda = 4545$  nm and  $n_g = 3.41$ , tuning enhancement factor 33 was estimated for DRQCL design. At the resonance, the 33rd peak of ring 1 will coincide with the 32nd peak of ring 2 and all other peaks will be suppressed. The wavelength tuning range ( $\Delta\lambda_{\text{tune}}$ ) is defined as  $\frac{\lambda^2}{2\pi n_g(R_1 - R_2)} = \text{FSR}_2 \cdot F$  [8]. The wavelength tuning range can be increased by increasing the radius of ring 2, and 155 nm tuning range was estimated for DRQCL design.

In broad outline, the tunable single-mode operation of the DRQCL is obtained as follows. Ring 1 is operated above threshold by injecting current pulses of around 100 ns duration with a 60 kHz repetition rate and amplitudes of  $1.3 \cdot I_{\text{th}}$  A (where  $I_{\text{th}} = 1.1$  A is the laser threshold current). Ring 1 is coupled to ring 2 and ring 2 has a much smaller dc (up to 100 mA) current applied to it that is below laser threshold and used to control the effective refractive index of the ring 2 waveguide and thus its resonance condition. The resonance wavelength of the DRQCL can be tuned by the small dc current

applied to ring 2. The coupling matrix in the directional coupler regions can be represented by [9]

$$\begin{bmatrix} b_1 \\ b_2 \\ \vdots \\ b_n \end{bmatrix} = \begin{bmatrix} K_{11} & \cdots & K_{n1} \\ \vdots & \ddots & \vdots \\ \vdots & \vdots & \vdots \\ K_{n1} & \cdots & K_{nn} \end{bmatrix} \cdot \begin{bmatrix} a_1 \\ a_2 \\ \vdots \\ a_n \end{bmatrix}, \quad (4)$$

where  $a$  and  $b$  are the SM parameters at coupling region and  $K$ s are the amplitude coupling ratio for directional couplers. In this work, DRQCLs are composed with two rings of slightly different radii and one straight waveguide coupled by two directional couplers. The transmission equation from the input port (port 1 of section I of figure 1) to the output port (port 4 of section III of figure 1) can be derived using the condition and method described in [7]. The transmission equation is given by

$$\left| \frac{b_{43}}{a_{11}} \right|^2 = \left| \frac{jK_1^2 K_2 e^{-j(\phi_1 + \phi_2)}}{1 - \sqrt{(1-K_1^2)(1-K_2^2)}(e^{-j2\phi_1} + e^{-j2\phi_2}) + (1-K_1^2) e^{-j2(\phi_1 + \phi_2)}} \right|^2, \quad (5)$$

where  $\phi_1$  and  $\phi_2$  are the phase delays on the half of the ring and depend on propagation loss ( $\alpha$ ) and propagation constant ( $\beta$ ) of the waveguide, as given by

$$\phi_i = (\beta_i - j\alpha) \cdot \pi R_i \quad (i = 1, 2). \quad (6)$$

**Table 1.** Parameter used to simulate the DRQCL.

Parameter	Value
Group index ( $n_g$ )	3.41
$n_{\text{eff}1}$ (effective index ring 1)	3.25
$n_{\text{eff}2}$ (effective index ring 2) @ 0 mA	3.2496
$n_{\text{eff}2}$ (effective index ring 2) @ 30 mA	3.2494
$n_{\text{eff}2}$ (effective index ring 2) @ 60 mA	3.2492
$n_{\text{eff}2}$ (effective index ring 2) @ 90 mA	3.2490
$R_1$ ( $\mu\text{m}$ )	203
$R_2$ ( $\mu\text{m}$ )	197
$K_1$	0.036
$K_2$	0.026
$\alpha$ , propagation loss ( $\text{dB m}^{-1}$ )	$1 \times 10^{-6}$ [11]

The propagation constant ( $\beta$ ) for ring 1 is given by

$$\beta_1 = \frac{2\pi n_{\text{eff}1}}{\lambda} \quad (7)$$

and for ring 2

$$\beta_2 = \frac{2\pi n_{\text{eff}2}(i)}{\lambda}, \quad (8)$$

where  $n_{\text{eff}1}$  is the effective refractive index for ring 1,  $n_{\text{eff}2}(i)$  is the dc current-dependent refractive index for ring 2 and  $\lambda$  is the resonance wavelength.

The DRQCL structure employed in this work is analyzed using the above transmission equation (5) with simulation parameters given in table 1. Figure 4(a) shows the simulation results of the DRQCL. The coupling fraction of the coupler between ring 2 and the output waveguide ( $K_1 \sim 0.036$ ) and the coupling fraction between the rings ( $K_2 \sim 0.026$ ), required for the SM theory, were calculated using the beam propagation method as implemented in the software package RSoft [12].

### 3. Fabrication

The DRQCLs reported in this work are based on a double-phonon resonant QCL wafer structure reported previously in [10].

Device processing started with deposition of a 500 nm thick SiO<sub>2</sub> hard mask on the sample, followed by spin coating of 500 nm of ZEP520A electron beam resist. Resist patterning was carried out using a Vistec VB6 electron beam lithography tool. After SiO<sub>2</sub> hard mask reactive ion etching, inductively coupled plasma (ICP) etching in chlorine/nitrogen (Cl<sub>2</sub>/N<sub>2</sub>) chemistry was used to define the ring and output coupler waveguide. 500 nm of Si<sub>3</sub>N<sub>4</sub> followed by 500 nm of SiO<sub>2</sub> were deposited as an insulating layer through which contact windows were etched on top of the waveguides.

The substrate was mechanically thinned to 200  $\mu\text{m}$  and then polished by etching in a solution of HBr:Nitric:H<sub>2</sub>O<sub>2</sub>:H<sub>2</sub>O (1:1:1:10) to improve the ohmic contact. Ti/Pd/Au (30 nm/30 nm/250 nm) was deposited on the top and bottom of the sample to form ohmic contacts. The two rings were electrically isolated using a metal lift-off technique. Finally, the processed sample was annealed at 380 °C. Figure 2(a) shows a scanning electron micrograph (SEM) image of the DRQCL, (b) detail coupling area between waveguide and ring

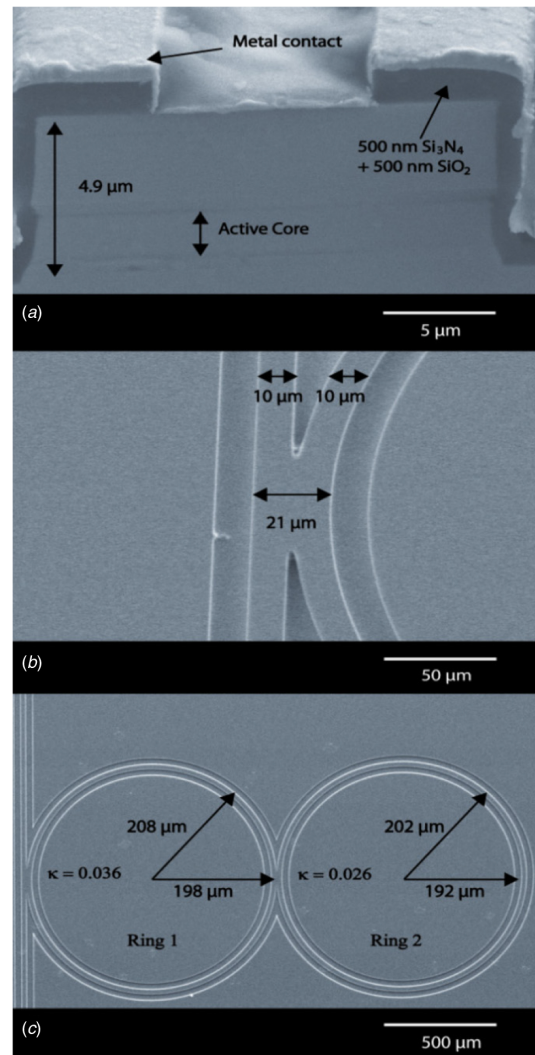


**Figure 2.** (a) The SEM image of DRQCL, (b) detail coupling area between waveguide and ring1 after ICP etching and 3 and (c) shows the front facet of fully processed DRQCL.

1 after ICP etching and (c) the front facet of fully processed DRQCL. Detailed step-by-step information of the fabrication process can be found in [11, 12].

### 4. Characterization and results

For characterization, the DRQCL was soldered epilayer-up onto a ceramic submount with wire bonds connecting the rings to contact pads on the submount. Spectral characteristics and optical power were measured using a Bruker Vertex 70 Fourier transform infrared (FTIR) spectrometer. A liquid nitrogen cooled indium antimonide (InSb) detector was used

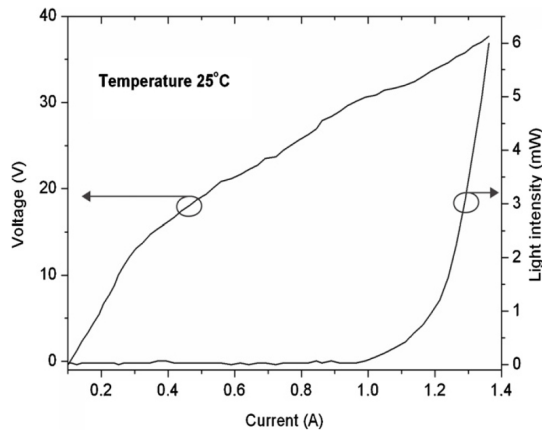


**Figure 3.**  $L$ - $I$ - $V$  curves of the DRQCL the current is the peak current into Ring 1.

with a lock-in amplifier for signal recovery. Measurements were carried out at room temperature, using 100 ns duration current pulses at a 60 kHz repetition rate.

Figure 3 shows the light-current-voltage ( $L$ - $I$ - $V$ ) curve from DRQCLs measured at 25 °C with zero dc current into ring 2. The threshold current of the DRQCL was around 1.1 A. At a drive current of  $1.3 \cdot I_{th}$ , optical peak powers of 6 and 7 mW were measured at 0 and 90mA dc injected into ring 2. The threshold peak current divided by the area of ring 1 gives a threshold current density of  $8.62 \text{ kA cm}^{-2}$  for the DRQCL, which compares to  $1.65 \text{ kA cm}^{-2}$  for a typical Fabry-Perot (FP) laser made from the same wafer.

Figure 4(b) shows the observed emission spectra and tuning as a function of dc current at 30 mA steps applied into ring 2 at drive pulse current  $1.3 \cdot I_{th}$  into ring 1. Single-mode emission was observed with a side mode suppression ratio of more than 19 dB for all dc currents injected into ring 2.

In figure 4 we compare the results of current tuning with the SM theory as summarized in equation (12). Table 1 shows the parameters input into the theory to fit the theory to the observed wavelengths of the single-mode outputs at different dc currents injected into ring 2 of the DRQCL. Estimated from SM theory, the effective index at zero injection current is  $n_{eff2, i=0}$ .

If we assume the following form of linear dependence of the  $n_{eff2}(i)$  on the dc current,

$$n_{eff2}(i) = n_{eff2, i=0} + i \frac{dn_{eff2}}{di}, \quad (9)$$

then by comparing with results shown in table 1 this gives  $dn_{eff2}/di = 6.6 \times 10^{-6} \text{ mA}^{-1}$  which is in approximate agreement with results reported in [13] and thus the SM theory gives a reasonable prediction of the resonance condition as illustrated in figure 4.

Figure 5 shows the wavelength tuning of the DRQCL measured as a function of the dc current injection into ring 2. It also illustrates the limitations of the SM theory which

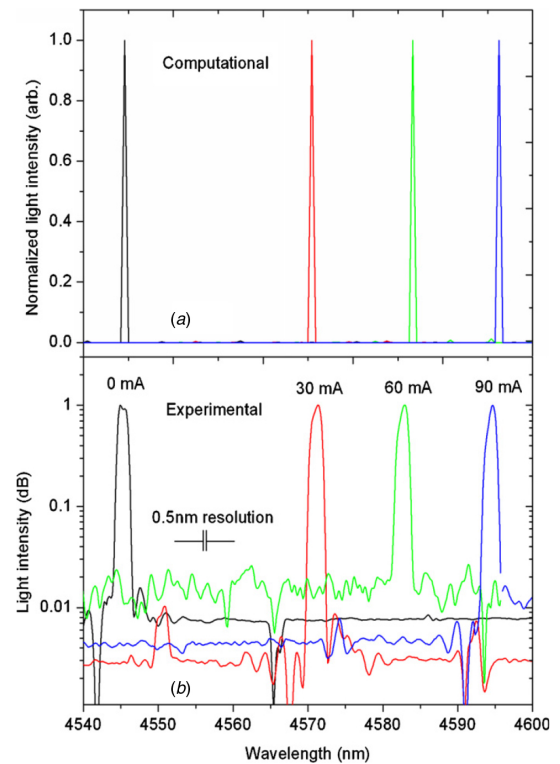


**Figure 4.** (a) The tuning curve estimated by the SM theory for various dc current applications into ring 2. If we assume a linear dependence of the refractive index with injection current at  $6.6 \times 10^{-6} \text{ mA}^{-1}$  then we can fit the SM theory to the results and (b) show the normalized spectra for DRQCL device measured at dc current from 0, 30, 60 and 90 mA with the spectral resolution of 0.5 nm.

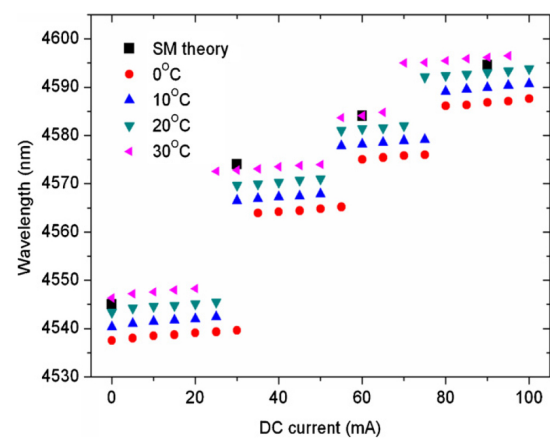


**Figure 5.** The wavelength tuning as a function of dc current measured at different heat sink temperatures.

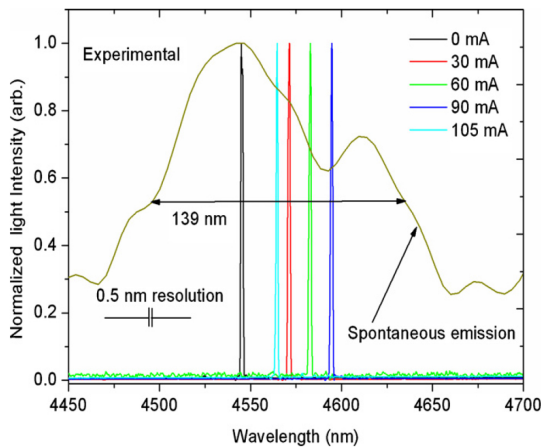


**Figure 6.** The spontaneous emission spectra measured using 3000  $\mu\text{m}$  long and 8  $\mu\text{m}$  wide Fabry-Perot laser (from the same wafer as the DRQCL) and the normalized single-mode output of the DRQCL at various dc current injected into Ring 2.

can only predict the resonance wavelengths of the DRQCL as a passive resonance structure. However, what we observe is discontinuous tuning over a range of 59 nm in a mode pulling and hopping manner which covers almost half of the gain width shown in figure 6. There are mode pulling regions of slow tuning at  $0.04 \text{ nm mA}^{-1}$  followed by mode hops of order 10 nm. To fully understand this type of discontinuous tuning requires further experimental work and the application of nonlinear dynamical theory [14] which is beyond the scope of the current paper.

Although the mode pulling and hopping complicates the use of the DRQCL as a spectroscopic source, it is still possible to utilize it if we combine the tuning obtained by the dc current in ring 2 with heat sink temperature tuning and the chirp tuning arising from the current pulse into ring 1. We demonstrate this by carrying out spectroscopy of selected absorption lines in CO gas.

## 5. Spectroscopy

Carbon monoxide (CO) gas has a strong fundamental vibrational-rotational absorption lines in the Mid-IR region centered at around 4666 nm [15]. Using the DRQCL as the IR source for an FTIR spectrometer we were able demonstrate the detection of CO gas.

Initially, for reference, an absorption spectrum was measured by FTIR spectroscopy using a broadband silicon carbide (SiC) Globar IR source (the blackbody source supplied with the FTIR) [16]. The FTIR sample cell was filled with  $^{12}\text{C}_{16}\text{O}$  at a pressure 105 Torr and had a path length of 11 cm. Figure 7(a) shows the IR absorption spectrum of the CO from 4540 to 4600 nm.

The DRQCL then replaced the Globar as the IR source in the FTIR spectrometer and spectra were measured using two different DRQCL drive conditions. Figures 7(b) and (e)

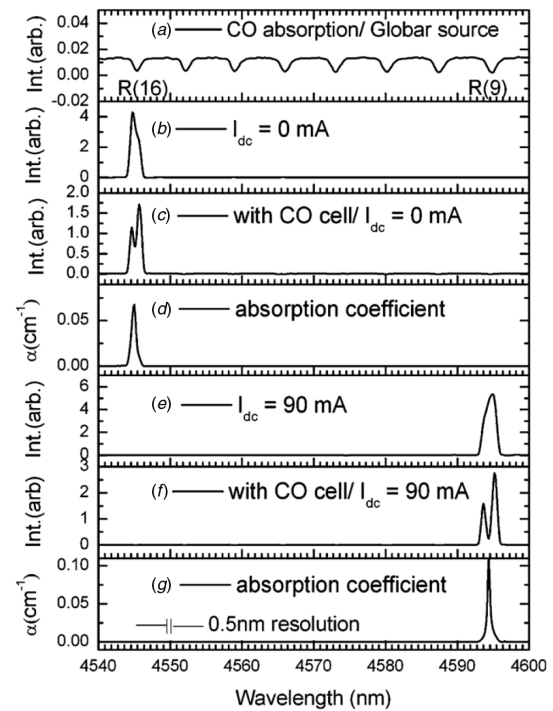


**Figure 7.** (a) CO absorption spectra using Globar source. (b) and (c) Laser and CO absorption spectra at 0 mA dc current, (e) and (f) laser and CO absorption spectra at 90 mA dc current, (d) and (g) experimental absorption coefficient at 0 and 90 mA, respectively.

show the FTIR spectra of the DRQCL without the CO cell present and at dc bias currents of 0 and 90 mA, respectively, at 25  $^{\circ}\text{C}$ . The DRQCL emission lines at these bias currents approximately align with the R(16) and R(9) lines of the CO absorption spectrum. Due to temperature induced chirp [17], the width of the DRQCL emission lines ( $\sim 1.5 \text{ nm}$ ) are broadened beyond the FTIR resolution (0.5 nm). This effect is used to tune the laser through absorption line.

The emission spectra of the DRQCL with the CO cell present are shown in figures 7(c) and (f) and exhibit a dip in transmission where the laser emission exactly coincides with the CO absorption lines. Figures 7(d) and (g) show the experimentally derived absorption coefficients ( $\alpha$ ) of 0.116 and  $0.0674 \text{ cm}^{-1}$  for the R(9) and R(16) lines.

## 6. Conclusion

We have described the design, fabrication and characterization of a DRQCL and demonstrated its application to CO spectroscopy.

Using the SM theory of a passive device we could estimate the resonance condition of the DRQCL and thereby predict a current-dependent refractive index of  $6.6 \times 10^{-6} \text{ mA}^{-1}$ . We observed mode pulling and hopping in the active devices as a function of dc injected into ring 2. Further work on

active devices is required to gain detailed understanding of the nonlinear dynamics that leads to mode pulling. To some extent, the discontinuous tuning can be mitigated by changing the temperature of the heat sink.

However, even with fixed heat sink temperature, we are able to tune the laser to align the output wavelength with a CO gas absorption line using pulse-induced chirp of the output wavelength. We could then measure the absorption coefficient of the CO absorption. By combining both dc current and temperature, 59 nm quasi-continuous tuning from  $\sim 4537$  to  $\sim 4596$  nm was observed and this plus the chirp tuning can be used for spectroscopy of the absorption lines R(16) and R(9) of the CO gas.

## References

- [1] Faist J, Capasso F, Sivco D L, Sirtori C, Hutchinson A L and Cho A Y 1994 Quantum cascade laser *Science* **264** 553–6
- [2] Yu N and Capasso F 2010 Wavefront engineering for mid-infrared and terahertz quantum cascade Lasers *J. Opt. Soc. Am.* **27** B18–35
- [3] Lee B G *et al* 2009 DFB quantum cascade laser arrays *IEEE J. Quantum Electron.* **45** 554–65
- [4] Slight T J, Tandoi G, Revin D G, McKee Zhang S Y, Meredith W, Cockburn J W and Ironside C N 2011  $\lambda \sim 3.35$  distributed-feedback quantum cascade lasers with high-aspect-ratio lateral grating *IEEE Photon. Technol. Lett.* **23** 420–2
- [5] Phelan R *et al* 2010 Room-temperature operation of discrete-mode InGaAs–AlAsSb quantum-cascade laser with emission at  $\lambda = 3.3 \mu\text{m}$  *IEEE Photon. Technol. Lett.* **22** 1273–5
- [6] Fuchs P, Seufert J, Koeth J, Semmel J, Höfling S, Worschech L and Forchel A 2010 Widely tunable quantum cascade lasers with coupled cavities for gas detection *Appl. Phys. Lett.* **97** 181111
- [7] Oda K and Takato N 1991 A wide-FSR waveguide double-ring resonator for optical FDM transmission system *J. Lightwave Technol.* **9** 728–36
- [8] Kim D G and Choi Y W 2009 Wide tuning characteristics of double-ring coupled lasers *Opt. Commun.* **282** 2516–23
- [9] Harvey A F 1963 *Microwave Engineering* (London: Academic) pp 99–101
- [10] Yu J S, Evans A, Slivken S and Razeghi M 2008 High-performance continuous-wave operation of  $\lambda \sim 4.6 \mu\text{m}$  quantum cascade laser above room temperature *IEEE Quantum Electron.* **44** 747–54
- [11] Nshii C C, Ironside C N, Sorel M, Slight T J, Zhang S Y, Revin D G and Cockburn 2010 A unidirectional quantum cascade ring laser *Appl. Phys. Lett.* **97** 231107
- [12] Nshii C C 2011 Tunable Mid-infrared light sources based on intersubband transitions *PhD Thesis* University of Glasgow, Glasgow submitted <http://theses.gla.ac.uk/2603/>
- [13] Lerttamrab M, Chuang S L, Gmachl C, Sivco D L, Capasso F and Cho A Y 2003 Linewidth enhancement factor of a type-I quantum-cascade laser *J. Appl. Phys.* **94** 5426–8
- [14] Wojcik A K, Yub N, Capasso F and Belyanina A 2011 Nonlinear optical interactions of laser modes in quantum cascade lasers *J. Mod. Opt.* **58** 727–42
- [15] Banwell C N and McCash E L 2007 *Fundamentals of Molecular Spectroscopy* 4th edn (New Delhi: Tata McGraw-Hill) pp 66–69
- [16] Morris J C 1961 Comments on the measurement of emittance of the Globar radiation source *J. Opt. Soc. Am.* **51** 798–9
- [17] Garcia M, Normand E, Stanley C R, Ironside C N, Farmer C D, Duxbury G and Langford N 2003 An AlGaAs–GaAs quantum cascade laser operating with a thermoelectric cooler for spectroscopy of  $\text{NH}_3$  *Opt. Commun.* **226** 39–43

# Quantum cascade lasers with an integrated polarization mode converter

D. Dhirhe,<sup>1,\*</sup> T. J. Slight,<sup>2</sup> B. M. Holmes,<sup>1</sup> D. C. Hutchings,<sup>1</sup> and C. N. Ironside<sup>1</sup>

<sup>1</sup>*School of Engineering, University of Glasgow, Glasgow, G12 8LT, UK*

<sup>2</sup>*CST Global Ltd, Hamilton International Technology Park, Blantyre, Glasgow, G72 0BN, UK*  
[d.dhirhe.1@research.gla.ac.uk](mailto:d.dhirhe.1@research.gla.ac.uk)

**Abstract:** We discuss the design, fabrication and characterization of waveguide polarization mode converters for quantum cascade lasers operating at 4.6  $\mu\text{m}$ . We have fabricated a quantum cascade laser with integrated polarization mode converter that emits light of 69% Transverse Electrical (TE) polarization from one facet and 100% Transverse Magnetic (TM) polarization from the other facet.

©2012 Optical Society of America

**OCIS codes:** (250.5960) Semiconductor lasers; (310.2790) Guided waves; (310.5448) Polarization, other optical properties.

---

## References and links

1. J. Faist, F. Capasso, D. L. Sivco, C. Sirtori, A. L. Hutchinson, and A. Y. Cho, "Quantum cascade laser," *Science* **264**(5158), 553–556 (1994).
  2. Y. Yao, A. J. Hoffman, and C. F. Gmachl, "Mid-infrared quantum cascade lasers," *Nat. Photonics* **6**(7), 432–439 (2012).
  3. P. Kluczynski, S. Lundqvist, J. Westberg, and O. Axner, "Faraday rotation spectrometer with sub-second response time for detection of nitric oxide using a cw DFB quantum cascade laser at 5.33  $\mu\text{m}$ ," *Appl. Phys. B: Lasers and Optics* **103**(2), 451–459 (2011).
  4. A. Roeseler, *Infrared Spectroscopic Ellipsometry* (Akademie-Verlag, 1990).
  5. N. Yu, Q. J. Wang, C. Pflugle, L. Diehl, F. Capasso, T. Edamura, S. Furuta, M. Yamanishi, and H. Kan, "Semiconductor lasers with integrated plasmonic polarizers," *Appl. Phys. Lett.* **94**(15), 151101 (2009).
  6. J. J. Bregenzer, S. McMaster, M. Sorel, B. M. Holmes, and D. C. Hutchings, "Compact polarization mode converter monolithically integrated within a semiconductor laser," *J. Lightwave Technol.* **27**(14), 2732–2736 (2009).
  7. J. S. Yu, A. Evans, S. Slivken, and M. Razeghi, "High-performance continuous-wave operation of  $\lambda \sim 4.6 \mu\text{m}$  quantum-cascade lasers above room temperature," *IEEE J. Quantum Electron.* **44**(8), 747–754 (2008).
  8. T. J. Slight, G. Tandoi, D. G. Revin, A. McKee, S. Y. Zhang, W. Meredith, J. W. Cockburn, and C. N. Ironside, " $\lambda \sim 3.35 \mu\text{m}$  distributed-feedback quantum-cascade lasers with high-aspect-ratio lateral grating," *IEEE Photon. Technol. Lett.* **23**(7), 420–422 (2011).
  9. B. M. Holmes and D. C. Hutchings, "Realization of novel low-loss monolithically integrated passive waveguide mode converters," *IEEE Photon. Technol. Lett.* **18**(1), 43–45 (2006).
  10. D. C. Hutchings and B. M. Holmes, "A waveguide polarization toolset design based on mode beating," *IEEE Photon. Journal* **3**(3), 450–461 (2011).
  11. C. D. Farmer, *Fabrication and evaluation of  $\text{In}_{0.52}\text{Al}_{0.48}\text{As}/\text{In}_{0.53}\text{Ga}_{0.47}\text{As}/\text{InP}$  quantum cascade lasers*, PhD thesis submitted to University of Glasgow (2000).
  12. D. Dhirhe, T. J. Slight, C. C. Nshii, and C. N. Ironside, "A tunable single mode double-ring quantum-cascade laser," *Semicond. Sci. Technol.* **27**(9), 094007 (2012).
  13. D. G. Revin, R. S. Hassan, A. B. Krysa, Y. Wang, A. Belyanin, K. Kennedy, C. N. Atkins, and J. W. Cockburn, "Spectroscopic study of transparency current in mid-infrared quantum cascade lasers," *Opt. Express* **20**(17), 18925–18930 (2012).
  14. D. Dhirhe, T. J. Slight, B. M. Holmes, D. C. Hutchings, and C. N. Ironside, "An integrated tunable birefringent filter for quantum cascade lasers," presented at the International Quantum Cascade Lasers School & Workshop 2012, Vienna, Austria, 2–6 Sept. 2012.
  15. B. M. Holmes, M. A. Naeem, D. C. Hutchings, J. H. Marsh, and A. E. Kelly, "A semiconductor laser with monolithically integrated dynamic polarization control," *Opt. Express* **20**(18), 20545–20550 (2012).
- 

## 1. Introduction

First demonstrated in 1994, Quantum Cascade Lasers (QCLs), based upon semiconductor, intersubband transitions in quantum wells [1], now cover an extensive range of output

wavelengths from the mid-infrared [2] to the far infrared and terahertz. Under the selection rules for intersubband transitions, only interaction with light polarized with the electric field perpendicular to the plane of the quantum wells is allowed. Consequently, in the typical semiconductor optical waveguides employed in quantum cascade lasers, gain is only achieved in Transverse Magnetic (TM) waveguide modes. However, many applications would benefit from an elliptically polarized output, as required in some forms of spectroscopy [3] and ellipsometry [4], and work on producing linearly and right circularly polarized light from QCLs by employing integrated plasmonic polarizers on the output facets of the laser has recently been reported [5].

In this paper we show how it is possible to control the polarization of the light from a QCLs using coupled modes. The work presented here is based upon similar work on conventional interband semiconductor lasers [6] where integrated polarization mode converters (PMCs) are reported. We describe how the design of PMCs are adapted for QCLs and how the PMCs are fabricated and characterized for a QCLs with an emission wavelength of  $\sim 4.6 \mu\text{m}$ .

## 2. Theory of Polarization Mode Converters (PMCs)

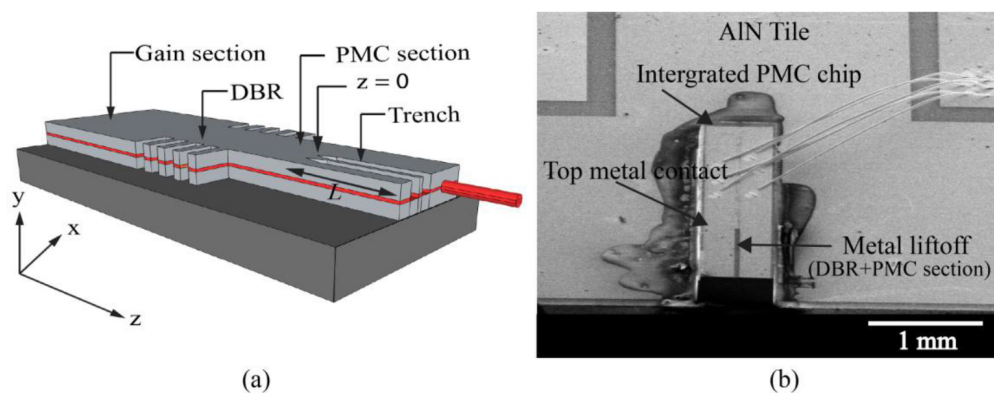


Fig. 1. (a) Schematic illustration of the chip layout of a quantum cascade laser that includes a gain section, lateral distributed Bragg reflector and an integrated polarization mode converter (PMC), the trenches of the PMC were etched using the reactive ion etching lag effect. There is no electrical contact to the PMC section. (b) SEM image of fully fabricated and mounted integrated PMC device.

Figure 1(a) shows a schematic illustration of the integrated PMC and scanning electron micrograph (SEM) image of fully fabricated and mounted integrated PMC device shown in Fig. 1(b). Details of the wafer design can be found in [7] and a discussion of the lateral DFB gratings and be found in [8]. As in the case of conventional interband semiconductor lasers [6], the PMCs are based upon waveguides with asymmetric cross-sectional profiles. This asymmetric cross-section results in a rotation of the optical axis of the birefringent guide, such that as a TM mode enters this asymmetric section, it excites both the single lobed fundamental modes of the guide (Hybrid TE-TM modes), with the relative propagation constant being dependent upon the degree of asymmetry and birefringence of the guide. For an offset of the optical axis of 45 degrees these modes are, essentially, fully hybridised which leads to beating with the characteristics half beat length given by  $L = (\pi/\Delta\beta)$ , where  $\Delta\beta = \beta_1 - \beta_2$  is the difference in propagation constants between two fundamental (single-lobed) modes that propagate in the asymmetric guide [6,9,10]. By varying the length, and/or, the asymmetry of the waveguide, it is possible to adjust the fraction of TM and TE polarization emerging from the asymmetric section, and fabricate waveguide versions of bulk optic polarization components, such as, quarter waveplates or half waveplates. A desirable feature of PMCs, particularly if they are to be incorporated in a QCL resonator, is that they be low loss.

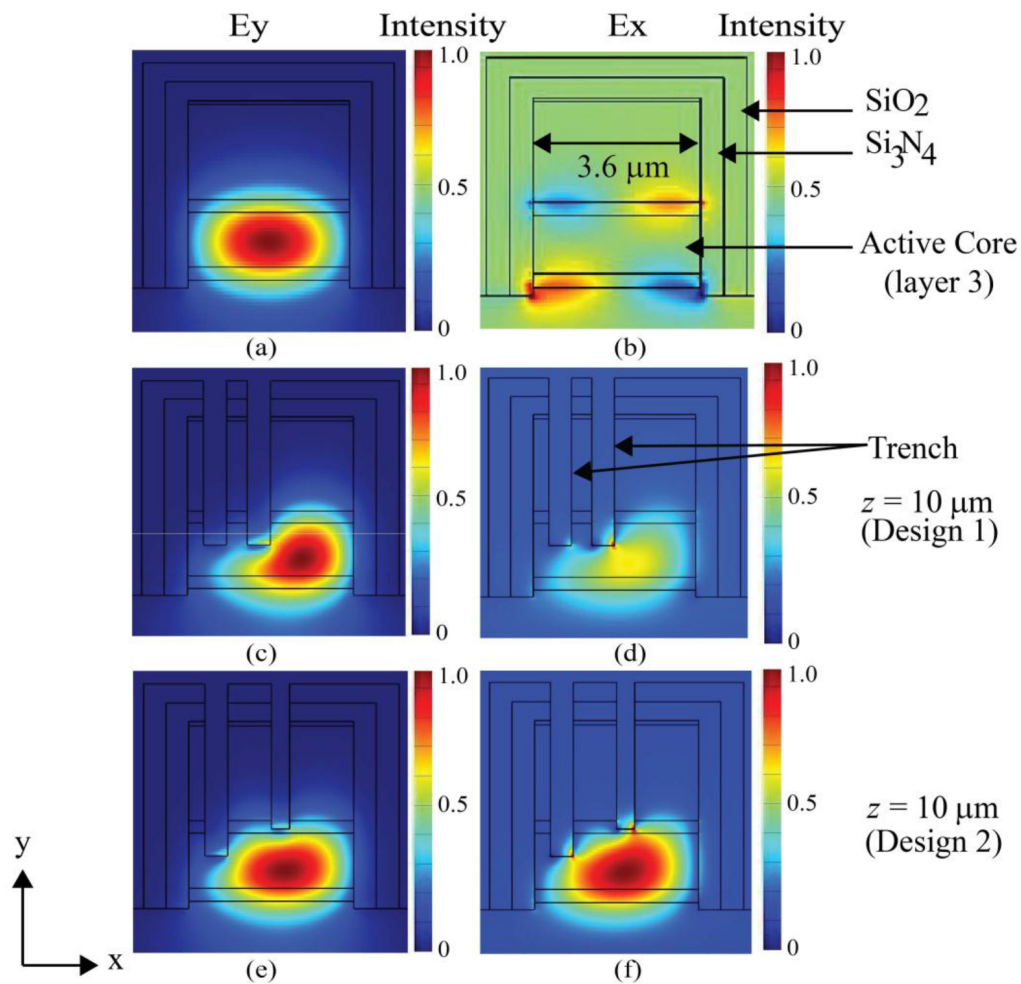


Fig. 2. (a) and (b) Show the simulated mode profiles of the TM and TE components respectively of the lowest order guided mode (without asymmetric cross-section). (c) and (d) show the TM and TE components respectively of the lowest order guided mode within the asymmetric section of design 1. (e) and (f) show the TM and TE components respectively of lowest order guided mode within the asymmetric section of design 2. Both  $z = 10 \mu\text{m}$  just after tapered region of PMC.

Design 1 has two trenches of  $0.5 \mu\text{m}$  width on a  $3.6 \mu\text{m}$  wide, and  $4.9 \mu\text{m}$  high waveguide. Design 2 has two trenches, one of  $0.5 \mu\text{m}$  and one of  $0.4 \mu\text{m}$  widths, on a  $3.6 \mu\text{m}$  wide, and  $4.9 \mu\text{m}$  height waveguide. The Table 1 shows the values of refractive indices and thickness of the layers used in the calculation of the mode profile for the TM mode.

To model the operation of the PMC, we first calculate the mode profiles for the hybrid mode in the asymmetric waveguide (Fig. 2) with the hybrid mode separated into TM and TE components at the start of PMC for two different waveguide cross-sections. Figure 2(a)-2(f) shows the mode profile of the TM and TE components of the lowest order guided mode for two designs, optimized using a full-vectorial, 3D eigensolver, as implemented in the software package Lumerical Mode Solutions (LMS). Figure 3(a) shows the normalised TM and TE transmission as a function of propagation distance within the mode conversion sections of two optimised designs. In order to ensure a smooth mode transition with low fluctuation and low insertion losses between the symmetric and asymmetric sections, a graded degree of asymmetry and birefringence (of the guides) were created by tapering the trenches.

**Table 1. Refractive indices of the QCL material at  $\lambda=4.6\ \mu\text{m}$  as used in the model to calculate TM & TE mode profiles (obtained from [11]).**

Layer	Layer name	Semiconductor	Index	Thickness ( $\mu\text{m}$ )
6	Contact	InGaAs	3.0	0.1
5	Upper cladding layer	InP	3.008	2.5
4	Upper waveguide	InGaAs/AlInAs	3.39	0.324
3	Active core	InGaAs/AlInAs	3.36	1.447
2	Lower waveguide	InGaAs/AlInAs	3.39	0.344
1	Buffer layer	InP	3.06	0.2
0	Substrate	InP	3.06	-

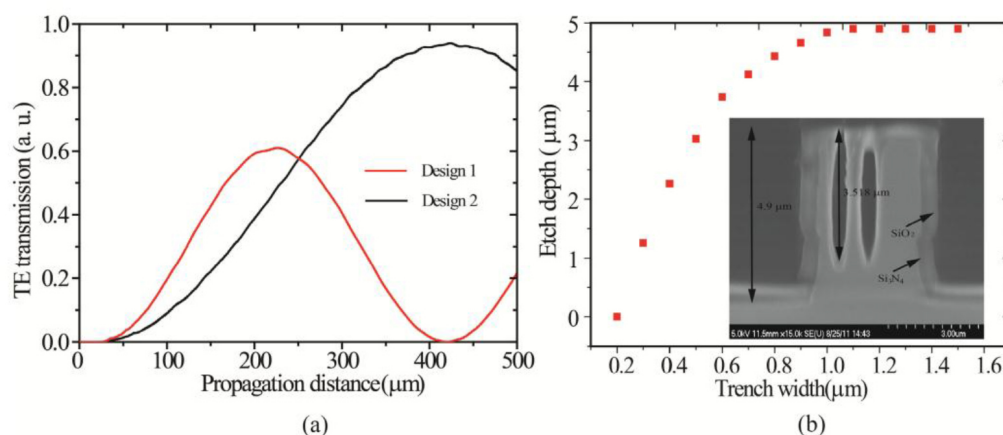


Fig. 3. (a) Calculated TE conversion versus propagation distance using BPM of two designs. (b) Plot of etch depth vs. trench width at etch times of 6 minutes for QCL wafer. Inset SEM image shows the etch profile of a PMC waveguide after ICP etching (design 1).

### 3. Fabrication of PMCs

The PMC designs used in this work are based upon the fabrication of “trenches” within the waveguide which are positioned to produce an asymmetric cross-sectional profile structure, that results in an effective rotation of the optical axis [9] of the guide. The depth of the trenches was controlled using the reactive ion etching (RIE) lag effect [9,10], where smaller trenches etch at a lower rate than larger ones. The effect was investigated in QCL material using an Inductively Coupled Plasma (ICP) etch tool. The results are given in Fig. 3(b) and clearly show how the etch depth significantly decreases as the trench width drops below 0.8  $\mu\text{m}$ . The advantages of the RIE lag effect for fabricating the PMC include: a one step etch and a naturally occurring taper region of the PMC asymmetric waveguide.

The QCLs used in this work are based upon a double phonon resonant QCL wafer structure reported previously in [7] that emitted at a wavelength of approximately 4.6  $\mu\text{m}$ .

Samples were deposited with 500 nm of  $\text{SiO}_2$  to act as a hard mask and coated with ZEP520A positive electron beam resist. Resist patterning was carried out using a Vistec VB6 electron beam lithography (EBL) tool, using a proximity error correction algorithm generated from a Monte Carlo simulation. After the  $\text{SiO}_2$  hard mask was formed, using a  $\text{CF}_4/\text{Ar}$  plasma in a standard RIE tool, inductively coupled plasma (ICP) etching in a chlorine/nitrogen ( $\text{Cl}_2/\text{N}_2$ ) chemistry was used to define the asymmetric waveguide and DBR grating. 500 nm of  $\text{Si}_3\text{N}_4$  followed by 500 nm of  $\text{SiO}_2$  was deposited as an insulating layer and contact windows were opened on top of the waveguides. Samples were thinned to 200  $\mu\text{m}$  and finally 30 nm Ti, 30 nm Pd and 250 nm Au were deposited to form ohmic top and bottom contacts. Figure 4(a)-4(c) shows the SEM of an integrated PMC device after ICP etching and the inset of Fig. 3(b) shows the cross section of a PMC (design 1). Further information on the fabrication steps can be found in reference [12].

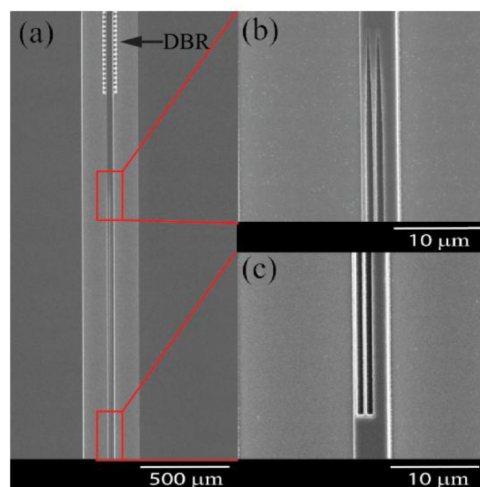


Fig. 4. (a) Shows the SEM top view of integrated PMCs device after ICP etching. (b) Magnified SEM view of taper input section of PMC. (c) Magnified SEM view of output section of PMC.

#### 4. Characterization

The QCLs incorporating PMCs were soldered, epilayer-up, onto aluminum nitride tiles (shown in Fig. 1(b)) and then mounted onto the cold finger of closed cycle helium cryostat. Both the spectral characteristics and optical power were measured using a Bruker Vertex 70 Fourier transform infrared (FTIR) spectrometer. The spectrometer was equipped with a liquid nitrogen cooled indium antimonide (InSb) detector, with a lock-in amplifier used for detector signal recovery. A grid polarizer, comprising 0.12  $\mu\text{m}$  strips of aluminium, on a thallium bromoiodide (KRS-5) window, was mounted in front of the detector, in a rotatable mount. Design 1 characterization was carried out at 298K and design 2 at 250K, with devices driven by 100 ns duration current pulses at a 60 kHz repetition rate.

Figure 5(a) shows the light – injection current (L-I) characteristics of a 265 $\mu\text{m}$  long PMC device, based upon design 2, where the power emitted from the PMC facet was measured: a) without the grid polarizer, b) with the grid polarizer axis parallel to QCL waveguide (TM polarization), and c) with the grid polarizer axis perpendicular to the QCL waveguide (TE polarization). The inset in Fig. 5(a) shows the emission spectra measured with similar conditions to those described above. A threshold current density of 2.19  $\text{kA}/\text{cm}^2$  was obtained for this device. Polarization purities ( $= P_{\text{TE}}/(P_{\text{TE}} + P_{\text{TM}}) \times 100\%$ ) of 18% for a 115  $\mu\text{m}$  long PMC (design 1) and 69% for 265 $\mu\text{m}$  long (design 2) PMC were obtained from L-I characteristics and emission spectra.

For devices based upon design 1, with 56  $\mu\text{m}$  and 119  $\mu\text{m}$  long PMCs, threshold current densities of 3.25  $\text{kA}/\text{cm}^2$  and 3.5  $\text{kA}/\text{cm}^2$ , respectively, were measured, and for one without a PMC section, 3  $\text{kA}/\text{cm}^2$  (Fig. 5(b)).

At a drive current of  $1.3 \cdot I_{\text{th}}$ , an peak optical power of  $\sim 2$  mW (1.18 mW for TE and 0.53 mW for TM) was measured from the PMC facet for the device with a 265  $\mu\text{m}$  long PMC (design 2) and 18 mW from the gain section facet. However, from measurements of a device with no PMC section, 9 mW was measured at the gain facet, and only 1 mW from the grating facet, implying the majority of the power of our QCLs was emitted from the gain section facets.

For comparison, a 6  $\mu\text{m}$  wide, 3000  $\mu\text{m}$  long, Fabry-Perot (FP) laser processed from the same wafer and measured at 298K, yielded a threshold current density of 2.4  $\text{kA}/\text{cm}^2$  with a power of 35 mW at  $1.3 \cdot I_{\text{th}}$ .

With PMC lengths of around 419  $\mu\text{m}$  (design 2), PMC conversion efficiencies of upto 94% could be obtained. The polarization conversion can approach 100%, but requires increasingly stringent tolerance requirements for a single waveguide element. We have identified an alternative approach of exploiting a universal 50% converter [10] in a half-beat-length which can approach 100% by using two elements.

The polarization of the beam can be determined by recording the detector signal as a function of wire-grid polarizer rotation angle ( $\theta = 0^\circ$  to  $360^\circ$ ), where  $\theta = 0^\circ$  is defined as the angle of the first maxima in transmission for TM light through the wire grid polarizer. First and for reference, polarization was measured from a DBR QCL laser without PMCs (from front and back facets) and pure TM emission was recorded (red dots) as shown in Fig. 6. For lasers with integrated PMCs, the maxima of the beam intensity was recorded at  $20^\circ$  for design 1 with a 119  $\mu\text{m}$  long PMC and  $65^\circ$  for design 2 with a 265  $\mu\text{m}$  long PMC, as shown in Fig. 6.

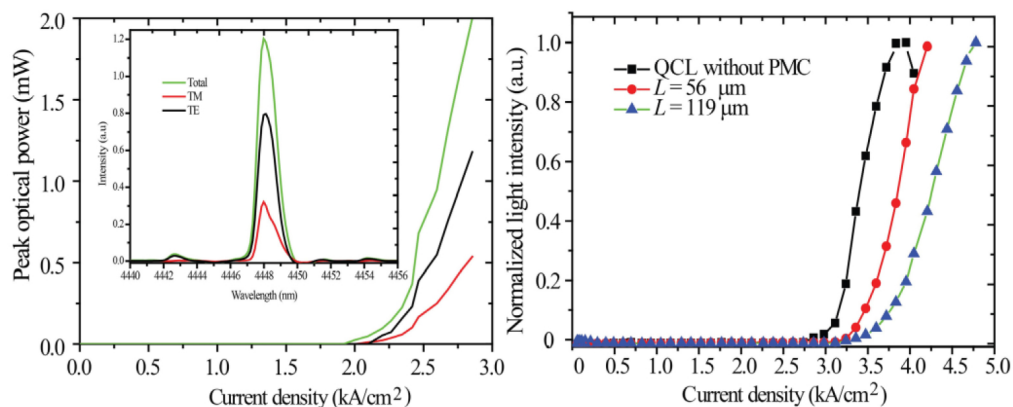


Fig. 5. (a) L-I characteristics of 265 $\mu\text{m}$  PMC device with inset showing the TM, TE and total emission spectra. (b) L-I characteristics of QCLs DBR and no PMC, 56  $\mu\text{m}$  PMC and 119  $\mu\text{m}$  PMC.

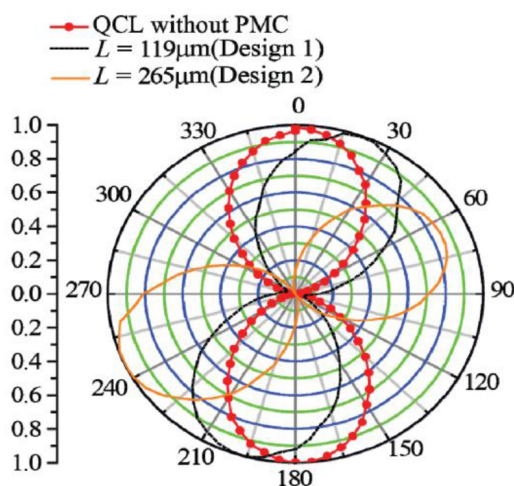


Fig. 6. Polar plots of normalized output power from PMC & DBR facet of the QCL as function of wire-grid polarizer angle for different PMC lengths and asymmetric waveguide cross-sections.

Table 2 shows the relative TE polarization component of different integrated PMCs with PMC lengths experimentally derived from both L-I characteristics and emission spectrum.

The calculated values in Table 2 come from a simulation using the full vectorial 3-D BPM as described above.

**Table 2. Compares calculated and measured TE polarization fraction as a function of PMC length.**

Design	PMC length ( $\mu\text{m}$ )	TE (%)	
		Measured	Calculated
1	56	8	7
	71	7	11
	119	18	27
2	256	69	65

To estimate the losses associated with the PMCs, we compared light – threshold current density curves of several QCLs each with different lengths of PMC. The results are summarized in Fig. 5(b) where it can be clearly seen that longer PMCs are associated with higher threshold current densities. From these results it can be estimated that the extra loss introduced by a PMC of design 1 is approximately  $6\text{ cm}^{-1}$  estimated from the change in the threshold current density [13] with the length of the PMC. Since the loss for TE light in QCL structures has been reported as lower [13] we attribute the extra loss associated with the PMC to scattering losses arising from the rib and trenches of the PMC and possible modal mismatches at their input and output.

## 5. Conclusion

We have described the design and fabrication of a PMC for QCLs operating in the mid-infrared and demonstrated that by integrating a PMC with a QCL, the output polarization can be controlled. We have demonstrated that it is possible to have a QCL that emits TM from one facet and predominately (69%) TE from the other facet. We have shown that there is good agreement between our simulation and experiment – for the typical case the simulation predicts to within approximately 10% accuracy. From a consideration of the threshold conditions, with our PMC design (design 1), we have estimated that the increased scattering losses, introduced by the PMCs, are approximately  $6\text{ cm}^{-1}$ .

We anticipate that with further optimization, control of the polarization of a QCL will become important in several applications and in the operation of future designs of QCLs. For example, as indicated in [10], if we combine PMCs with an integrated waveguide section that tunes the relative phase between TM and TE modes, a so called differential phase shift (DPS) section, then a tunable integrated birefringent filter [14] can be integrated with a QCL to electronically tune the output wavelength and/or polarization as demonstrated in conventional interband lasers recently [15].

# Appendix D

## Communicated Paper

# Active polarisation control of a quantum cascade laser using tuneable birefringence in waveguides

D. Dhirhe,<sup>1,\*</sup> T. J. Slight,<sup>2</sup> B. M. Holmes,<sup>1</sup> and C. N. Ironside<sup>1</sup>

<sup>1</sup>*School of Engineering, University of Glasgow, Glasgow, G12 8LT, UK*

<sup>2</sup>*CST Global Ltd, Hamilton International Technology Park, Blantyre, Glasgow, G72 0BN, UK*

*\*d.dhirhe.1@research.gla.ac.uk*

**Abstract:** We discuss the design, modelling, fabrication and characterisation of an integrated tuneable birefringent waveguide for quantum cascade lasers. We have fabricated quantum cascade lasers operating at wavelengths around 4450 nm that include polarisation mode converters and a differential phase shift section. We employed below laser threshold electroluminescence to investigate the single pass operation of the integrated device. We use a theory based on the electro-optic properties of birefringence in quantum cascade laser waveguides combined with a Jones matrix based description to gain an understanding of the electroluminescence results. With the quantum cascade lasers operating above threshold we demonstrated polarisation control of the output.

©2013 Optical Society of America

**OCIS codes:** (140.5965) Semiconductor lasers, quantum cascade; (250.5960) Semiconductor lasers; (310.2790) Guided waves; (310.5448) Polarisation, other optical properties.

---

## References and links

1. I. Moreno, J. A. Davis, T. M. Hernandez, D. M. Cottrell, and D. Sand, "Complete polarization control of light from a liquid crystal spatial light modulator," *Opt. Express* **20**(1), 364-376 (2012).
2. A. Kasapi, G. Y. Yin, and M. Jain, "Pulsed Ti:sapphire laser seeded off the gain peak," *Appl. Optics* **35**(12), 1999-2004 (1996).
3. G. Holtom and O. Teschke, "Design of a birefringent filter for high-power dye lasers," *IEEE J. Quantum Elect.* **10**(8), 577-579 (1974).
4. J. Faist, F. Capasso, D. L. Sivco, C. Sirtori, A. L. Hutchinson, and A. Y. Cho, "Quantum cascade laser," *Science* **264**, 553-556 (1994).
5. I. Bar-Joseph, C. Klingshirn, D. A. B. Miller, D. S. Chemla, U. Koren, and B. I. Miller, "Quantum-confined Stark effect in InGaAs/InP quantum wells grown by organometallic vapor phase epitaxy," *Appl. Phys. Lett.* **50**, 1010-1012 (1987).
6. R. P. G. Karunasiri, Y. J. Mii, and K. L. Wang, "Tunable infrared modulator and switch using Stark shift in step quantum wells," *IEEE Electron Device Lett.* **11**(5), 227-229 (1990).
7. G. Almogly, A. Shakouri, and A. Yariv, "Observation of birefringence induced by intersubband transition in quantum wells," *Appl. Phys. Lett.* **63**(20), 2720-2722 (1993).
8. B. M. Holmes, M. A. Naeem, D. C. Hutchings, J. H. Marsh, and A. E. Kelly "A semiconductor laser with monolithically integrated dynamic polarization control," *Opt. Express* **20**(18), 20545-20550 (2012).
9. D. C. Hutchings, and B. M. Holmes, "A waveguide polarisation toolset design based on mode-beating," *IEEE photon. J.* **3**(3), 450-461 (2011).
10. D. Dhirhe, T. J. Slight, B. M. Holmes, D. C. Hutchings, and C. N. Ironside, "Quantum cascade lasers with an integrated polarisation mode converter," *Opt. Express* **20**(23), 25711-25717 (2012).
11. A. Gerald and J.M. Burch, *Introduction to Matrix Methods in Optics* (John Wiley & Sons, 1975).
12. A. J. Kemp, G. J. Friel, T. K. lake, R. S. Conroy, and B. D. Sinclair, "Polarization effects, birefringent filtering and single frequency operation in lasers containing a birefringent gain crystal," *IEEE Quantum Elect.* **36**(2), 228-235 (2000).
13. J. S. Yu, A. Evans, S. Slivken, and M. Razeghi, "High-performance continuous-wave operation of  $\lambda\sim 4.6\ \mu\text{m}$  quantum cascade laser above room temperature," *IEEE Quantum Elect.* **44**(8), 747-753 (2008).
14. T. J. Slight, G. Tandoi, D. G. Revin, A. McKee, S. Y. Zhang, W. Meredith, J. W. Cockburn, and C. N. Ironside, " $\lambda\sim 3.35\ \mu\text{m}$  distributed-feedback quantum-cascade lasers with high-aspect-ratio lateral grating," *IEEE Photon. Technol. Lett.* **23**, 420-422 (2011).
15. D. C. Hutchings, M. S. Bahae, D. J. Hagan, and E. W. V. Stryland, "Kramers-Kronig relation in nonlinear optics," *Opt. Quantum Electron* **24**, 1-30 (1992).

16. J. J. Bregenzler, S. McMaster, M. Sorel, B. M. Holmes, and D. C. Hutchings, "Compact polarization mode converter monolithically integrated within a semiconductor laser," *J. Lightwave Technol.* **27**(14), 2732-2736 (2009).
17. J. Teissier, S. Laurent, C. Manquest, C. Sirtori, A. Bousseksou, J. R. Coudevylle, R. Colombelli, G. Beaudoin, and I. Sagnes, "Electrical modulation of the complex refractive index in mid-infrared quantum cascade lasers," *Opt. Express* **20**(2), 1172-1183 (2012).
18. S. D. McDougall and C. N. Ironside, "Measurements of reverse and forward bias absorption and gain spectra in semiconductor laser material," *Electron. Lett.* **31**(25), 2179-2180 (1995).
19. D. G. Revin, J. W. Cockburn, S. Menzel, Q. Yang, C. Manz, and J. Wagner, "Waveguide optical losses in InGaAs/AlAsSb quantum cascade laser," *J. Appl. Phys.* **103**, 043106 (2008).
20. N. C. Pistoni, "Simplified approach to the Jones calculus in retracing optical circuits," *Appl. Opt.* **34**(34), 7870-7876 (1995).
21. D. Dhirhe, T. J. Slight, C. C. Nshii, and C. N. Ironside, "A tunable single-mode double-ring quantum-cascade laser," *Semicond. Sci. Technol.* **27**(9), 094007 (2012).
22. M. Lerttamrab, S. L. Chuang, C. Gmachl, D. L. Sivco, F. Capasso, and A. Y. Cho, "Linewidth enhancement factor of a type-I quantum-cascade laser," *Appl. Phys. Lett.* **94**(8), 5426-5428 (2003).
23. T. Aellen, R. Maulini, R. Terazzi, N. Hoyler, M. Giovannini, and J. Faist, "Direct measurement of the linewidth enhancement factor by optical heterodyning of an amplitude-modulated quantum cascade laser," *Appl. Phys. Lett.* **89**, 091121 (2006).
24. P. Kluczynski, S. Lundqvist, J. Westberg, and O. Axner, "Faraday rotation spectrometer with sub-second response time for detection of nitric oxide using a cw DFB quantum cascade laser at 5.33  $\mu\text{m}$ ," *Appl. Phys. B* **103**, 451-459 (2011).
25. H. Fujiwara, *Spectroscopic ellipsometry: principles and applications* (John Wiley & Sons Inc., 2007).

## 1. Introduction

For many applications including laser diode spectroscopy and ellipsometry the control of wavelength and polarisation of a laser is required. Presently, bulk optics elements are routinely used for polarisation control [1] and wavelength tuning [2, 3]. In this paper we describe the design, fabrication and characterisation of an integrated electro-optically tuneable birefringent waveguide for polarisation control and wavelength tuning of a semiconductor laser, the quantum cascade laser (QCL) [4].

QCLs are based on intersubband transitions in quantum wells but we can expect that QCL material will exhibit electro-optic properties based on intersubband transitions and interband transitions [5, 6]. The selection rules for intersubband transitions dictate that only light polarised with its electric vector perpendicular to the plane of the quantum well can couple to the intersubband transitions. In the typical waveguide arrangement used in a QCL this means that there is only optical gain for Transverse Magnetic (TM) polarised modes. In addition it means that, at the operating wavelengths, QCL waveguides exhibit birefringence and indeed it has been previously reported [7] that intersubband transitions can lead to birefringence. In the QCL waveguides the strength of the intersubband transition can be altered by injecting current into the waveguide and therefore the QCL waveguides have birefringence that can be adjusted with injection current. Also associated with the quantum wells that make up the QCL material are interband transitions and these transitions are strong and highly dispersive at photon energies close to the band gap resonance [6]; at the photon energies well away from the band-edge where the QCL operates the effect of the interband transitions is weaker and much less dispersive. The interband transitions are also a function of applied electric field and injected current and so at the QCL operating wavelength we can expect an interband electro-optic effect which is not dispersive. Altering the phase relationship between the polarisations is the basis of the wavelength tuning and polarisation control of birefringent waveguides – but wavelength and polarisation tuning requires that both TM and TE modes are present and that is usually achieved by incorporating waveplates into the laser.

The feasibility of an electro-optically altering the phase relationship between the polarisations has been recently demonstrated for quantum well semiconductor laser diodes by monolithically integrating the laser, polarisation mode convertor (PMC) section and differential phase shift (DPS) section [8].

The integrated equivalents of waveplates are polarisation mode convertors [8, 9]. We have previously report how PMCs are fabricated for QCLs [10]. The PMCs are made by etching trenches on the waveguides to make the waveguide cross-section asymmetric. With PMCs it is possible to make the integrated equivalent of a bulk quarter waveplate and to produce a hybrid mode that is 50% TE and 50% TM. The other component required for a tuneable waveguide is a DPS section; this is a section of the QCLs waveguide with electrical contacts that allow injection of current that alters the strength of the intersubband transitions.

In this paper we discuss the design of the integrated tuneable birefringent waveguide (ITBW) and we report results on experiments that employ the sub-threshold electroluminescence (EL) to probe the operation of the ITBW. We develop a theory of the operation based on a Jones matrix [11] description of the ITBW and a description of the electro-optic properties of the birefringence of the QCLs waveguide that splits the electro-optic birefringence into a current dependent but wavelength independent effect that arises from intersubband transitions and current and wavelength dependent birefringence that arises from the intersubband transitions. Finally we demonstrate wavelength and polarisation tuning of the quantum cascade laser operating above threshold.

## 2. ITBW design

Our design for an ITBW for QCLs is shown in Fig. 1. It consists of 2 PMCs configured as quarter waveplates with a DPS section between them. The PMCs are passive optical waveguides that are made asymmetric by, for example, etching trenches on one side on the waveguide. Full theoretical and design description of PMCs on QCLs can be found in [10]. The DPS section adjusts the relative phase of the TM and TE components of the circularly polarised light from the first PMCs. This is achieved because of the selection rules of the intersubband transitions and in a QCL structure the strength of the intersubband transitions can be altered by the injection of current so the birefringence of DPS section can be adjusted by injection current. The relative phase of the TE and TM components at the input into the second birefringent waveguide determines the output polarisation of the second PMC. In a QCL, only TM light will be amplified and the wavelengths that are rotated back to TM polarisation are determined by the current in the DPS section thus we have a QCL that has its operating wavelength selected by an electro-optic tuneable birefringent waveguide.

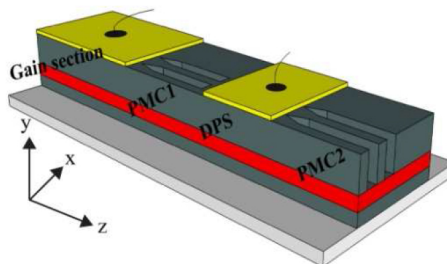


Fig. 1. Schematic design for an integrated tuneable birefringent waveguide for QCLs, it shows the gain section (GS) and trenches in the upper part of the waveguide that form the polarisation mode convertors (PMCs) [9, 10] between the PMCs is the differential phase shift (DPS) section where current can be applied to alter the phase relationship between the TE and TM modes. The approximate position of the active region is indicated in red.

## 3. Electro-optic birefringence of the QCL and the Jones matrix description

In the DPS section of the ITBW we utilize the electro-optic birefringent properties of the quantum cascade laser structure to tune the polarisation and wavelength. We regard the electro-optic birefringence of the DPS section as made up three parts, a natural birefringence (i.e birefringence with zero injection current into the DPS section),  $\Delta n$ , an interband birefringence,  $\Delta n_{IB}(i_{DPS})$ , and an intersubband birefringence,  $\Delta n_{IS}(\lambda, i_{DPS})$ . The electro-optic

interband birefringence comes from interband transitions and arises from the effect of current on interband transitions and the electro-optic intersubband birefringence arises from the effect of the current on the intersubband transitions. For  $\Delta n_{IB}(i_{DPS})$ , we ignore the wavelength dependence because a QCL operates at wavelengths far from the band-gap resonance of our quantum well material and so is almost constant for wavelengths close to the laser wavelength. For  $\Delta n_{IS}(\lambda, i_{DPS})$ , we explicitly include the wavelength dependence because it is much more dispersive for wavelengths close to the laser wavelength [7]. Note that the  $\Delta n_{IS}(\lambda, i_{DPS})$ , only gives rise to a change to the TM mode. So we have:-

$$\Delta n(\lambda, i_{DPS}) = \Delta n + \Delta n_{IB}(i_{DPS}) + \Delta n_{IS}(\lambda, i_{DPS}) \quad (1)$$

Jones matrices are routinely used to describe the polarisation behaviour of bulk optics systems [11] and have been used to describe the operation of a laser incorporating a birefringent crystal and gain medium [12]. Here we use Jones matrices to describe the operation of the ITBW. The coordinate system we use is as follows; y is the direction of growth of the epilayer (so TM light is y-polarised) and x is perpendicular to the direction of growth (TE light is x-polarised).

In what follows we assume that the PMCs can be described by a Jones matrix description and that their operation is wavelength independent [9]. For the co-ordinate system illustrated in Fig. 1 the generic Jones matrix is:-

$$\begin{bmatrix} \cos^2(\theta) + e^{-i\delta} \sin^2(\theta) & (1 - e^{-i\delta}) \cos(\theta) \sin(\theta) \\ (1 - e^{-i\delta}) \cos(\theta) \sin(\theta) & \sin^2(\theta) + e^{-i\delta} \cos^2(\theta) \end{bmatrix} \quad (2)$$

Where  $\theta$  is the angle the optic axis makes with the x direction and  $\delta$  is the phase retardation.

From our previous work on PMCs [10] we have designed a PMC that converts a TM mode into a hybrid mode that is 50% TM and 50% TE. Our experiments do not allow us to measure the relative phase between the TM and TE modes and so we can adapt the generic Jones matrix to describe this behaviour in various ways; for example an optics axis rotation of  $\theta = \pi/4$  and phase retardation of  $\delta = \pi/2$ , or we could set  $\theta = \pi/8$  and  $\delta = \pi$ . As explained in [9] it appears that PMCs that conversion to 50% TM and 50% TE in a half beat length are best described by setting  $\theta = \pi/8$  and  $\delta = \pi$ :- Using these values we obtain the Jones matrix for the PMC.

$$\mathbf{PMC} = \frac{1}{\sqrt{2}} \begin{bmatrix} 1 & 1 \\ 1 & -1 \end{bmatrix} \quad (3)$$

The Jones matrix for the DPS is given by setting  $\theta = 0$ , because the plane of the quantum wells is in the x- direction and  $\delta = \frac{2\pi\Delta n(\lambda, i_{DPS})L}{\lambda}$ , where  $L$  is the length of the DPS,  $\lambda$  is the free space wavelength. Thus the Jones matrix for DPS section is,

$$\mathbf{DPS} = \begin{bmatrix} 1 & 0 \\ 0 & e^{-i\frac{2\pi\Delta n(\lambda, i_{DPS})L}{\lambda}} \end{bmatrix} \quad (4)$$

Thus the overall single pass Jones matrix (or Transfer Matrix),  $T_D$  for the ITBW is given by:-

$$T_D = \mathbf{PMC} \cdot \mathbf{DPS} \cdot \mathbf{PMC} \quad (5)$$

We assume the input into the ITBW section is TM polarised because the QCL gain section selects for TM polarisation,  $\begin{bmatrix} 0 \\ 1 \end{bmatrix}$ , then the polarisation vector representing the ITBW response is given by:-

$$ITBW = T_D \cdot \begin{bmatrix} 0 \\ 1 \end{bmatrix} = \frac{1}{2} \begin{bmatrix} 1 - e^{-i \frac{2\pi\Delta n(\lambda, i_{DPS})L}{\lambda}} \\ 1 + e^{-i \frac{2\pi\Delta n(\lambda, i_{DPS})L}{\lambda}} \end{bmatrix} \quad (6)$$

For TM and TE polarisation intensity fraction of the ITBW response is given by:-

$$I_{TM}(\lambda, i_{DPS}) = \frac{1}{2} \left| 1 + e^{-i \frac{2\pi\Delta n(\lambda, i_{DPS})L}{\lambda}} \right|^2 \quad (7)$$

$$I_{TE}(\lambda, i_{DPS}) = \frac{1}{2} \left| 1 - e^{-i \frac{2\pi\Delta n(\lambda, i_{DPS})L}{\lambda}} \right|^2 \quad (8)$$

The ITBW device structure employed in this work is analyzed using ITBW response Eq. (7) with the conditions described above.

In the dynamic polarisation control operation of ITBW we measure the angle of polarisation,  $\varphi$ , of the output from the QCL as a function of input current into the DPS and if we assume a single pass through the ITBW then that is given by

$$\varphi(\lambda, i_{DPS}) = \arctan \left( \frac{I_{TM}(\lambda, i_{DPS})}{I_{TE}(\lambda, i_{DPS})} \right) \quad (9)$$

#### 4. Fabrication of QCL-ITBW devices

The QCLs used in this work are based upon a double phonon resonance QCL wafer structure reported previously in [13] that emitted at a wavelength of around 4600 nm.

Figure 2(a) shows the SEM image of a PMC after ICP etching and Fig. 2(b) a SEM image of the cross section of a PMC. Figure 2(c) shows a photograph of the wire bonded QCL-ITBW device with different sections (GS, PMC1, DPS and PMC2) indicated on the micrograph. Fabrication processes were similar to those used for the PMCs described in [10]. In the ITBW device, only the GS and DPS section contact windows were opened on the top of the waveguides with the rest of the structure protected by  $\text{Si}_3\text{N}_4$  and  $\text{SiO}_2$  insulating layers. GS and DPS section metal contacts were electrically isolated using a metal lift-off technique. Detailed step-by-step information of the fabrication process can be found in [10].

Using the design methodology outlined in [10] the PMCs were designed to convert 50% TM and 50% TE in a half beat length; so that in the first PMC (PMC1) in Fig. 1 light from the GS, (polarised TM), originating from intersubband transitions is converted into to 50% TM and 50% TE light at the output of the PMC and input to the DPS. This required trenches to be etched into the PMC waveguides, the trenches were 0.5  $\mu\text{m}$  wide and 3.518  $\mu\text{m}$  deep and were fabricated using a reactive ion etching technique [14]. PMC1 and PMC2 are designed to be identical.

#### 5. Characterisation and results

The QCL-ITBW devices were soldered epilayer-up onto aluminium nitride tiles and then mounted onto the cold finger of closed cycle helium cryostat. Spectral characteristics were measured using a Bruker Vertex 70 Fourier transform infrared (FTIR) spectrometer. The spectrometer was equipped with a liquid nitrogen cooled indium antimonide (InSb) detector, with a lock-in amplifier used for detector signal recovery. For polarisation measurements, a

grid polariser was mounted in front of the detector, in a rotatable mounting. Characterisation was carried out at a laser heat sink temperature of 250K. The results that we report here were for devices that had the gain section length of 2500  $\mu\text{m}$  then DPS section length 1125  $\mu\text{m}$  and the PMC sections were designed to be half waveplates [9] with length 151  $\mu\text{m}$  to give 50%, 50% TE, TM mode intensity split and cross-section of 3.6  $\mu\text{m}$  wide and 4.9  $\mu\text{m}$  high waveguides.

The GS current density was pulse injection with values around 4.2  $\text{kA}/\text{cm}^2$  and the DPS had direct current (DC) injection at around 1/10 of the GS current density – to avoid excessive TM gain in the DPS section.

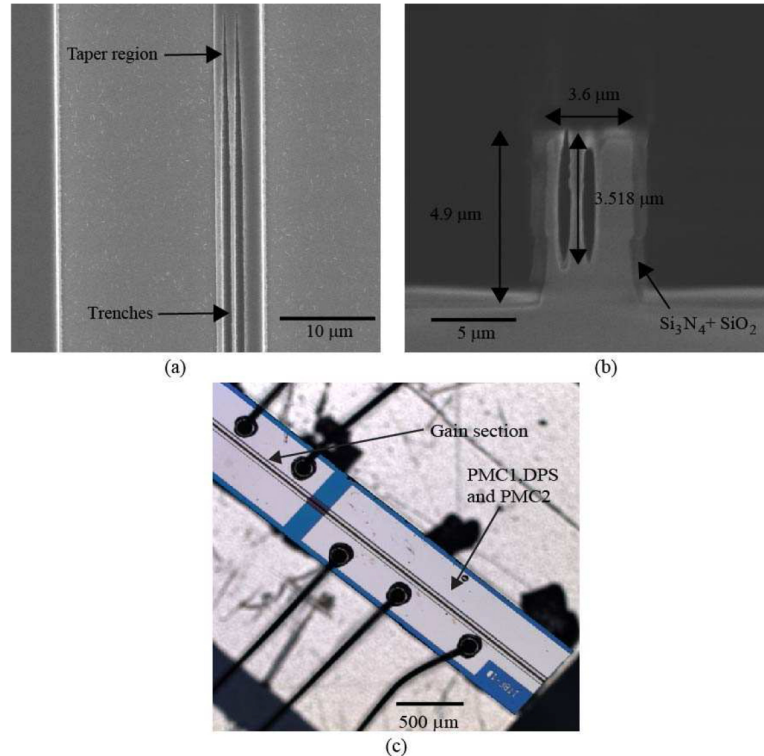


Fig. 2. (a) SEM (top view) of a PMC after ICP etching. (b) SEM image showing the etch profile of a PMC waveguide. (c) Photograph of the top of the processed ITBW device. Underneath the Gain Section (GS) and DPS section waveguide contact windows were open for current injection and rest of the structure as protected by  $\text{Si}_3\text{N}_4$  and  $\text{SiO}_2$  insulating layers.

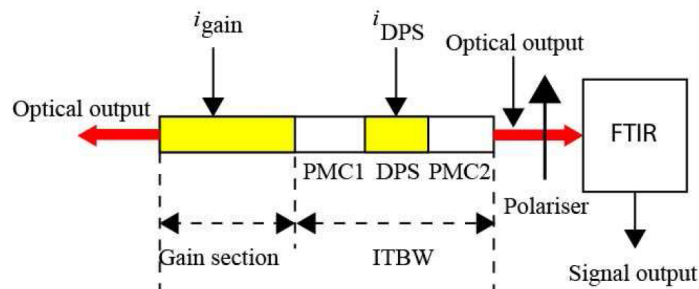


Fig. 3. Shows a schematic of the experimental setup for characterising the QCL that includes an ITBW; the GS is injected with current  $i_G$  and the ITBW has a current  $i_{DPS}$  injected that electro-optically alters the birefringence of the DPS section. The polarisation is selected using a linear polariser and the output spectrum of device is measured using a FTIR spectrometer. All experiments were conducted at 250K QCL heat sink temperature.

### 5.1 Sub-threshold single pass measurements

To gain an insight into the operation of the ITBW we carried out single pass measurement using the sub-threshold EL from the GS. This allows us to estimate the values of  $\Delta n$ , natural birefringence without DPS current and  $\Delta n(\lambda, i_{DPS})$  of the DPS. The intersubband birefringence,  $\Delta n_{IS}(\lambda, i_{DPS})$ , was estimated by measuring the small amount of current dependent gain as a function of wavelength in the DPS and taking a Kramers-Kronig (KK) transformation [15] of the gain spectra.

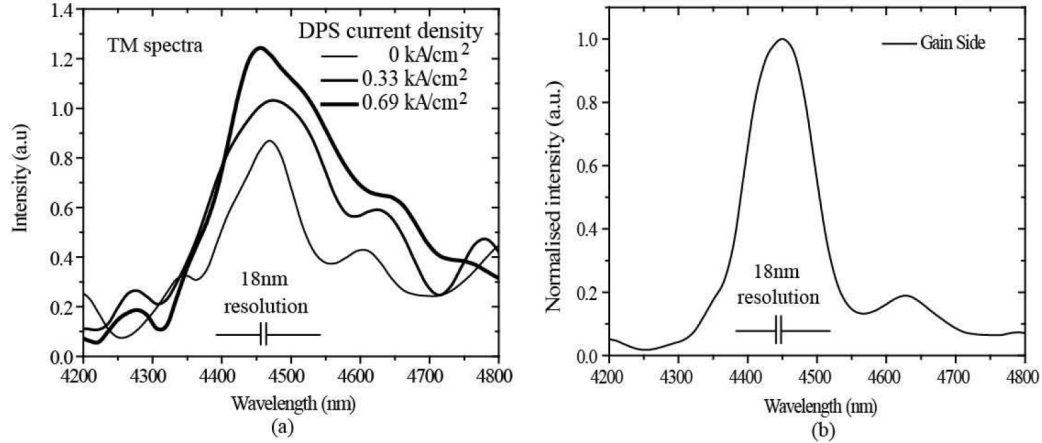


Fig. 4. (a) The TM spectrum of the sub-threshold EL spectra of a QCL incorporating an ITBW measured at various DC current densities injected into the DPS section. (b) Shows the sub-threshold TM EL spectra emitted from the facet next to the GS of the QCL-ITBW device.

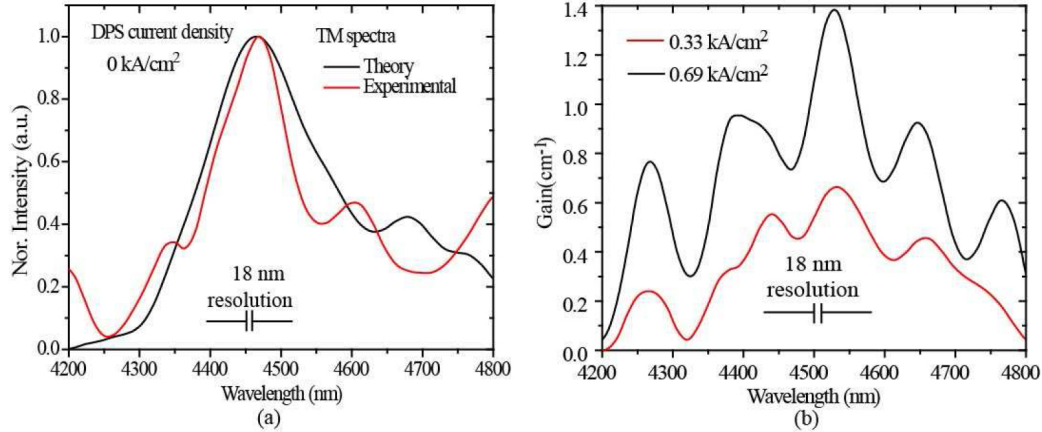


Fig. 5. (a) Experimental and Jones matrix model curve of the EL spectra of the ITBW device without current injected into the DPS section. (b) Measured gain spectra by injecting DC current into DPS section.

Figure 3 shows the experimental setup used to characterise the ITBW. The GS was driven with 100 ns duration current pulses ( $i_G = 4.2 \text{ kA/cm}^2$ ) with a 60 kHz repetition rate and the DPS section driven with DC current. The device was driven below the lasing threshold current to ensure single-pass operation and avoid multimode beating effects on PMCs [9, 16]. The TM fraction of the EL spectra was measured by placing a grid polariser between the ITBW device and FTIR (with the optical axis of the grid polariser parallel to the QCL waveguide).

Figure 4(a) shows the experimental TM response curve of the sub-threshold EL spectra emitted from the ITBW device with and without application of DC current into the DPS

section. When DC current ( $0.33 \text{ kA/cm}^2$  and  $0.69 \text{ kA/cm}^2$ ) is applied into the DPS section, increased transmission is observed through electrically modulating the gain [17].

To gain an insight into the operation of the QCL-ITBW device we compare the theory of the electro-optic birefringence and the Jones matrix description of the ITBW against the experimental results. To make the comparison we calculate the TM intensity fraction of the ITBW response function using Eq. (7) and multiply the result with the EL spectra measured from the GS facets, shown in Fig. 4(b). We assume that when no current is injected that the birefringence is entirely dominated by the material birefringence,  $\Delta n$ , thus in Eq. (1)  $\Delta n(\lambda, i_{DPS})$  replace with  $\Delta n$ , and we regard  $\Delta n$ , as an adjustable parameter. We take  $\Delta n$  as positive when the TE refractive index is greater than the TM refractive index. To fit the Jones matrix model to the experimental result, we adjust the value of  $\Delta n = 0.005$ , with  $\Delta n(\lambda, i_{DPS} = 0)$  with these values we obtain an approximate fit with the experimental result as is shown in Fig. 5(a).

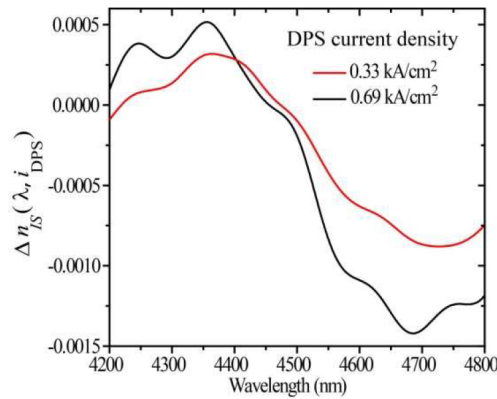


Fig. 6. Shows wavelength dependence of the refractive index which is calculated from the data using a Kramers-Kronig-transformation of the gain spectra.

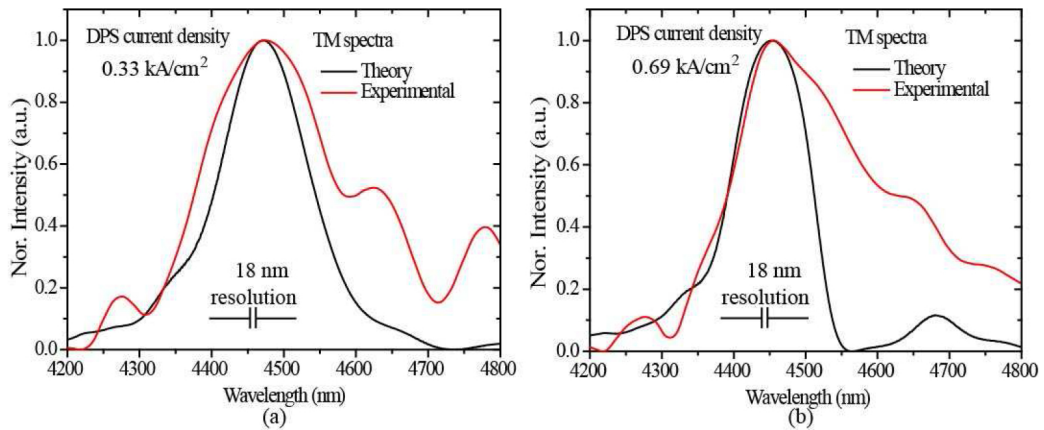


Fig. 7. The experimental EL spectra and Jones matrix model curve fit of the ITBW device (a)  $i_{DPS} = 0.33 \text{ kA/cm}^2$  and (b)  $i_{DPS} = 0.69 \text{ kA/cm}^2$ .

In order to fit the Jones matrix model with the experimental results, when DC current is applied into the DPS section, we require to estimate the value of  $\Delta n_{IS}(\lambda, i_{DPS})$ . To estimate the  $\Delta n_{IS}(\lambda, i_{DPS})$ , we required to measure the gain using  $I = I_0 e^{-\alpha L}$ , where  $I_0$  is TM EL intensity without the DPS current,  $I$  is the TM EL intensity with the DPS current,  $L$  is the length of the DPS section and  $-\alpha$  is the gain [18]. Fig. 5(b) shows the measured gain at DPS current of  $0.33 \text{ kA/cm}^2$  and  $0.69 \text{ kA/cm}^2$ , the modulation observed with a period of  $\sim 130 \text{ nm}$

in the gain spectra fits with a Fabry-Perot resonance associated with an additional  $\sim 40 \mu\text{m}$  long waveguide section between the end of PMC2 and the end facet (present due to imprecise cleaving). Using the KK relation [15] the gain measurement is transformed into  $\Delta n_{IS}(\lambda, i_{DPS})$  and shown in Fig. 6. In our model we include the electro-optic interband birefringence contribution,  $\Delta n_{IB}(i_{DPS})$ ,  $-0.0014$  and  $-0.0022$  were the values used, for  $0.33 \text{ kA/cm}^2$  and  $0.69 \text{ kA/cm}^2$  respectively that gave the best fit to the results.

So using the Jones matrix description, regarding  $\Delta n$  and  $\Delta n_{IB}(i_{DPS})$  as an adjustable parameters and calculating  $\Delta n_{IS}(\lambda, i_{DPS})$  from the gain measurements we obtain an approximate fit of the theory to the experimental results - see Fig. 7. Clearly, from Fig. 7(b), for high current densities and at the longer wavelengths there is substantial deviation of the theory from the measured response and some more refinements to the theory may be required, for example taking account of relative TE and TM losses [19], for a more complete understanding of the QCL-ITBW device.

### 5.2 Theory of laser operation with birefringent components

As is discussed in [12], the operation of a laser with polarisation dependent gain and including birefringent components is a more complex situation than the single pass case we have analysed in the previous section.

In general the resonance requirement for a resonator with birefringent components imposes the following conditions, first the phase change in a round trip must be a multiple of  $2\pi$  and second the polarisation must repeat after a round trip. These two conditions were expressed in the following equation:-

$$\mathbf{M}\mathbf{X} = \beta\mathbf{X} \quad (10)$$

Where  $\mathbf{M}$  is the round trip Jones matrix,  $\mathbf{X}$  is the two-component vector representing polarisation and  $\beta$  is a positive real number.

We can some insight into the operation of the laser by analysing the QCL that includes the ITBW optical circuit using Jones matrix method as described in [20]. In this analysis we will derive the phase conditions for laser action and so we ignore the amplitude of the modes and assume an amplitude normalised to one for all the components.

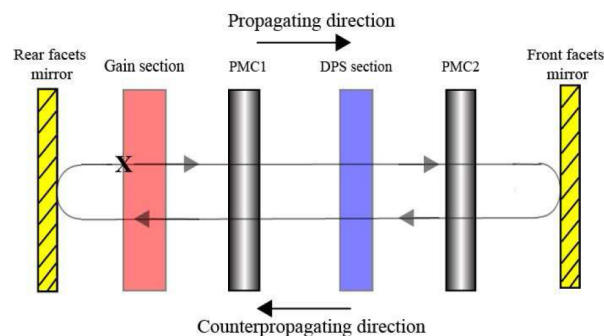


Fig. 8. Shows the equivalent optical circuit of ITBW for full round trip consideration. Figure also indicates the different components of optical circuit. The X marks the starting point for the round trip analysis

The Jones matrix of an ideal mirror ( $\sim 100\%$  reflection) is given by

$$\mathbf{MR} = \begin{bmatrix} 1 & 0 \\ 0 & -1 \end{bmatrix} \quad (11)$$

Using the convention described in [20], when the direction of light propagation through a reciprocal element is reversed, the Jones matrix of the element is transformed as follows:

$$\begin{bmatrix} m_1 & m_4 \\ m_3 & m_2 \end{bmatrix} \rightarrow \begin{bmatrix} m_1 & -m_3 \\ -m_4 & m_2 \end{bmatrix}$$

In the ITBW the only element modified by the above transformation is that of the PMC. Thus, the Jones matrix of the PMC for forward propagation is given by Eq. (3), and for counterpropagating light is given by

$$\mathbf{PMC}_{cp} = \frac{1}{\sqrt{2}} \begin{bmatrix} 1 & -1 \\ -1 & 1 \end{bmatrix} \quad (12)$$

The gain section (GS) provides gain for TM modes only, we approximate its effect on the polarisation by describing it as TM linear polariser. So the Jones matrix for GS is given by

$$\mathbf{GS} = \begin{bmatrix} 0 & 0 \\ 0 & 1 \end{bmatrix} \quad (13)$$

For the DPS section the Jones Matrix is given by Eq. (4). Starting at the position indicated on Fig. 8, the overall round trip Jones matrix,  $\mathbf{M}$ , for the ITBW is given by the following multiplication of matrices:-

$$\mathbf{M} = \mathbf{MR.GS.PMC}_{cp}.\mathbf{DPS.PMC}_{cp}.\mathbf{MR.PMC.DPS.PMC.GS} \quad (14)$$

$$= \begin{bmatrix} 0 & 0 \\ 0 & 0.5 + 0.5e^{-i\frac{4\pi\Delta n(\lambda, i_{DPS})L}{\lambda}} \end{bmatrix} \quad (15)$$

In the above we have followed the usual convention for the Jones matrices and omitted the phase factor that describes the common phase change for TM and TE modes as the wave travels through the component. In order to completely take account of the phase change in the round trip matrix we follow [12] and explicitly include the phase factor that is common for TM and TE modes. If we assign the following variables  $L_d$  is the average path for a single pass and the average refractive index for the round trip of the whole device  $n_d$  is as follows - then Eq. (15) becomes:-

$$\mathbf{M} = \begin{bmatrix} 0 & 0 \\ 0 & 0.5 + 0.5e^{-i\frac{4\pi\Delta n(\lambda, i_{DPS})L}{\lambda}} \end{bmatrix} e^{\frac{4\pi n_d L_d}{\lambda}} \quad (16)$$

Returning to Eq. (10) and setting  $\mathbf{X} = \begin{bmatrix} 0 \\ 1 \end{bmatrix}$  that is TM polarisation we have

$$\begin{bmatrix} 0 & 0 \\ 0 & 0.5 + 0.5e^{-i\frac{4\pi}{\lambda}(\Delta n(\lambda, i_{DPS}) + n_d L_d)} \end{bmatrix} \begin{bmatrix} 0 \\ 1 \end{bmatrix} = 0.5 + 0.5e^{-i\frac{4\pi}{\lambda}(\Delta n(\lambda, i_{DPS}) + n_d L_d)} \begin{bmatrix} 0 \\ 1 \end{bmatrix} \quad (17)$$

If we compare Eq. (17) with Eq. (10) then it is apparent that the exponential factor in Eq. (17) can only be a real number, that is 1, if the following phase condition is satisfied:-

$$\frac{1}{\lambda}(\Delta n(\lambda, i_{DPS}) + n_d L_d) = 0, 0.5, 1, 1.5, \dots \quad (18)$$

The laser modes in the QCL-ITBW device have to satisfy this phase condition.

In general  $n_d$  and  $L_d$  ( $L_d \approx$  total length of device) will be a weighted mixture of TM and TE refractive indices and paths as the laser mode swaps between TM and TE propagation. In an approximate approach we can expect that  $n_d \approx \frac{(n_{TM} + n_{TE})}{2}$  and  $n_{TM}$  effective index for the TM mode and  $n_{TE}$  effective index for the TE mode.

According to this simple analysis the mechanism for tuning the QCL-ITBW will be the injection current induced change of the phase condition given by Eq. (18) and although this gives some insight it does not include the effect of gain. For lasing to occur, in addition to the phase condition the optical gain experienced by the TM mode must equal the optical loss after a round trip. But it can be seen from Eq. (18) that the phase condition for positive feedback in the QCL-ITBW device can be tuned by injecting current in the DPS section and altering the  $\Delta n(\lambda, i_{DPS})$  factor. However, there will also be some injection current dependence of the  $n_d$  factor.

### 5.3 Measurement of laser operation with birefringent components

Figure 9 shows the observed emission spectra and tuning at different DC current densities from 0 to 1.11 kA/cm<sup>2</sup> applied to the DPS while a fixed pulsed peak current of  $1.3 \cdot I_{th}$  (6.8 kA/cm<sup>2</sup>) is applied to the GS. No single mode emission was observed and 24 nm discontinuous tuning with tuning rate of 25 nm/(kA/cm<sup>2</sup>) was recorded.

The spacing between the modes shown in Figs. 9(b) and 9(e) is 11 nm. According to the phase condition theory in section 5.2, Eq. (18), and using the values  $\Delta n(\lambda, i_{DPS})L \approx 10^3$  nm and  $n_d L_d \approx 10^6$  nm the mode spacing is dominated by the second factor and we would have expected mode spacing more like 0.7 nm. The 11 nm spacing that we do observe is consistent with there being sub-cavities present in the device.

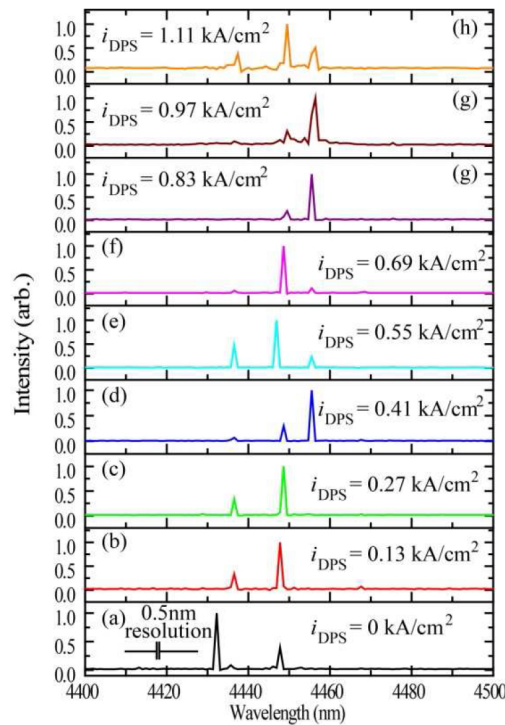


Fig.9. (a)- (h), Comparison of QCL-ITBW device output wavelengths for different DC current densities injected into the DPS section.

The PMC, employed in the ITBW, is an asymmetric waveguide and is formed by etching trenches into one side of the symmetric waveguide. The index contrast between symmetric and asymmetric waveguide can lead to reflections and we have from a finite- difference time-domain analysis estimated that the mirror reflectivity could be as large as 20%. This reflectivity may lead to the formation of sub-cavities. The 11 nm spacing that we observe is consistent with the gain section and DPS section acting as coupled sub-cavities. This is similar to the Vernier mode selection described in [21]. To eliminate this effect the interfaces between waveguide elements will need to be redesigned with optimized etch depths and tapering, ensuring smooth mode transitions without reflections.

## 6. Active polarisation control

For polarisation control measurements, the GS pulsed current was fixed at  $6.8 \text{ kA/cm}^2$  ( $1.3 * I_{th}$ ) and the current to the DPS section was varied between  $0 \text{ kA/cm}^2$  and  $0.97 \text{ kA/cm}^2$  in steps of  $0.13 \text{ kA/cm}^2$ . We measured the maximum transmission as a function of wire-grid polariser rotation angle ( $\varphi = 0^\circ$  to  $360^\circ$ ), where  $\varphi = 0^\circ$  is defined as the angle of the first maxima in transmission for the TM light through the wire grid polariser. This experiment does not completely determine the output polarisation; for example, it cannot discriminate between elliptical and linear polarisation but it does indicate that the polarisation state can be tuned by the current injected into the DPS.

Figure 10 shows the change in polarisation angle for maximum transmission as a function of the current injection into the DPS section. At  $0 \text{ kA/cm}^2$  a polarisation angle of  $37^\circ$  (TM fraction  $>$  TE fraction) was recorded and the polarisation angle increases upto  $82^\circ$  (TM fraction  $<$  TE fraction) with an applied DC current of  $0.97 \text{ kA/cm}^2$  with no further change in polarisation angle recorded above  $0.97 \text{ kA/cm}^2$  current.

In order to fit the polarisation angle measurement result with the Jones matrix model, we are required to estimate the phase retardation with and without the DPS current. Phase retardation of DPS section can be written as:

$$\delta_{DPS} = \delta(i_{DPS} = 0) + \delta(\lambda, i_{DPS}) \quad (19)$$

where,

$$\delta(i_{DPS} = 0) = \frac{2\pi\Delta n L}{\lambda} \quad (20)$$

and

$$\delta(\lambda, i_{DPS}) = \frac{2\pi\Delta n_{i_{DPS}} i_{DPS} L}{\lambda} \quad (21)$$

$\Delta\delta(i_{DPS} = 0)$  and  $\Delta\delta(\lambda, i_{DPS})$  are the phase retardation without and with DPS current,  $\Delta n$  is the birefringence before current is applied,  $\Delta n_{i_{DPS}}$  is the rate of change of birefringence with respect to current density,  $i_{DPS}$ , we assume a simple linear dependence. Equation (19) is substituted with the single pass Jones matrix Eqs. (7) and (8), the polarisation control operation is then analysed using Eq. (9). To fit the Jones matrix model to the experimental result, we adjust the value of  $\Delta n = 0.005$ , and,  $\Delta n_{i_{DPS}} = -1 \times 10^{-3} \text{ cm}^2/\text{kA}$  and with these values we obtain a good fit with the experimental result for lower current densities as is shown in Fig. 10. The discrepancy between the theory and experiment at higher current densities may be due the fact that the theory is incomplete and it does not take account of gain and loss for the TE and TM mode in the DPS section. At the higher DPS injection currents there will be some gain for TM light and this prevents the output from being completely TE polarised.

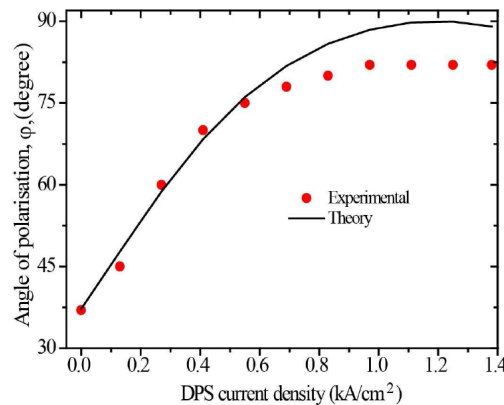


Fig.10. Shows the change in polarisation angle as various current densities are injected into the DPS section- 90 degrees corresponds to TE linear polarisation; the corresponding wavelength response is given in Fig. 9. The experimental results are compared with the Jones matrix theory- see Eq. (9).

## 7. Conclusions

We have described the design, modelling, fabrication and characterisation of integrated tunable birefringence waveguide (ITBW) for QCLs and demonstrated that an electro-optically tuneable birefringent property can be used in quantum cascade laser waveguides to achieve active control of polarisation and wavelength. We have used a simple Jones matrix description of the polarisation components in the QCL-ITBW device to construct a Jones matrix model that gives a good fit to the results obtained by measuring the output polarisation rotation as a function of DPS injection current. The model also helps explain the single pass experiments obtained by operating the device below the laser threshold. Further, from the Jones matrix description, we developed a simple phase only theory for the phase condition for modes in a laser with birefringent components, however applying our theory to the observed wavelength output spectra and DPS injection current tuning was complicated by sub-cavity effects.

By comparing the active polarisation angle measurement result with the Jones matrix model, we estimate the natural birefringence (no DPS current),  $\Delta n$  around 0.005 for the QCL employed in this work. This compares with the value that we obtain from the single pass measurements which is also 0.005. Also we can fit the dynamical polarisation angle control results if we assume a value of  $\Delta n_{DPS} = -1 \times 10^{-3} \text{ cm}^2/\text{kA}$  – the value indicated by the fit to the single pass measurements is  $-3.1 \times 10^{-3} \text{ cm}^2/\text{kA}$ . The results in Fig. 6 indicate that at the laser wavelengths, the intersubband contribution,  $\Delta n_{IS}$ , to birefringence is small at around  $1.0 \times 10^{-5}$  compared to the values given above. This value of  $\Delta n_{IS}$  is in approximate agreement for the values reported in [22, 23] for the linewidth enhancement factor for QCL albeit for different structures and wavelengths. Therefore we conclude that for laser operation, the electro-optic effect– the current dependent birefringence, is dominated by the interband transition and is not highly dispersive. This limits the wavelength tuning. To obtain significant wavelength tuning requires a redesign of the QCL active region.

Further experimental and theory work is required to obtain a more complete understanding of the operation of the QCL-ITBW device. Experimentally a QCL active region designed specifically to enhance the electro-optic properties is required and a variety of device architectures should be investigated. The theory of birefringent effects in lasers needs to be extended to include both amplitude and phase effects.

The polarisation angle control range is  $45^\circ$  and we are not aware of any other QCL device that is capable of electronically controlling the output polarisation. Active control of the

polarisation state of a QCL output could find applications in polarisation dependent spectroscopy [24] or in infrared ellipsometry [25].

**Acknowledgments**

The authors acknowledge helpful conversations with D. C. Hutchings. First Author, D. Dhirhe acknowledges the financial support from Ministry of Social Justice and Empowerment, Government of India, New Delhi, India.

# Bibliography

- [1] G. Wysocki. (2012) Iqclsw@ONLINE. [Online]. Available: <http://www.iqclsw.phys.ethz.ch/pres/wysocki18.pdf>
- [2] J. S. Yu, S. Slivken, A. Evans, and M. Razeghi, “High-performance continuous-wave operation of  $\lambda \sim 4.6 \mu\text{m}$  quantum-cascade lasers above room temperature,” *Quantum Electronics, IEEE Journal of*, vol. 44, no. 8, pp. 747–754, 2008.
- [3] K. Oda, N. Takato, and H. TOBA, “A wide-fsr waveguide double-ring resonator for optical fdm transmission systems,” *Lightwave Technology, Journal of*, vol. 9, no. 6, pp. 728–736, 1991.
- [4] Lumerical solutions@ONLINE. [Online]. Available: <http://www.lumerical.com/tcad-products/mode/>
- [5] Rsoft design@ONLINE. [Online]. Available: <http://www.rsoftdesign.com/>
- [6] D. Hutchings and B. Holmes, “A waveguide polarization toolset design based on mode beating,” *Photonics Journal, IEEE*, vol. 3, no. 3, pp. 450–461, 2011.
- [7] D. Dhirhe, T. J. Slight, B. M. Holmes, D. C. Hutchings, and C. N. Ironside, “Quantum cascade lasers with an integrated polarization mode converter,” *Opt. Express*, vol. 20, no. 23, pp. 25 711–25 717, Nov 2012. [Online]. Available: <http://www.opticsexpress.org/abstract.cfm?URI=oe-20-23-25711>

- [8] S. McDougall and C. Ironside, “Measurements of reverse and forward bias absorption and gain spectra in semiconductor laser material,” *Electronics Letters*, vol. 31, no. 25, pp. 2179–2181, 1995.
- [9] C. D. Farmer, “Fabrication and evaluation of In<sub>0.52</sub>Al<sub>0.48</sub>As/In<sub>0.53</sub>Ga<sub>0.47</sub>As/InP quantum cascade lasers,” PhD Thesis, Faculty of Engineering, University of Glasgow, September 2000.
- [10] J. Faist, F. Capasso, D. L. Sivco, C. Sirtori, A. L. Hutchinson, and A. Y. Cho, “Quantum cascade laser,” *Science*, vol. 264, no. 5158, pp. 553–556, 1994. [Online]. Available: <http://www.sciencemag.org/content/264/5158/553.abstract>
- [11] Y. Yao, A. J. Hoffman, and C. F. Gmachl, “Mid-infrared quantum cascade lasers,” *Nat Photon*, vol. 6, no. 7, pp. 432–439, 2012. [Online]. Available: <http://dx.doi.org/10.1038/nphoton.2012.143>
- [12] HITRAN. (2013) Hitran @ONLINE. [Online]. Available: <http://www.cfa.harvard.edu/hitran/>
- [13] D. T. Cassidy and J. Reid, “Atmospheric pressure monitoring of trace gases using tunable diode lasers,” *Appl. Opt.*, vol. 21, no. 7, pp. 1185–1190, Apr 1982. [Online]. Available: <http://ao.osa.org/abstract.cfm?URI=ao-21-7-1185>
- [14] R. A. Ellis, J. G. Murphy, E. Pattey, R. van Haarlem, J. M. O’Brien, and S. C. Herndon, “Characterizing a quantum cascade tunable infrared laser differential absorption spectrometer (qc-tildas) for measurements of atmospheric ammonia,” *Atmospheric Measurement Techniques*, vol. 3, no. 2, pp. 397–406, 2010. [Online]. Available: <http://www.atmos-meas-tech.net/3/397/2010/>
- [15] C. Banwell and E. Mccash, *Fundamentals of Molecular Spectroscopy*, 4th ed. McGraw-Hill Higher Education, 1994.

- [16] R. Q. Yang, "Infrared laser based on intersubband transitions in quantum wells," *Superlattices and Microstructures*, vol. 17, no. 1, pp. 77–, 1995. [Online]. Available: <http://www.sciencedirect.com/science/article/pii/S0749603685710178>
- [17] C.-H. Lin, R. Yang, D. Zhang, S. Murry, S. Pei, A. Allerman, and S. Kurtz, "Type-ii interband quantum cascade laser at 3.8  $\mu\text{m}$ ," *Electronics Letters*, vol. 33, no. 7, pp. 598–599, 1997.
- [18] I. Vurgaftman, J. Meyer, and L. Ram-Mohan, "Mid-ir vertical-cavity surface-emitting lasers," *Quantum Electronics, IEEE Journal of*, vol. 34, no. 1, pp. 147–156, 1998.
- [19] C. H. Grein, P. M. Young, and H. Ehrenreich, "Theoretical performance of InAs/ In<sub>x</sub>Ga(1-x)Sb superlattice-based midwave infrared lasers," *Journal of Applied Physics*, vol. 76, no. 3, pp. 1940–1942, 1994. [Online]. Available: <http://link.aip.org/link/?JAP/76/1940/1>
- [20] I. Vurgaftman, W. Bewley, C. Canedy, C. S. Kim, M. Kim, C. Merritt, J. Abell, and J. Meyer, "Interband cascade lasers with low threshold powers and high output powers," *Selected Topics in Quantum Electronics, IEEE Journal of*, vol. 19, no. 4, pp. 1 200 210–1 200 210, 2013.
- [21] S. Lundqvist, P. Kluczynski, R. Weih, M. von Edlinger, L. Nähle, M. Fischer, A. Bauer, S. Höfling, and J. Koeth, "Sensing of formaldehyde using a distributed feedback interband cascade laser emitting around 3493  $\mu\text{m}$ ," *Appl. Opt.*, vol. 51, no. 25, pp. 6009–6013, Sep 2012. [Online]. Available: <http://ao.osa.org/abstract.cfm?URI=ao-51-25-6009>
- [22] J. Faist, C. Gmachl, F. Capasso, C. Sirtori, D. L. Sivco, J. N. Baillargeon, and A. Y. Cho, "Distributed feedback quantum cascade lasers," *Applied Physics Letters*, vol. 70, no. 20, pp. 2670–2672, 1997. [Online]. Available: <http://link.aip.org/link/?APL/70/2670/1>
- [23] C. Gmachl, J. Faist, J. Bailargeon, F. Capasso, C. Sirtori, D. L. Sivco, S. N. G. Chu, and A. Y. Cho, "Complex-coupled quantum cascade

- distributed-feedback laser,” *Photonics Technology Letters, IEEE*, vol. 9, no. 8, pp. 1090–1092, 1997.
- [24] T. Slight, G. Tandoi, D. Revin, A. McKee, S. Zhang, W. Meredith, J. Cockburn, and C. Ironside, “ $\lambda=3.35\mu\text{m}$  distributed-feedback quantum-cascade lasers with high-aspect-ratio lateral grating,” *Photonics Technology Letters, IEEE*, vol. 23, no. 7, pp. 420–422, 2011.
- [25] R. Phelan, T. Slight, B. Kelly, J. O’Carroll, A. McKee, D. Revin, S. Zhang, A. B. Krysa, K. Kennedy, J. Cockburn, C. Ironside, W. Meredith, and J. O’Gorman, “Room-temperature operation of discrete-mode ingaas/alassb quantum-cascade laser with emission at  $3.6\mu\text{m}$ ,” *Photonics Technology Letters, IEEE*, vol. 22, no. 17, pp. 1273–1275, 2010.
- [26] J. Semmel, W. Kaiser, H. Hofmann, S. Höfling, and A. Forchel, “Single mode emitting ridge waveguide quantum cascade lasers coupled to an active ring resonator filter,” *Applied Physics Letters*, vol. 93, no. 21, p. 211106, 2008. [Online]. Available: <http://link.aip.org/link/?APL/93/211106/1>
- [27] P. Q. Liu, K. Sladek, X. Wang, J.-Y. Fan, and C. F. Gmachl, “Single-mode quantum cascade lasers employing a candy-cane shaped monolithic coupled cavity,” *Applied Physics Letters*, vol. 99, no. 24, p. 241112, 2011. [Online]. Available: <http://link.aip.org/link/?APL/99/241112/1>
- [28] J. Wojtas, J. Mikolajczyk, and Z. Bielecki, “Aspects of the application of cavity enhanced spectroscopy to nitrogen oxides detection,” *Sensors*, vol. 13, no. 6, pp. 7570–7598, 2013. [Online]. Available: <http://www.mdpi.com/1424-8220/13/6/7570>
- [29] P. Fuchs, J. Seufert, J. Koeth, J. Semmel, S. Höfling, L. Worschech, and A. Forchel, “Widely tunable quantum cascade lasers with coupled cavities for gas detection,” *Applied Physics Letters*, vol. 97, no. 18, p. 181111, 2010. [Online]. Available: <http://link.aip.org/link/?APL/97/181111/1>
- [30] B. G. Lee, J. Kansky, A. K. Goyal, C. Pflügl, L. Diehl, M. A. Belkin, A. Sanchez, and F. A. Capasso, “Beam combining of quantum

- cascade laser arrays,” *Opt. Express*, vol. 17, no. 18, pp. 16 216–16 224, Aug 2009. [Online]. Available: <http://www.opticsexpress.org/abstract.cfm?URI=oe-17-18-16216>
- [31] B. G. Lee, M. A. Belkin, R. Audet, J. MacArthur, L. Diehl, C. Pflügl, F. Capasso, D. C. Oakley, D. Chapman, A. Napoleone, D. Bour, S. Corzine, G. Höfler, and J. Faist, “Widely tunable single-mode quantum cascade laser source for mid-infrared spectroscopy,” *Applied Physics Letters*, vol. 91, no. 23, p. 231101, 2007. [Online]. Available: <http://link.aip.org/link/?APL/91/231101/1>
- [32] B. G. Lee, M. Belkin, C. Pflugl, L. Diehl, H. Zhang, R. Audet, J. MacArthur, D. Bour, S. Corzine, G. Huffer, and F. Capasso, “DFB quantum cascade laser arrays,” *Quantum Electronics, IEEE Journal of*, vol. 45, no. 5, pp. 554–565, 2009.
- [33] G. P. Luo, C. Peng, H. Q. Le, S. S. Pei, W.-Y. Hwang, B. Ishaug, J. Um, J. N. Baillargeon, and C.-H. Lin, “Grating-tuned external-cavity quantum-cascade semiconductor lasers,” *Applied Physics Letters*, vol. 78, no. 19, pp. 2834–2836, 2001. [Online]. Available: <http://link.aip.org/link/?APL/78/2834/1>
- [34] G. Luo, C. Peng, H. Le, S.-S. Pei, H. Lee, W.-Y. Hwang, B. Ishaug, and J. Zheng, “Broadly wavelength-tunable external cavity, mid-infrared quantum cascade lasers,” *Quantum Electronics, IEEE Journal of*, vol. 38, no. 5, pp. 486–494, 2002.
- [35] A. Hugi, R. Maulini, and J. Faist, “External cavity quantum cascade laser,” *Semiconductor Science and Technology*, vol. 25, no. 8, p. 083001, 2010. [Online]. Available: <http://stacks.iop.org/0268-1242/25/i=8/a=083001>
- [36] G. Totschnig, F. Winter, V. Pustogov, J. Faist, and A. Müller, “Mid-infrared external-cavity quantum-cascade laser,” *Opt. Lett.*, vol. 27, no. 20, pp. 1788–1790, Oct 2002. [Online]. Available: <http://ol.osa.org/abstract.cfm?URI=ol-27-20-1788>

- [37] B. G. Lee, J. Kinsky, A. K. Goyal, C. Pflügl, L. Diehl, M. A. Belkin, A. Sanchez, and F. A. Capasso, “Beam combining of quantum cascade laser arrays,” *Opt. Express*, vol. 17, no. 18, pp. 16 216–16 224, Aug 2009. [Online]. Available: <http://www.opticsexpress.org/abstract.cfm?URI=oe-17-18-16216>
- [38] C. Gmachl, D. L. Sivco, R. Colombelli, F. Capasso, and A. Y. Cho, “Ultra-broadband semiconductor laser,” *Nature*, vol. 64, no. 11, p. 1533, 2002. [Online]. Available: <http://dx.doi.org/10.1038/415883a>
- [39] M. Wojcik, M. Phillips, B. Cannon, and M. Taubman, “Gas-phase photoacoustic sensor at 8.41  $\mu$ m using quartz tuning forks and amplitude-modulated quantum cascade lasers,” *Applied Physics B*, vol. 85, no. 2-3, pp. 307–313, 2006. [Online]. Available: <http://dx.doi.org/10.1007/s00340-006-2394-8>
- [40] S.-J. Choi, Z. Peng, Q. Yang, S. J. Choi, and P. D. Dapkus, “Tunable narrow linewidth all-buried heterostructure ring resonator filters using vernier effects,” *Photonics Technology Letters, IEEE*, vol. 17, no. 1, pp. 106–108, 2005.
- [41] T. Segawa, S. Matsuo, T. Kakitsuka, T. Sato, Y. Kondo, and H. Suzuki, “Tunable double-ring-resonator-coupled laser over full c-band with low tuning current,” in *Indium Phosphide Related Materials, 2007. IPRM '07. IEEE 19th International Conference on*, 2007, pp. 598–601.
- [42] B. Liu, A. Shakouri, and J. Bowers, “Wide tunable double ring resonator coupled lasers,” *Photonics Technology Letters, IEEE*, vol. 14, no. 5, pp. 600–602, 2002.
- [43] D. G. Kim and Y.-W. Choi, “Wide tuning characteristics of double-ring coupled lasers,” *Optics Communications*, vol. 282, no. 13, pp. 2516 – 2523, 2009. [Online]. Available: <http://www.sciencedirect.com/science/article/pii/S0030401809002806>

- [44] R. Todt, T. Jacke, R. Laroy, G. Morthier, and M. C. AMANN, “Demonstration of vernier effect tuning in tunable twin-guide laser diodes,” *Optoelectronics, IEE Proceedings -*, vol. 152, no. 2, pp. 66–71, 2005.
- [45] G. Almogy, A. Shakouri, and A. Yariv, “Observation of birefringence induced by intersubband transitions in quantum wells,” *Applied Physics Letters*, vol. 63, no. 20, pp. 2720–2722, 1993. [Online]. Available: <http://link.aip.org/link/?APL/63/2720/1>
- [46] Y. Shani, R. Alferness, T. Koch, U. Koren, M. Oron, B. I. Miller, and M. G. Young, “Polarization rotation in asymmetric periodic loaded rib waveguides,” *Applied Physics Letters*, vol. 59, no. 11, pp. 1278–1280, 1991. [Online]. Available: <http://link.aip.org/link/?APL/59/1278/1>
- [47] M. Razeghi, “Quantum cascade lasers,” in *Technology of Quantum Devices*. Springer US, 2010, pp. 271–319. [Online]. Available: <http://dx.doi.org/10.1007/978-1-4419-1056-1.7>
- [48] J. Cockburn, “Mid-infrared quantum cascade lasers,” in *Mid-infrared Semiconductor Optoelectronics*, ser. Springer Series in Optical Sciences, A. Krier, Ed. Springer London, 2006, vol. 118, pp. 323–355. [Online]. Available: <http://dx.doi.org/10.1007/1-84628-209-8.10>
- [49] C. Gmachl, F. Capasso, D. L. Sivco, and A. Y. Cho, “Recent progress in quantum cascade lasers and applications,” *Reports on Progress in Physics*, vol. 64, no. 11, p. 1533, 2001. [Online]. Available: <http://stacks.iop.org/0034-4885/64/i=11/a=204>
- [50] J. Faist, *Quantum Cascade Lasers*. OUP Oxford, 2013. [Online]. Available: [http://www.amazon.co.uk/Quantum-Cascade-Lasers-J%C3%A9r%C3%B4me-Faist/dp/0198528248/ref=la\\_B00BQC5YUM\\_1\\_1?ie=UTF8&qid=1369238244&sr=1-1](http://www.amazon.co.uk/Quantum-Cascade-Lasers-J%C3%A9r%C3%B4me-Faist/dp/0198528248/ref=la_B00BQC5YUM_1_1?ie=UTF8&qid=1369238244&sr=1-1)
- [51] R. Paiella, Ed., *Quantum Cascade Lasers*. McGraw-Hill Professional, 2006. [Online]. Available: <http://www.amazon.co>

uk/Intersubband-Transitions-Structures-McGraw-Hill-Nanoscience/dp/0071457925/ref=sr\_1\_sc\_2?s=books&ie=UTF8&qid=1369238587&sr=1-2-spell&keywords=intersubband+transsition

- [52] J. Yu, S. Slivken, A. Evans, and M. Razeghi, “High-performance continuous-wave operation of  $\lambda = 4.6 \mu\text{m}$  quantum-cascade lasers above room temperature,” *IEEE Journal of Quantum Electronics*, vol. 44, no. 8, pp. 747–754, 2008, cited By (since 1996)23. [Online]. Available: <http://www.scopus.com/inward/record.url?eid=2-s2.0-58149162647&partnerID=40&md5=4375227386432cd61dbc9e75f87c3cf9>
- [53] C. C. Nshii, “Tunable mid-infrared light sources based on intersubband transitions.” Ph.D. dissertation, School of Engineering, University of Glasgow, 2011.
- [54] vistec. (2013) @online. [Online]. Available: <http://www.vistec-semi.com/company/overview/?L=6>
- [55] Z. CORPORATION. (2013) Zeon corporation. [Online]. Available: <http://www.nanophys.kth.se/nanophys/facilities/nfl/resists/zep520a-7-2.pdf>
- [56] C. Nshii, C. Ironside, M. Sorel, T. Slight, S. Zhang, D. Revin, and J. Cockburn, “Quantum cascade ring lasers: Unidirectional operation and coupled ring tuning,” in *CLEO/Europe and EQEC 2011 Conference Digest*. Optical Society of America, 2011, p. CB4<sub>2</sub>. [Online]. Available: [http://www.opticsinfobase.org/abstract.cfm?URI=CLEO\\_Europe-2011-CB4\\_2](http://www.opticsinfobase.org/abstract.cfm?URI=CLEO_Europe-2011-CB4_2)
- [57] R. Phelan, T. Slight, B. Kelly, J. O’Carroll, A. McKee, D. Revin, S. Zhang, A. B. Krysa, K. Kennedy, J. Cockburn, C. Ironside, W. Meredith, and J. O’Gorman, “Room-temperature operation of discrete-mode InGaAs-AlAsSb quantum-cascade laser with emission at  $\lambda = 3.3 \mu\text{m}$ ,” *Photonics Technology Letters, IEEE*, vol. 22, no. 17, pp. 1273–1275, 2010.
- [58] A. F. Harvey, *Microwave engineering*, 2nd ed. Academic Press, 1963.

- [59] D. L. Lee, *Electromagnetic Principles of Integrated Optics*, 1st ed. John Wiley & Sons, 1986.
- [60] C. C. Lee, C. M. Wang, C. L. Xu, J. Y. Chen, J. Y. Chang, Y. M. Liao, and G. C. Chi, "Nanostructured diffractive optical elements on sinx membrane for uv-visible regime applications," pp. 170–179, 2004. [Online]. Available: [+http://dx.doi.org/10.1117/12.559296](http://dx.doi.org/10.1117/12.559296)
- [61] P. Hansen, G. Raybon, M.-D. Chien, U. Koren, B. Miller, M. Young, J.-M. Verdiell, and C. Burrus, "A 1.54-  $\mu$  m monolithic semiconductor ring laser: Cw and mode-locked operation," *Photonics Technology Letters, IEEE*, vol. 4, no. 5, pp. 411–413, 1992.
- [62] A. S.-H. Liao and S. Wang, "Semiconductor injection lasers with a circular resonator," *Applied Physics Letters*, vol. 36, no. 10, pp. 801–803, 1980. [Online]. Available: <http://link.aip.org/link/?APL/36/801/1>
- [63] T. Krauss, R. M. DeLaRue, I. Gontijo, P. J. R. Laybourn, and J. S. Roberts, "Strip-loaded semiconductor ring lasers employing multimode interference output couplers," *Applied Physics Letters*, vol. 64, no. 21, pp. 2788–2790, 1994. [Online]. Available: <http://link.aip.org/link/?APL/64/2788/1>
- [64] O. Bryngdahl, "Image formation using self-imaging techniques," *J. Opt. Soc. Am.*, vol. 63, no. 4, pp. 416–419, Apr 1973. [Online]. Available: <http://www.opticsinfobase.org/abstract.cfm?URI=josa-63-4-416>
- [65] L. Soldano and E. C. M. Pennings, "Optical multi-mode interference devices based on self-imaging: principles and applications," *Lightwave Technology, Journal of*, vol. 13, no. 4, pp. 615–627, 1995.
- [66] M. Lerttamrab, S. L. Chuang, C. Gmachl, D. L. Sivco, F. Capasso, and A. Y. Cho, "Linewidth enhancement factor of a type-i quantum-cascade laser," *Journal of Applied Physics*, vol. 94, no. 8, pp. 5426–5428, 2003. [Online]. Available: <http://link.aip.org/link/?JAP/94/5426/1>

- [67] A. K. Wjcik, N. Yu, F. Capasso, and A. Belyanin, “Nonlinear optical interactions of laser modes in quantum cascade lasers,” *Journal of Modern Optics*, vol. 58, no. 9, pp. 727–742, 2011. [Online]. Available: <http://www.tandfonline.com/doi/abs/10.1080/09500340.2011.573590>
- [68] C. Banwell and E. Mccash, *Fundamentals of Molecular Spectroscopy*, 4th ed. McGraw-Hill Higher Education; 4 edition, 1 Jun 1994.
- [69] J. C. MORRIS, “Comments on the measurement of emittance of the global radiation source,” *J. Opt. Soc. Am.*, vol. 51, no. 7, pp. 798–1–799, Jul 1961. [Online]. Available: <http://www.opticsinfobase.org/abstract.cfm?URI=josa-51-7-798.1>
- [70] M. Garcia, E. Normand, C. Stanley, C. Ironside, C. Farmer, G. Duxbury, and N. Langford, “An algaasgaas quantum cascade laser operating with a thermoelectric cooler for spectroscopy of NH<sub>3</sub>,” *Optics Communications*, vol. 226, no. 16, pp. 39 – 43, 2003. [Online]. Available: <http://www.sciencedirect.com/science/article/pii/S0030401803018704>
- [71] Y. Shani, R. Alferness, T. Koch, U. Koren, M. Oron, B. I. Miller, and M. G. Young, “Polarization rotation in asymmetric periodic loaded rib waveguides,” *Applied Physics Letters*, vol. 59, no. 11, pp. 1278–1280, 1991. [Online]. Available: <http://link.aip.org/link/?APL/59/1278/1>
- [72] V. P. Tzolov and M. Fontaine, “A passive polarization converter free of longitudinally-periodic structure,” *Optics Communications*, vol. 127, no. 13, pp. 7 – 13, 1996. [Online]. Available: <http://www.sciencedirect.com/science/article/pii/0030401896000399>
- [73] M. Fontaine, “Theoretical approach to investigating cross-phase modulation phenomena in waveguides with arbitrary cross sections,” *J. Opt. Soc. Am. B*, vol. 14, no. 6, pp. 1444–1452, Jun 1997. [Online]. Available: <http://josab.osa.org/abstract.cfm?URI=josab-14-6-1444>

- [74] H. El-Refaei and D. Yevick, "An optimized InGaAsP-InP polarization converter employing asymmetric rib waveguides," *Lightwave Technology, Journal of*, vol. 21, no. 6, pp. 1544–1548, 2003.
- [75] H. El-Refaei, D. Yevick, and T. Jones, "Slanted-rib waveguide InGaAsP-InP polarization converters," *Lightwave Technology, Journal of*, vol. 22, no. 5, pp. 1352–1357, 2004.
- [76] L. Augustin, J. J. G. M. Van der Tol, E.-J. Geluk, and M. Smit, "Short polarization converter optimized for active-passive integration in InGaAsP-InP," *Photonics Technology Letters, IEEE*, vol. 19, no. 20, pp. 1673–1675, 2007.
- [77] C. Brooks, P. E. Jessop, H. Deng, D. O. Yevick, and G. Tarr, "Polarization rotating waveguides in silicon on insulator," in *Optical Amplifiers and Their Applications/Integrated Photonics Research*. Optical Society of America, 2004, p. IFG4. [Online]. Available: <http://www.opticsinfobase.org/abstract.cfm?URI=IPR-2004-IFG4>
- [78] U. Khalique, Y. C. Zhu, J. J. van der Tol, L. M. Augustin, R. Hanfoug, F. H. Groen, P. J. van Veldhoven, M. K. Smit, M. van de Moosdijk, W. de Laat, and K. Simon, "Ultrashort polarization converter on InP/InGaAsP fabricated by optical lithography," in *Integrated Photonics Research and Applications/Nanophotonics for Information Systems*. Optical Society of America, 2005, p. IWA3. [Online]. Available: <http://www.opticsinfobase.org/abstract.cfm?URI=IPRA-2005-IWA3>
- [79] B. Holmes and D. Hutchings, "Realization of novel low-loss monolithically integrated passive waveguide mode converters," *Photonics Technology Letters, IEEE*, vol. 18, no. 1, pp. 43–45, 2006.
- [80] B. M. Holmes and D. C. Hutchings, "High efficiency and low loss fully integrated passive waveguide mode converters," in *Lasers and Electro-Optics, 2006 and 2006 Quantum Electronics and Laser Science Conference. CLEO/QELS 2006. Conference on*, 2006, pp. 1–2.

- [81] D. Hutchings and B. Holmes, "A waveguide polarization toolset design based on mode beating," *Photonics Journal, IEEE*, vol. 3, no. 3, pp. 450–461, 2011.
- [82] W. Huang and Z. Mao, "Polarization rotation in periodic loaded rib waveguides," *Lightwave Technology, Journal of*, vol. 10, no. 12, pp. 1825–1831, 1992.
- [83] F.-J. Mustieles, E. Ballesteros, and F. Hernandez-Gil, "Multimodal analysis method for the design of passive TE/TM converters in integrated waveguides," *Photonics Technology Letters, IEEE*, vol. 5, no. 7, pp. 809–811, 1993.
- [84] M. Gustavsson, "Analysis of polarization independent optical amplifiers and filters based on polarization rotation in periodically asymmetric waveguides," *Quantum Electronics, IEEE Journal of*, vol. 29, no. 4, pp. 1168–1178, 1993.
- [85] S. S. A. Obayya, B. M. A. Rahman, and H. A. El-Mikati, "Vector beam propagation analysis of polarization conversion in periodically loaded waveguides," *Photonics Technology Letters, IEEE*, vol. 12, no. 10, pp. 1346–1348, 2000.
- [86] J. Bregenzler, S. McMaster, M. Sorel, B. Holmes, and D. Hutchings, "Compact polarization mode converter monolithically integrated within a semiconductor laser," *Lightwave Technology, Journal of*, vol. 27, no. 14, pp. 2732–2736, 2009.
- [87] B. M. Holmes, M. A. Naeem, D. C. Hutchings, J. H. Marsh, and A. E. Kelly, "A semiconductor laser with monolithically integrated dynamic polarization control," *Opt. Express*, vol. 20, no. 18, pp. 20 545–20 550, Aug 2012. [Online]. Available: <http://www.opticsexpress.org/abstract.cfm?URI=oe-20-18-20545>
- [88] N. Yu, Q. J. Wang, C. Pflügl, L. Diehl, F. Capasso, T. Edamura, S. Furuta, M. Yamanishi, and H. Kan, "Semiconductor lasers with integrated plasmonic polarizers," *Applied Physics Letters*, vol. 94, no. 15, p. 151101, 2009. [Online]. Available: <http://link.aip.org/link/?APL/94/151101/1>

- [89] P. Kluczynski, S. Lundqvist, J. Westberg, and O. Axner, “Faraday rotation spectrometer with sub-second response time for detection of nitric oxide using a cw DFB quantum cascade laser at  $5.33\ \mu\text{m}$ ,” *Applied Physics B*, vol. 103, no. 2, pp. 451–459, 2011. [Online]. Available: <http://dx.doi.org/10.1007/s00340-010-4336-8>
- [90] A. Roeseler, *Infrared Spectroscopic Ellipsometry*. Akademie-Verlag, 1990.
- [91] D. Dhirhe, T. J. Slight, B. M. Holmes, D. C. Hutchings, and C. N. Ironside, “Quantum cascade lasers with an integrated polarization mode converter,” *Opt. Express*, vol. 20, no. 23, pp. 25 711–25 717, Nov 2012. [Online]. Available: <http://www.opticsexpress.org/abstract.cfm?URI=oe-20-23-25711>
- [92] M. A. Naeem, B. M. Holmes, A. E. Kelly, J. H. Marsh, and D. C. Hutchings, “Passive polarization mode convertor monolithically integrated within a semiconductor laser,” in *Photonics Conference (IPC), 2012 IEEE*, 2012, pp. 326–327.
- [93] Yariv A. and Yeh P., *Optical Waves in Crystals*, 1st ed. John Wiley & Sons, New York, USA, 1984.
- [94] Y. Bai, S. Slivken, Q. Y. Lu, N. Bandyopadhyay, and M. Razeghi, “Angled cavity broad area quantum cascade lasers,” *Applied Physics Letters*, vol. 101, no. 8, p. 081106, 2012. [Online]. Available: <http://link.aip.org/link/?APL/101/081106/1>
- [95] R. Phelan, T. Slight, B. Kelly, J. O’Carroll, A. McKee, D. Revin, S. Zhang, A. B. Krysa, K. Kennedy, J. Cockburn, C. Ironside, W. Meredith, and J. O’Gorman, “Room-temperature operation of discrete-mode InGaAs-AlAsSb quantum-cascade laser with emission at  $\lambda = 3.3\ \mu\text{m}$ ,” *Photonics Technology Letters, IEEE*, vol. 22, no. 17, pp. 1273–1275, 2010.
- [96] J. Faist, C. Gmachl, F. Capasso, C. Sirtori, D. L. Sivco, J. N. Baillargeon, and A. Y. Cho, “Distributed feedback quantum cascade lasers,” *Applied*

- Physics Letters*, vol. 70, no. 20, pp. 2670–2672, 1997. [Online]. Available: <http://link.aip.org/link/?APL/70/2670/1>
- [97] T. Slight, G. Tandoi, D. Revin, A. McKee, S. Zhang, W. Meredith, J. Cockburn, and C. Ironside, “Distributed-feedback quantum-cascade lasers with high-aspect-ratio lateral grating,” *Photonics Technology Letters, IEEE*, vol. 23, no. 7, pp. 420–422, 2011.
- [98] T. J. S. D. Dhirhe, B. M. Holmes, D. C. Hutchings, and C. N. Ironside, “An integrated tunable birefringent filter for quantum cascade lasers.” International Quantum Cascade Lasers School & Workshop 2012, Vienna, Austria, 26 Sept. 2012., 2012.
- [99] B. M. Holmes, M. A. Naeem, D. C. Hutchings, J. H. Marsh, and A. E. Kelly, “A semiconductor laser with monolithically integrated dynamic polarization control,” *Opt. Express*, vol. 20, no. 18, pp. 20 545–20 550, Aug 2012. [Online]. Available: <http://www.opticsexpress.org/abstract.cfm?URI=oe-20-18-20545>
- [100] B. Lyot, “Optical apparatus with wide field using interference of polarized light,” *C. R. Acad. Sci.*, vol. 197, p. 1593, (1933).
- [101] J. W. EVANS, “Solc birefringent filter,” *J. Opt. Soc. Am.*, vol. 48, no. 3, pp. 142–143, Mar 1958. [Online]. Available: <http://www.opticsinfobase.org/abstract.cfm?URI=josa-48-3-142>
- [102] A. Kasapi, G. Y. Yin, and M. Jain, “Pulsed ti:sapphire laser seeded off the gain peak,” *Appl. Opt.*, vol. 35, no. 12, pp. 1999–2004, Apr 1996. [Online]. Available: <http://ao.osa.org/abstract.cfm?URI=ao-35-12-1999>
- [103] G. Holtom and O. Teschke, “Design of birefringent filter for high-power dye lasers,” *Quantum Electronics, IEEE Journal of*, vol. 10, no. 8, pp. 577–579, 1974.
- [104] I. Moreno, J. A. Davis, T. M. Hernandez, D. M. Cottrell, and D. Sand, “Complete polarization control of light from a liquid crystal spatial light

- modulator,” *Opt. Express*, vol. 20, no. 1, pp. 364–376, Jan 2012. [Online]. Available: <http://www.opticsexpress.org/abstract.cfm?URI=oe-20-1-364>
- [105] I. Bar-Joseph, C. Klingshirn, D. A. B. Miller, D. S. Chemla, U. Koren, and B. I. Miller, “Quantum-confined stark effect in ingaas/inp quantum wells grown by organometallic vapor phase epitaxy,” *Applied Physics Letters*, vol. 50, no. 15, pp. 1010–1012, 1987. [Online]. Available: <http://link.aip.org/link/?APL/50/1010/1>
- [106] R. P. G. Karunasiri, Y. J. Mii, and K. Wang, “Tunable infrared modulator and switch using stark shift in step quantum wells,” *Electron Device Letters, IEEE*, vol. 11, no. 5, pp. 227–229, 1990.
- [107] G. Almogy, A. Shakouri, and A. Yariv, “Observation of birefringence induced by intersubband transitions in quantum wells,” *Applied Physics Letters*, vol. 63, no. 20, pp. 2720–2722, 1993. [Online]. Available: <http://link.aip.org/link/?APL/63/2720/1>
- [108] A. GERRARD, *Introduction to Matrix Methods in Optics (Pure & Applied Optics)*. Wiley-Blackwell, 1995.
- [109] A. Kemp, G. Friel, T. Lake, R. Conroy, and B. Sinclair, “Polarization effects, birefringent filtering, and single-frequency operation in lasers containing a birefringent gain crystal,” *Quantum Electronics, IEEE Journal of*, vol. 36, no. 2, pp. 228–235, 2000.
- [110] D. Hutchings, M. Sheik-Bahae, D. Hagan, and E. Stryland, “Kramers-krnig relations in nonlinear optics,” *Optical and Quantum Electronics*, vol. 24, no. 1, pp. 1–30, 1992. [Online]. Available: <http://dx.doi.org/10.1007/BF01234275>
- [111] D. Hutchings and B. Holmes, “A waveguide polarization toolset design based on mode beating,” *Photonics Journal, IEEE*, vol. 3, no. 3, pp. 450–461, 2011.

- [112] J. Bregenzer, S. McMaster, M. Sorel, B. Holmes, and D. Hutchings, “Compact polarization mode converter monolithically integrated within a semiconductor laser,” *Lightwave Technology, Journal of*, vol. 27, no. 14, pp. 2732–2736, 2009.
- [113] J. Teissier, S. Laurent, C. Manquest, C. Sirtori, A. Bousseksou, J. R. Coudevylle, R. Colombelli, G. Beaudoin, and I. Sagnes, “Electrical modulation of the complex refractive index in mid-infrared quantum cascade lasers,” *Opt. Express*, vol. 20, no. 2, pp. 1172–1183, Jan 2012. [Online]. Available: <http://www.opticsexpress.org/abstract.cfm?URI=oe-20-2-1172>
- [114] D. G. Revin, J. W. Cockburn, S. Menzel, Q. Yang, C. Manz, and J. Wagner, “Waveguide optical losses in ingaas/alassb quantum cascade laser,” *Journal of Applied Physics*, vol. 103, no. 4, p. 043106, 2008. [Online]. Available: <http://link.aip.org/link/?JAP/103/043106/1>
- [115] T. Aellen, R. Maulini, R. Terazzi, N. Hoyler, M. Giovannini, J. Faist, S. Blaser, and L. Hvozdar, “Direct measurement of the linewidth enhancement factor by optical heterodyning of an amplitude-modulated quantum cascade laser,” *Applied Physics Letters*, vol. 89, no. 9, p. 091121, 2006. [Online]. Available: <http://link.aip.org/link/?APL/89/091121/1>
- [116] P. Kluczynski, S. Lundqvist, J. Westberg, and O. Axner, “Faraday rotation spectrometer with sub-second response time for detection of nitric oxide using a cw dfb quantum cascade laser at 5.33  $\mu\text{m}$ ,” *Applied Physics B*, vol. 103, no. 2, pp. 451–459, 2011. [Online]. Available: <http://dx.doi.org/10.1007/s00340-010-4336-8>
- [117] H. Fujiwara, *Spectroscopic Ellipsometry: Principles and Applications*. Wiley-Blackwell, 2007.
- [118] N. Yu, Q. J. Wang, C. Pflugl, L. Diehl, F. Capasso, T. Edamura, S. Furuta, M. Yamanishi, and H. Kan, “Semiconductor lasers with integrated plasmonic polarizers,” *Applied Physics Letters*, vol. 94, no. 15, p. 151101, 2009. [Online]. Available: <http://link.aip.org/link/?APL/94/151101/1>

- 
- [119] M. Gould, A. Pomerene, C. Hill, S. Ocheltree, Y. Zhang, T. Baehr-Jones, and M. Hochberg, “Ultra-thin silicon-on-insulator strip waveguides and mode couplers,” *Applied Physics Letters*, vol. 101, no. 22, p. 221106, 2012. [Online]. Available: <http://link.aip.org/link/?APL/101/221106/1>
- [120] B. Holmes and D. Hutchings, “Realization of novel low-loss monolithically integrated passive waveguide mode converters,” *Photonics Technology Letters, IEEE*, vol. 18, no. 1, pp. 43–45, 2006.